4-21-1990

Proceedings of the Twentieth Annual Biochemical Engineering Symposium

L. E. Erickson
Kansas State University

L. T. Fan
Kansas State University

PROCEEDINGS
OF THE TWENTIETH ANNUAL
BIOCHEMICAL ENGINEERING SYMPOSIUM

Report No. 88

Edited by

L.E. Erickson

L.T. Fan

April 21, 1990

INSTITUTE FOR SYSTEMS
DESIGN AND OPTIMIZATION

Kansas State University - Manhattan

PROCEEDINGS OF THE TWENTIETH ANNUAL BIOCHEMICAL ENGINEERING SYMPOSIUM

Editors

L.E. Erickson and L.T. Fan

Department of Chemical Engineering
Durland Hall
Kansas State University
Manhattan, Kansas 66502-5102

April 21, 1990

PREFACE

The 20-th Annual Biochemical Engineering Symposium was held at Kansas State University on April 21, 1990. The objectives of the symposium were to provide: (i) a forum for informal discussion of biochemical engineering research being conducted at the participating institutions and (ii) an opportunity for students to present and publish their work.

Twenty-eight papers presented at the symposium are included in this proceedings. Some of the papers describe the progress of ongoing projects, and others contain the results of completed projects. Only brief summaries are given of the papers that will be published in full elsewhere. The program of the symposium and a list of the participants are included in the proceedings.

We would like to thank all authors for participating in the symposium and for preparing the papers for the proceedings. Financial support from the Kansas State University Department of Chemical Engineering, Center for Hazardous Substance Research, Hazardous Substance Research Center for U.S. EPA Regions 7 and 8, and the National Science Foundation is gratefully acknowledged.

Larry E. Erickson
L.T. Fan
Editors

December 31, 1990

TABLE OF CONTENTS

20th ANNUAL BIOCHEMICAL ENGINEERING SYMPOSIUM
KANSAS STATE UNIVERSITY
DURLAND HALL, ROOM 173 (PASLAY LECTURE HALL)
April 21, 1990

8:20 Welcome and Introductions
8:30 Continuous Yeast Fermentation with Cell Recycle for Protein Overproduction - C. Y. Lee, R. H. Davis, and R. A. Sclafani, Univ. of Colorado
8:50 Micromixing and its Relationship to Metabolism and Yields in S. Cerevisiae - K. S. Wenger and E.H. Dunlop, Colorado State Univ.
9:10 Production, Purification, and Hydrolysis Kinetics of Wild-Type and Mutant Glucoamylases from Aspergillus awamori - U. Bakir, P. D. Oates, and H. M. Chen, Iowa State Univ.
9:30 Dynamic Modeling of Lymphocyte Interactions - B. Vant-Hall and D. Kompala, Univ. of Colorado
9:50 Break to View Posters
10:20 Dynamic Modeling of Free Energy Transduction Across a Biological Cell: A Stochastic Approach - B. C. Shen, S. T. Chou, Y. Y. Chiu, and L. T. Fan, Kansas State Univ.
10:40 Adaptive Control of Solid Substrate Fermentation with Rhizopus oligosporus - D. Ryoo, V. G. Murphy, R. Tengerdy, and M. N. Karim, Colorado State Univ.
11:00 Electrokinetic and Extractive Isolation of Bacterial Vesicles and Ribosomes - D. Hawker, R. H. Davis, and P. Todd, Univ. of Colorado
11:20 Simulation and Real Time Application of Dynamic Programming for Fermentative Ethanol Production - S. L. Rivera, and M. N. Karim, Colorado State Univ.
11:40 Lunch and Poster Viewing
1:20 Kinetics of Growth, Acclimation and PCP-degradation by Pseudomonas cepacia - R. Rayavarapu, S. K. Banerji, and R. K. Bajpai, Univ. of Missouri
1:40 Modeling of the Bioremediation of Contaminated Soil Aggregates: A Phenomenological Approach - S. Dhawan, L. E. Erickson and L. T. Fan, Kansas State Univ.
2:00 Adsorption of Glucoamylase-I from Aspergillus niger on Raw Starch - B. K. Dalmia, Z. L. Nikolov, Iowa State Univ.
2:20 Break to View Posters
2:50 The Effects of Foreign Protein Expression on the Growth Characteristics of Recombinant Mammalian Cells - J. A. Kern and D. S. Kompala, Univ. of Colorado
3:10 Structured Mathematical Modeling of Xylose Fermentation - A. K. Hilaly, M. N. Karim, J. C. Linden, and S. Lastick, Colorado State Univ.
3:30 A New Culture Medium for Carbon-Limited Growth of Bacillus thuringiensis - W. M. Liu and R. K. Bajpai, Univ. of Missouri
3:50 Poster Viewing and Laboratory Tours

POSTER PAPERS

Analytical Determination of Technically Produced Oligosaccharides by High-Performance Ion Chromatography - T. Paskach, H. P. Lieker, P. J. Reilly, and K. Thielecke, Iowa State Univ.

Characterization of Poly-Asp Tailed Beta-Galactosidase - M. D. Niederauer and C. E. Glatz, Iowa State Univ.

Computations of Conformations and Energies of Glucosyl Disaccharides - J. Zeng, M. K. Dowd, and P. J. Reilly, Iowa State Univ.

Role of Environmental Factors in Adsorption/Desorption of PCP on Soils - S. M. Wei, S. K. Banerji, and R. K. Bajpai, Univ. of Missouri

Factors Affecting Choice of an Appropriate Solvent for Recovery Coupled Fermentations - B. Su, C. J. Wang, and R. K. Bajpai, Univ. of Missouri

Oxygen Transfer to Viscous Liquid Medium in Three-Phase Fluidized Beds of Floating Bubble Breakers - Y. Kang and L. T. Fan, Kansas State Univ., B. T. Min, Chungnam National Univ., and S. D. Kim, Korea Advanced Institute of Science and Technology

Studies on In Vitro Development of Chick Embryo - A. Venkatraman, Kansas State Univ.

Design and Operation of a Novel Phase Separated Bioreactor for Use in Both Terrestrial and Microgravity Space Environments - E. H. Dunlop and P. E. Villeneuve, Colorado State Univ.

Microbial Gold Recovery - M. Szoychen, V. G. Murphy, and M. N. Karim, Colorado State Univ.

Effect of Peracetic Acid Pretreatment on Enzymatic Hydrolysis of Several Lignocellulosic Substrates - R. Rodriguez, H. A. Schroeder, L. L. Henk, and V. G. Murphy, Colorado State Univ.

Biodegradation of Diethyl Phthalate - G. Zhang, V. G. Murphy, and K. F. Reardon, Colorado State Univ.

Evaluation of a New Electrophoretic Separation Devicé - M. J. Juang and R. G. Harrison, Univ. of Oklahoma

Utilization of Genetic Engineering and Affinity Separations to Improve Peptide Production - N. T. Ma and R. G. Harrison, Univ. of Oklahoma

Microcosm Treatability Study of Soil Contaminated with Petroleum Hydrocarbons - P. Tuitemwong, S. Dhawan, B. M. Sly, L. E. Erickson, J. R. Schlup, and L. T. Fan, Kansas State Univ.

LIST OF PARTICIPANTS

Colorado State University

Eric Dunlop, Ahmad Hilaly, Sheyla L. Rivera, R. Rodriguez, Doohyun Ryoo, Meropi Samara, Marvin B. Szoychen, Pete E. Villeneuve, Kevin Wenger, and G. Zhang

Iowa State University

Ufuk Bakir, Hsiu-mei Chen, Bipin K. Dalmia, Michael K. Dowd, Roque L. Evangelista, Meng H. Heng, Mark Jensen, Ann Kusnadi, Jeff Langstraat, John R. Luther, Peeyush Maheshwari, Mark Niederauer, Douglas O'Brien, Peter Reilly, Claudio Alberto Torres Suazo, Lourdes Taladriz, and Jing Zeng

Kansas State University

S. T. Chou, Dale Coffin, Sanjay Dhawan, Larry E. Erickson, L. T. Fan, Rodney Fox, Jiaming Hua, Yong Kang, Xiaoge Liu, Pat McDonald, John Schlup, Baochun Shen, Kooranee Tuitemwong, Pravate Tuitemwong, and Ananthakrishnan Venkatraman

University of Colorado

Rob Davis, Tuba Diker, Hatice Gecol, Debra T. L. Hawker, Jeff Kern, Dhinakar S. Kompala, Ching-Yuan Lee, and Barry Vant-Hull

University of Missouri - Columbia

Rakesh Bajpai, W. M. Liu, George W. Preckshot, Ramarao V. Rayavarapu, Ying-Tsung Su, Paul Yeh, and Shein-ming Wei

University of Oklahoma

Roger Harrison, Johnny Hsu, Ming Jiing Juang, Nien-Tung Ma, and Dave Wilkinson

CELL SEPARATIONS AND RECYCLE USING AN INCLINED SETTLER

Ching–Yuan Lee and Robert H. Davis
Department of Chemical Engineering
University of Colorado
Boulder, CO 80309–0424

Robert A. Sclafani
Department of Biochemistry, Biophysics and Genetics
University of Colorado
Denver, CO 80262–0121

Introduction

Recombinant biotechnology has become a promising way to produce valuable pharmaceuticals and chemicals, such as proteins, hormones and amino acids. The most common mode for manufacture of these products is batch fermentation. From the engineering point of view, continuous processes are better than batch processes in terms of productivity. However, in large scale continuous fermentations, some non-productive cells can either outgrow the productive ones or inhibit the production by the productive cells. This is one of the major reasons why biotechnology companies generally do not use continuous fermentation processes to manufacture biological products. Thus, developing large-scale methods to maintain productive cells as dominant in the bioreactores is a key step for future mass biotechnological production.

Cell separation is also an important step in product recovery. In modern biotechnology, selective cell separations, in which certain groups of cells are separated from the bulk culture due to their specific properties, become more important because they can be used to remove the non-productive cells from the bioreactors.

In this work, steady-state experiments of cell separations between non-dividing & dividing yeast cells and flocculent & non-flocculent yeast cells using an inclined settler were done. The results were compared with the predictions by the inclined settler theory. Good agreement is obtained. Experiments of continuous fermentations with cell recycle using an inclined settler were also done. The results show that the protein production can be maintained for a long period of time with cell recycle.

Inclined Settler Theory of Steady–State Operation

The theory of an inclined settler operated under steady-state and transient conditions is discussed in detail by Davis *et al.* (1989). Consider steady-state operation of an inclined settler as shown in Figure 1. A fluid suspension with a continuous particle size distribution and a particle mass concentration X_f is fed into the settler at the volumetric flowrate Q_f. The particles are separated on the basis of differences in settling velocities, with an overflow stream and underflow stream exiting the settler with flowrates Q_o and Q_u, respectively. The overflow stream contains primarily smaller particles which do not settle out of suspension, whereas the underflow is enriched in the larger particles.

Steady-state mass balances on total suspension, total particles, and those particles which have

settling velocity v are given as follows:

$$Q_f = Q_o + Q_u \tag{1}$$

$$Q_f X_f = Q_o X_o + Q_u X_u \tag{2}$$

$$Q_f X_f P_f(v) = Q_o X_o P_o(v) + Q_u X_u P_o(v) \tag{3}$$

where the $P(v)'s$ are the normalized probability density functions and are defined such that $P(v)dv$ is the fraction of particles by mass in a given stream that have settling velocities between v and $v + dv$. The subscripts f, o, and u refer to the feed, overflow, and underflow streams, respectively. Each $P(v)$ is normalized so that

$$\int_0^\infty P(v)dv = 1 \tag{4}$$

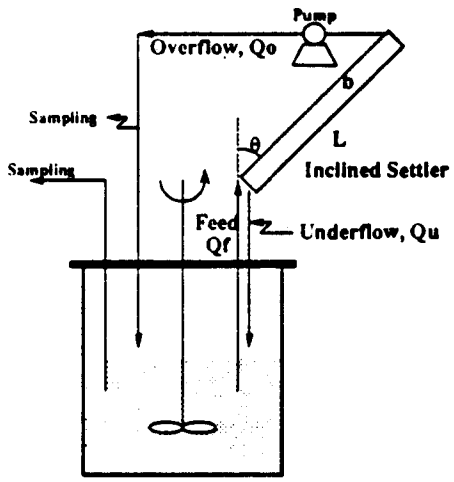

Figure 1. Experimental Setup for Steady-State Runs

The probability density function of a culture sample can be determined either directly by a laser light extinction experiment (Davis and Hunt, 1986) or indirectly by measuring the cell size distribution with a particle size analyzer and then using an expression such as Stokes' law to relate the sedimentation velocity of each particle to its size:

$$v = \frac{kD^2(\rho_c - \rho)g}{18\mu} \tag{5}$$

where D is the equivalent cell diameter, ρ_c is the cell density, ρ is the fluid density, μ is the fluid viscosity, and g is the gravitational acceleration constant. The correction factor k takes into account wall effects, hindered settling effects, irregularity of cell shapes, and any calibration differences in the measured diameter and the appropriate effective diameter for the Stokes' settling velocity. The rate of sedimentation for particles having the same sedimentation velocity, v, in an inclined channel can be described by the PNK theory. This theory states that the volumetric rate of production of clarified fluid due to particle sedimentation is equal to the vertical settling velocity of the particles multiplied by the horizontal projected area of the upward-facing surfaces of the channel onto which the particles may settle. By referring to Figure 1, for a rectangular channel this is expressed as

$$S(v) = vw(Lsin\theta + bcos\theta) \tag{6}$$

where θ is the angle of inclination of the plates from the vertical, and b, w, and L are the height, width, and length of the rectangular settler, respectively.

Material entering the overflow is comprised of a mixture of clarified fluid, which enters the overflow at the volumetric rate $S(v)$, and unsettled suspension, which enters the overflow at the volumetric rate $Q_o - S(v)$. A mass balance on the mixing of these two streams yields the following equation

$$Q_o X_o = (Q_o - S(v))X_f \qquad S(v) < Q_o \tag{7}$$

If $Q_o < S(v)$, all of the particles settle out of suspension before reaching the overflow, and $X_o = 0$.

The above equation may be applied to any given fraction of the particle distribution in a dilute suspension with different sizes of particles. The mass concentration, X, is then replaced by the mass concentration of particles having settling velocities between v and $v+dv$, which is $XP(v)dv$. Therefore

$$Q_o X_o P_o(v) = (Q_o - S(v))X_f P_f(v) \qquad S(v) < Q_o \tag{8}$$

$$P_o(v) = 0 \qquad S(v) \geq Q_o \tag{9}$$

where $S(v)$ is now interpreted as the volumetric rate at which suspension which lacks particles with settling velocities greater than or equal to v is produced as a result of the sedimentation of these particles.

Integrating equation (8) over all particle settling velocities, with the normalization constraint given by equation (4) applied, an expression for the total particle mass concentration in the overflow stream is obtained as

$$X_o = X_f \int_0^{v_o} \frac{(Q_o - S(v))}{Q_o} P_f(v)dv \tag{10}$$

where v_o is the cutoff sedimentation velocity and is defined by $S(v_o) = Q_o$. Particles with settling velocities greater than v_o should settle out of suspension before reaching the overflow. The probability density function for the particles in the overflow stream is obtained by substituting equations (8) and (9) into equation (10)

$$P_o(v) = \frac{(Q_o - S(v))P_f(v)}{\int_0^{v_o}(Q_o - S(v))P_f(v)dv} \qquad v < v_o \tag{11}$$

$$P_o = 0 \qquad v \geq v_o \tag{12}$$

These equations allow the composition of the overflow stream to be determined, given the operating conditions and the feed stream composition. The underflow stream composition may then be found using equations (1) - (3).

Materials and Methods

Cell Separation Between Dividing and Non-dividing Yeast Cells

The settler has dimensions of $L = 20$ cm, $w = 4$ cm, and $b = 0.5$ cm. The angle of inclination was typically chosen to be 45 degrees. However, one set of experiments was carried out to test the effect of varying this angle on the performance of the inclined settler. The yeast strain used was *S. cerevisiae* 378 with the plasmid pBM746. This strain has a bar1 chromosomal mutation which enables cell divisions to be stopped in the presence of α-factor, a 13-amino peptide. This strain cannot grow in a -Ura medium if cells lose the plasmids. When cell divisions are stopped, cells begin to increase

their sizes and become very irregular in shape. The average sizes of yeast cells were measured by an Elzone 180XY particle size analyzer manufactured by Particle Data, Inc. Typical average equivalent sphere diameters are 4.5 μm for normal dividing cells and 7.4 μm for nondividing cells. In order to maintain steady-state operation without cell growth, distilled water was used as the suspending fluid. The operating temperature was chosen as 30°C. Observations through a microscope showed that the morphology of yeast cells in water did not have any visible change for 48 hours, which was the time needed for accomplishing both the experiments and data analysis. Results from plating also showed that the viability of yeast cells in water remained the same for this period of time.

The method used to study the agreement between experimental results and theory was to vary the overflow flowrate, Q_o, analyze the overflow samples to obtain X_o and $P_o(v)$, and compare these quantities with theoretical predictions. The experimental setup is shown schematically in Figure 1. The overflow flowrate, Q_o, was controlled by a pump. The steady-state operation was achieved by recycling the overflow and underflow back to the reservoir. For each experiment, approximately three hours were required for steady state to be reached, with the slow step being the equilibrium formation of the sediment deposit on the lower wall of the settler. Samples were taken from the feed reservoir as well as the overflow stream for later analysis.

The samples were analyzed by the Elzone 180XY for cell number concentrations and size distributions. Mass concentrations were then calculated from the number concentrations. Equation (5) was used to calculate the settling velocity distributions of each sample. The cell density, ρ_c, is 1.13 g/cm^3 (Szlag, 1988). Te correction factor, k, in the Stokes' law equation was determined to be 0.7 (Davis *et. al.* , 1989) for dividing cells, with a nearly spherical shape, and 0.5 for non-dividing cells in order to account for their irregular shape.

Cell Separation Between Flocculent and Non-flocculent Yeast Cells

Yeast strain *S. cerevisiae* 402 was used for this part of study. This strain is moderately flocculent. It ranges from single cell to flocs consisting of more than one hundred cells. In the actual experiment, this is the only strain used. Those single cells and flocs having only two or three cells can be treated as non-flocculent ones. Steady-state experiments were done using similar setup and procedures as those described in the previous section. A different settler was used. This one has dimensions of L = 20 cm, w = 5 cm, and b = 0.5 cm. The probability density functions of both overflow and feed samples, $P_o(v)$ and $P_f(v)$, were obtained by running laser light extinction experiments. The cell mass concentration of each sample can be obtained by measuring the cell dry weight, calculating the number of cells per volume of culture, and calculating the mass concentration of wet cells per volume by using the cell density and single cell size. However, this method might introduce some errors due to any uncertainty from the cell density and single cell's size. This can be avoided by non-dimensionalizing each overflow cell mass concentration by the cell mass concentration in the feed.

Continuous Fermentation with Cell Recycle

The experimental setup for continuous fermentations is shown in Figure 2. The medium used was YEPD + Trp which contained 10 g/l of yeast extract, 20 g/l of peptone, 20 g/l of dextrose, and 1 g/l of tryptophan. This medium was sterilized and continuously fed into the fermentor. The culture was continuously removed from the system through the overflow of the inclined settler at the flowrate Q_o. Yeast strain *S. cerevisiae* 445 with plasmid pSM12, which produces a secreted protein, α- amylase, was used. This strain has a *ste2* chromosomal mutation which makes it sensitive to α-factor. The fermentation unit used was Bioflo II manufactured by New Brunswick Scientific.

Fermentations started with batch mode with α-factor present in the medium. After the yeast cells increased in size, the continuous line was turned on. The total volume of the culture in the fermentor was 700 ml. The dilution rate was 0.12 hr^{-1}. Most of the cells entering the settler were recycled back to the fermentor. Overflow samples were taken for the protein activity assays. Samples from the fermentor were also taken to analyze the fraction of plasmid-bearing cells.

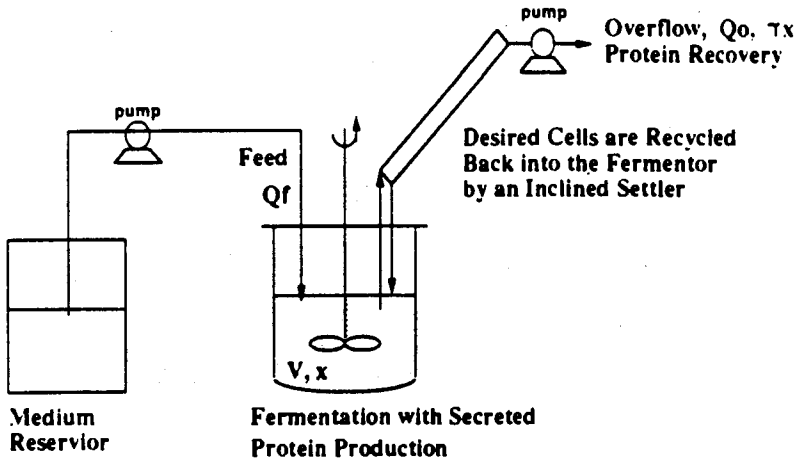

Figure 2. Experimental Setup for Continuous Fermentation with Cell Recycle

Results and Discussion

Cell Separation Between Dividing and Non-Dividing Yeast Cells

In Figure 3, the cell size distribution of the feed stream, which had a 50:50 (by counts) mixture of dividing and non-dividing cells, is represented by the solid line. The larger, non-dividing cells were plasmid-bearing while the smaller, dividing cells were plasmid-free. The two subpopulations result in the two partially resolved peaks. At the operating conditions of Q_o = 0.622 ml/min and θ = 45°, which correspond to a theoretical prediction of a cutoff diameter of D_o = 6.2 μm for the largest cells to reach the overflow, the overflow should contain mainly dividing cells. This prediction (dotted line in Figure 3) was found to be in good agreement with the measured size distributions (dashed line in Figure 3) of the overflow sample. An effective separation was obtained. However, the experimental data show that a small portion of cells larger than the cutoff size reached the overflow. There are two possible reasons. The first one is the hydrodynamic dispersion phenomenon which happens druing sedimentation, and the second one is the enlongated shape of those non-dividing cells. Their actual settling velocities are slower than that predicted by equation (5) when their major axis is oriented normal to the gravity vector.

Figure 4 shows the total cell mass concentration of both subpopulations combined in the overflow, non-dimensionalized by the cell mass concentration in the feed, vs. the overflow flowrate. At low flowrate, the hold-up time is long enough for a large protion of cells to settle so that the cell mass concentration in the overflow is small. As the overflow flowrate increases, more cells are carried out due to a decreasing hold-up time. The experimental data are in good agreement with the theoretical predictions by equation (10).

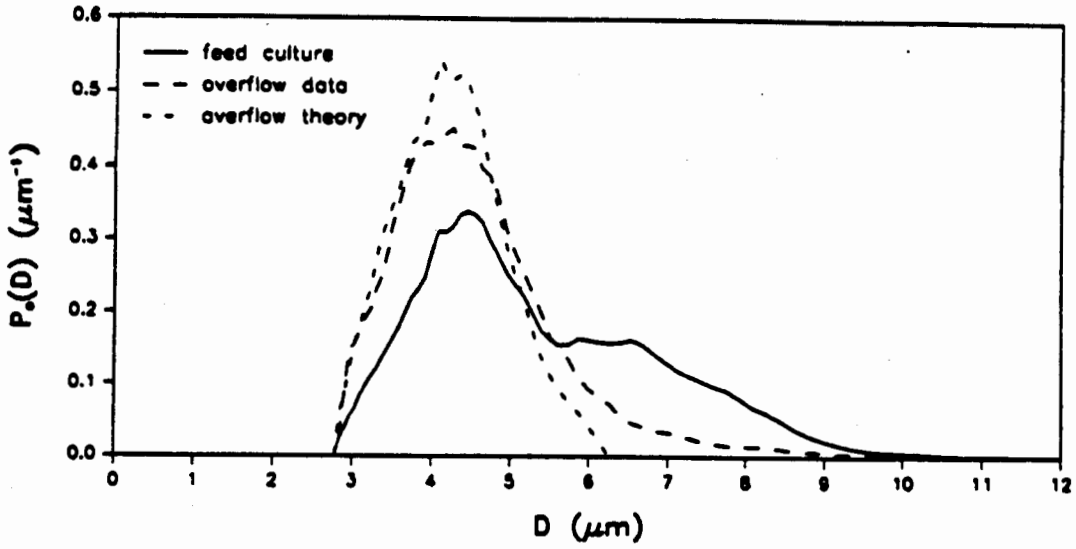

Figure 3. Cell Size Distribution in the Overflow of a Mixed Culture

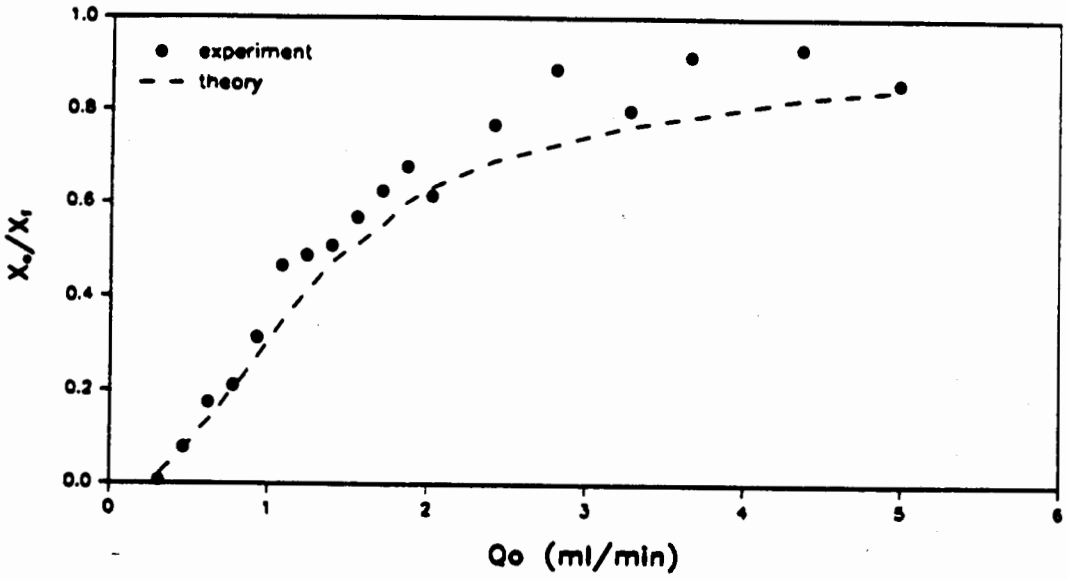

Figure 4. Dimensionless Overflow Cell Mass Concentration vs. Overflow Flowrate

Figure 5 shows the relationship of cell separation effect and overflow flowrate. At low flowrates, the larger, non-dividing cells have sufficient time to settle down and roll back to the tank so that the fractions of non-dividing cells in the overflow are low. As the overflow flowrate increases, more non-dividing cells reach the overflow, and, thus, the fraction increases. Finally, at very high overflow flowrates, the composition approaches the 50:50 ratio of the original feed culture, since neither subpopulation has sufficient time to settle. There is a good agreement between the experimental results and the theoretical predictions by applying equation (10) to the two subpopulations separately.

Experiments were also done to examine the overflow cell mass concentration as a function of both the overflow flowrate and the angle of inclination of the settler. According to the theory, when X_o and Q_o are properly non-dimensionalized, the result should be independent on the angle of inclination. This is demonstrated by Figure 6, where $\bar{Q}$ is the overflow flowrate at which the cells having median settling velocity are retained in the settler.

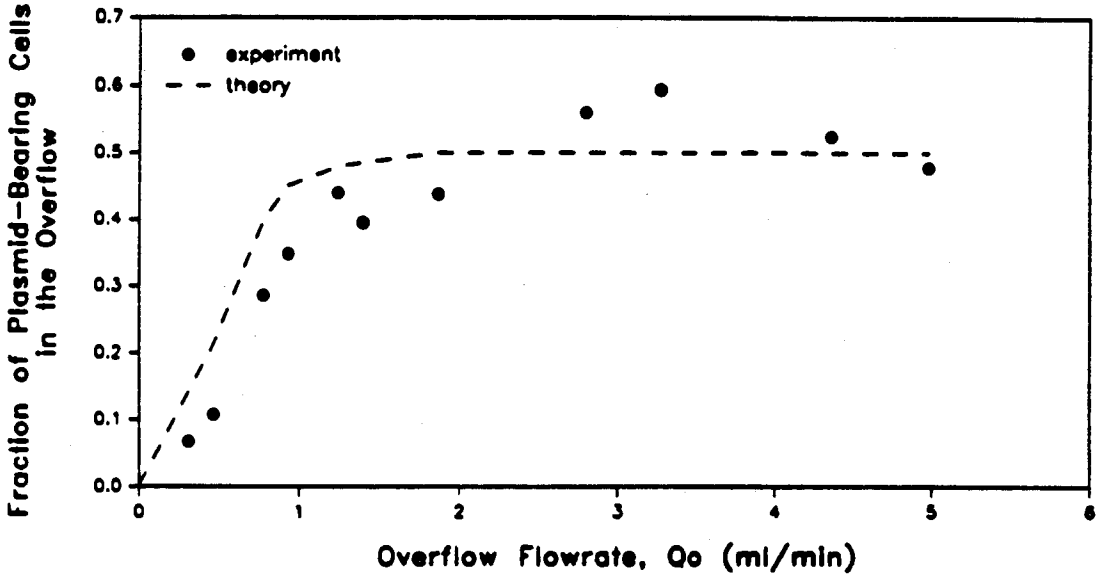

Figure 5. Fraction of Plasmid-Bearing Cells in the Overflow vs. Overflow Flowrate

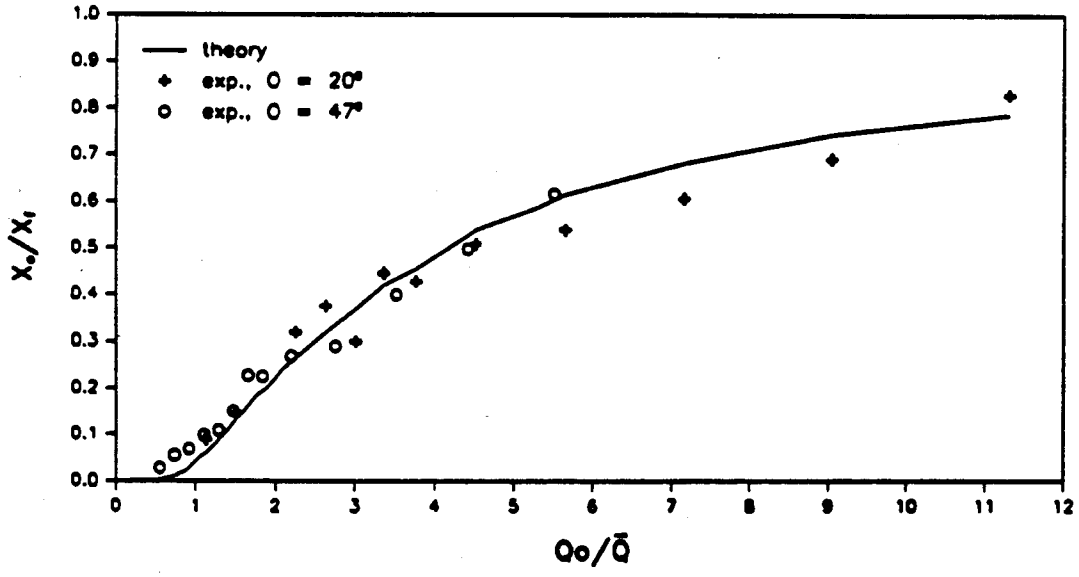

Figure 6. Dimensionless Overflow Cell Mass Concentration vs. Overflow Flowrate

Cell Separation Between Flocculent and Non-flocculent Yeast Cells

Figure 7 shows a dimensionless plot of overflow cell mass concentration, normalized by the cell mass concentration of the feed, versus overflow flowrate, normalized by $\bar{Q}$. Two different angles of inclination were used. A good agreement is shown between the theoretical prediction and experimental data.

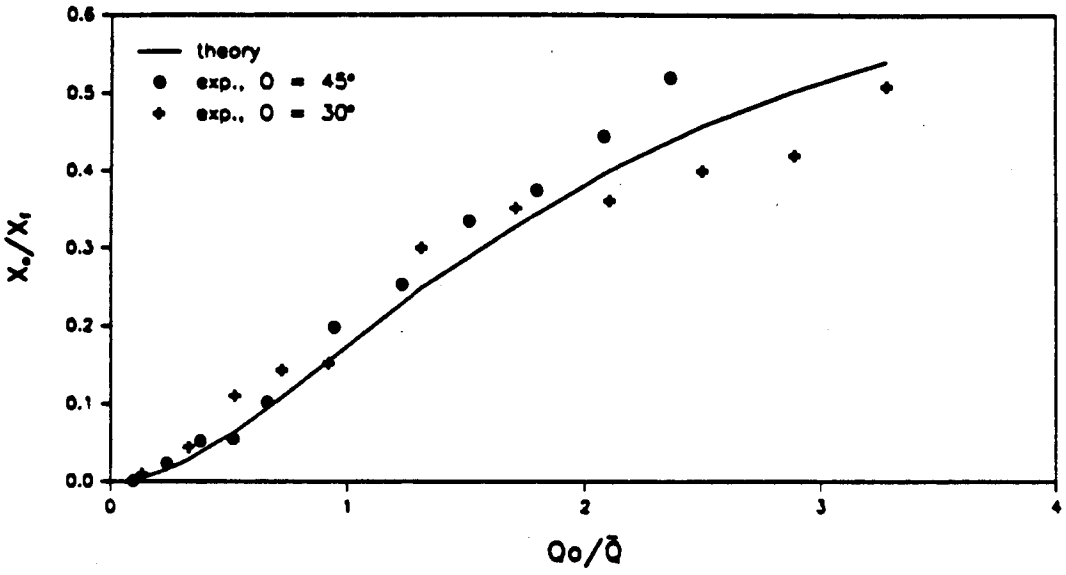

Figure 7. Dimensionless Overflow Cell Mass Concentration vs. Overflow Flowrate

Continuous Fermentations with Cell Recycle

The original idea of these experiments was to use non-dividing, plasmid-bearing yeast cells to overproduce a foreign protein, and to keep recycling these productive cells back to the bioreactor using an inclined settler to maintain the production of protein. However, experimental data show that the cell divisions can be arrested for only a limited period of time. Three different yeast strains have been tried. Each of them has a different mechanism of arresting cell divisions. Yet none of them can stay non-dividing for more than two days.

Although the idea of using non-dividing cells does not work as expected, the idea of recycling proves to be very helpful in maintaining the foreign protein overproduction. Experimental results from two experiments are compared. The first one was without recycle and without the addition of α- factor. In the second experiment, both the addition of α-factor and cell recycle by an inclined settler were applied. Figure 8 shows the α-amylase activity comparison. The difference can easily be seen: the α-amylase production in the first experiment is virtually stopped after about 2 days, while in the second one, it lasts for more than 10 days. Although yeast cells resumed their divisions after less than one day, high levels of protein production were maintained by recycle since most of the cells, including plasmid-bearing cells, were recycled. Figure 9 shows the percentage of plasmid-bearing cells in the fermentor. In the first experiment, the percentage went to almost zero at the end of the second day. But, in the second one, a significant percentage of plasmid-bearing cells still existed even after 10 days. The gradual decrease of the fraction of plasmid-bearing cells is expected in the second experiment since the plasmid-bearing cells grow slower than plasmid-free cells, and

since a small fraction of daughter cells do not receive any plasmids upon division of plasmid-bearing, parent cells.

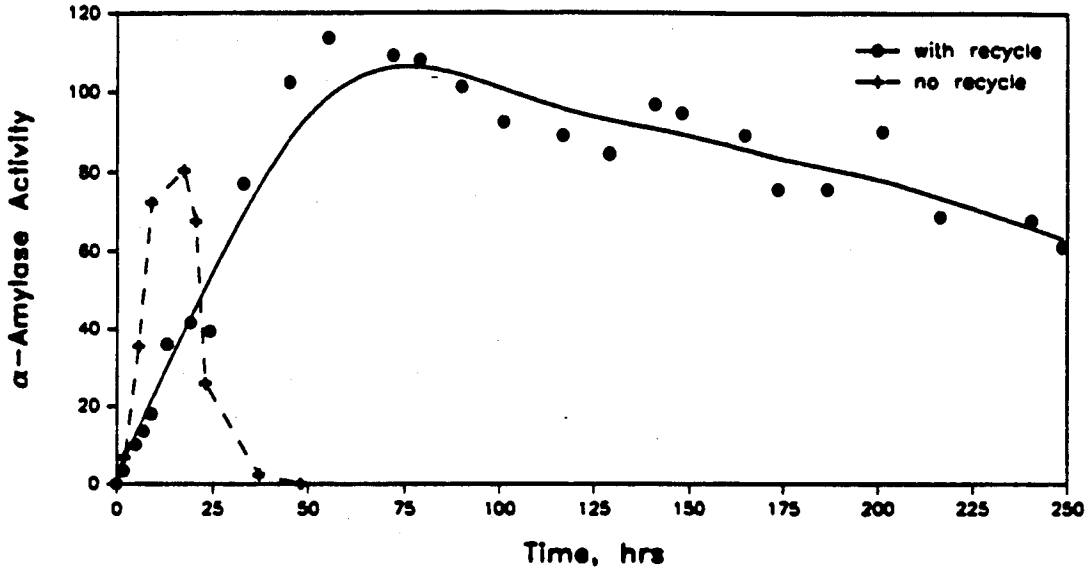

Figure 8. α-amylase Activity in the Fermentor vs. Time

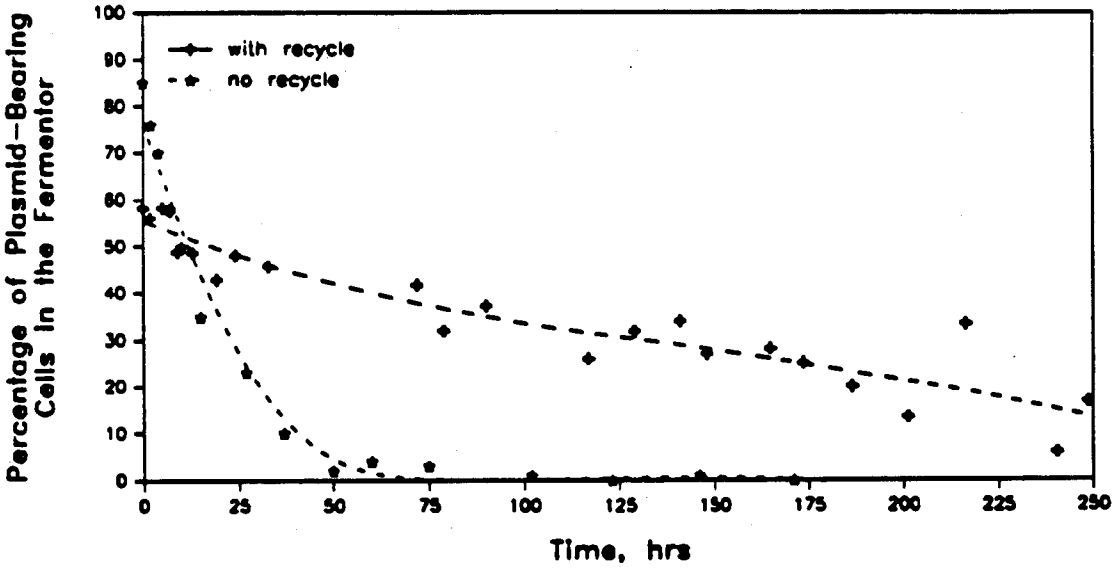

Figure 9. Percentage of Plasmid-Bearing Cells in the Fermentor vs. Time

Concluding Remarks

In this study, we have demonstrated that the theory of inclined settling is applicable in separating non-dividing yeast cells from dividing ones and flocculent yeast cells from non-flocculent ones. Steady-state experiments show good agreement between the theoretical predictions and experimental data for both the cell mass concentration and the size distributions in the overflow streams. Experimental results of continuous fermentations show that using an inclined settler to retain productive cells in the system can maintain a high level protein production for a long period of time.

The authors wish to acknowledge the National Science Foundation (grants No. EET-8611305 and BCS-8912259) for support of this work.

References

Davis, R. H. and M. A. Hassen (1988) Spreading of the interface at the top of a slightly polydisperse suspension. *J. Fluid Mech.* **196**, 107–134.

Davis, R. H. and T. P. Hunt (1986) Modeling and measurement of yeast flocculation. *Biotech. Prog.* **2**, 91–97.

Davis, R. H., X. Zhang, and J. P. Agarwala (1989) Particle classification for dilute suspensions using an inclined settler. *Ind. Eng. Chem. Res.* **28**, 785–793.

Ponder, E. (1925) On sedimentation and rouleaux formation. *Q. J. Exp. Physiol.* **15**, 235–252.

Nakamura, N. and K. Kuroda (1937) La Cause de l'acceleration de la vitesse de sedimentation des suspensions dans les recipients inclines. *Kerjo J. Med.* **8**, 256–296.

Szlag, D. (1988) *Factors Affecting Yeast Flocculation*, M.S. Thesis, Univ. Colo.

MICROMIXING AND METABOLISM IN BIOREACTORS: CHARACTERIZATION OF A 14 L FERMENTER

K.S. Wenger and E.H. Dunlop
Department of Chemical Engineering
Colorado State University
Ft. Collins, CO 80521

Abstract

In an attempt to study the effects of micromixing on the metabolism of microorganisms, we are studying the micromixing characteristics of a New Brunswick 14 liter stirred tank fermenter. A mixing sensitive reaction, the reaction of 1-napthol with diazotized sulfanilic acid, is being used to measure the intensity of micromixing in different regions of the fermenter. Results obtained by using this reaction will constitute a micromixing "map" of the fermenter which will be useful in explaining observed behavior in subsequent fermentations.

Introduction

Often in the scale-up of fermentation processes it is observed that a change in the metabolism of the microorganisms occurs. This change may manifest itself, for example, in the observed yield, carbon conversion, or specific growth rate. Such changes can have dramatic effects on the economics of a large scale fermentation process.

It is not immediately obvious why such changes in metabolism would occur when bulk conditions such as substrate concentration, dissolved oxygen, pH, etc. do not change on scale-up. Furthermore, these changes may occur when the fermenter appears to be well mixed on the bulk scale.

Closer examination reveals that micromixing, measured on the scale of the microorganism, is more important than bulk measurements of mixing, such as the residence time distribution. The size of the smallest eddy in a turbulent spectrum can be calculated and is generally 20-50 microns in lab scale fermenters and can be as high as 200 microns in larger fermenters. This is large in comparison to the size of a microorganism, typically 1-5 microns. Therefore, the mixing environment that the microorganism experiences can be substantially different from that observed on a bulk scale. A microorganism may spend significant amounts of time in a stagnant eddy, which quickly becomes deprived of nutrients.

It is our objective to study the effects of micromixing on the metabolism of microorganisms. A conventional stirred tank fermenter is being used, which provides a variation in micromixing intensity at different locations in the fermenter. A chemical tracer technique provides an independent measurement of the degree of micromixing with which observed changes in metabolic activity of a Saccharomyces cerevisiae culture can be correlated.

Description of the Chemical Tracer Technique

The reaction of 1-napthol with diazotized sulfanilic acid has been extensively developed by Bourne and co-workers [1,2,3] as a measurement of micromixing. The reaction is a competitive consecutive reaction, described by the following scheme:

$$A + B \xrightarrow{k_1} R \tag{1}$$

$$R + B \xrightarrow{k_2} S \tag{2}$$

where $k_1 >> k_2$ [1]. Figure 1 shows the chemical structures of A,B,R and S.

The first reaction which forms R is fast enough to be under diffusion limitation. It is therefore sensitive to mixing intensity, and the observed rate is faster under more intensely mixed conditions. The second reaction is under kinetic control, and is insensitive to mixing. An index to the degree of micromixing can therefore be defined as the relative yield of S in the product mixture:

$$X_s = \frac{2c_s}{c_R + 2c_s} \tag{3}$$

R and S are dyes with peaks in the visible spectrum (Figure 2), thus their concentrations can be determined spectrophotometrically. Since the peaks are overlapping, the concentrations were determined by linear regression of the Lambert-Beer law over the range of wavelengths from 400-600 nm :

$$E = dc_R\epsilon_R + dc_S\epsilon_S \tag{4}$$

where ϵ_R and ϵ_S are the molar extinction coefficients of R and S and are functions of wavelength.

Previous Work

Studies involving the effects of micromixing on cell metabolism have been quite limited. Experimental data relating these two is even less available. One study which suggested the

current experimental approach was by Hansford and Humphrey [4] who set up a fermenter with several different feed injection points. This fermenter was used to grow cultures of Baker's yeast in continuous mode under carbon limitation. Large differences in the fermentation yield (dry weight of cells/glucose consumed) were observed for different glucose injection points.

Work by Dunlop and Ye[5] characterized a 3 liter fermenter with 5 different injection points. The fermenter was first characterized on a micromixing basis by using the previously described diazodye technique. This gives an independent measurement of the degree of micromixing in different areas of the fermenter which can then be compared to what is observed in real fermentations. By modeling the reaction zone as a stagnant sphere through which A must diffuse to react with B [3], a length scale of turbulence was estimated under different conditions at the individual injection points.
Continuous Baker's yeast fermentations were then carried out under carbon limitation using the different injection points as glucose injection points. Figure 3 shows the effect of switching the glucose injection point between two areas where the length scales were 50 and 160 microns.

Experimental Materials and Methods

As a follow-up to the work of Dunlop and Ye, a New Brunswick 14 liter fermenter has been fitted with 10 different feed pipes. Schematics of this fermenter are shown in Figure 4(a,b,c). The pipes have been positioned to investigate different extremes of mixing intensity as well as symmetry of mixing intensity within the fermenter. As before, the experimental work with this fermenter is divided into two parts:

1) Microscale characterization of the fermenter using the diazodye reaction.
2) A study of the effects of micromixing, characterized in step 1, on the growth of Baker's yeast.

Experiments with the diazodye have been carried out with the following procedure. The reactor was initially charged with 10.0 liters of deionized water and 0.0833 g of 1-napthol to make a 5.78×10^{-5} M solution. This solution was buffered with 11×10^{-3} moles each of $Na_2CO_3/NaHCO_3$ to give a solution with a final pH of 10.1 at 30 C. This quantity of buffer was sufficient to maintain constant pH throughout the experiment.

1 liter of a 5.5×10^{-4}M solution of diazotized sulfanilic acid was prepared following the method of Kozicki [6] . Both the napthol and the diazo solutions were degassed for 2 hrs. with nitrogen before use. The diazotized sulfanilic acid solution was

then pumped into the fermenter through the desired injection pipe. A Masterflex peristaltic pump was used to maintain the flowrate at 33 ±1 ml/min. A Masterflex flow integrator effectively eliminated pulsations in the flow. Temperature was maintained at 30. C throughout the experiment by the New Brunswick fermenter. Gas flowrate was monitored by a rotameter on the fermenter assembly.

After all of the diazotized sulfanilic acid solution was pumped into the fermenter, the bright red product solution was stirred for an additional 5 minutes before being sampled for spectrophotometric analysis. All samples were assayed by the spectrophotometer immediately after collection.

The product solution was analyzed in a Varian Cary 3 UV-Vis spectrophotometer. Absorbances were measured at 5 nm intervals in the range of 400-600 nm. The concentrations of R and S were determined by a standard two-parameter linear regression of equation 4, the Lambert-Beer Law, over this range. This method of regression gives significantly different results than a single parameter regression based on, [8]

$$\frac{E}{\epsilon_R d} = \frac{\epsilon_S}{\epsilon_R} c_S + c_R \tag{5}$$

A mass balance, or percent of theoretical yield, was determined for each run by using the equation

$$\%closure = \frac{N_R + 2N_S}{N_{R0}} \tag{6}$$

Once the fermenter has been characterized on a microscale basis, experiments will be conducted with Saccharomyces cerevisiae. The objective of these experiments will be to determine the effects of the local micromixing intensity on the growth of these organisms.

In order to control dissolved oxygen in the fermentation while keeping the mixing parameters constant, a fermenter with a O_2/N_2 ratio system is being designed. This method of dissolved oxygen control has been used successfully by Seigell[7]. Such a control system will be able to deliver varying amounts of oxygen to the solution without changing the total gas flowrate or stirring speed.

Fermentation off-gas will be monitored using an Albion Instruments laser raman gas analyzer. This instrument provides percentages of CO_2, O_2, N_2, and hydrocarbons in the off-gas without the maintenance requirements and cost of a mass spectrometer.

Results and Discussion

Experiments have been conducted using the two impeller system shown in Figure 4 using several different agitation speeds and injection points. These results are summarized in Figure 5. The results, while hardly complete, do show a definite difference in the product mixture under different mixing conditions.

Following these experiments, we felt that switching to a single impeller system would make the results more comparable to previous work. The single impeller system is shown in Figure 4c. Results so far for this system are shown in Figure 2. These results are consistent with what was observed in the two impeller system.

Mass balances were calculated for each run, according to equation 6. The percent closure for all runs averaged 106% with a standard deviation of 2.6%.
This consistently high yield indicates a systematic error in the calculation of c_R and c^S, and suggests that the extinction coefficients be re-examined.

The injection ports have been designed with a 0.001 m orifice, which gives a linear velocity of 6.91 m/sec at the flowrate used. This velocity exceeds the tip speed of the impeller, the largest velocity in the system, at 800 rpm. Hence, backmixing into the feed pipe is eliminated as a potential problem. However, the kinetic energy of this stream is dissipated locally around the injection point and surely contributes to mixing in this region. The rate of kinetic energy input by this stream is $1.31X10^{-2}$Watts, a small fraction of the total energy input to the system. However, the local mixing depends upon over which volume this kinetic energy is dissipated, which is difficult to estimate. A detailed study of the effect of this kinetic energy input on the local micromixing needs to be performed.

Conclusions

The reaction of 1-napthol with diazotized sulfanilic acid has been used to begin characterizing the different regions of micromixing in a New Brunswick 14 liter fermenter. While the data generated is strongly dependent upon the pure component extinction coefficients being used, relative values of

micromixing intensity are easily gained. Further experiments need to be performed to determine the repeatability and accuracy of these measurements.

Nomenclature

A - 1-Napthol
B - diazotized sulfanilic acid
c - concentration (mol/l)
d - path length (mm)
E - extinction (absorbance)
k - reaction rate constant
N - number of moles in solution
R - 2-(4'-Sulphophenylazo)-1-napthol
S - 2,4-bis-(4'-Sulphophenylazo)-1-naphthol

ϵ - molar extinction coefficient (absorptivity, m^2/mol)

References

1. Bourne J.R., Kozicki F., And Rys P., Chem Eng Sci, 36 (1981) 10 1643-1648.
2. Belevi H., Bourne J.R., and Rys P., Chem Eng Sci, 36 (1981) 10 1649-1654.
3. Bourne J.R, Kozicki F., and Moergeli U, Chem Eng Sci, 36 (1981) 10 1655-1663.
4. Hansford G.S., and Humphrey A.E., Biotech Bioeng, 8 (1966) 85-96.
5. Dunlop E.H., and Ye S.J., Biotech Bioeng, in press (1990).
6. Kozicki F., Dissertation # 6618 ETH Zurich, Switzerland (1980).
7. Seigell S.D., and Gaden E.L., Biotech Bioeng, 4 (1962) 345-356.
8. Ye S.J, Masters Thesis, Washington University, St. Louis (1984).

Fig. 1 – Chemistry of the diazodye reaction

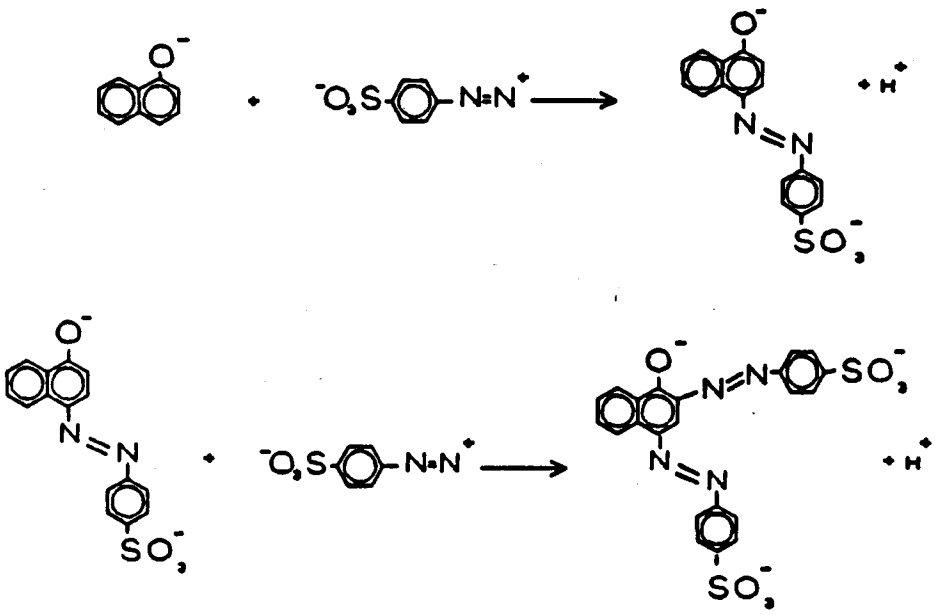

Figure 2 – R & S Extinction Coefficients

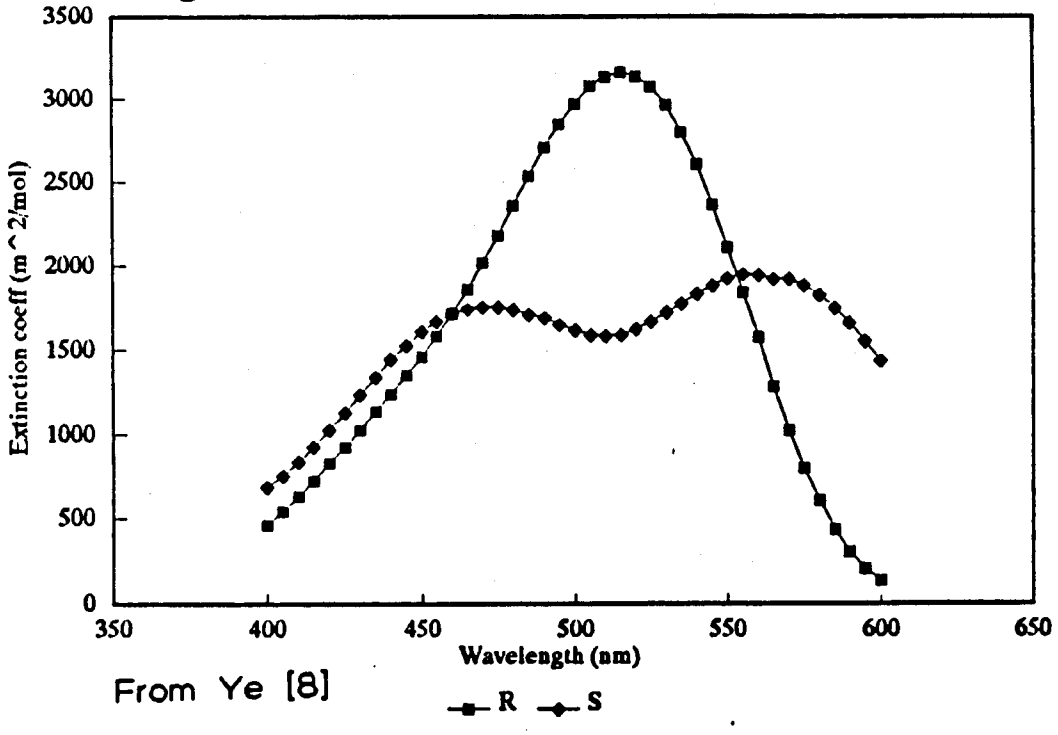

From Ye [8]

Figure 3 – Effect of injection port on optical density of Baker's Yeast

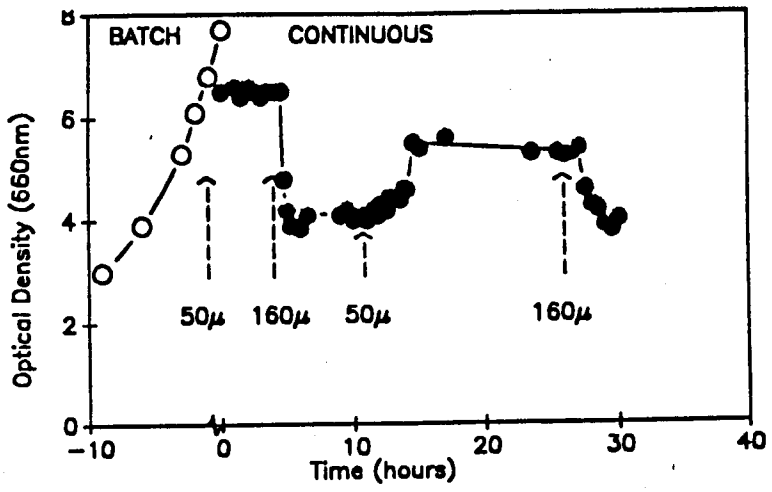

From Dunlop & Ye [5]

Figure 4a – Two Impeller System

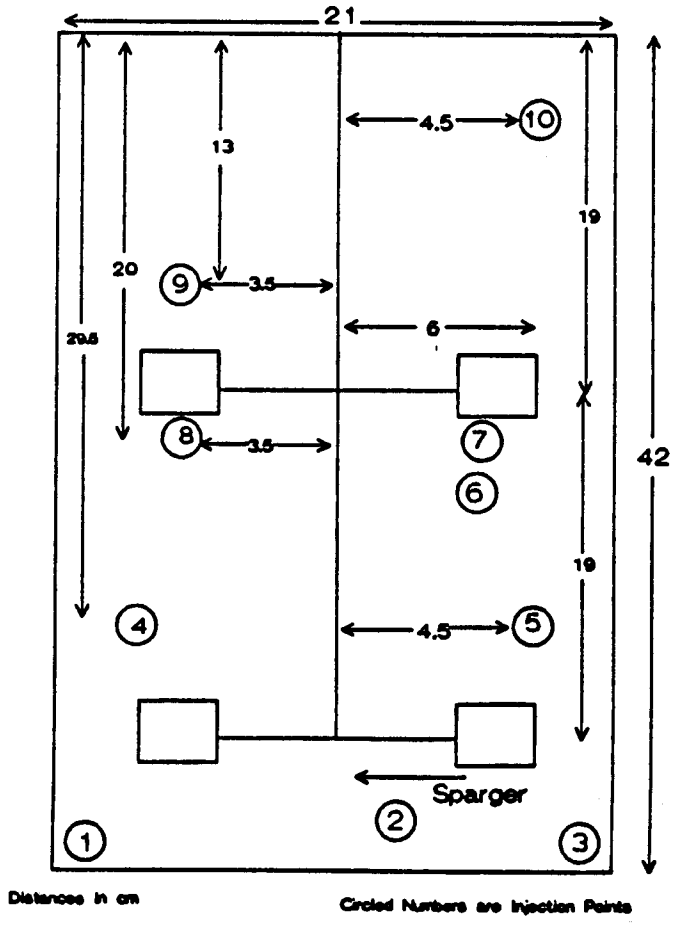

Distances in cm

Circled Numbers are Injection Points

Figure 4b – Single Impeller System

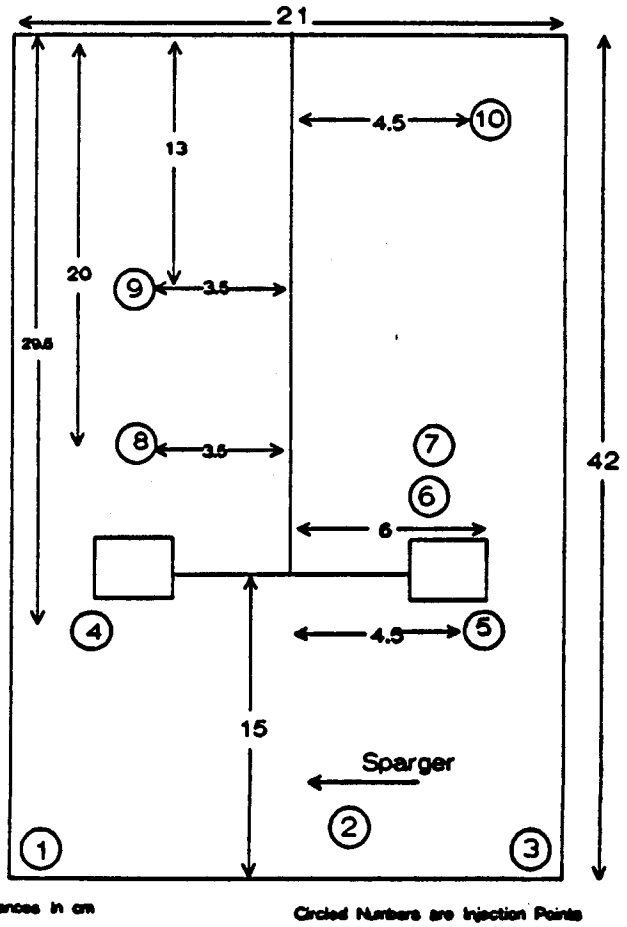

Distances in cm

Circled Numbers are Injection Points

Figure 4c - Top View of Fermenter

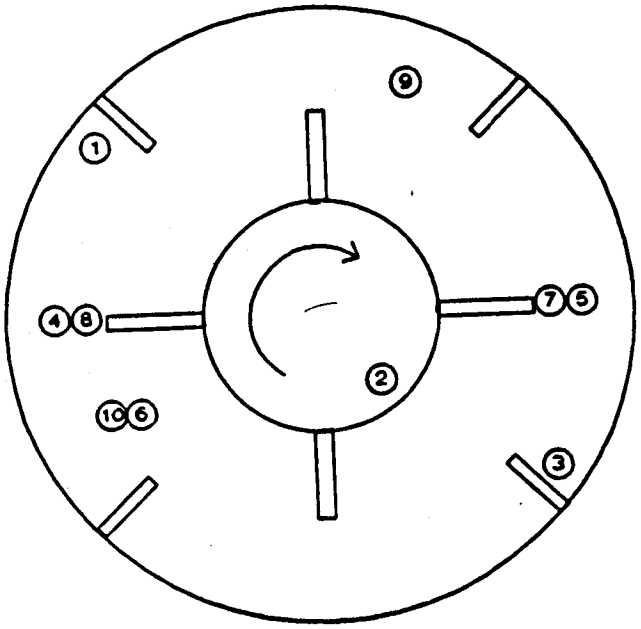

Figure 5 - Two Impeller System

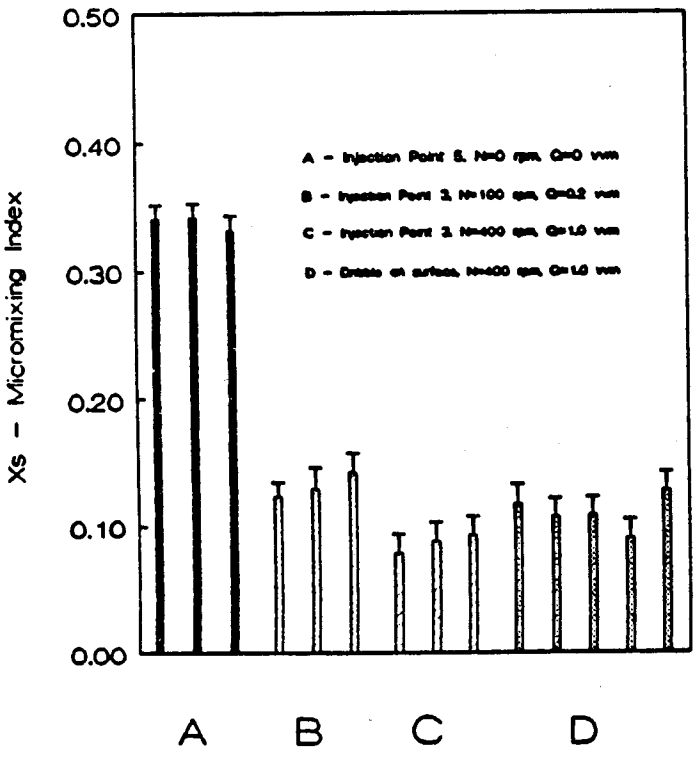

Figure 6 - One Impeller System

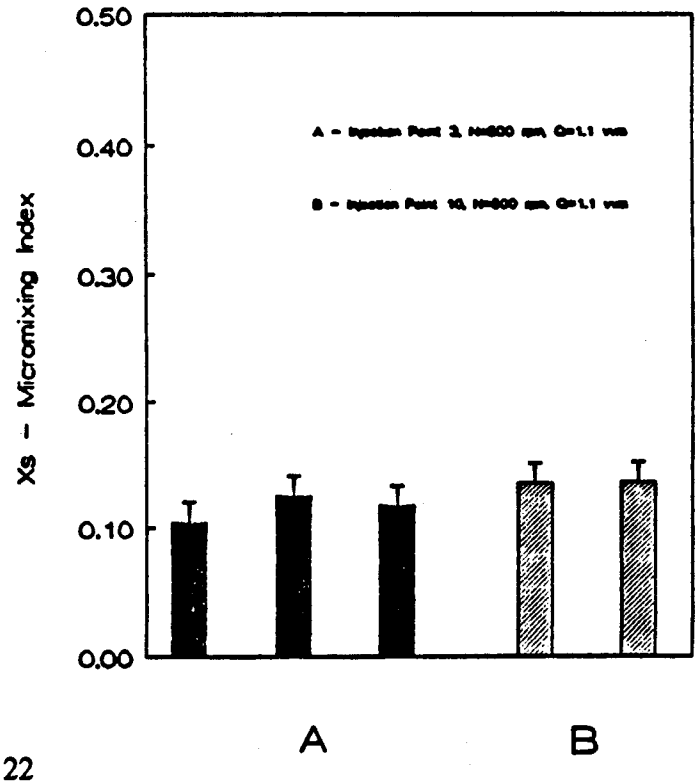

PRODUCTION, PURIFICATION, AND HYDROLYSIS KINETICS OF WILD-TYPE AND MUTANT GLUCOAMYLASES FROM *ASPERGILLUS AWAMORI*

Ufuk Bakir, Paul D. Oates, Hsiu-Mei Chen, and Peter J. Reilly
Department of Chemical Engineering, Iowa State University,
Ames,IA 50011, USA

ABSTRACT

Wild-type and mutant glucoamylases were produced by *Saccharomyces cerevisiae* containing genes for each from *Aspergillus awamori*. A selective minimal medium for plasmid-bearing cells was used, and cell density and glucoamylase activity were maximized for each enzyme form using different strategies of glucose addition. Fed-batch addition of glucose at 48 h gave the best results. The enzyme was extracellular and 89% of the glucoamylase produced was secreted to the medium.

Glucose yield from dextrin hydrolysis by glucoamylase reaches a maximum at intermediate incubation times because of reverse reactions that occur at high glucose concentrations. Production of glucose and disaccharides was measured at different incubation times for mutant and wild-type glucoamylases and for a native glucoamylase produced by *A. awamori*, either alone or in combination with either of the debranching enzymes, pullulanase or isoamylase. Sligth increases in maximum glucose yield were observed when mutant glucoamylase replaced wild-type glucoamylase and when debranchers were added. Significant differences in disaccharide production rates between different enzyme mixtures did not follow a consistent pattern.

INTRODUCTION

Glucoamylase (1,4-α-D-glucan glucohydrolase, EC 3.2.1.3) hydrolyzes primarily α-(1→4) and α-(1→6) glucosidic linkages from the non-reducing ends of D-glucosyl oligo- and polysaccharides to produce β-D-glucose (Reilly, 1979). However, at high glucose concentrations it can catalyze reverse reactions to produce di-, tri-, and tetrasaccharides from glucose (Harada, 1984).

Glucoamylase has been found in numereous microorganisms, animals, and plants. However, the most important industrial source is filamenteous fungi such as *Aspergillus* and *Rhizopus* (Manjunath *et al.*, 1983).

Glucoamylase is one of the most important industrial enzymes. It is used in the commercial production of glucose, most of which is then used to produce high-fructose corn syrup and ethanol. The idea of simultaneous hydrolysis of starch by glucoamylase and then fermentation to ethanol has led to the research on glucoamylase production by yeast, especially *Saccharomyces cerevisiae* (Nam *et al.*, 1988). For this purpose glucoamylase has been cloned in *S. cerevisiae* (Innis *et al.*, 1985).

The hydrolysis reactions with glucoamylase does not obey simple Michaelis-Menten kinetics because of the complex and continually changing substrate mixture, which results in a multitude of

simultaneous reactions, each with a different rate. Linear dextrins are rapidly converted to D-glucose, whereas α-(1→6) bonds at branch points are more resistant. Thus D-glucose content reaches a maximum before glucose condensation by reversion reactions significantly reduces yield. The reverse reaction favors the formation of α-(1→6) linkages (Harada, 1984; Linko, 1987). Lee *et al.* (1976) showed that the reaction approaches about DX 91- 92 at 45°C, 30% solids.

The low hydrolysis rate of α-(1→6) linkages and the maximum glucose yield may be increased by using debranching enzymes of the 1,6-α-glucosidase family, such as isoamylase and pullulanase. These enzymes may be used either before or at the same time as glucoamylase (Linko, 1987).

In this study a *S. cerevisiae* strain containing either wild-type or mutant *Aspergillus awamori* glucoamylase genes was used to produce glucoamylase, and then hydrolysis kinetics were determined for these two glucoamylases, as well as for the native glucoamylase from *A. awamori*, with and without debranching enzymes. The mutant glucoamylase used had been generated in our laboratory previously (Sierks *et al.*, 1990).

MATERIALS AND METHODS

Wild-type and mutant glucoamylases were produced by using a *Saccharomyces cerevisiae* strain containing an autonomously replicating plasmid (pGAC9) with a leucine-producing gene (Innis *et al.*, 1985), into which either wild-type or mutant *A. awamori* glucoamylase genes had been cloned (Innis *et al.*, 1985; Sierks *et al.*, 1990). Fermentation was performed in a 19-L fermentor containing yeast minimal salts medium without leucine for 72 h at 30°C, pH 4.5, and dissolved oxygen was kept constant at 80% saturation (Innis *et al.*, 1985). pH was controlled by adding 0.5 N ammonium hydroxide or, if ammonium sulfate was added during the fermentation, 0.5 N sodium hydroxide. Samples were taken and analyzed for glucose concentration, cell growth, and glucoamylase activity during the fermentation. Glucoamylase activity was assayed using 2% soluble starch in 0.05 M acetate buffer at pH 4.5 as a substrate and incubating at 50°C. The amount of glucose formed was estimated by a glucose oxidase method (Banks and Greenwood, 1971). One unit of enzyme is defined as the amount of enzyme required to produce 1 μmol of glucose per minute at pH 4.5 and 50°C. Glucose concentrations and cell densities were detected by means of a glucose analyzer and spectrophotometer at 680 nm, respectively.

During purification, all operations were carried out at 4 °C. After fermentation, yeast cells were separated from supernatant by means of a Amicon hollow-fiber filter with a pore diameter of 0.1 μm, then concentrated 50-fold by using another Amicon hollow-fiber filter with a molecular cut-off of 30 kDa. Then the concentrate was freeze-dried, resuspended into a smaller volume, dialyzed against 0.05 M citrate-phosphate buffer at pH 6.0, and applied to a DEAE-Fractogel column (15 mm i.d x 270 mm long). Before loading, the column was equilibrated with the same buffer. The enzyme was eluted with a linear gradient from 0 to 0.4 M NaCl in the same buffer. The enzyme pool was concentrated by ultrafiltration, dialyzed against 0.5 M NaCl/0.1M NaOAc buffer at pH 4.4, and applied to an acarbose-Sepharose affinity column (10 mm i.d. x 40 mm long). The column was equilibrated with the same buffer. After loading, the column was rinsed with the same buffer until the eluent reached a low but constant absorbance at 280 nm. Afterwards the bound enzyme was eluted with a 1.7 M Tris buffer at pH 7.6. The purified enzyme was concentrated, dialyzed against water, and freeze-dryed. Purity was checked by polyacrylamide gel electrophoresis.

In order to determine what fraction of the enzyme produced was secreted to the medium, yeast cells were suspended in 0.05 M acetate buffer at pH 4.5 and broken open by using a homogenizer at a pressure of 500 kg_f/cm^2. Samples were taken at various time intervals until a constant glucoamylase activity was reached, and the solution was cooled at those intervals.

Hydrolysis kinetics were determined for both wild-type and mutant glucoamylases and also for a commercial *A. awamori* glucoamylase used as a control. For each of these three glucoamylases, three sets of experiments were performed, one with glucoamylase only, one with glucoamylase and pullulanase, and one with glucoamylase and isoamylase. 30% Maltrin 15 in 0.05 M acetate buffer at pH 4.5 was used as substrate and 0.02% sodium azide was used to inhibit microbial growth in the hydrolysis mixtures. Hydrolysis was performed at 35°C and pH 4.5 for 120 h. Samples were taken in various time intervals, and reaction was stopped by 2.5 M Tris buffer at pH 7.1. They were frozen immediately, and were then analyzed for glucose, disaccharide, and trisaccharide concentrations, the former by a glucose oxidase method and the latter two by capillary gas chromatography after trimethylsilylation and trifloroacetylation respectively (Nikolov *et al.*, 1989).

RESULTS AND DISCUSSION

In the first part of the research, wild-type and mutant glucoamylases were produced by fermentations in which a special *S. cerevisiae* strain containing wild-type and mutant *Aspergillus awamori* glucoamylase genes were used. The medium used in the fermentation was yeast minimal salts medium without leucine but with histidine. The reason to use this minimal medium in the fermentation was its selectivity towards only plasmid-bearing cells. The plasmid containing glucoamylase also contains the leucine gene, which gives the plasmid-bearing cells the ability to grow in a leucine-deficient medium (Innis *et al.*, 1985).

The initial glucose concentration of the medium was 2%, and under the fermentation conditions used the glucose concentration dropped to zero in the first 20 h. Since the fermentation was performed up to 72 h, glucose should be added somehow to continue the process and to obtain the maximum glucoamylase concentration possible. Therefore, we attempted to maximize both cell density and glucoamylase activity by using different glucose concentrations, as shown in Table 1. In the first run, glucose concentration was returned to 2% at 48 h. Results for glucose concentration, cell density, and glucoamylase activity are shown in Figure 1, and are the best of all five runs. Glucoamylase activity was low until 40 h and then increased rapidly, especially after 48 h, to a maximum value of 314 U/mL. The ratio of carbon to nitrogen offered to the cells throughout the fermentation was 9. Typical C/N values for yeast are given as 5-6 (Rose and Harrison, 1970), however it is desirable to have higher C/N values in the medium since a fraction of this carbon is converted to carbon dioxide.

For the second case glucose concentration was returned to 2% at 28, 50, and 60 h, leading to a C/N ratio of 18. Cell density and glucoamylase activity at the end of this fermentation were 83% and 64% those of the first run, respectively. To maintain the C/N ratio at 9.5 and to hold the glucose concentration near 2%, in the third run a 40% glucose - 7.5% ammonium sulfate mixture was added nine times between 14 and 60 h. However, this led to the production of ethanol through the Crabtree effect, to which *S. cerevisiae* is very susceptible (Polakis and Bartley, 1965; de Dekken, 1966). Cell density and glucose concentration were very low, only 72% and 31% those of the first fermentation, respectively. In the fourth and fifth runs, glucose concentrations were held constant near 0.03% and 0.3% respectively, and the C\N ratio was held at 7 by the continuous addition of a 40% glucose -11.4% ammonium sulfate solution after 24 h. This again led to low values of cell density, 50% and 47%, respectively, and glucoamylase activity, 34% and 39%, respectively, those of the first run.

When cells from the run to produce mutant glucoamylase were ruptured, some further glucoamylase was released. However, 89% of the total glucoamylase activity produced by the cells was released to the medium before their rupture.

In the second part of the study, production of glucose and individual disaccharides from starch dextrin by *A. awamori* mutant and wild-type glucoamylases produced by *S. cerevisiae* and by

native *A. awamori* glucoamylase with and without pullulanase or isoamylase, was measured. Results for the three enzyme forms are shown in Figures 2-4. Similar curves were obtained for all cases, with maximum glucose yields being obtained at about halfway through the 120 h fermentation. Very slight increases in glucose yield were obtained when the mutant glucoamylase was used, and when pullulanase and isoamylase, especially the former, were added to any of the glucoamylases. Almost no difference was observed between native and wild-type glucoamylases. The lowest rate of loss of glucose to disaccharides after the glucose peak occured with mutant glucoamylase.

Di- and trisaccharide concentrations were determined for all nine hydrolysis runs. Large amounts of isomaltose were produced, along with smaller amounts of nigerose and kojibiose.. Although there are significant differences in the production rates of the three disaccharides from one enzyme preparation to the next, they are inconsistent when all runs are compared. Maltose and maltulose, which are present in the initial dextrin feed, decreased during the hydrolyses, maltose rapidly to a constant level, and maltulose very slowly. No production of α,β–trehalose or trisaccharides was noted during any run, unlike the results of Nikolov *et al.* (1989), probably because the runs were not sufficiently long.

REFERENCES

Banks, W., and Greenwood, C. T. (1971) *Stärke*, **23**, 222-227.

De Deken, R. H. (1966) *J. Gen. Microbiol.*, **44**, 149-156.

Harada, T. (1984) *Biotechnol. Gen. Eng. Rev.*, **1**, 39-64.

Innis, M. A., Holland, M. J., McCabe, P. C., Cole, G. E., Wittman, V. P., Tal, R., Watt, K. W. K., Gelfand, D. H., Holland, J. P., and Meade, J. H. (1985) *Science*, **228**, 21-26.

Lee, D. D., Lee, Y. Y., Reilly, P. J., Collins, E. V., Jr., and Tsao, G.T. (1976) *Biotechnol. Bioeng.*, **18**, 253-267.

Linko, P. (1987) in *Enzymes and Their Role in Cereal Technology*, Kruger, J. E., Lineback, D., and Stauffer, E., Editors. American Association of Cereal Chemists, St. Paul, pp. 351-391.

Manjunath, P., Shenoy, B. C., and Raghavendra, R. (1983) *J. Appl. Biochem.*, **5**, 235-260.

Nikolov, Z. L., Meager, M. M., and Reilly, P. J. (1989) *Biotechnol. Bioeng.*, **34**, 694-704.

Nam, K. D., Choi, M. H., Kim, W. S., Kim, H. S., and Ryu, B. H. (1988) *J. Ferment. Technol.*, **64**, 427-432.

Peppler, H. J. (1970) in *The Yeasts; Yeast Technology*, Rose, A. H., and Harrison, J. S., Editors. Academic Press, New York, Vol.3, pp. 430.

Polakis, E. S., Bartley, W. (1965) *Biochem. J.*, **97**, 284-297.

Reilly, P. J. (1979) *Appl. Biochem. Bioeng.*, **2**, 185-206.

Sierks, M. R., Ford, C., Reilly, P. J., and Svensson, B.(1990) submitted for publication.

RUN #	CELL DENSITY OD @ 680 nm	GLUCOAMYLASE ACTIVITY IU/L
1	7.8	314
2	6.5	200
3	5.6	96
4	3.9	108
5	3.7	121

Table 1. *Saccharomyces cerevisiae* fermentations for wild-type glucoamylase production.

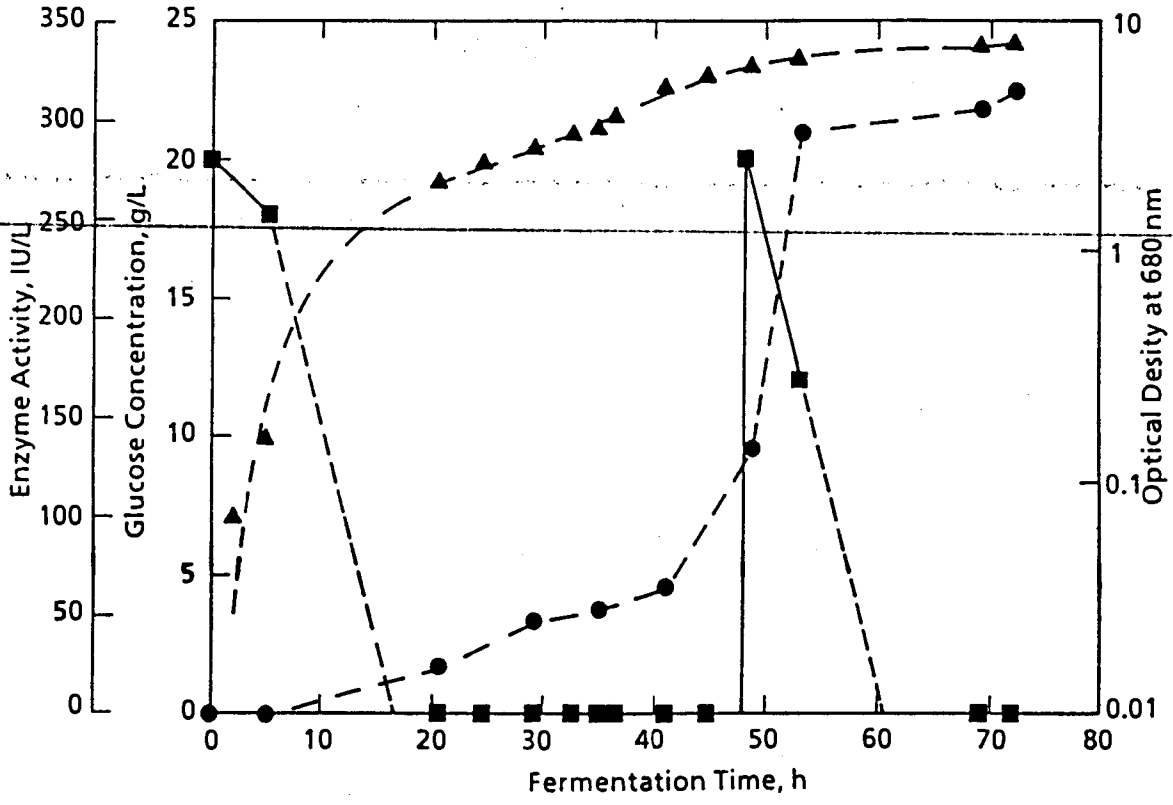

Figure 1. Growth curve, glucose consumption, and glucoamylase production of *Saccharomyces cerevisiae* ((▲) - optical density at 680 nm, (■) - glucose concentration, g/L, (●) - enzyme activity, IU/L).

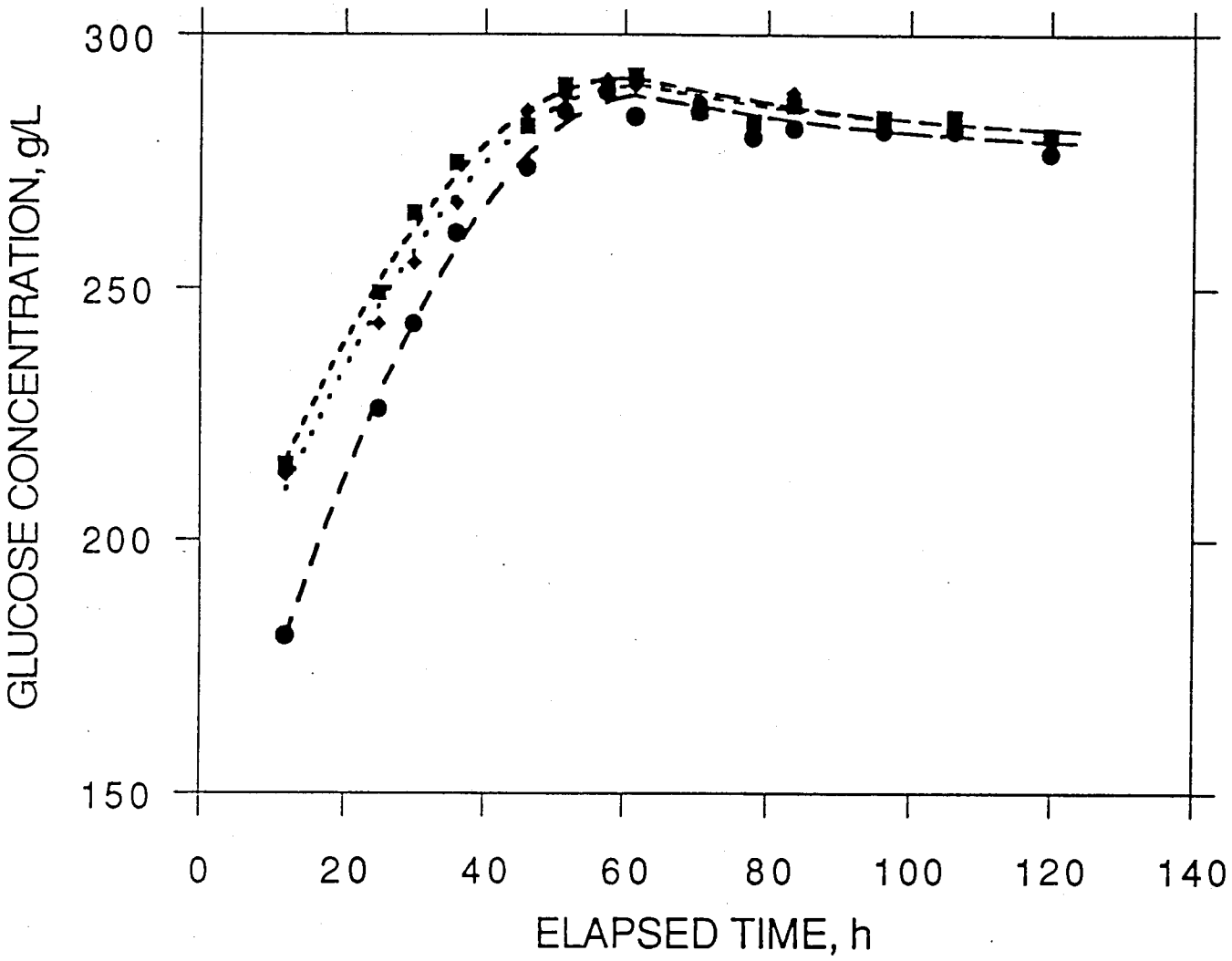

Figure 2. Production of glucose by glucoamylase from *Aspergillus awamori* ((●) - glucoamylase, (■) - with pullulanase, (◆) - with isoamylase).

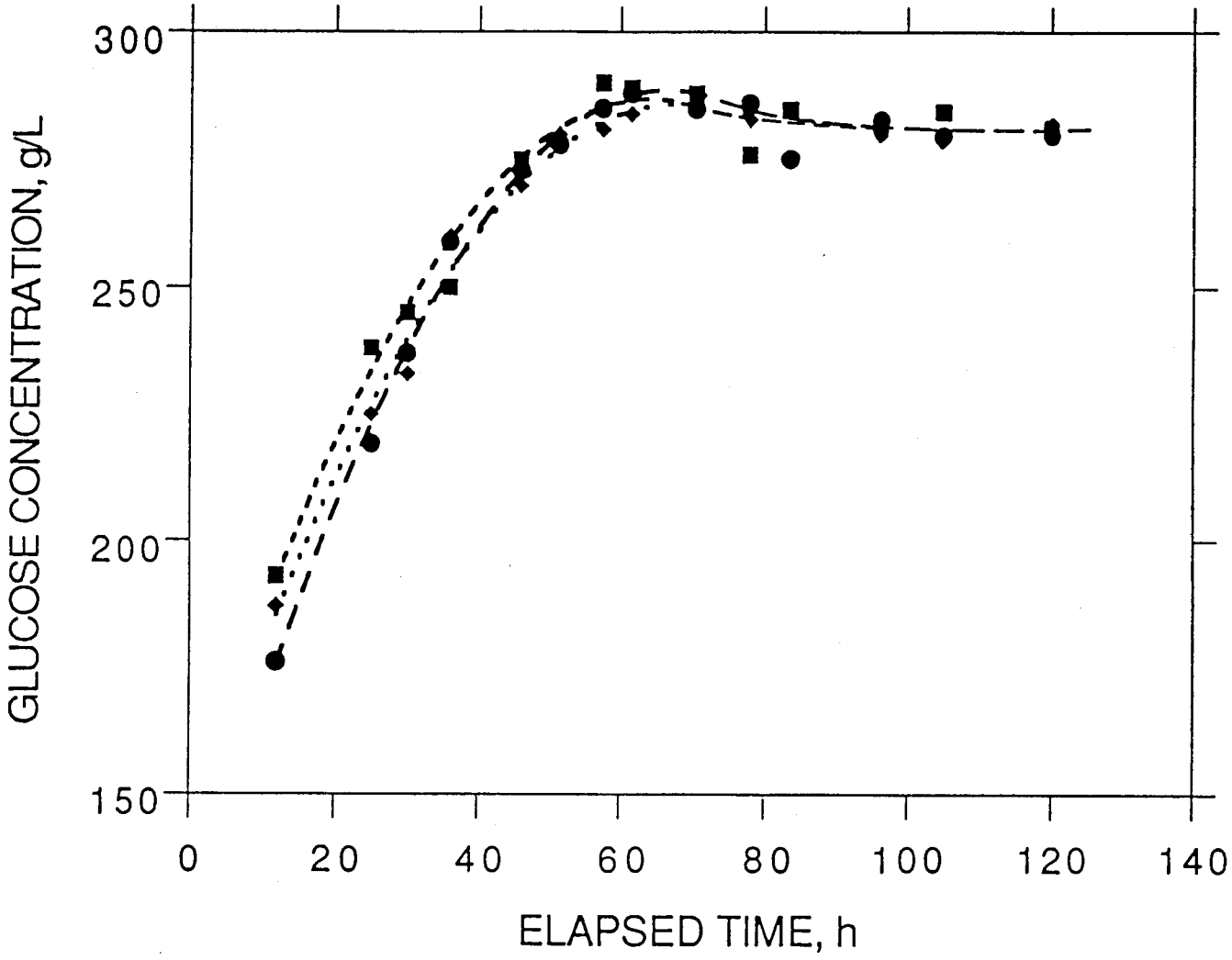

Figure 3. Production of glucose by glucoamylase from *Saccharomyces cerevisiae* ((●) - glucoamylase, (■) - with pullulanase, (◆) - with isoamylase).

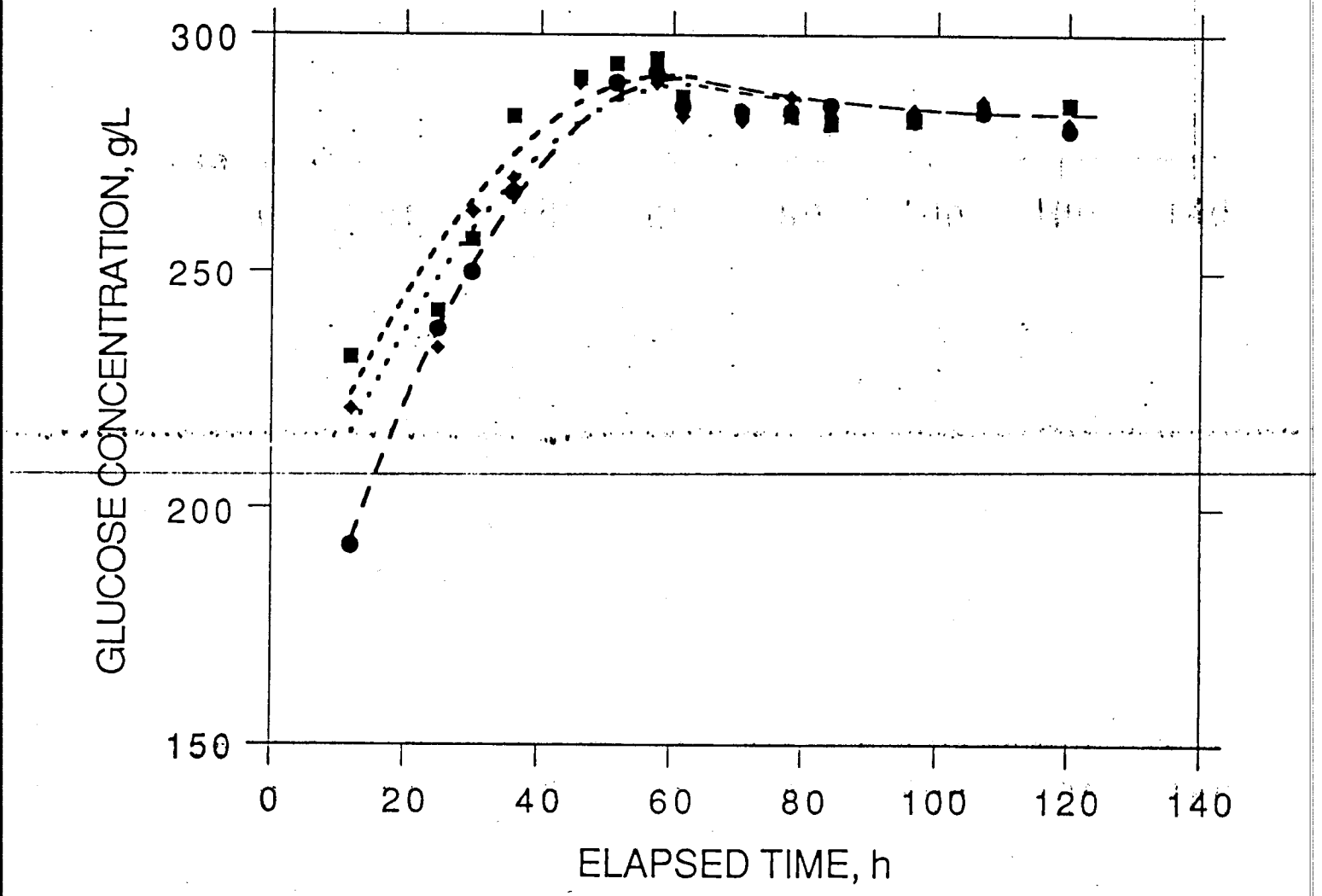

Figure 4. Production of glucose by mutant glucoamylase from *Saccharomyces cerevisiae* ((●) - glucoamylase, (■) - with pullulanase, (◆) - with isoamylase).

DYNAMIC MODELING OF THE IMMUNE SYSTEM

Barry Vant-Hull and Dhinakar S. Kompala
University of Colorado at Boulder

October 1, 1990

"No more things should be presumed to exist than are absolutely necessary"
William Occam 1280-1349

". . . it appears as if immunobiology falls outside the domain of Occam's razor"
Joshua Lederburg

Introduction

When primitive life evolved from the unicellular organism to the multicellular, it faced an interesting dilemma: how does one distinguish a cell which is part of "self" from one that is not "self"? This is not a trivial problem. It is important to be able to tell when our self is being invaded by a foreign organism such as a bacteria or a parasite. It is equally important to know when part of our self begins to behave differently, due, perhaps, to cancer or mutations. The vertebrate solution to the problem is the immune system, an amazingly complex network of cells and cell products which determines what things are self, and thus worthy of respect, and what things are not self, and therefore targets for ruthless elimination. In order to preserve life, our immune system must dispense death. If the signals ever get crossed there is catastrophe. That is the reason for the system's incredible specificity, so that nonself cells, and nonself cells only, are eliminated. In a very real sense, our immune system defines our identity.

Background

The scenario of an immune response as accepted by most immunologists is shown in Figure 1.

An invading particle, in this case a **virus**, is intercepted by a type of macrophage known as an **antigen-presenting cell**, which functions as a doorkeeper to the body. The APC engulfs the invader, digests it and processes it into a form suitable to be displayed on its outer membrane, where its antigenic determinant can be recognized by the appropriate helper-T cells. At the same time, the APC secretes the hormone **interleukin 1**, which serves to activate the helper-T cells and stimulate them to produce **interleukin 2**, necessary for T cell proliferation.

On making the hand-off, one group of these helper cells activates **amplification-T cells**, which in turn stimulate activated **cytotoxic-T cells** into proliferation (studies have shown that the effector T cell subsets (T_C and T_S) may be activated by the presence of viral antigens alone). These cytotoxic- or killer-T cells have the responsibility for destroying **body cells** which have been virally infected, thus preventing the proliferation of the virus.

Presence of the virus stimulates the **virgin B cells** to transform into **large lymphocytes**, which have proliferation and **antibody** production capabilities. There are several different classes of antibodies. In a primary immune response, the initial antibody

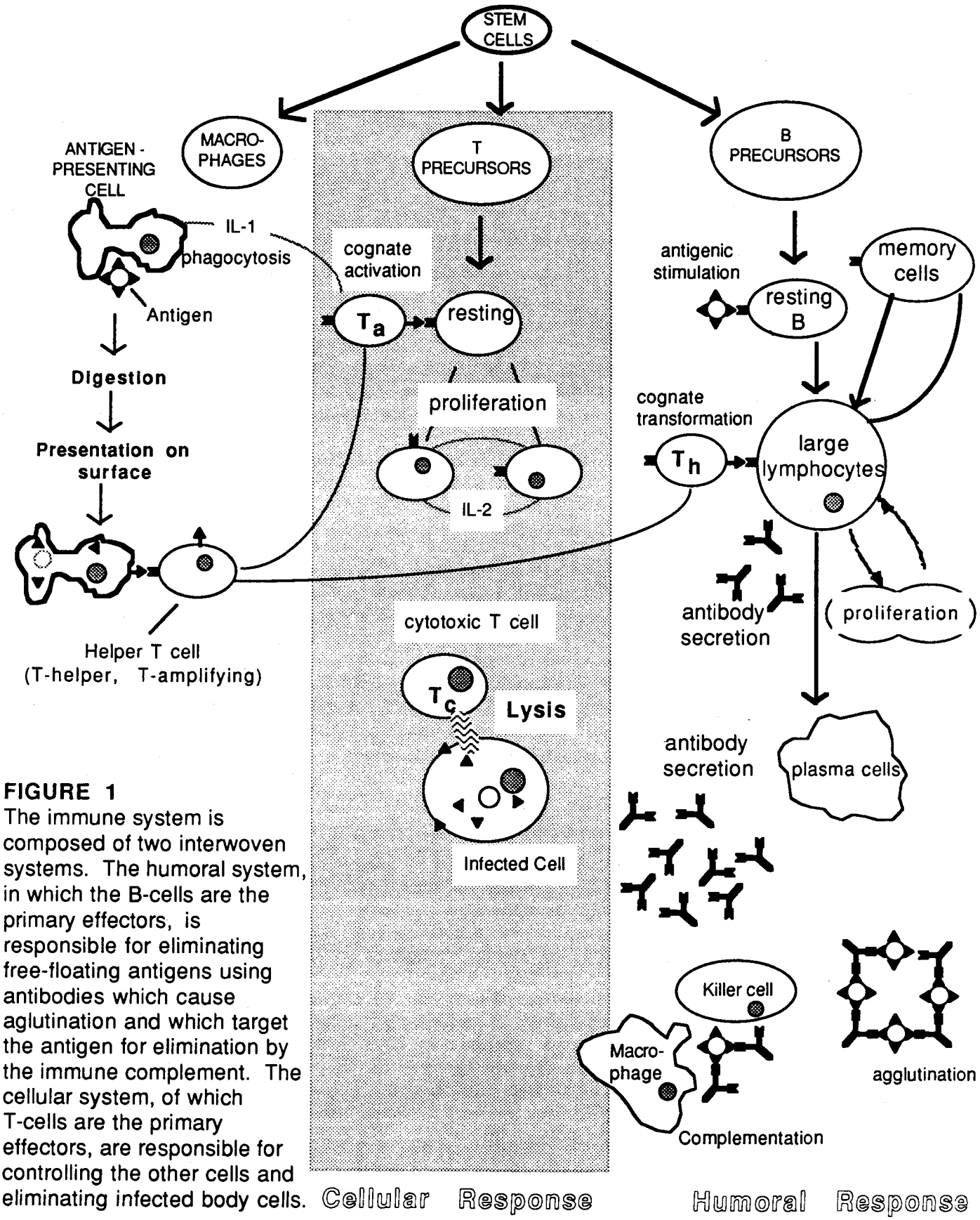

FIGURE 1
The immune system is composed of two interwoven systems. The humoral system, in which the B-cells are the primary effectors, is responsible for eliminating free-floating antigens using antibodies which cause aglutination and which target the antigen for elimination by the immune complement. The cellular system, of which T-cells are the primary effectors, are responsible for controlling the other cells and eliminating infected body cells.

production is of the IgM (immunoglobulin M) class, followed by production of the IgG class. If the viral infection recurs, the bulk of the antibody produced is of the IgG class. If the infection is severe enough, the **helper-B T cells** or just plain helper-T cells, stimulate the large lymphocytes to differentiate into **plasma cells**, which have a much greater antibody production capability at the expense of all proliferation capability.

The simplified version we have adapted for our model may be seen in Figure 2. Though the practice is common in immunology textbooks, the division of the T cells into the subsets we have used is rather arbitrary. There are likely dozens of different T subsets having highly specific functions. The suppressor T cells are particularly good candidates for this wide diversity of function. Conversely, there may be T cells which share the functions of two or more of these subsets, or cells which undergo transformations between these subsets.

The model

The dynamic model presented below includes all the fairly well accepted theories outlined above, as well as some of our own hypothetical mechanisms. The appearance of these less-championed hypotheses will be clearly marked with the pronoun "we" in their explanations. In order to keep things simple, saturation kinetics are used for all interactions.

In general, cell populations are segregated into activated and unactivated subpopulations, with the rate of shuttling between the two groups being determined by the concentration of various inducers or suppressors. The constants k_{dx} correllate to the specific death or specific degradation rate of cell or molecule x. The constants k_{trans} or k_{tXY} refer to the specific transformation rate between activated and unactivated T cells, or the specific transformation rate from cell type x to cell type y. The constants r_x refer to either the production rate of substance x, or the production rate by cell type x. Constants S_x refer to source terms of cell x.

Macrophages (antigen-presenting cells)

APC's intercept and devour the invading virus G, and thus charged, pass the antigenic determinant onto the various helper T cells, in the process becoming inactivated. As nothing interior to

Figure 2 SCHEMATIC OF DYNAMIC MODEL

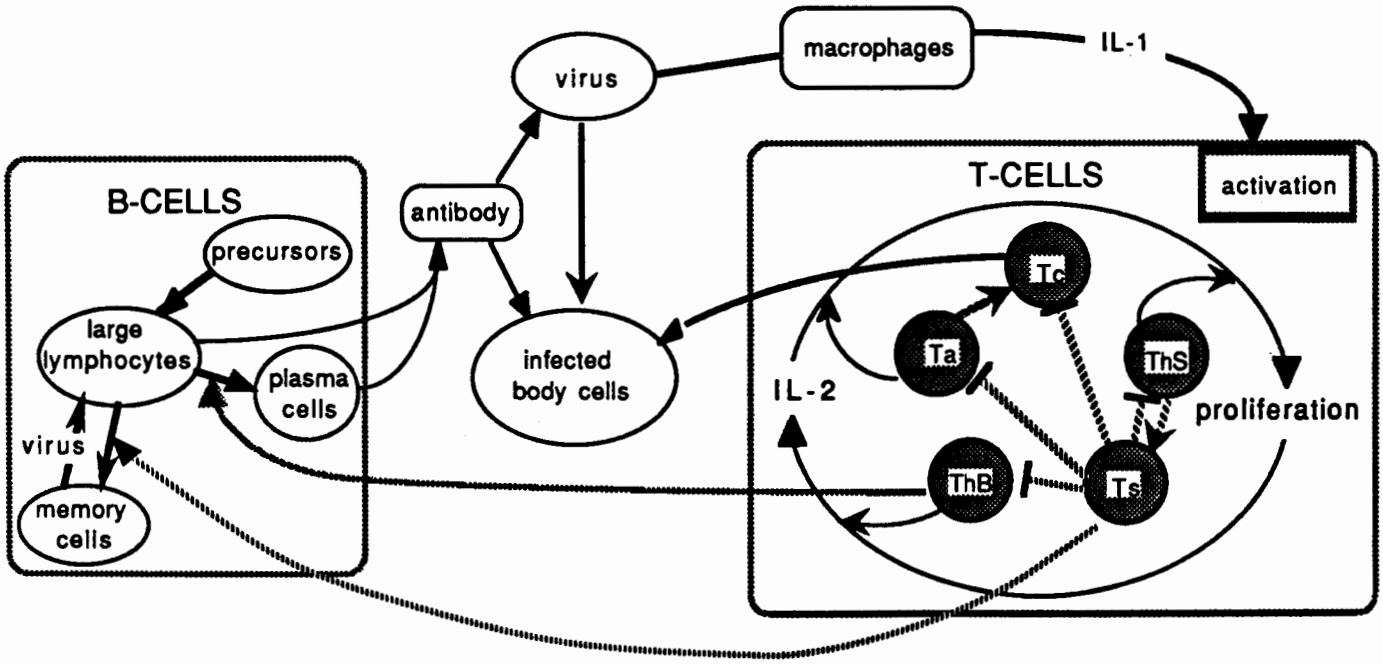

the model is expected to affect growth or death rates, the total number of macrophages remains constant.

$$\frac{dM}{dt} = -k_{tM1}\frac{G}{K_G + G}M + k_{tM2}\frac{\Sigma T_h}{K_{Th} + \Sigma T_h}M_{act}$$

$$\frac{dM_{act}}{dt} = k_{tM1}\frac{G}{K_G + G}M - k_{tM2}\frac{\Sigma T_h}{K_{Th} + \Sigma T_h}M_{act}$$

Antigen (virus)

Entry of viruses into the body depends on environmentally imposed conditions, staying over at a sick friend's for instance, and thus is represented here by an arbitrary source term S_G. In these simulations, S_G was taken to be a step input of 10 time unit duration. Cells which have succumbed to infection **N** lyse at a specific rate k_N, releasing n_G viruses back into the bloodstream. Viruses are also picked up by macrophages **M** in the course of activation. Antibodies **Ab** bind to viruses in a certain stochiometry k_G, removing them through agglutination as well as by marking them for elimination. The specific degradation term, k_{dG}, includes the uptake of viruses by body cells (zero order in body cells as the pool is near infinite), some of which proceed on to become infected cells **N**.

$$\frac{dG}{dt} = S_G(t) + k_{dN}\,N\,n_G - k_{tM1}\frac{G}{K_G + G}M - r_{titre}\,k_{G/Ab}\,G\,Ab - k_{dG}\,G$$

Infected cells

As uninfected cells are in great excess, the rate of infection, k_{inf}, depends only on the virus concentration **G**. Despite infection, these cells may continue to proliferate at some specific growth rate μ_N. We are assuming that the killer cells T_C are able to home in on the infected cells, so that there is a saturation term in **N** and not T_C.

$$\frac{dN}{dt} = k_{inf}\frac{G}{K_{GN} + G} + \mu_N N - k_c T_c \frac{N}{K_N + N} - k_{dN} N$$

Interleukins

IL_1 is produced by activated macrophages, and taken up by all the different subsets of T cells. IL_2 is produced by activated helper T cells (T_A, T_{HB}, T_{HS}), and is taken up by all subsets of T cells. We assume here that the uptake and production rates are identical for all T cell subsets.

$$\frac{dIL_1}{dt} = r_M M_{act} - u_{TL1}\frac{IL_1}{K_{L1} + IL_1}\Sigma T_P - k_{dL1}\,IL_1$$

$$\frac{dIL_2}{dt} = r_T\frac{IL_1}{K_{L1} + IL_1}\Sigma T_h - u_{TL2}\frac{IL_2}{K_{L2} + IL_2}\Sigma T - k_{dL2}\,IL_2$$

$$\Sigma T = T_A + T_C + T_S + T_{HS} + T_{HB}$$

$$\Sigma T_h = T_A + T_{HS} + T_{HB}$$

T cells

The equations for all five subsets have the same basic structure. We assume the specific growth rates for all to have the same maximum, μ_{Tmax}, and otherwise be functions of the IL_2 concentration and auxiliary cell concentrations. A logistic term, μ_{Tlog}, is present to put a limit on the population density.

Except for T_C and T_S cells, IL_1 is responsible for transformation to an active state in the presence of virus G, sometimes in the context of the APC macrophage concentration M or some other auxiliary cell. We hypothesize that suppressor cell concentration T_S is responsible for transformation back to the inactivated state. As it is likely that a second infection of virus would occur soon after a primary response has run its course and is in the suppression phase, it is necessary that the presence of viral antigen inhibit suppression. In lieu of another mechanism, we propose the following:

$$F_{Ts} = \frac{T_s}{K_{GS} + T_s} \frac{\varepsilon}{\varepsilon + G}$$

Cytotoxic or killer T cells

Responsible for lysing body cells infected with virus. Though they do not require IL_1 for activation, T_A are needed for proliferation.

$$\mu_C = \mu_{Tmax} \frac{IL_2}{K_{I2} + IL_2} \frac{T_A}{K_{Th} + T_A} - \mu_{Tlog} T_C$$

$$\frac{dT_{Cpre}}{dt} = S_{Tc} - k_{trans} \frac{G}{K_{GT} + G} T_{Cpre} + k_{trans} F_{Ts} T_C - k_{dT} T_{Cpre}$$

$$\frac{dT_C}{dt} = \mu_C T_C + k_{trans} \frac{G}{K_{GT} + G} T_{Cpre} - k_{trans} F_{Ts} T_C - k_{dT} T_C$$

Amplification cells (help T_C to proliferate)

$$\mu_A = \mu_{Tmax} \frac{IL_2}{K_{I2} + IL_2} - \mu_{Tlog} T_A$$

$$\frac{dT_{Apre}}{dt} = S_{Ta} - k_{trans} \frac{IL_1}{K_{I1} + IL_1} \frac{M_{act}}{K_M + M_{act}} T_{Apre} + k_{trans} F_{Ts} T_A - k_{dT} T_{Apre}$$

$$\frac{dT_A}{dt} = \mu_A T_A + k_{trans} \frac{IL_1}{K_{I1} + IL_1} \frac{M_{act}}{K_M + M_{act}} T_{Apre} - k_{trans} F_{Ts} T_A - k_{dT} T_A$$

Suppressor T cells

These caused the most problems in the model, which is not surprising, as the suppressor cells are the control system of the immune system. After shutting down the rest of the system, the T_S cells must shut themselves down. We took the tack of putting the control of the T_S cells with the T_{HS} cells, thus deferring the problem one step. Note that the T_S cells suppress themselves as well as their helper cells.

$$\mu_S = \mu_{Tmax} \frac{IL_2}{K_{I2} + IL_2} \frac{T_{HS}}{K_{Ths} + T_{HS}} - \mu_{Tlog} T_S$$

$$\frac{dT_{Spre}}{dt} = S_{Ts} - k_{trans} \frac{T_{HS}}{K_{Ths} + T_{HS}} T_{Spre} + k_{trans} F_{Ts} T_S - k_{dT} T_{Spre}$$

$$\frac{dT_S}{dt} = \mu_S T_S + k_{trans} \frac{T_{HS}}{K_{Ths} + T_{HS}} T_{Spre} - k_{trans} F_{Ts} T_S - k_{dT} T_S$$

Supressor-helper T cells

Though the T_{HS} cells are activated by rising virus concentration like the other T cells, they do not proliferate until the concentration falls again, thereby stimulating the T_S cells into action only after the infection has been taken care of.

$$\mu_{HS} = \mu_{Tmax} \frac{IL_2}{K_{I2} + IL_2} \frac{\varepsilon}{\varepsilon + G} - \mu_{Tlog} T_{HS}$$

$$\frac{dT_{HSpre}}{dt} = S_{Ths} - k_{trans} \frac{IL_1}{K_{I1} + IL_1} \frac{G}{K_{GT} + G} T_{HSpre} + k_{trans} F_{Ts} T_{HS} - k_{dT} T_{HSpre}$$

$$\frac{dT_{HS}}{dt} = \mu_{HS} T_{HS} + k_{trans} \frac{IL_1}{K_{I1} + IL_1} \frac{G}{K_{GT} + G} T_{HSpre} - k_{trans} F_{Ts} T_{HS} - k_{dT} T_{HS}$$

B-helper T cells

These cells help transform the large lymphocytes into plasma cells.

$$\mu_{HB} = \mu_{Tmax} \frac{IL_2}{K_{I2} + IL_2} - \mu_{Tlog} T_{HB}$$

$$\frac{dT_{HBpre}}{dt} = S_{Thb} - k_{trans} \frac{IL_1}{K_{I1} + IL_1} \frac{M_{act}}{K_M + M_{act}} T_{HBpre} + k_{trans} F_{Ts} T_{HB} - k_{dT} T_{HBpre}$$

$$\frac{dT_{HB}}{dt} = \mu_{HB} T_{HB} + k_{trans} \frac{IL_1}{K_{I1} + IL_1} \frac{M_{act}}{K_M + M_{act}} T_{HBpre} - k_{trans} F_{Ts} T_{HB} - k_{dT} T_{HB}$$

B cells

The B cells are responsible for the humoral immune response and are distributed into three different types which take on the three different tasks of proliferation, large scale antibody production, and memory in preparation for future infections. Two types of antibodies are produced, IgM, dominant in the initial portion of a primary immune response, and IgG, dominant in secondary immune responses. In order to provide a mechanism for the different production modes of antibody, we have divided the large lymphocytes and the plasma cells into two lines, a lineage directly from the virgin B cells, which produces IgM, and a lineage directly from the memory cells, which produces IgG. We have developed the mechanisms given below for transformation between the cell types based mainly on logical arguments rather than experimental evidence.

Virgin B lymphocytes

$$\frac{dB_v}{dt} = S_B - k_{tPL} \frac{T_{HB}}{K_{Thb} + T_{HB}} B_v - k_{dV} B_V$$

Large lymphocytes

The large lymphocytes are the hub of the B cell cycle. IgM producers are transformed by the presence of virus from virgin cells to large lymphocytes. IgG producers are transformed by the presence of virus from memory cells to large lymphocytes. High T_{HB} concentrations cause large lymphocytes to be transformed into plasma cells. As the immune response winds down, T_S cells initiate a conversion from large lymphocytes to memory cells.

$$\mu_{LL} = \mu_B \frac{IL_2}{K_{I2} + IL_2} \frac{G}{K_G + G} - \mu_{Blog} B_{LL}$$

$$B_{LL} = B_{LLM} + B_{LLG}$$

$$\frac{dB_{LLM}}{dt} = \mu_{LL} B_{LLM} + k_{tVL} \frac{G}{K_{GB} + G} B_v - k_{tLM} F_{Ts} B_{LLM}$$

$$- k_{tLP} \frac{T_{HB}}{K_{Thb} + T_{HB}} B_{LLM} - k_{dBl} B_{LLM}$$

$$\frac{dB_{LLG}}{dt} = \mu_{LL} B_{LLG} + k_{tML} \frac{G}{K_{GB} + G} B_{mem} - k_{tLM} F_{Ts} B_{LLG}$$

$$- k_{tLP} \frac{T_{HB}}{K_{Thb} + T_{HB}} B_{LLG} - k_{dBl} B_{LLG}$$

Plasma cells

When the viral infection grows extreme enough, large lymphocytes are transformed by the T_{HB} cells into plasma cells, which have enhanced antibody production capabilities, but no proliferation capabilities.

$$B_{plas} = B_{plasM} + B_{plasG}$$

$$\f(dB_{plasM},dt) = k_{tLP} \\f(T_{HB},K_{Thb}+T_{HB}) B_{LLM} - k_{dBp} B_{plasM}$$

$$\frac{dB_{plasG}}{dt} = k_{tLP} \frac{T_{HB}}{K_{Thb} + T_{HB}} B_{LLG} - k_{dBp} B_{plasG}$$

Memory cells

At the temination of the immune response, large lymphocyte are transformed into memory cells through the interaction of the T_S cells. When a secondary response is initiated, the antigen concentration initiates transformation back to large lymphocytes which are IgG producers.

$$\frac{dB_{mem}}{dt} = k_{tLM} F_{Ts} B_{LL} - k_{tML} \frac{G}{K_{GB} + G} B_{mem}$$

Antibodies

The IgM and IgG antibodies are produced by their respective large lymphocytes and plasma cells at their respective production rates, and are titrated out by the viral antigen. We have assumed that the rates are equal for both IgM and IgG on a mass basis, leading to the presence of the r_{MG} factor (the IgM molecule is approximately 2.5 times more massive than.the IgG molecule).

$$Ab = IgG + IgM$$

$$\frac{dIgM}{dt} = r_{LL}/r_{MG} B_{LLM}(1-F_{Ts})/r_{MG} + r_p B_{plasM} (1-F_{Ts}) - \frac{r_{titre}}{k_{G/Ab}} G\, IgM - k_{dAb}\, IgM$$

$$\frac{dIgG}{dt} = r_{LL} B_{LLG}(1-F_{Ts}) + r_p B_{plasG} (1-F_{Ts}) - \frac{r_{titre}}{k_{G/Ab}} G\, IgG - k_{dAb}\, IgG$$

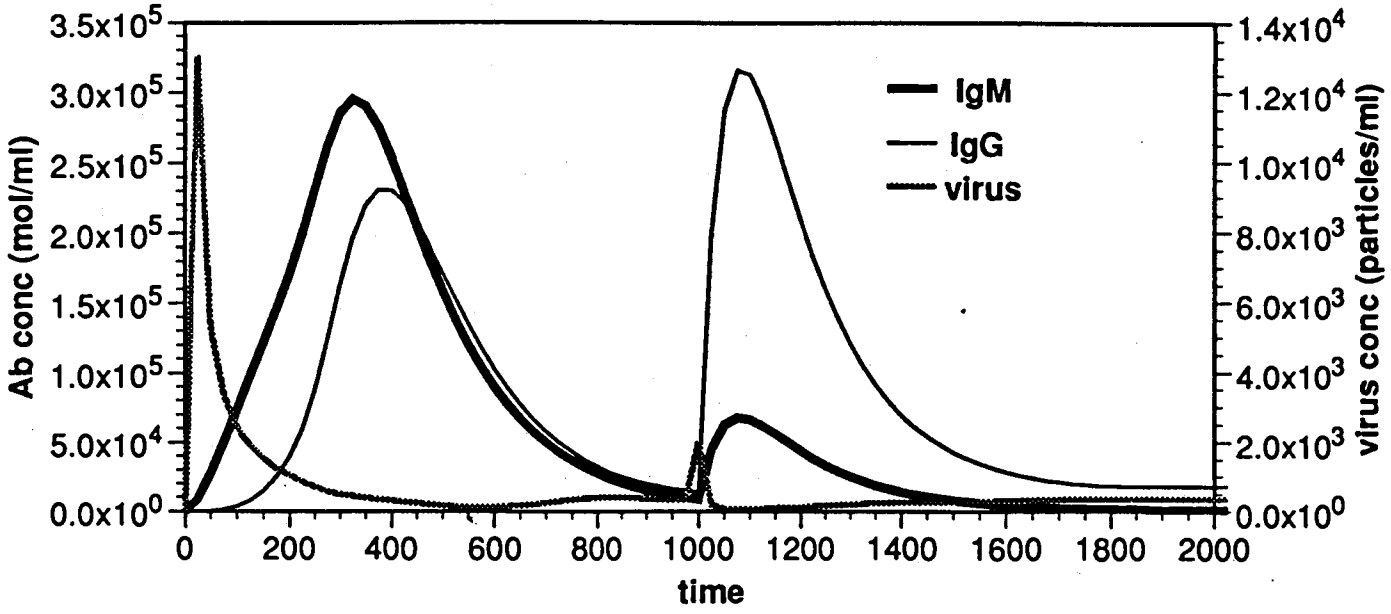

Figure 3. The concentrations of IgM and IgG antibodies during a primary and secondary response. Note that IgM is dominant in the primary response, while IgG is dominant in the secondary response and is of greater magnitude.

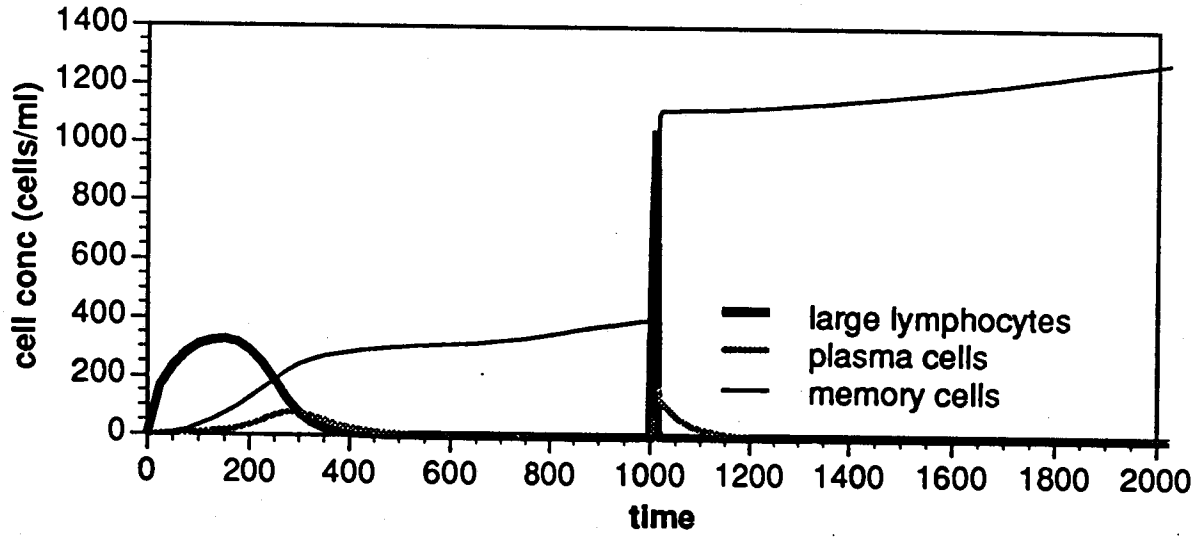

Figure 4. The concentrations of the various B cells during two immune responses. The large lymphocytes are active first, proliferating and producing antibodies. As $T_{H\,B}$ concentrations rise in response to rising viral concentrations, the large lymphocytes are transformed into plasma cells. As viral concentrations fall and T_S concentrations rise, large lymphocytes are transformed into memory cells. This allows a faster and larger response to the secondary infection.

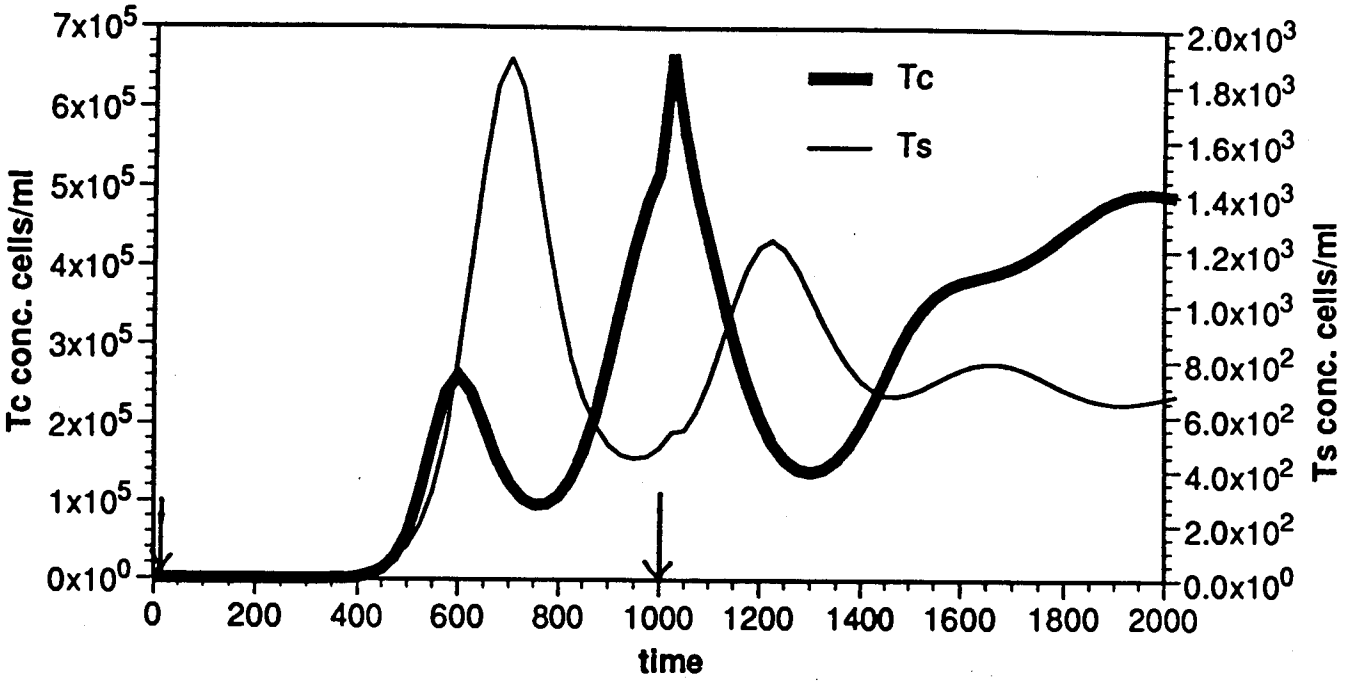

Figure 5. The concentrations of the cytotoxic and the suppressor T cells over the course of two immune responses. The suppressor cells do not rise as early in the first response as would be hoped, nor do they drop to low concentrations fast enough afterwards. The high concentrations of T_s cell keeps the magnitude of the second response from rising as high as would be expected. The T_c cells also fail to drop down after the second response as expected.

References

Batt, B. C. & Kompala, D. S. (1990). Verification of Immune Response Optimality through Cybernetic Modeling. *J. Theor. Biol.* 142:317-340.

Bell, G. I., Perelson, A. S. & Pimbley, G. H. (1978). *Theoretical Immunology.* Immunology Series v. 8. 646 pp. New York: Dekker.

Cantor, H. & Boyse, E. A. (1976). Regulation of Cellular and Humoral Immune Responses by T-cell Subclasses. *J. Exp. Med.* 23-31.

De Boer, R. J. & Hogeweg, P. (1987). Immunological Discrimination between Self and Non-Self by Precursor Depletion and Memory Accumulation. *J. Theor. Biol.* 124:343-369.

Grey, H. M., Sette, A. & Buus, S. (1989). How T Cells See Antigen. *Sci. Amer.* Nov.: 56-64.

Hood, L. E., Weissman, I. L., Wood, W. B. & Wilson, J. H. (1984). *Immunology.* 2nd edn. 558 pp. Menlo Park, CA: Benjamin/Cummings.

Langham, Rodney E. (1989). *The Immune System.* 209 pp. San Diego: Academic Press, Inc.

MacDonald, H. R. & Nabholz, M. (1986). T-Cell Activation. *Ann. Rev. Cell Biol.*, 2:231-253.

DYNAMIC MODELING OF ACTIVE TRANSPORT ACROSS A BIOLOGICAL CELL: A Stochastic Approach

B.C. Shen, S.T. Chou, Y.Y. Chiu, and L.T. Fan

Department of Chemical Engineering
Kansas State University
Manhattan, Kansas 66506

June 23, 1990

ABSTRACT

The free energy transduction in a biological cell involving the active transport of small molecules across the membrane against their concentration gradient is rendered possible only through the intervention of a protein complex. This process has been viewed as a Markov process. The distribution of molecules of the protein complex among its different structures or states has been obtained both analytically by solving the master equations of the process and numerically by means of Monte Carlo simulation. The results of the Monte Carlo simulation are compared with the corresponding analytical solutions for verification.

INTRODUCTION

Active transport, the migration of molecules or ions across a cell's membrane against their concentration gradient, is an essential process for all of life's activities. It generates ionic gradients necessary for the excitability of nerve and muscle. In addition, it regulates cell volume and maintains the intracellular pH and ionic composition within a narrow range to provide a favorable environment for enzyme activity (Stryer, 1988). The mechanism underlying the active transport is not well-understood; however, a simplified mechanism has been proposed recently by Hill (1989), who has also developed the stochastic models for the free energy transduction based on the assignment of a free energy level to a given state of a macromolecular unit, e.g., a protein complex (Hill, 1977).

The cells of a multicellular organism usually vary in shape and size; however, an individual cell contains a nucleus in its inside which is separated by a membrane from its surroundings or outside (see, *e.g.,* De Robertis *et al.,* 1970). Suppose that two types of small molecules, L and M, are located both inside and outside a cell. The concentration of small molecules of M inside the cell is much larger than that outside, i.e., $C_{Mi} >> C_{Mo}$, while the concentration of small molecules of L outside is somewhat larger than that inside, i.e., $C_{Lo} > C_{Li}$; thus, $C_{Mi}/C_{Mo} > C_{Lo}/C_{Li}$ (Hill, 1989). Given a mechanism or pathway across the cell's membrane, the molecules of M would tend to move spontaneously from the inside to the outside, whereas the molecules of L would tend to move in the opposite direction. If there exists a large protein complex capable of spanning the membrane and interacting suitably with both M and L, then it is possible for the larger concentration gradient of M to be exploited to drive L from the inside to the outside against the smaller opposite concentration gradient. This gives rise to the active transport of L. In this paper, the active transport has been simulated by considering the protein complex which reveals itself through various structures as the system.

The transition of the system, i.e., the transition among the various structures of the protein complex, is viewed as a Markov process.

SYSTEM DESCRIPTION

Consider an ensemble of the protein complex consisting of N_0 equivalent and independent molecules of the protein complex that are embedded in the lipid layer of the cell membrane. It is assumed that each molecule of the protein complex can exist in two interconvertible conformations, denoted by E and E^* (Figure 1a). Furthermore, suppose that both E and E^* contain one binding site for M and one for L. The binding sites in conformation E, however, are open only to the inside, while those in conformation E^* are open only to the outside. Assume further that L can be bound on its site only if M is already bound on its neighboring site (i. e., the presence of M stabilizes the binding of L); then,

$$\left.\begin{array}{ll} L + EM \longrightarrow LEM & (1) \\ L + E^*M \longrightarrow LE^*M & (2) \end{array}\right\}$$

The binding of L to EM initiates the transformation $E \rightarrow E^*$, that is,

$$L + EM \longrightarrow LEM \longrightarrow LE^*M \qquad (3)$$

L and M are bound less strongly to E^* than to E, and thus, it is possible for them to be released to the outside; this mechanism is summarized in Figure 1b. For each molecule of the protein complex, six possible structures or states (E, EM, LEM, LE^*M, E^*M, E^*) can exist in the transition process. The arrows between any pair of adjacent states in Figure 1c indicate that the transitions are reversible, and that the transition intensities, α_{ij}, determine the propensities of the protein complex to transfer from state i to state j.

If the protein complex completes one cycle in the counterclockwise direction (Figure 1b), the net effect is the transport of one molecule of M and one molecule of L across the membrane from the inside to the outside. M moves down its concentration gradient and experiences a decrease in free energy; therefore, the process occurs spontaneously. On the other hand, L is moved from the low concentration to the high concentration. The free energy change for this process is positive; this implies that some external force or an input of free energy is required to drive it. Thus, through the participation of the protein complex, which remains invariant after completion of the cycle, the free energy associated with the concentration gradient of M is consumed in forcing L to move against its concentration gradient. In summary, the larger concentration gradient of M is exploited to drive L from the inside to the outside against the smaller concentration gradient of L, thereby effecting the active transport.

STOCHASTIC MODELING

To simulate the active transport, a stochastic model has been developed. First, consider the transition of the protein complex among its six possible states, E, EM, LEM, LE^*M, E^*M, E^*, or simply states 1, 2, 3, 4, 5, and 6, respectively. Let X(t) be a random variable representing the state in which the protein complex is at time t, and $p_i(t)$, $i = 1,2,...,6$, be the probability of the protein complex to be in state i at that instant. The protein complex is further assumed to

exist initially in state 1, or equivalently in state E. Then, the initial conditions are

$$p_1(0) = 1.0 \tag{4}$$
$$p_i(0) = 0.0, \quad i=2,3,...,6 \tag{5}$$

Consider a time interval $(t,t+\Delta t)$ where Δt is sufficiently small such that at most one event, the transition of the protein complex from one state to its adjacent state, will occur with a probability governed by the probabilistic laws during this time interval. Thus, if the complex is in state 1 at time t, it will (see Figure 2)

1. transfer to state 2 with a probability of $[\alpha_{12}\Delta t + o(\Delta t)]$,
2. transfer to state 6 with a probability of $[\alpha_{16}\Delta t + o(\Delta t)]$, or
3. remain in the same state with a probability of $[1-\alpha_{12}\Delta t - \alpha_{16}\Delta t + o(\Delta t)]$ at time $t+\Delta t$.

Note that $o(\Delta t)$ approaches zero faster than Δt, i.e.,

$$\lim_{\Delta t \to 0} \frac{o(\Delta t)}{\Delta t} = 0 \tag{6}$$

The following mutually exclusive events determine the probability of the protein complex to be in state 1, $p_1(t+\Delta t)$, at time $t+\Delta t$.

1. The protein complex is in state EM (state 2) at time t, and transfers to state E (state 1) during the time interval, $(t,t+\Delta t)$, with a probability of $p_2(t)[\alpha_{21}\Delta t + o(\Delta t)]$.
2. The protein complex is in state E^* (state 6) at time t, and transfers to state E (state 1) during the time interval, $(t,t+\Delta t)$, with a probability of $p_6(t)[\alpha_{61}\Delta t + o(\Delta t)]$.
3. The protein complex is in state E (state 1) at time t, and remains in the same state during the time interval, $(t,t+\Delta t)$, with a probability of $p_1(t)[1-\alpha_{12}\Delta t-\alpha_{16}\Delta t + o(\Delta t)]$.

By taking into account all the probabilities listed above and noting that the order of magnitude of $p_i(t)o(\Delta t)$ is the same as that of $o(\Delta t)$, we have

$$p_1(t+\Delta t) = p_2(t)\alpha_{21}\Delta t + p_6(t)\alpha_{61}\Delta t + p_1(t)[1-\alpha_{12}\Delta t - \alpha_{16}\Delta t] + o(\Delta t) \tag{7}$$

Rearranging this equation and taking the limit as $\Delta t \to 0$ yield

$$\frac{dp_1(t)}{dt} = \alpha_{61}p_6(t) + \alpha_{21}p_2(t) - (\alpha_{16}+\alpha_{12})p_1(t) \tag{8}$$

Proceeding in the same manner for p_i, $i=2,3,...,6$, gives rise to

$$\frac{dp_2(t)}{dt} = \alpha_{12}p_1(t) + \alpha_{32}p_3(t) - (\alpha_{21}+\alpha_{23})p_2(t) \tag{9}$$
$$\frac{dp_3(t)}{dt} = \alpha_{23}p_2(t) + \alpha_{43}p_4(t) - (\alpha_{32}+\alpha_{34})p_3(t) \tag{10}$$
$$\frac{dp_4(t)}{dt} = \alpha_{34}p_3(t) + \alpha_{54}p_5(t) - (\alpha_{43}+\alpha_{45})p_4(t) \tag{11}$$

$$\frac{dp_5(t)}{dt} = \alpha_{45}p_4(t) + \alpha_{65}p_6(t) - (\alpha_{54}+\alpha_{56})p_5(t) \quad (12)$$

$$\frac{dp_6(t)}{dt} = \alpha_{56}p_5(t) + \alpha_{16}p_1(t) - (\alpha_{65}+\alpha_{61})p_6(t) \quad (13)$$

Equations 8 through 13 comprise the master equations of the system under consideration. Solving these master equations yields the probability distribution of the state in which the protein complex is at time t, X(t).

From the probability distribution of the protein complex, the number distribution of the total population, i.e., N_0 molecules of the protein complex, among the different states, can be determined based on the properties of the joint multinomial distribution(see, *e.g.,* Chiang, 1980). If all the N_0 molecules of the protein complex are assumed to be initially in state 1, each molecule of the protein complex will be in one of the six states with a probability of $p_i(t)$, $i = 1,2,...,6$, at time t. Hence, the number of the molecules of the protein complex in each of the six states at time t follows a multinomial distribution. Let $N_i(t)$, $i = 1,2,...,6$, be the random variables representing the numbers of the molecules of the protein complex in state i at time t. Then, the joint multinomial distribution of $[N_1(t),N_2(t),...,N_6(t)]$ is

$$\Pr[N_1(t)=n_1,N_2(t)=n_2,...,N_6(t)=n_6]$$

$$= \frac{N_0!}{\{\prod_{i=2}^{6} n_i!\}(N_0 - \sum_{i=2}^{6} n_i)!} \{\prod_{i=2}^{6} [p_i(t)]^{n_i}\}\{1-\sum_{i=2}^{6} p_i(t)\}^{[N_0 - \sum_{i=2}^{6} n_i]} \quad (14)$$

The mean number of the molecules of the protein complex that reside in state i, $i = 1,2,...,6$, at time t is given by

$$E[N_i(t)] = N_0 p_i(t), \quad i = 1,2,...,6 \quad (15)$$

while the corresponding variance and covariance are, respectively,

$$\mathrm{Var}[N_i(t)] = N_0 p_i(t)[1-p_i(t)], \quad i = 1,2,...,6 \quad (16)$$

$$\mathrm{Cov}[N_i(t),N_j(t)] = -N_0 p_i(t)p_j(t), \quad i,j = 1,2,...,6;\ i \neq j \quad (17)$$

SOLUTIONS TO THE MODEL

If the transition intensities, α_{ij}, are not functions of time, the stochastic model can be solved analytically or through Monte Carlo simulation to yield the probability distributions, means, variances and covariances of the random variables.

Laplace Transformation

The master equations for the case of identical transition intensities, i.e., for the case of

$$\alpha_{ij} = \alpha, \tag{18}$$

have been solved analytically for all stages of the process. The Laplace and inverse transformations (see, *e.g.,* Mickley *et al.*, 1957) of Eqs. 8 through 13 and taking the expected value of the resultant solutions give

$$E[N_1(t)] = N_0(1 + 2e^{-\alpha t} + 2e^{-3\alpha t} + e^{-4\alpha t})/6 \tag{19}$$
$$E[N_2(t)] = N_0(1 + e^{-\alpha t} - e^{-3\alpha t} - e^{-4\alpha t})/6 \tag{20}$$
$$E[N_3(t)] = N_0(1 - e^{-\alpha t} - e^{-3\alpha t} + e^{-4\alpha t})/6 \tag{21}$$
$$E[N_4(t)] = N_0(1 - 2e^{-\alpha t} + 2e^{-3\alpha t} - e^{-4\alpha t})/6 \tag{22}$$
$$E[N_5(t)] = N_0(1 - e^{-\alpha t} - e^{-3\alpha t} + e^{-4\alpha t})/6 \tag{23}$$
$$E[N_6(t)] = N_0(1 + e^{-\alpha t} - e^{-3\alpha t} - e^{-4\alpha t})/6 \tag{24}$$

Note that

$$E[N_2(t)] = E[N_6(t)] \tag{25}$$
$$E[N_3(t)] = E[N_5(t)] \tag{26}$$

Equations 19 through 24 indicate that as $t \to \infty$, the molecules of the protein complex distribute themselves equally among all states, i.e.,

$$\lim_{t \to \infty} E[N_i(t)] = N_0/6, \quad i = 1,2,...,6 \tag{27}$$

Gaussian Elimination

If the transition intensities, α_{ij}, are not identical, it is somewhat tedious to obtain the analytical solution of the master equations, Eqs. 8 through 13, by Laplace transformation for the unsteady stage. Nevertheless, when the stationary stage is reached, i.e., when

$$\frac{dp_i(t)}{dt} = 0, \quad i = 1,2,...,6, \tag{28}$$

Eqs. 8 through 13 become linear which can be solved by the Gaussian elimination.

Monte Carlo Simulation

Monte Carlo simulation has been performed for both unsteady and stationary processes according to the following procedure (see, *e.g.,* Rajamani *et al.*, 1986).

1. Choose the desired number of simulations, S, and the total length of time of each simulation, T_f. For convenience, S has been chosen as 10,000, and T_f as 100 second for the stationary stage to be reached.

2. Initiate a simulation by generating a uniform random number, u, between 0 and 1; then, calculate the waiting time, t_w, of a molecule of the protein complex in state i before it undergoes a transition, according to

$$t_w = \frac{1}{\alpha_{i,i+1} + \alpha_{i,i-1}} \ell n(1-u) \tag{29}$$

3. Calculate the probability that a molecule will transfer from state i to state (i + 1), R_i, by the following expression;

$$R_i = \frac{\alpha_{i,i+1}}{\alpha_{i,i+1} + \alpha_{i,i-1}} \tag{30}$$

Then, generate another uniform random number, r, between 0 and 1; if $r \geq R_i$, the molecule will transfer to state (i + 1); otherwise, the molecule will move to state (i – 1).

4. Repeat steps 2 and 3 until the total time exceeds T_f; this terminates the simulation.

5. Perform the same procedure as steps 2 through 4 for S times; then, calculate the number of the molecules in state i at time t, s_i. This yields the probability of the protein complex to be in state i at time t as

$$p_i(t) \sim \frac{s_i}{S} \tag{31}$$

From the probability $p_i(t)$, the mean number of the molecules of the protein complex that reside in state i at time t can be calculated from Eq. 15.

RESULTS AND DISCUSSION

As stated earlier, if the transition intensities are identical at $\alpha_{ij} = \alpha = 0.1(1/s)$, the mean number distribution of the molecules of the protein complex among its various structures or states can be obtained both analytically by solving the master equations and numerically through Monte Carlo simulation. Figure 3 displays the resultant mean number distribution when the total number of the molecules of the protein complex, N_0, is 10,000. Note that as time progresses, the mean numbers of the molecules of the protein complex in its various states, $E[N_i(t)]$, become identical as predicted by Eq. 23.

Generally, when the transition intensities, α_{ij}'s, are different, the analytical solutions of the master equations by the Gaussian elimination are possible only for the stationary stage. A comparison of the stationary limits of the Monte Carlo simulation with the corresponding results of the Gaussian elimination indicates that they are in good agreement; see Figure 4. The mean numbers of the molecules of the protein complex in its various states are different even though the stationary stage is reached; this is attributable to the difference in transition intensities.

Transition Intensities

The transition intensities have been assumed to be independent of time in the present work; thus, the mean numbers of the molecules of the protein complex approach a stable distribution as $t \to \infty$, i.e., the active transport eventually becomes stationary. In general, the

active transport is triggered by the phosphorylation and dephosphorylation of the ATPase, that stabilize conformations E and E^* of the protein complex, respectively. Sodium ions trigger phosphorylation, whereas potassium ions trigger dephosphorylation (see, *e.g.*, Stryer, 1988). Consequently, the transition intensities depend on the concentrations of the transported small molecules both inside and outside the cell, and also, on the interactions between the transported small molecules and on the difference in conformations of the protein complex. Thus, the transition intensities may vary with time, or with the change in the concentrations of the transported small molecules, i.e., the molecules of L and M. It is highly desirable, therefore, that the transport mechanism be reflected in expressions for the transition intensities. Such expressions would probably be functions of the concentration gradients of the transported small molecules.

Molecular Fluxes across the Membrane

Figure 1c reveals that if one molecule of the protein complex completes one cycle in the counterclockwise direction, the net effect is to transport one molecule of M and one molecule of L across the membrane from the inside to the outside. Participation by a multitude of molecules of the protein complex in this process induces the fluxes of the molecules of M and L across the membrane. The transitions of the protein complex among its various structures are reversible, thereby triggering the molecular fluxes across the membrane in both directions.

Fluctuations of the Process

Note that only the stationary stage is of any theoretical or practical importance since the exact time when active transport commences will generally be unknown and the process can come into consideration only long after its initiation. The inherent fluctuations of the process in this stationary stage are negligibly small since the process involves a relatively large number of molecules of the protein complex; these fluctuations are inversely proportional to the square root of the number of molecules. Nevertheless, the stochastic model proposed in this paper, encompassing both unsteady (initial period) and stationary stages, may facilitate our understanding of the nature of active transport.

CONCLUDING REMARKS

The mean number distribution of the molecules of the protein complex among its different structures or states calculated by the Monte Carlo simulation is in good accord with the analytical solutions of the master equations of the model. These mean numbers eventually will approach stable states when the transition intensities are independent of time. The mean number distribution would generate the necessary information for estimating other quantities and parameters of the system such as molecular fluxes across the membrane and the effects of energy slippage.

ACKNOWLEDGEMENT

The authors wish to acknowledge the Engineering Experiment Station of Kansas State University for partial financial support of this work.

NOTATION

c_{Li} = concentration of molecules of L inside the cell
c_{Lo} = concentration of molecules of L outside the cell
c_{Mi} = concentration of molecules of M inside the cell
c_{Mo} = concentration of molecules of M outside the cell
$Cov[N_i(t),N_j(t)]$ = covariance between the random variables $N_i(t)$ and $N_j(t)$
$E[N_i(t)]$ = expected value of the given random variable $N_i(t)$
n_i = realization of the number of molecules in state i at time t
$N_i(t)$ = number of molecules in state i at time t
N_0 = total number of molecules of the protein complex at time $t=0$
$p_i(t)$ = probability of a protein complex to be in state i at time t
r = random number
R_i = probability of a molecule transfering from state i to state $(i+1)$
s_i = number of molecules in state i
S = number of simulations
t = time
T_f = total length of time of each simulation
t_w = waiting time
u = random number
$Var[N_i(t)]$ = variance of the given random variable $N_i(t)$
X(t) = random variable representing the state of the protein complex at time t

Greek Letters

α = transition intensity (uniform)
α_{ij} = transition intensity

LITERATURE CITED

Chiang, C. L., *Introduction to Stochastic Processes and Their Applications*, pp. 16–17, Robert E. Krieger, New York (1980).

De Robertis, E. D. P., W. W. Nowinski, and F. A. Saez, *Cell Biology,* pp. 17-24, W. B. Saunders, Philadelphia (1970).

Hill, T. L., *Free Energy Transduction in Biology,* pp. 130–155, Academic Press, New York (1977).

Hill, T. L., *Free Energy Transduction and Biochemical Cycle Kinetics*, pp. 2–6, Springer-Verlag, New York (1989).

Mickley, H. S., T. K. Sherwood, and C. E. Reed, *Applied Mathematics in Chemical Engineering, pp. 281–307,* McGraw-Hill, New York (1957).

Rajamani, K., W. T. Pate, and D. L. Kinneberg, "Time-Driven and Event-Driven Monte Carlo Simulation of Liquid-Liquid Dispersions: A Comparison," *Ind. Eng. Chem. Fundam.*, **25**, 746 (1986)

Stryer, L., *Biochemistry*, pp. 949–972, W. H. Freeman and Company, New York (1988).

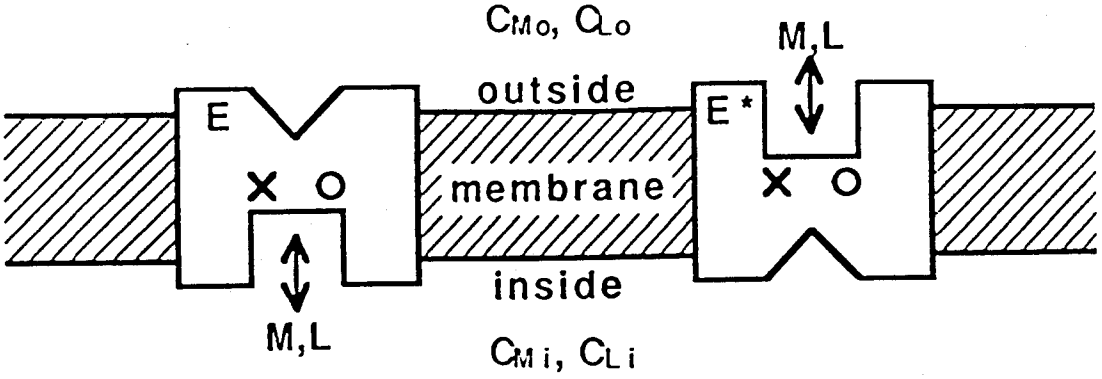

a

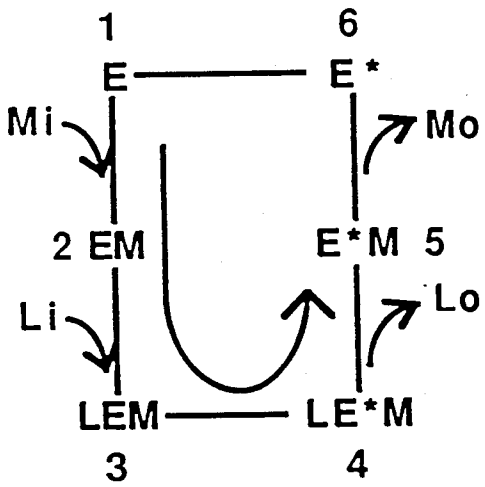

b

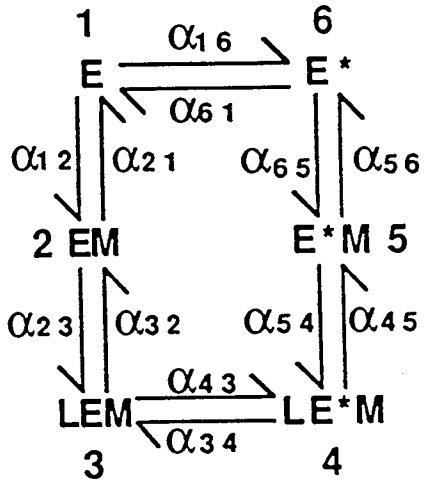

c

Figure 1. Illustration of the active transport (see, e.g., Hill, 1989):

a. hypothetical protein complex in a membrane with the two different conformations, E and E^*; x is the binding site for M, and o for L;
b. mechanism for transport of M and L across the membrane; and
c. transition intensities dominating the direction of the cycle.

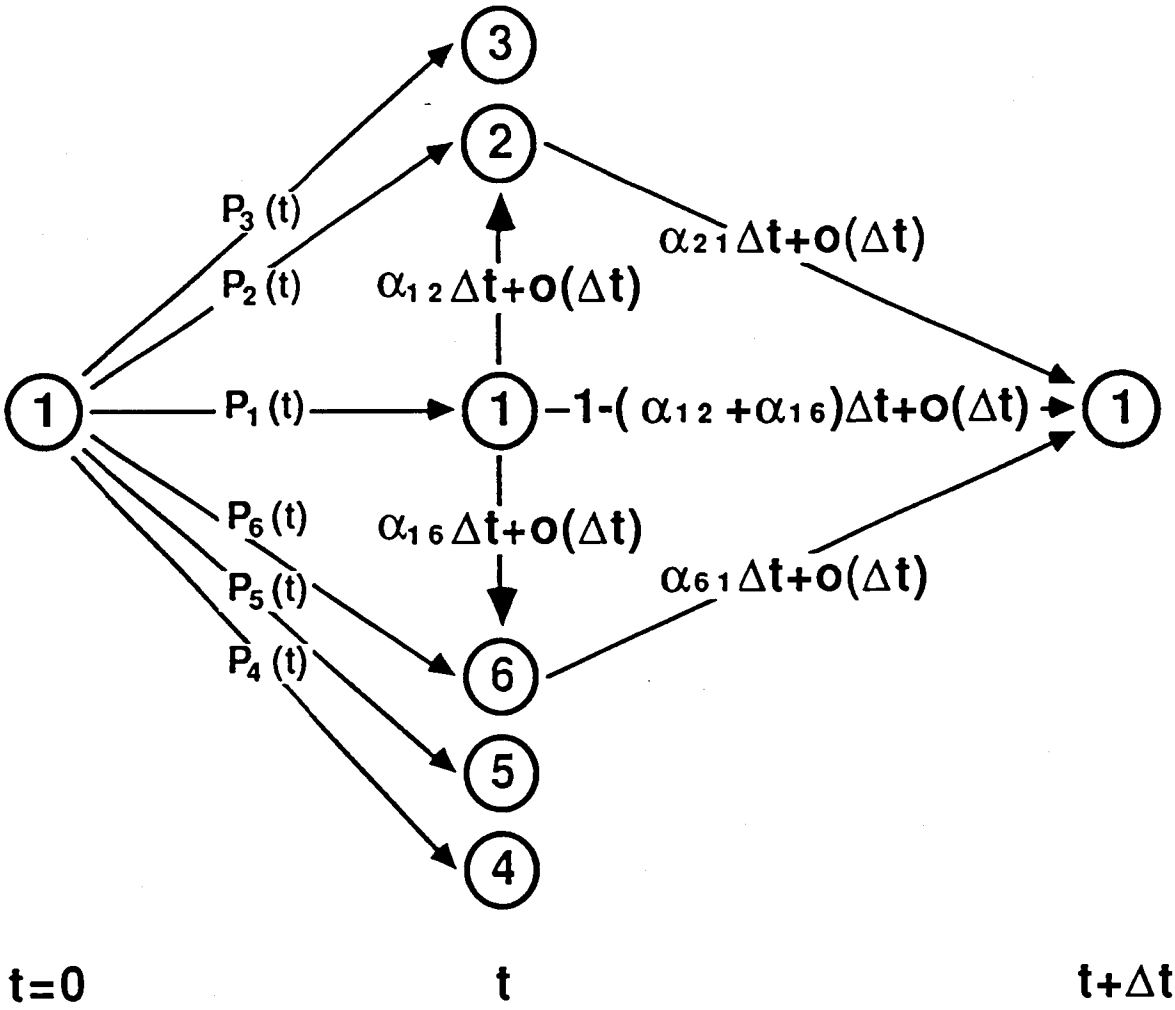

$$p_1(t+\Delta t) = p_2(t)\alpha_{21}\Delta t + p_6(t)\alpha_{61}\Delta t + p_1(t)[1-(\alpha_{12}+\alpha_{16})\Delta t] + o(\Delta t)$$

Figure 2. Possible events associated with the transition of state 1 or E.

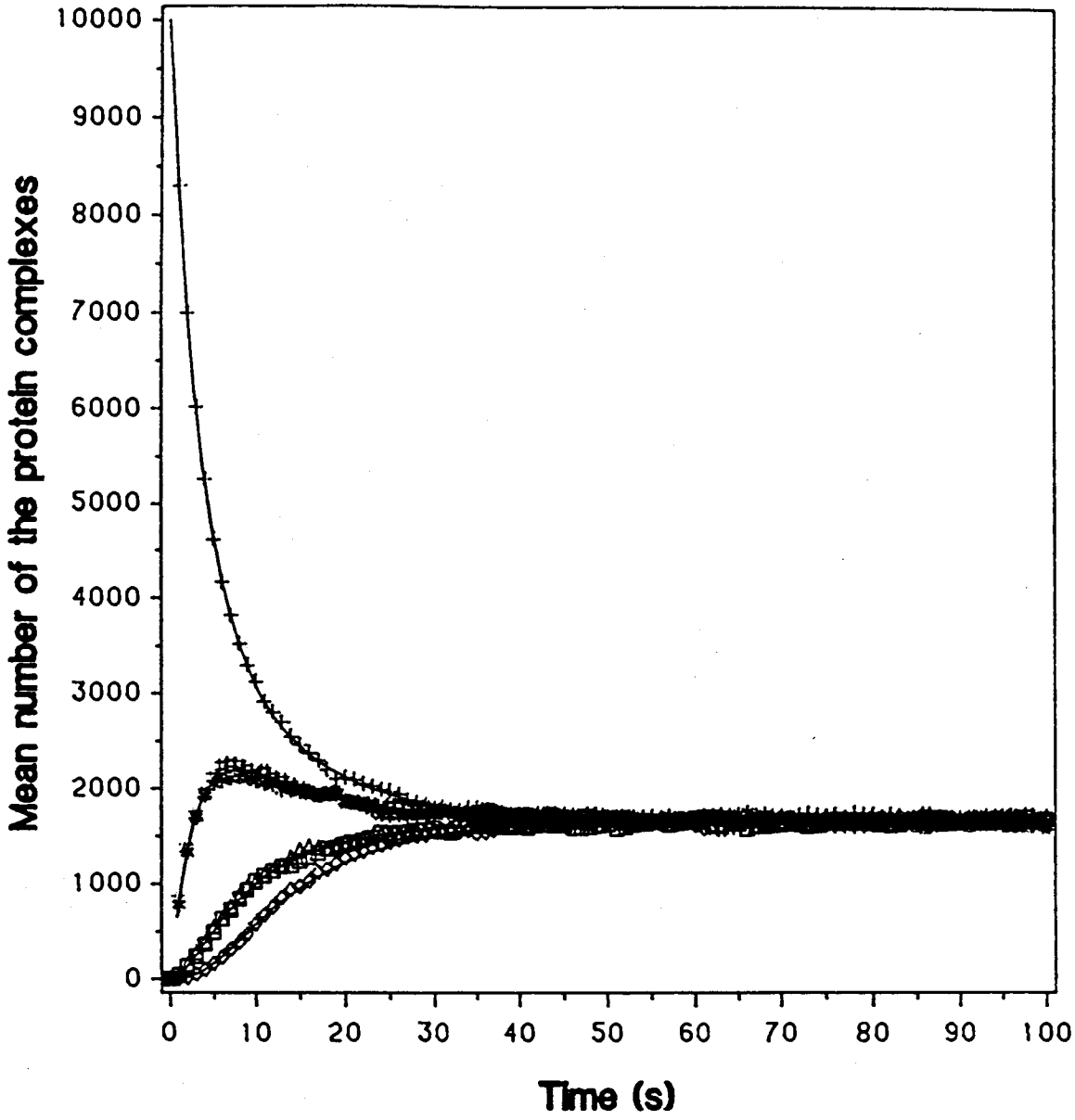

Figure 3. Mean numbers of the molecules of the protein complex with various structures or in different states at time t for $\alpha_{ij} = \alpha = 0.1$ (1/s) and the total number of the molecules of the protein complex of 10,000:

— analytical solutions for all states
\+ Monte Carlo simulation for state 1
x Monte Carlo simulation for state 2
Δ Monte Carlo simulation for state 3
◊ Monte Carlo simulation for state 4
□ Monte Carlo simulation for state 5
\# Monte Carlo simulation for state 6.

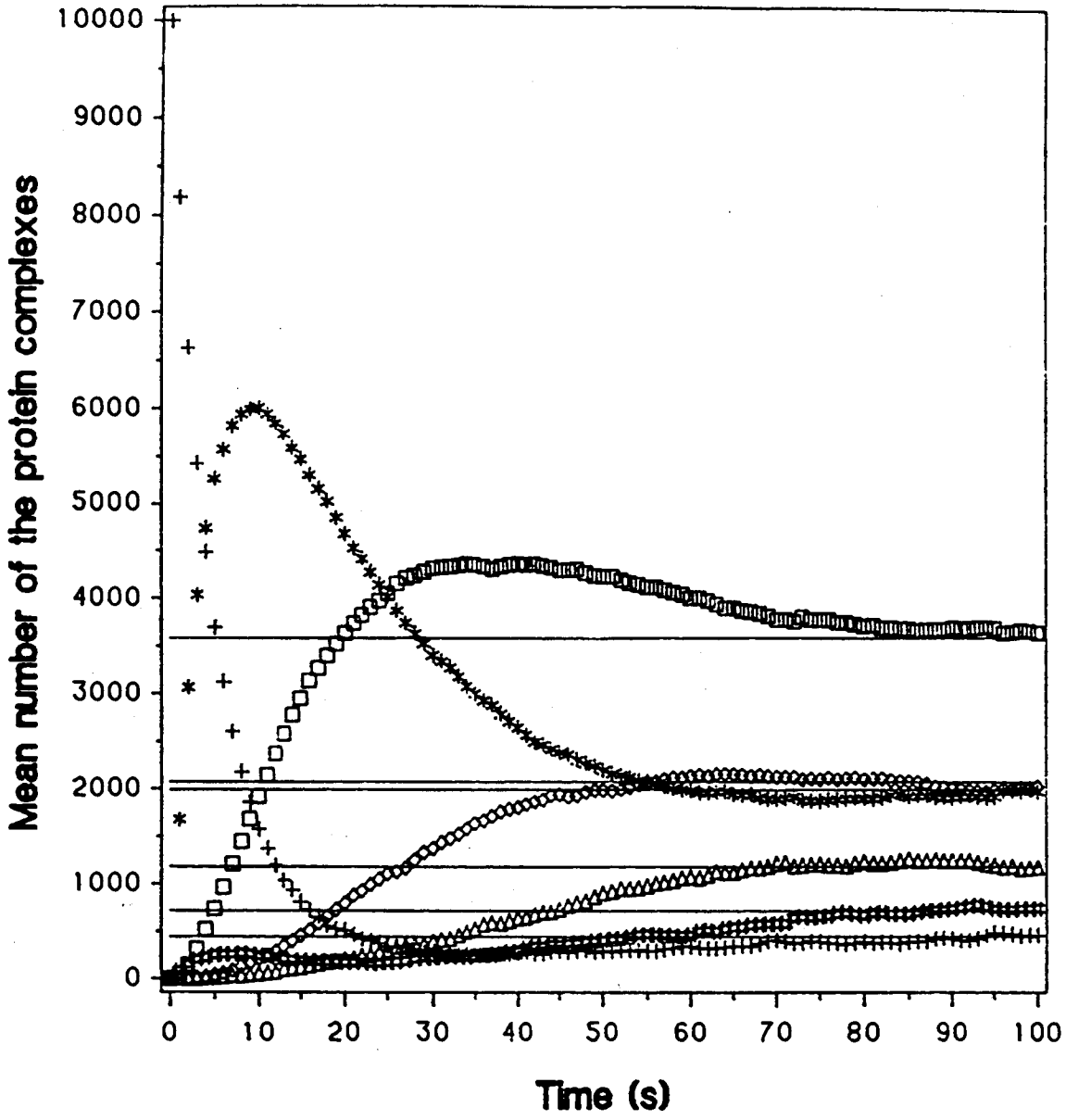

Figure 4. Mean numbers of the molecules of the protein complex with various structures or in different states at time t for various transition intensities and the total number of the molecules of the protein complex of 10,000:

$\alpha_{12}=0.2$ $\alpha_{23}=0.05$ $\alpha_{34}=0.03$ $\alpha_{45}=0.04$ $\alpha_{56}=0.04$ $\alpha_{61}=0.07$
$\alpha_{21}=0.01$ $\alpha_{32}=0.01$ $\alpha_{43}=0.02$ $\alpha_{54}=0.01$ $\alpha_{65}=0.02$ $\alpha_{16}=0.01$,

— analytical solutions for stationary stages of all states
\+ Monte Carlo simulation for state 1
x Monte Carlo simulation for state 2
Δ Monte Carlo simulation for state 3
◊ Monte Carlo simulation for state 4
□ Monte Carlo simulation for state 5
\# Monte Carlo simulation for state 6.

ELECTROKINETIC ISOLATION OF BACTERIAL VESICLES AND RIBOSOMES

Debra T. L. Hawker[1], Robert H. Davis[1] , Paul W. Todd[2] and Robert Lawson[3]
Department of Chemical Engineering, University of Colorado, Boulder, CO 80309-0424

Abstract

Conventional biochemical separation processes in the production of biotechnology products tend to be the most expensive and limited capacity steps, and novel separation methods are needed. The purpose of our research is to study the isolation of bacterial ribosomes and vesicles from a cleared cell lysate using density gradient electrophoresis and aqueous two-phase extraction. This paper describes the work completed using density gradient electrophoresis. Electrophoresis provided a clean separation of solubles, ribosomes and vesicles. Electrophoretic mobilities derived from experimental data show that the solubles have the highest mobility, followed by the ribosomes, then the vesicles. Electrophoresis demonstrated a potential to isolate bacterial ribosomes and vesicles from each other and solubles.

1 Introduction

Separation processes tend to be the most expensive and most the time consuming steps in the production of biotechnology products [1, 2]. Many separation methods have been studied and characterized for the preparation of soluble products (such as proteins) and large particulate products (such as cells). However, comparatively little has been done concerning the study of separation processes required for the purification of intermediate sized products (such as ribosomes and vesicles). The purpose of our research is to study the application of two separation techniques to a biotechnology product, ImuVert®, produced by Cell Technology, Inc. of Boulder, Colorado, which consists of bacterial ribosomes and vesicles. This paper describes the work completed using density gradient electrophoresis.

1.1 ImuVert®—A Separation Problem

ImuVert® is a biological response modifier which increases natural killer cell activity. Increasing the natural killer cell activity is important in instances when humans or animals are suffering from a defective, or not fully active immune system. One example of the possible applications of this technology is in the treatment of cancers. Thus, it is concievable that a large market will exist for this product. As a result, industrial scale separation processes will be required. The separation processes currently used are inadequate for industrial scale processing.

Current production of ImuVert® occurs in several steps. First, cells of the gram negative bacterium *Serratia marcescens* are grown following specific procedures. Once the growth phase has been completed, the cells are lysed in a French press. This procedure frees the ribosomes from the cell and causes the cell membranes to reform into vesicles which are much smaller than the parent cell. In addition, cell fragments are created, and intracellular proteins and RNA are released into the solution. This solution of lysed cells is referred to as the lysate. Only the ribosomes and vesicles from the lysate are components of the desired product. At this point, the lysate undergoes ultracentrifugation to remove the larger debris, namely the cell fragments. The remaining supernatant is referred to as the cleared cell lysate. The cleared cell lysate then undergoes an ultracentrifugation step to pellet the desired ribosomes and vesicles.

Although the current purification strategy works satisfactorily for small scale production of the product, it will not be effective for industrial scale production, since the process depends quite heavily on ultracentrifugation. Ultracentrifugation is limited to small volumes and is expensive. Volume is

[1]Department of Chemical Engineering, University of Colorado, Boulder CO 80309-0424
[2]National Institute of Standards and Technology, Div. 583.10, 325 Broadway, Boulder CO 80303
[3]Cell Technology Inc., 1668 Valtec Lane, Boulder CO 80301

limited since a continuous system is currently not available for ultracentrifugation. The expense is due to several facts: ultracentrifuges are expensive and require a large amount of maintainence, and a large number of them is required for industrial scale production because of the volume limitations. Thus, for industrial scale production of this product, other separation techniques need to be investigated.

1.2 Separation Techniques Explored

Two separation techniques were chosen for this study: electrophoresis and aqueous two-phase extraction. Both of these techniques can be used on a wide range of particle sizes (from solubles to cells), and have the potential to be scaled up. Here, separations using electrophoresis are described.

Electrophoresis produces a separation by utilizing the fact that different particles or solubles may have different electrophoretic mobilities or isoelectric points. Electrophoretic mobility reflects how rapidly a particle or molecule moves through a specified medium when an electric field is applied. Electrophoretic mobility is a function of the ionic strength of the specified medium, the surface charge density of the particle, the viscosity of the specified medium, pH and in some cases the size of the particle. The isoelectric point is the pH at which the particle has a net charge of zero, and therefore has no motion due to an electric field. Isoelectric point is a function of surface properties of the particle and the ionic strength of the specified medium. Here, it was desired to separate the ribosomes and the vesicles from the solubles remaining in the cleared cell lysate, and also to separate the ribosomes and the vesicles from each other. This was accomplished by using density gradient zone electrophoresis (DGZE).

Zone electrophoresis is a rate process. In zone electrophoresis the particles move in the direction specified by the orientation of the electric field. Ideally, all particles with the same electrophoretic mobility would move at the same rate within a specified electric field; however, this is not the case. Forces and flows in addition to the electric field act on the material. These additional forces and flows include gravity and diffusion forces and free convection and electroosmotic flows. The net result of the presence of these additional forces and flows is the spreading of the sample band and thus a reduction in resolution of the separands. In density gradient zone electrophoresis, a vertical density gradient is formed in the region in which electrophoresis is to be performed in order to stabilize the system against free convection. Thus, in the ideal case, DGZE would be performed in the shortest possible time under conditions that would minimize these effects. In DGZE, all of the solutions are essentially at a single pH, which is chosen so that the product is not damaged, and the difference between electrophoretic mobilities of separands is maximized.

DGZE has been applied by several researchers to various types of cell separations. Plank et al studied the electrophoretic mobilities of fixed rat Red Blood Cells (RBC), fixed rabbit RBC and living mouse leukemia cells in a ficoll density gradient [3]. It was found that the RBC from different species could be separated using DGZE, and that the leukemia cells were not harmed by electrophoresis. Sedimentation was found to contribute greatly to the motion of these cells; in fact, two classes of the leukemia cells were separated by sedimentation rather than by electrophoresis in the DGZE apparatus. A theory for the motion of the cells, including electrophoretic and sedimentation effects, was presented and is in good agreement with the experimental results. Boltz and Todd studied the electrophoretic mobilities of rat, chicken and rabbit fixed RBC [4]. The cells obtained from these three sources were separated using DGZE, and the apparatus, cell preparation and required solutions were described in detail. In addition, the movement of particles in DGZE as a function of several of the forces and flows affecting the particles was described. Todd et al examined the electrophoretic mobilities of latex spheres and human kidney cells in a continuous free-flow electrophoresis unit on the Earth and in microgravity [5]. Several classes of human kidney cells were separated, and the relationship between electrophoretic mobility and size for the latex spheres, was examined under both gravity conditions. It was found that spheres of different sizes, but equivalent electrophoretic mobilities, were located in a single peak. Thus, under certain conditions, sedimentation does not significantly contribute to the

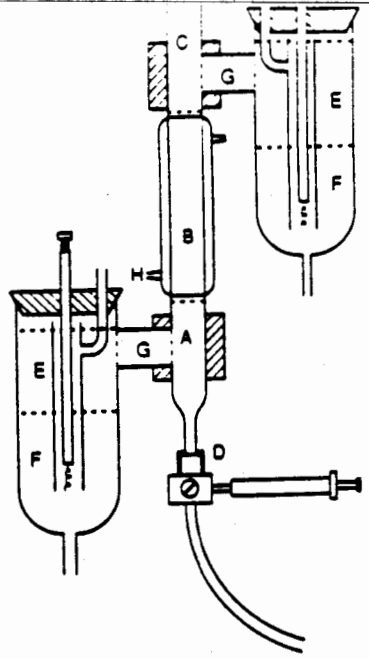

A. 60% sucrose floor
B. 0 - 25% sucrose gradient
C. 0% sucrose top solution
D. Three-way stopcock
E. Electrode top solution
F. Saturated NaCl
G. 15% polyacrylamide gel plugs
H. Cooling jacket

Figure 1: Density gradient electrophoresis column

motion of particles in vertical electrophoretic techniques.

Joseleau-Petit and Kepes applied DGZE to vesicles formed from *Escherichia coli* [6]. The vesicles studied were prepared using a method similar to that used for preparing ImuVert®, and, as this was the case, the samples presumably included ribosomes. Three peaks were apparent in the elution profile. The first two peaks corresponded to vesicles, while the last peak appeared to contain ribosomes.

The goal of our research was to determine if zone electrophoresis is a feasible method for isolating bacterial vesicles and ribosomes from a cleared cell lysate. This technique has been investigated for use with solubles and whole cells, but few investigations have involved subcellular particles. In addition, each cell type produces particles with unique surface characteristics, which in turn affect the electrophoretic characteristics of the particles. As this is the case, it was desired to study this separation technique on particles derived from *Serratia marcescens*.

2 Materials and Methods

2.1 Electrophoresis Column

DGZE was performed in a density gradient electrophoresis column. The column is shown in Figure 1 and it consists of a density gradient column connected to two glass electrode sidearms via two teflon blocks. The two sidearms provide a location for the electrochemical reactions to occur without disturbing the sample or the buffer conditions within the density gradient. The electrochemical reactions occur in the saturated sodium chloride solution (F), while the top solution (E) consists of a buffer which has an ionic composition similar to that within the density gradient and allows conduction of ions while protecting the density gradient from ionic composition or pH changes. The polyacrylamide gel plugs (G) provide a physical barrier to fluid flow while allowing the conduction of ions into and out of the density gradient. Recently the gel plugs were replaced with semi-permeable membranes. These membranes serve the same function as the polyacrylamide gel plugs, but they are easier to work with. Electrophoresis occurs within the density gradient (B). The density gradient is established to help stabilize the system against the effects of convection and also stabilizes the fluids while they are being pumped into or out of the density gradient column. All of the solutions are added to the column through the three-way stopcock (D). The ceiling (C) and the floor (A) solutions stabilize the position of the density gradient and are in electrical contact with the polyacrylamide gel plugs or the semi-

Buffer	Trizmabase	$MgSO_4$	NH_4Cl	Glycine
DGEZ	4.0	10.0	10.0	50.0
ImuVert®	20.0	20.0	50.0	00.0

Table 1: DGZE buffer and ImuVert® buffer, all quantities are in mM

Solution	7.0 cm Gradient	13.0 cm Gradient
Top Solution	0.0	0.0
Top of Gradient	0.0	0.0
Bottom of Gradient	15.0	25.0
Floor Solution	25.0	40.0
Pumping Solution	40.0	60.0

Table 2: Sucrose density gradients for various column lengths, all quantities are in % w/w

permeable membranes. The density gradient column is jacketed to maintain the desired temperature in the column and to provide a heat sink for the heat generated by the flow of current in the system. During the electrophoresis runs, the jacket was maintained at 4°C. The density gradient columns used have an internal diameter of 2.2 cm and a gradient length of 7.0 cm or 13.0 cm. The length of the column used was determined by the run conditions; longer runs at higher currents required the longer column so that the sample did not move into the ceiling.

2.2 Buffer and Gradient Systems

Tables 1 and 2 show the buffer compositions and the density gradient system used for DGZE. The buffer was designed to be compatible with ImuVert®; this required that a magnesium source be included. This fact, and a desire to use a buffer which could be used in an industrial scale process, resulted in the buffer resembling a dilute ImuVert® buffer. Glycine was added to the system to aid in pH control. Without glycine, the buffer system was susceptible to drastic pH changes during long electrophoresis runs. The density gradient system developed by Boltz and Todd [4] is based on ficoll and sucrose. This was adapted to a sucrose only system for several reasons. First, it is easier to establish known densities of solutions using a single concentrated solute, such as sucrose, in cases where an isotonic medium is not required, as in the case of subcellular particles. In addition, it was found that ficoll interfered with optical absorbance measurements at 260 nm and 280 nm, which were necessary for sample analysis.

2.3 Sample Preparation

Two sample types were available from Cell Technology. These sample types were the purified product, ImuVert®, and cleared cell lysate.

Before DGZE, several steps were required to prepare the samples for electrophoresis. First, the density of the sample was determined using a Mettler/Paar model DMA45 densometer. The densometer was kept at 4 °C using a water bath, and the density was read from the digital display, after the sample was applied and the reading had stabilized. Once this was completed, the proper amount of sucrose required for the sample to sit on the density shelf (between the floor and the bottom of the density gradient) was added to the sample, and the sample was mixed gently until the sucrose was

dissolved. The sample was kept in an ice bath during all procedures. At this point, the sample was loaded onto the column, and it was checked to see if the sample was sitting properly on the density shelf. Typically the samples were .10 — 2.00 ml, which correspond to .2 — 4.0 mg of particulate product. For the first few trials with ImuVert®, 200 μl of saturated bromophenol blue were added to the sample to check density shelf stability and pH stability. Once the system was characterized, human RBC were added to the sample. The electrophoretic mobility of human RBC is well characterized under many ionic strength conditions [7]. As this is the case, it was possible to use the human RBC as electrophoretic mobility markers, and, using their motion as a reference, the electrophoretic mobilities of the ribosomes and the vesicles were calculated. Cleared cell lysate was used without any additives.

2.4 Procedure

2.4.1 Sidearm Preparation

The sidearms were prepared by either filling the bridges with 12 % polyacrylamide gel plugs, or by attaching membranes to a support material which was inserted into the sidearm and the teflon blocks. The apparatus was then assembled as shown in Figure 1. If polyacrylamide gels plugs were used, it was necessary to purge them of contamination prior to beginning an electrophoresis trial. This was done by loading the sidearms and the density gradient column with distilled water, connecting all electrical connections, and applying an electric field overnight.

Once the sidearms were purged, they were loaded with the appropriate solutions. First, the top buffer solution was poured into the sidearm. This top solution was the same as the top solution listed in the tables above, but was .5 M in glycine for the DGZE trials. Then the saturated sodium chloride was added to the sidearm slowly through the stopcock located at the bottom of the sidearm. This allowed for the formation of two separate layers of liquid within the sidearm. At this point, the refrigerated cooler which feeds the water jacket was turned on.

2.4.2 Loading the Density Gradient

Loading of the column proceeds as follows, with all solutions loaded through the stopcock at the bottom of the column. First, 30 ml of the top solution were added to form the ceiling, then 30 ml of the density gradient were added for the 7 cm density gradient column, or 50 ml for the 13 cm density gradient column. In both cases, the density gradient was formed with the use of a gradient maker, which forms the linear density gradient. The sample was then added with a syringe at the stopcock. Care was taken to not disturb the gradient while the sample was being added. The floor solution of approximately 35 ml was then added until the sample was visible just within the jacketed portion of the density gradient column.

2.4.3 Run Conditions

After the column was loaded, the run was started. This was done by closing off the column, attaching all electrical connections, and starting the power supply with the desired current. Normal runs were completed in the constant current mode at 9 to 30 mA for 2 to 20 hours.

2.4.4 Sample Collection

Following completion of the run, fractions were collected by pumping the pumping solution into the column and collecting fractions from the top of the column using a fraction collector. Fraction sizes ranged from .5 ml to 2.0 ml.

2.5 Sample Analysis

Samples were analyzed using three assays to trace the ribosomes, vesicles, free proteins and free nucleic acids within the samples.

2.5.1 Protein Assay

Protein concentrations were determined in the product, solubles or a combination of the two, using a bicinchoninic acid protein assay kit obtained from Sigma Chemical Company. The principle behind this assay is the reaction of proteins with Cu^{+2} in alkaline solution to form Cu^{+1}. Cu^{+1} then reacts with bicinchoninic acid to form a purple complex. This purple complex absorbs strongly at 562 nm, which allows for the measurement of protein concentrations in solution [8, 9].

There were several steps to the procedure for performing this assay. First, a standard solution of bovine serum albumin, obtained from Sigma Chemical Company, was made. This standard solution underwent several dilutions to form the desired standard set. This standard set was stored at -20 °C until it was needed. The assay protocol described by the Pierce Chemical Company was then followed [9] with the standard set and the samples of unknown protein concentration. Spectrophotometric readings were obtained using a Hewlett-Packard 8452 series spectrophotometer. A calibration curve was made using the data obtained from the readings of the standard set. This calibration curve was then used to determine the concentration of protein in each of the samples of unknown protein concentration.

2.5.2 Optical Density Measurements

Optical density measurements were used to trace the ribosomes, vesicles and solubles. Amino acids and nucleic acids both absorb strongly in the ultraviolet light range. In particular, most of the nucleic acids have an absorbance maximum at approximately 260 nm, while several amino acids have an absorbance maximum at approximately 280 nm [10]. In addition, it is known that the ratio of the optical density readings at 260 nm to that at 280 nm is approximately 2.0 for ribosomes and is approximately 1.4 for vesicles [11]. Thus, it is possible to distinguish between vesicles and ribosomes by comparing the optical density ratios.

To perform this assay, the samples were diluted with ImuVert® buffer to concentrations within the linear range of the spectrophotometer (less than 1.75 optical density units). Samples were then placed in quartz cuvettes. Optical density measurements were taken using the Hewlett-Packard 8452 series spectrophotometer at 260 nm and 280 nm, and the data were saved on the Hewlett-Packard computer, which was attached to the spectrophotometer, for future analysis.

2.5.3 SDS-PAGE

The protein assay and the optical density readings determine how much material is present within a given sample, but these techniques do not give much information concerning the purity of the samples. As this is the case, purity of the samples was evaluated using polyacrylamide gel electrophoresis in sodium dodecyl sulfate (SDS-PAGE).

The resistance of the gel to the motion of macromolecules is determined by the amount of acrylamide monomer used in the production of the gel. The greater the amount of acrylamide, the greater the resistance in the gel. A detergent, SDS, is bound to the proteins to be assayed. This results in the protein obtaining a constant charge-to-mass ratio, which should give all proteins the same mobility in an electric field. However, the longer, and thus the higher molecular mass , proteins are retarded by the resistance of the gel. This results in the proteins being separated on the basis of molecular mass on the polyacrylamide gel. This technique was used as described by Laemmli [12]. After electrophoresis, the proteins on the gel, they were stained with Coomassie Brilliant Blue as described by Neuhoff [13]. This allows for visualization of the proteins.

Particle	Electrophoretic mobility
Human RBC	-1.7
Ribosomes	-2.3 ± .4
Vesicle 1	-1.2 ± .3
Vesicle 2	-.7 ± .3

Table 3: Electrophoretic mobilities of particles in μm-cm/[s-V]

The proteins of ribosomes and vesicles have specific banding patterns on SDS-PAGE [14], and the purity of these particles can be determined by comparing the banding of test particles with that of particles of known purity. SDS-PAGE was run following the protocol described by Cell Technology using 12.5 % polyacrylamide gels [15].

3 Results and Discussion

Figure 2 shows the optical density profiles from a typical separation using ImuVert® as the starting material. The fractions were 1 ml. By comparing the ratio of optical density at 260 nm to 280 nm, in each of the three peaks, it was determined that the first peak, located at fraction seventeen, consisted primarily of ribosomes, while the other two peaks consisted primarily of vesicles. This was confirmed using SDS-PAGE. However, Figures 3 and 4, both of which represent repititions using ImuVert® as the sample, show either one peak and a slight dip, or two peaks. Run # 18 had .5 ml fractions, while Run # 19 had 1.0 ml fractions. It was determined that the changes in the profiles were not due to the technique, but rather that there is significant variation in the ImuVert® samples available, even when the samples are obtained from the same vial.

The fact that two vesicle peaks were present is not surprising. Joseleau- Petit and Kepes separated inner and outer membranes from *E. coli* in a DGZE system when the sample was prepared in a manner similar to the preparation of ImuVert® [6]. Heidrich et al separated inner and outer membranes from rat liver mitochondria, and were able to identify proteins associated with each of the membranes, using free flow electrophoresis [16]. Leidenix et al also produced separate classes of vesicles from *E. coli* [17] using electrophoresis. In this case, electrophoresis was performed in a dilute agarose gel. Variation in the heights and widths of the peaks, even when the same electrophoretic conditions are used, is without satisfactory explanation.

There was less variation in peak characteristics when the cleared cell lysate was used as the sample, as can be seen in Figures 5 and 6. The fraction sizes are, respectively, 1 ml and 1.5 ml. Both of these separations were performed in the 13 cm electrophoresis column. These peaks appear similar primarily because there is a significantly higher ratio of ribosomes to vesicles in the cleared cell lysate than in ImuVert® . Thus, there are fewer vesicles present to disrupt the comparison of peak characteristics. Note that the solubles preceed the ribosomal peak.

Figure 7 shows a separation in which human RBC were added to ImuVert® . The RBC are tracked by the absorbance at 450 nm, the peak is located at fraction 24. Note that the ribosomes preceed the RBC, while both vesicle peaks travel slower. Using the RBC as a reference point, and their electrophoretic mobility as determined by Todd [7], the electrophoretic mobilities for ribosome and vesicle peaks are shown in Table 3.

4 Conclusions

It has been shown that it is possible to purify ribosomes and vesicles from *Serratia marcescens* from each other and from solubles present in the cleared cell lysate using DGZE. The electrophoresis system currently in use has a capacity of approximately 5 mg of product per run, which is significantly lower than that required for industrial scale production. As an industrial scale system is not currently available, research needs to be done to scale-up this separation technique, particularly in the area of characterizing flows within the systems.

This work has been supported by the Colorado Institute for Research in Biotechnology, the National Science Foundation, Cell Technology Inc. and the National Institute of Standards and Technology.

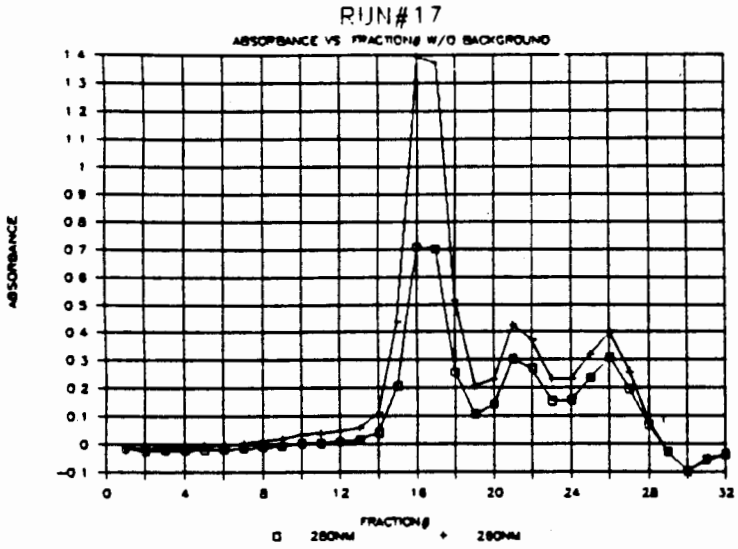

Figure 2: Absorbance vs. Fraction # for Run # 17

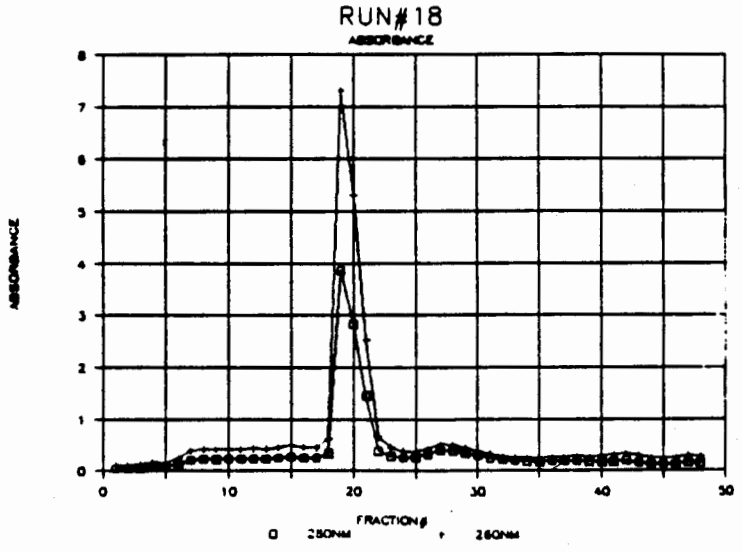

Figure 3: Absorbance vs. Fraction # for Run # 18

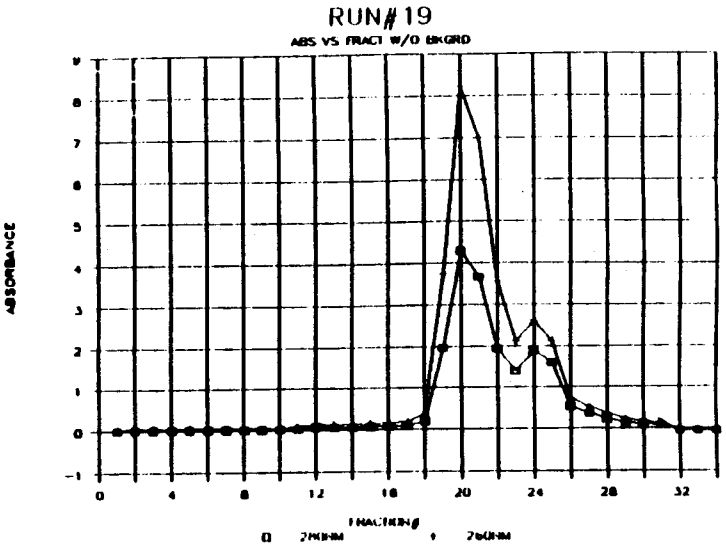

Figure 4: Absorbance vs. Fraction # for Run # 19

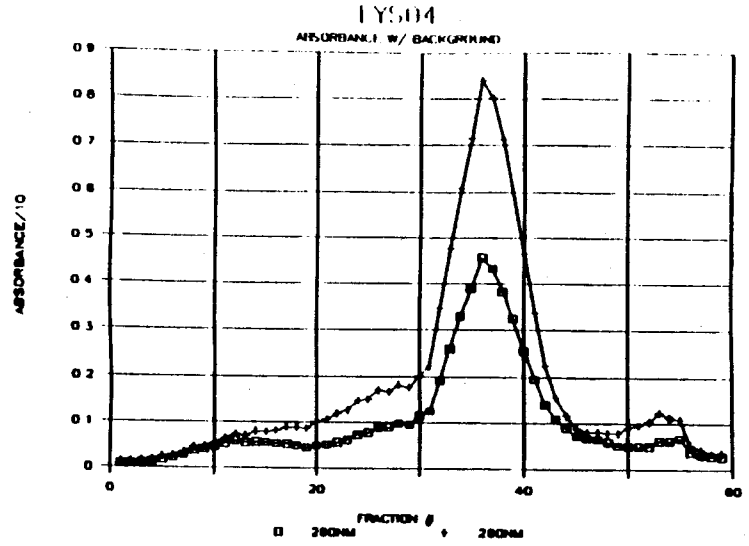

Figure 5: Absorbance vs. Fraction # for Lys 04

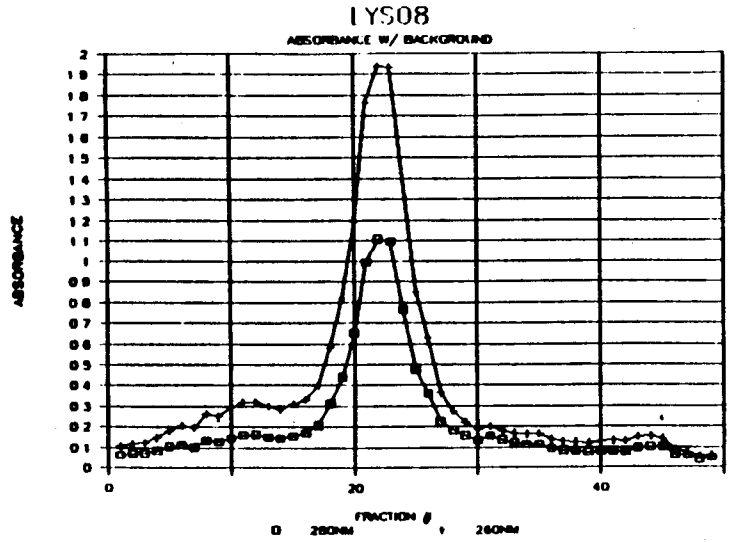

Figure 6: Absorbance vs. Fraction # for Lys 08

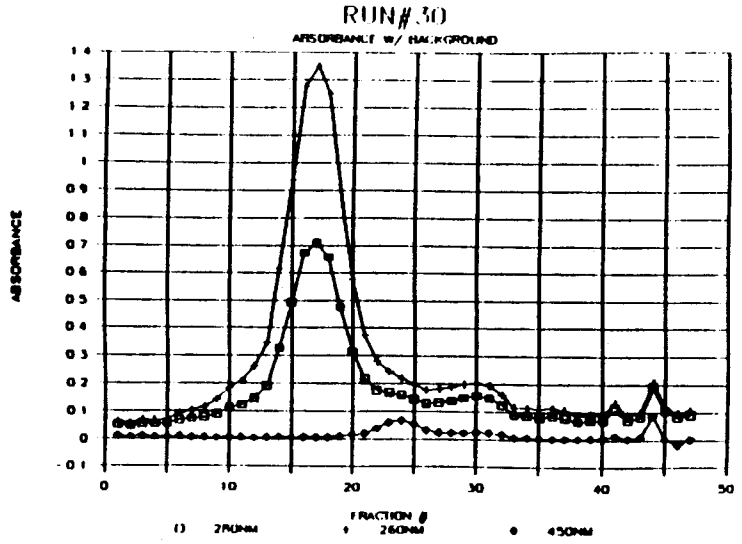

Figure 7: Absorbance vs. Fraction # for Run # 30—human RBC present

References

[1] P. Knight. *Bio/Technology*, 8:777, 1989.

[2] Paul A. Belter, E. L. Cussler, and Wei-Shou Hu. *Bioseparations: Downstream Processing for Biotechnology*. Wiley-Interscience, 1988.

[3] Lindsay D. Plank, M. Elaine Kunze, and Paul Todd. Electrophoretic migration of animal cells in a vertical ficoll gradient theory and experiment.

[4] Robert C. Boltz, Jr. and Paul Todd. Density gradient electrophoresis of cells in a vertical column. In P.G. Righetti, C.J. Van Oss, and J.W. Vanderhoff, editors, *Electrokinetic Separation Methods*, pages 229–250. Elsevier/North-Holland Biomedical Press, 1979.

[5] Paul Todd, Jeffery Kurdyla, Burton E. Sarnoff, and William Elsasser. Analytical cell electrophoresis as a tool in preparative cell electrophoresis. In S.K. Sidkar, M. Bier, and P. Todd, editors, *Frontiers in Bioprocessing*, 1989.

[6] Danièle Joseleau-Petit and Adam Kepes. A novel electrophoretic fractionation of *escherichia coli* envelopes. *Biochimica et Biophysica Acta*, 406:36–49, 1975.

[7] Paul Todd. Electrophoretic mobility tables for rbc. Tables of data, contact Paul Todd at Div. 583.10, NIST.

[8] P.K. Smith, R.I. Krohn, G.T. Hermanson, A.K. Mallia, F.H. Gartner, M.D. Provenzano, E.K. Fujimoto, N.M. Goeke, B.J. Olson, and D.C. Klenk. Measurement of protein using bicinchoninic acid. *Analytical Biochemistry*, 150:76–85, 1985.

[9] Pierce Chemical Company. Bca™ protein assay reagent, 1987.

[10] S.B. Brown. Ultraviolet and visible spectroscopy. In S. B. Brown, editor, *An Introduction to Spectroscopy for Biochemists*, pages 14–69. Academic Press, 1980.

[11] Robert Lawson. Vesicle and ribosome optical density ratios. Personal Communication.

[12] U. K. Laemmli. Cleavage of structural proteins during the assembly of the head of bacteriophage t4. *Nature*, 227:680–685, 1970.

[13] Volker Neuhoff, Norbert Arold, and Wolfgang Ehrhardt. Improved staining of proteins in polyacrylamide gels including isoelectric focusing gels with clear background at nanogram sensitivity using coomassie brilliant blue g-250 and r-250. *Electrophoresis*, 9:255–262, 1988.

[14] Robert Lawson. Vesicle and ribosome protein gel banding patterns. Personal Communication: Proprietary Information.

[15] Cell Technology. Procedure for characterizing the protiens of imuvert.

[16] Hans-G. Heidrich, Roland Stahn, and Kurt Hannig. The surface charge of rat liver mitochondria and their membranes. *The Journal of Cell Biology*, 46:137–150, 1970.

[17] Monte J. Leidenix, Gertrude H. Jacoby, Thomas A. Henderson, and Kevin D. Young. Separation of *escherichia coli* penicillin-binding proteins into differnet membran vesicles by agarose electrophoresis and sizing chromatography. *Journal of Bacteriology*, 171(10):5680–5686, 1989.

APPLICATION OF DYNAMIC PROGRAMMING FOR FERMENTATIVE ETHANOL PRODUCTION BY *Zymomonas mobilis*

Sheyla L. Rivera and M. Nazmul Karim
Agricultural and Chemical Engineering Department
COLORADO STATE UNIVERSITY; Fort Collins, Colorado 80523

ABSTRACT

This paper discusses the application of dynamic programming to the optimization of a batch fermentation for ethanol production. Using several experimental data sets available for *Zymomonas mobilis* culture at different environmental conditions, pH and temperature control policies are determined, which will maximize the yield of ethanol for batch culture. The influence of temperature was studied for the range from 30 to 40C and pH was varied from 5.0 to 7.5. A fermentation kinetics model was used in simulation studies to assess the positive effect of the time-varying profiles on the yield. The functionality with respect to temperature and pH was incorporated in the specific growth rate constant. These results showed that it is possible to obtain an ethanol yield more than twice the value obtained when pH and temperature are kept constant throughout the experiment.

1. Introduction

In recent years, considerable research in the biotechnology field has been directed towards finding advanced optimization techniques. This will allow fermentation industries to reduce their production costs and increase the yield, while at the same time maintain the quality of the metabolic products [1].

A number of publications have appeared investigating the effects of temperature and pH on the kinetics of ethanol production by *Zymomonas mobilis* in batch fermentation [2,3,4,5]. The interest in *Z. mobilis* arises due to the well-known fact that this organism can convert glucose efficiently and rapidly to ethanol with higher yields and higher ethanol productivities than industrially useful yeasts [4]. Temperature and pH have a profound effect on all the aspects of growth, metabolism and survival of microorganisms during ethanol fermentation, and therefore, these parameters play an important role in the optimum control of ethanol production [5].

Using several experimental data sets available, performed at different environmental conditions, and utilizing standard optimization techniques, pH and temperature control policies are determined for this fermentation process, which will maximize the yield of ethanol for a batch experiment. The procedure is based on the dynamic programming approach, and the effect of the time-varying profiles on the yield was assessed by simulation studies using a modified version of the Lee & Rogers fermentation kinetics model [6]. The functionality with respect to pH and temperature was incorporated in the specific growth rate constant [7].

2. Motivation

Previous studies on the strains of *Zymomonas mobilis* have revealed the effects of pH and temperature on the kinetic parameters for the growth of the organism in batch cultures. Results have been reported [2] for temperature values between 30 and 40 C, and for pH values between 5.0 and 8.0. Specific ethanol production rate shows a maximum -with 10% variations- over a pH range of 6.0 to 7.5. End-of-batch ethanol yield was a maximum between 30C and 37C, but decreased by 24% between 37C and 40C. It has been postulated that a rise in temperature enhances ethanol accumulation inside the cells and increases ethanol inhibition. Also, the maintenance coefficient of the cells increase, and in consequence, excessively high temperatures have a negative effect on yields [3].

Traditionally, pH and temperature are defined and kept constant during the fermentation. However, in batch fermentations, these values should not, as a rule, be maintained constant during the whole process, since optimal pH and temperature values are different for growth and production of secondary metabolites.

3. Materials and Methods

Zymomonas mobilis strain ATCC 10988 was obtained as lyophilized pellets from the ATCC of Rockville, Maryland. Cultures were maintained by transferring the organism every 2 weeks in minimal growth media. The nutrient broth contained 1.0 g/l yeast extract, 0.5 g/l Bacto-peptone, and 2.0 weight percent glucose. Cultures were grown anaerobically under a 85% nitrogen, 5% carbon dioxide, and 10% hydrogen atmosphere. Seed cultures were scaled up with 10 weight percent glucose, 1.0 g/l $(NH_4)_2SO_4$, 1.0 g/l KH_2PO_4, 0.5 g/l $MgSO_4 \cdot 7H_2O$, and 3.0 g/l yeast extract.

Batch fermentations were conducted in a 7-liter Chemap fermenter with a working volume of 3 liters. The cultures were made anaerobic by sparging N_2 gas. Temperature, pH, redox potential, turbidity, and reactor weight were monitored by a data acquisition and control system HP3497A. Temperature was controlled and pH was maintained at the desired value by 1 N NaOH addition. Off-line samples were taken and then centrifuged, filtered, and injected into a Waters HPLC to quantify the ethanol and glucose concentrations. A 25 ml. sample was centrifuged, washed twice with deionized water, and dried until constant weight for biomass determination.

4. Experimental Data

Grogan [5] reports several sets of experimental values of biomass and ethanol concentration -vs- time for temperature and pH challenge batch fermentations. Figures (1a) and (1b) show the results for the temperature challenge experiments for an initial glucose concentration of 4.1% and a temperature range 30C to 38.5C. The pH challenge experiments are shown in Figures (2a) and (2b) for pH range 5 to 7.5 and an initial glucose concentration of 4.8%. These data sets are used in this study to determine the optimal pH and temperature profiles, which maximize the yield of ethanol.

For the purpose of optimization, an analytical representation of the data was required. The time-dependent functions of the biomass and ethanol concentrations during the exponential growth phase were obtained for the fermentation data via least-squares polynomial fitting. In general, low-order polynomials, ranging from second to sixth order, were found to be appropriate. A data-smoothing first order filter was included, in order to minimize the uncertainty involved

during differentiation calculations. Figs. 1 and 2 also show the polynomial fitting for the pH and temperature challenge experiments.

The effect of the pH on the specific growth rate, μ, is shown in Fig. 3. The specific growth rate μ is defined by:

$$\mu = (1/x)\,(dx/dt) \qquad (1)$$

where x is the biomass (cell) concentration in g/l and t is time in hrs. The effect of the temperature on the specific growth rate is shown in Fig. 4. Both of these curves present a clearly defined maximum.

The product yield with respect to biomass is defined as:

$$Y_{px} = (dP/dt) / (dX/dt) \qquad (2)$$

where dP/dt is the instantaneous rate of change of the product concentration and dX/dt is the instantaneous rate of change of the biomass concentration. The optimization by dynamic programming was performed with respect to Ypx, calculated each hour, since it proved to be a sensitive parameter with respect to pH and temperature changes. Others, like specific ethanol production rate, specific glucose uptake rate, and specific growth rate were reported to be less affected by temperature over the range studied [2].

5. Fermentation Kinetics Model

The mathematical modelling of the fermentation kinetics was necessary to evaluate the increase of ethanol yield when time-varying pH and temperature schedules are used throughout the batch process. The model described by Lee and Rogers [6] was used as a basis, and some parameter values were changed, to account for the different *Z. mobilis* strain used. The fermentation model is of the unstructured type and considers the following predominating factors:

- Δ Substrate limitation kinetics. The Monod model was assumed for the effect of substrate limitation on both growth and ethanol production.
- Δ Substrate inhibition kinetics. The substrate inhibition term accounts for the threshold substrate concentration Si below which no inhibition of growth rate would occur.
- Δ Ethanol inhibition kinetics. Linear inhibition kinetics was assumed, with threshold and maximum ethanol concentrations, these being different values for the influence on specific growth rate and specific ethanol production rate.
- Δ Influence of pH and temperature. The maximum specific growth rate was modelled as a function of pH and temperature.

The kinetic equations for growth and product formation of *Z. mobilis* are:

Rate of Biomass production:

$$\frac{dx}{dt} = \mu_m \frac{S}{K_S+S}\left(1 - \frac{p - p_i}{p_m - p_i}\right)\frac{(K_i - s_i)}{(K_i - s_i) - (S - s_i)}\,x \qquad (3)$$

where the term $\{(p-p_i)/(p_m-p_i)\}$ is equal to 0 for $p \le p_i$ and equal to 1 for $p \ge p_m$.

Rate of Glucose uptake:

$$\frac{dS}{dt} = -\frac{1}{Y_{ps}}\frac{dP}{dt} \qquad (4)$$

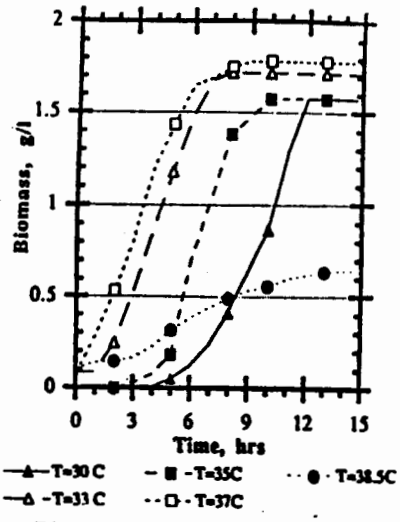

Figure 1a. Biomass growth curve for *Z. mobilis* in batch culture at different temperatures. No pH control.

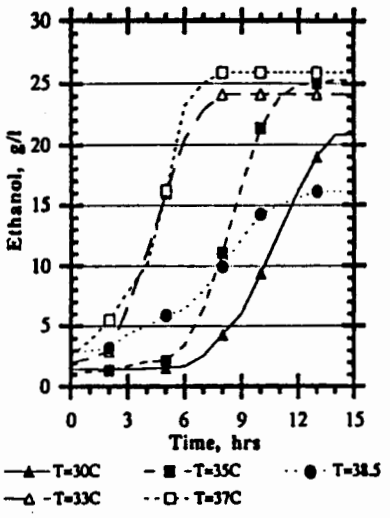

Figure 1b. Ethanol production rate for *Z. mobilis* in batch culture at different temperatures. No pH control.

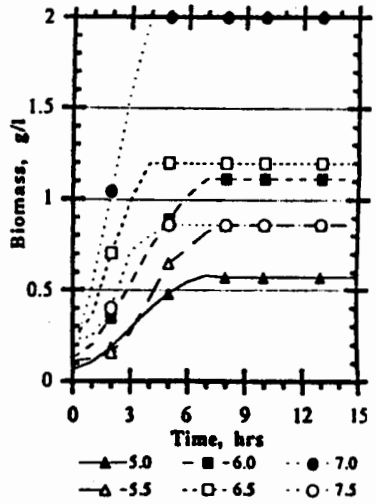

Figure 2a. Biomass growth curve for *Z. mobilis* in batch culture at different pH values. Temperature = 37 C.

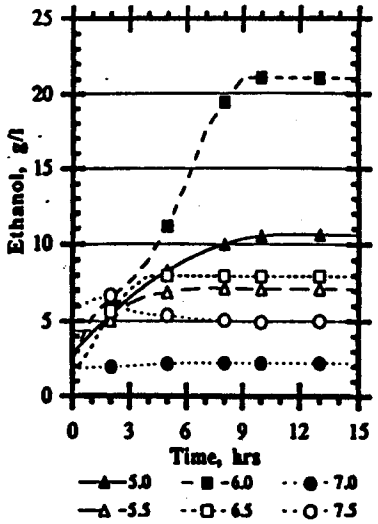

Figure 2b. Ethanol production rate for *Z. mobilis* in batch culture at different pH values. Temperature = 37 C.

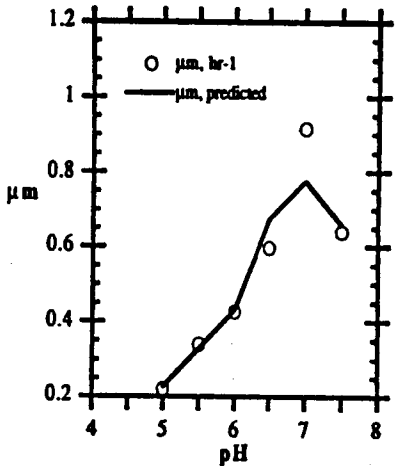

Figure 3. Effect of pH on the specific growth rate. Experimental and simulation values.

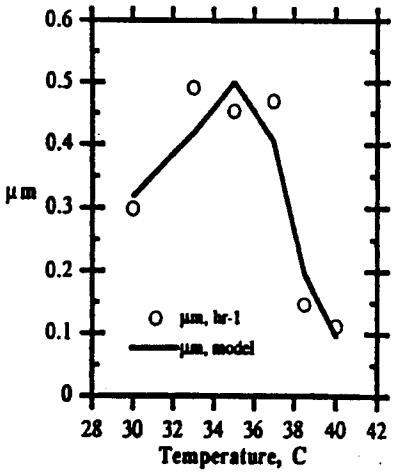

Figure 4. Effect of temperature on the specific growth rate. Experimental and simulation values.

Rate of Ethanol production:

$$\frac{dP}{dt} = (q_p)_m \frac{S}{K_S' + S}\left(1 - \frac{p - p_i}{p_m' - p_i'}\right)\frac{K_i'}{K_i' + S}\,x \qquad (5)$$

where the term $\{(p-p_i')/(p_m'-p_i')\}$ is equal to 0 for $p \le p_i'$ and equal to 1 for $p \ge p_m'$.

The specific growth rate used in the rate of biomass production was modelled as:

$$\mu_m = \sqrt{\mu_m(T)\,\mu_m(pH)} \qquad (6)$$

where $\mu_m(pH)$ is the specific growth rate as a function of pH given by

$$\mu_m(pH) = 0.206\,pH - 0.8037 \quad \text{for pH} = 5,\ldots,6 \quad \text{or}$$

$$\mu_m(pH) = \frac{\beta_{pH}}{1.0 + \frac{K_2}{[H^+]} + \frac{[H^+]}{K_1}} \quad \text{for pH} = 6,\ldots,7.5 \qquad (7)$$

The values of the constants were obtained from the pH challenge experiments as $K_1 = 1.37 \times 10^6$; $K_2 = 1.49 \times 10^{-8}$; and $\beta_{pH} = 0.998$. The fit is shown in Fig. 3. $\mu_m(T)$ is the specific growth rate as an Arrhenius function of temperature,

$$\mu_m(T) = A \exp\left[\frac{-E}{RT}\right] \qquad (8)$$

The values of the constants were obtained from the temperature challenge experiments. See fit in Fig. 4. The activation energy is 24.9 kcal/mol and the deactivation energy is -96.8 kcal/mol.

The values of the parameters used in the model equations are given in Table 1. These were estimated based on previous reported values for the strain 10988 and by sensitivity analysis.

Table 1. Values of the constants used in the model equations.

Constant	Value	Units
μ_m	0.2-0.6	1/h
K_s	0.5	g/L
K_i	130.0	g/L
s_i	10.0	g/L
p_i	7.0	g/L
p_m	27.0	g/L
$(q_p)_m$	5.0	g/g-h
K_s'	0.5	g/L
K_i'	2000.0	g/L
p_i'	15.0	g/L
p_m'	70.0	g/L
Y_{ps}	0.48	g/g

Comparisons of the model predictions for biomass and ethanol production with batch experimental data are shown in Figs. 5a and 5b. It can be seen that a good agreement was found between the model predictions and the experimental data.

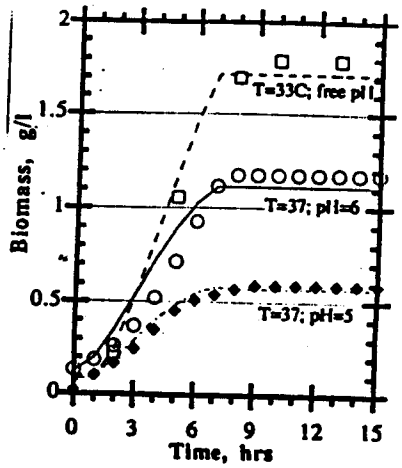

Figure 5a. Comparison of biomass production data with the model for batch culture of *Z. mobilis* for various conditions.

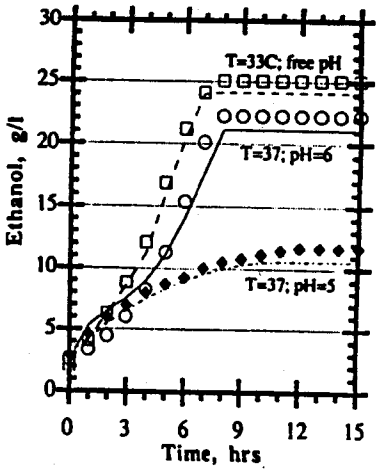

Figure 5b. Comparison of ethanol production data with the model for batch culture of *Z. mobilis* for various conditions.

6. Theory of Dynamic Programming

This method is due to Bellman [9]. The main philosophy of this approach is that if one takes optimum decision at every sample interval about a particular objective function which is calculated based upon a model, then the overall trajectory of the process will be optimum.

We need mathematical models for this. Let us take an example with an unstructured model of the following type:

$$dX/dt = X\,\mu(S, u) \tag{9}$$

$$dS/dt = -X\,q_s(S, u) \tag{10}$$

$$dP/dt = X\,q_p(S, u) \tag{11}$$

Here, μ is the specific growth rate, q_s is the specific substrate consumption rate, and q_p is the specific product formation rate. The control vector is u, defined by:

$$u = [\,T \quad pH \quad S_o \quad \ldots\ldots\,]^T \tag{12}$$

where T is temperature, pH = -log[H^+], and S_o is the initial substrate concentration.

Let us define an objective function,

$$J = P(t_f) \tag{13}$$

The idea is to maximize the function J, and obtain the operational conditions which will maximize the value of the objective function. The choice of J in equation (13) will vary from fermentation to fermentation, and is usually obtained from experience with a certain process.

It has been noted by many that one of the most important factors which influences the economics of a fermentation process is the yield of a particular fermentation. If we know q_p and μ, then one can find out the specific product yield with respect to specific growth rate. In other words,

$$Y_{px} = q_p/\mu \tag{14}$$

One can use this as an objective function, i.e.,

$$J = P(t_f) = \int_{x(0)}^{x(t_f)} Y_{px}dx + P(0) \tag{15}$$

The problem solution depends upon whether the harvest time is fixed or free.

For free harvest time,

$$P(t_f)_{max} = \int_{x(0)}^{x(t_f)} \left(\max_{u\in U} Y_{px}\right) dx + P(0) \tag{16}$$

For fixed harvest time:

$$P(t_f)_{max} = \max\left\{\int_{x(0)}^{x(t_f)} Y_{px}dx + \max_{\substack{u\in U \\ x\in[x(t),\,x(t_f)]}} \int_{x(0)}^{x(t_f)} Y_{px}dx\right\}$$

for $0 < t \le t_f$ (17)

The algorithm for application of the method is as follows:

1.- Obtain experimental data for N number of fermentation runs at different environmental conditions.

2. Obtain $x_i(t_i)$ and $P_i(t_i)$ at different sample intervals, i. Here the subscript "i" refers to the i-th experiment.

3. From the experimental data, obtain derivatives, dx_i/dt and dP_i/dt for each run. A reasonable way to calculate the derivatives is to fit a polynomial to each of the curves and obtain the parameters using a least squares method.

4. From the derivatives, the Y_{px} is calculated for each experiment and at each sample point. Defining Y_{px} as "y", we then have N number of y_x every sample interval.

When the final time is free, the process duration in this case is limited indirectly by the amount of substrate provided for the fermentation process:

5. For each discrete value of x_i, the maximum of N $\{y_i(x_i);\ i=1,\ldots,N,\ j=1,\ldots,k)\}$ is found. Then the optimum y_i is given by:

$$y_{i,opt,j} = \max\,\{\,y_1(x_j), \ldots, y_n(x_j)\,\} \tag{18}$$

For each i, we obtain an optimum $y_{i,opt,j}$ which gives the optimal control variables $u_{i,opt(j)}$.

6. Calculation of the expected optimal time trajectories: The optimum trajectories, $u_{opt}(t)$, $P_{opt}(t)$, $x_{opt}(t)$, are constructed from the k trajectories in accordance with the sequence of the optimal indices determined above.

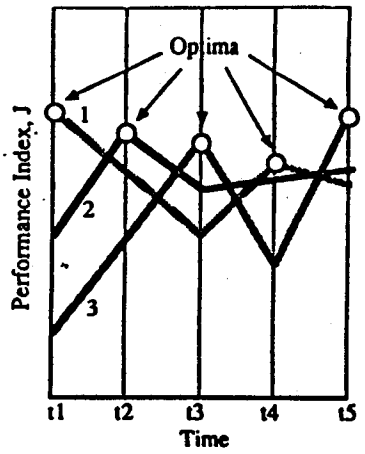

Figure 6. Dynamic programming method: Performance index J -vs- time for three cases.

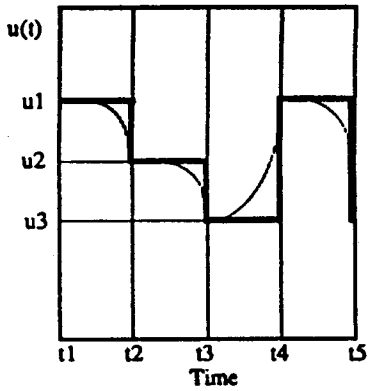

Figure 7. Dynamic programming method: Optimal profile for u1 based on information from Figure 6.

For the cases when the process time is fixed, the optimal trajectory in the phase-plane must be selected in such a way that the sum of time intervals, while the process passes the trajectories with fixed level of control variables, would satisfy the restriction on the process duration.

However, simultaneously, the area under the selected trajectory is maximum in the cell concentration levels (x(0), $x(t_f)$). Since, $x(t_f)$ is not fixed when t_f is fixed, optimal trajectories for some freely selected final values of cell concentration, x(t), are to be determined, and then the trajectory giving the maximum of the restricted area is to be selected.

A graphical example of the method is illustrated in Fig. 6, where the performance index J is shown as a function of time for three cases. Curves 1, 2, and 3 correspond to particular operating conditions. Each of the circles indicates new conditions for optimum operation. If we had only one variable, i.e., u_1, which needed to be varied in order to optimize the process, then we would get the profile for u_1, as shown in Fig. 7.

7. Results and Discussion

Once the polynomials were defined for each data set and for each variable (biomass and ethanol concentrations), their derivatives were calculated and evaluated at hourly increments over a 15-hour fermentation period. The ethanol yield was obtained at the same hour increments and the dynamic programming method was used to select the highest ethanol yield at each hour.

Figs. 8 and 9 show the pH and temperature profiles to be followed in a 15-hour batch fermentation. The profiles show step changes in the values of the pH and temperature throughout the experiment. Although, the calculations were performed in an hourly basis, the changes in the profiles did not take place more frequently than 2 hours. This enables the microorganisms to adjust to changes in their environment, before new changes are made.

The profiles were tested in a simulation program using the unstructured model to verify if the yield was indeed greater, than when the fermentation is carried out at a single constant value for pH and temperature. Fig. 10 shows the simulation results and Fig. 11 shows a comparison of the ethanol point yields obtained for three different simulation runs: using only the optimal pH profile, using only the optimal temperature profile, and using both temperature and pH optimal profiles. Table 2 shows the values of average ethanol yield for the same runs. The average ethanol yield found by using the optimal pH and temperature profiles during the fermentation is 28.3, whereas a typical batch run at a constant temperature of 37C and a constant pH of 6 gives an average ethanol yield of 9.5. This shows that the use of time-varying pH and temperature profiles increases the average ethanol yield more than twice the value obtained with constant conditions.

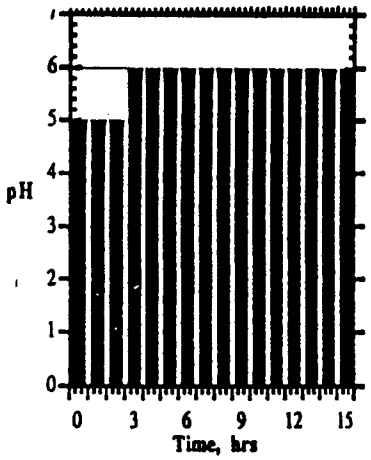

Figure 8. Optimal pH profile for *Z. mobilis* in batch culture.

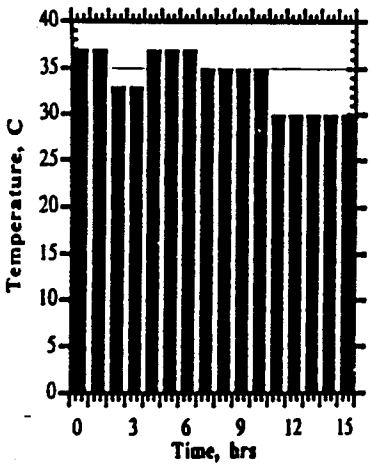

Figure 9. Optimal temperature profile for *Z. mobilis* in batch culture.

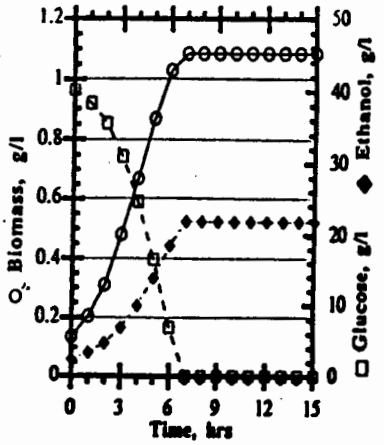

Figure 10. Simulation results for *Z. mobilis* in batch culture using optimal pH and temperature profiles.

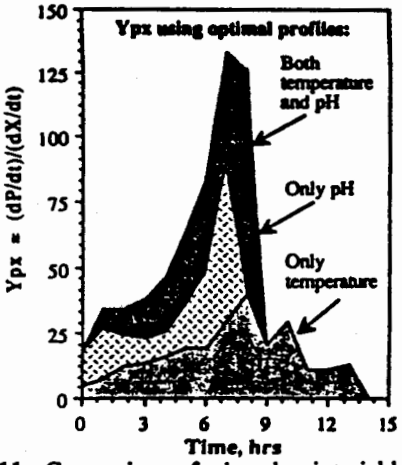

Figure 11. Comparison of ethanol point yields for three different cases using optimal time-varying pH and temperature profiles.

8. Implementation Strategies

The results shown, though based on models which validated experimental results, were obtained by simulations. Therefore, fine tuning will be necessary for the real-time implementation. The following guidelines are suggested:

- Δ If the temperature changes in the optimal profile are larger than 1l C, then a filter is used to minimize the effects of sudden temperature changes.
- Δ If the pH changes in the optimal profile are larger than l0.5l, a smoothing algorithm (filter) is used.

9. Conclusions

The optimization of a batch fermentation for ethanol production was presented. The dynamic programming optimization method used is simple and easily implementable. A mathematical representation of the fermentation was developed to test the effect of time-varying pH and temperature profiles throughout the fermentation. The temperature and pH models satisfactorily represented the *Z. mobilis* fermentation at different conditions. These models were used in simulation runs to test the optimal profiles. It was found that the use of time-varying temperature and pH profiles increases the average Ypx by more than twice the average yield of the best fermentation at fixed temperature and pH conditions, which is the traditional way of running industrial fermentations.

Table 2. Comparison of Average Ethanol Yields Y_{px} for Batch Fermentation at Different Conditions.

Temperature	pH	Avg. Ypx	Source
37 C	free	5.8	Experiment
37 C	6.0	9.5	Experiment
37 C	Optimal	9.5	Simulation
Optimal	6.0	16.8	Simulation
Optimal	Optimal	28.3	Simulation

NOMENCLATURE

A	Arrhenius preexponential constant, (1/h)
E	Energy of activation, (kcal/mol)
K_1, K_2	constants in equation (7)
K_i	substrate inhibition constant for growth (g/L)
K_i'	substrate inhibition constant for ethanol production (g/L)
K_s	substrate limitation constant for growth (g/L)
K_s'	substrate limitation constant for ethanol production (g/L)
P	product (ethanol) concentration (g/L)
P_i	threshold ethanol conc. for cell growth (g/L)
P_i'	ethanol threshold concentration for ethanol production (g/L)
P_m	maximum ethanol concentration for cell growth (g/L)
P_m'	maximum ethanol concentration for ethanol production (g/L)
q_s	specific substrate (glucose) uptake rate (g/g-h)
q_p	specific product (ethanol) formation rate (g/g-h)
$(q_p)_m$	maximum specific ethanol production rate (g/g-h)
R	ideal gas law constant, (kcal/mol-K)
S	substrate (glucose) concentration (g/L)
si	threshold substrate conc. for cell growth (g/L)
x	biomass (cell) concentration (g/L)
Y_{xs}	yield factor of biomass on substrate (g/g)
Y_{xp}	yield factor of biomass on product (g/g)
Y_{ps}	yield factor of product (ethanol) on substrate utilized (g/g)
μ	specific growth rate (1/h)
μ_m	maximal specific growth rate (1/h)
β_{pH}	constant in equation (7)

References

[1] P. K. Bajpai and A. Margaritis, 28, 824 (1986).

[2] F. G. King and M. A. Hossain, *Biotechnology*, 4, 531 (1982).

[3] J. Fieschko and A. E. Humphrey, *Biotechnology and Bioengineering*, 25, 1655, (1983).

[4] I. Laudrin and G. Goma, *Biotechnology Letters*, 4, 537 (1982).

[5] A. Grogan, M. Sc. Thesis, Colorado State University, (1984).

[6] K. J. Lee and P. L. Rogers, *The Chemical Engineering Journal*, 27, B31 (1983).

[7] L. N. Andreyeva and V. V. Biryukov, *Biotechnology and Bioengineering Symposium No. 4*, 61-76 (1973).

[8] I. M. L. Jöbses, G.T.C. Egberts, A. van Baalen, and J. A. Roels, *Biotechnology and Bioengineering*, 25, 984 (1985).

[9] R. Bellman and S. Dreyfuss, *Applied Dynamic Programming*, Princeton University Press, Princeton, N.J. (1962).

BIODEGRADATION OF PCP BY PSEUDOMONAS CEPACIA

R. Rayavarapu, S.K. Banerji, and R.K. Bajpai

Civil Engineering Department
Missouri University
Columbia, MO

Abstract

The PCP degradation was studied in shaken flasks in presence and absence of an easily degradable carbon source, glucose. PCP degradation was found out to be rapid in presence of glucose. Though there were no significant lag periods observed below PCP concentrations of 50 mg/l, the lag periods did increase for the PCP concentrations beyond 50 mg/l.

Introduction

Pentachlorophenol has, in the past, been used as an insecticide[1,2] as well as a wood-treating agent. As a result, several PCP contaminated sites exist. PCP in soils is quite recalcitrant[3] and several attempts are being made to remedify these contaminated sites. This study is a part of ongoing efforts at the University of Missouri, Columbia to develop effective methods for in-situ bioremediation.

Several microorganisms are known to metabolize PCP[4-8]. Yet the efficiency of biodegradation in soil environment is small [9-14]. In the present study, it has been postulated that this lack of biodegradation could be as a results of several factors such as the availability of PCP to the microorganisms, inhibition of metabolism by the concentrations of PCP, inability of microorganisms to metabolize PCP in soil, and the environmental conditions that microbial cells face in contaminated soils. This paper will report results from phase I of our work where studies have been conducted to characterize the biodegradation of PCP by Pseudomonas cepacia ATCC 1100 in relatively clean environment in absence of soil. Phase II will involve studies with soil in laboratory, followed by phase III studies in lysimeters.

Materials and Methods

Microorganism: Pseudomonas cepacia ATCC 1100 cells were used through out this study. The cells were kept on nutrient agar slants at 4 ^{o} C and were subcultured every two months.

Medium: The medium prescribed by Kilbane et al.[15] for Pseudomonas cepacia cells was used in this study. It consisted of Glucose 4 g/l, K_2HPO_4 5.8 g/l, KH_2PO_4 4.5 g/l, $(NH_4)_2$ SO_4 2 g/l, Mg Cl_2 0.16 g/l, Ca Cl_2 20 mg/l, Na MoO_4 2mg/l, $FeSO_4$ 1mg/l, Mn SO_4 1 mg/l. This solution was prepared in deionized ultra-clean water in order to avoid any interference with UV detection of PCP. Solutions of glucose, calcium chloride and magnesium chloride were autoclaved separately from the rest of the salts. After cooling, the solutions were mixed under sterile conditions in order to avoid formation of precipitate. Necessary amounts of PCP were added to this medium in the form of a solution in 0.05 N NaOH. pH of the medium was between

6.8-7.0. All the chemicals used in this study were procured from Sigma Chemical Co, St. Louis, MO.

Experimental Procedure: Experiments were initiated by transferring cells from stock-slant to a new nutrient agar slant. After 12 hours of incubation at 30°C, the cells were transferred in to a flask containing the above mentioned medium. PCP at 5 mg/l level was also added to the solution in order to acclimatize the cells. Inocula for all the experiments were taken after 17 hours of incubation in a rotary shaker rotating at 200 rpm. Absorbance (540 nm) of the broth at the time of transfer was between 1.0 to 1.2. The level of inoculum was 10 % v/v.

The experiments were conducted in 300/500/1000 ml Erlenmeyer flasks. Samples (5-10 ml) were withdrawn at appropriate times under sterile conditions. Optical density of the samples were measured immediately and the cells were removed by centrifugation. The supernatants were stored in freezer pending further analysis. Mostly the analysis was conducted immediately.

Analysis of samples: Dry cell weight in the samples was estimated by measurements of optical density at 540 nm. The optical density readings were converted in to dry weight units using a calibration curve previously developed for Pseudomonas cepacia cells.

Sugar in samples was analyzed on HPLC using a refractive index detector. The detailed procedure is reported else where[16].

Analysis for PCP was conducted using three different methods. A *spectrophotometric method* reported by Edgehill and Finn [17] was used for rapid on the spot measurements of PCP in samples. The calibration between absorbance at 320 nm and PCP concentration was linear up to 50 mg/l PCP. The minimum concentration that could be detected using this method was 5 mg/l. No interference was observed from any other broth constituents. A *HPLC* procedure based upon a gradient method employed in the Environmental Trace Substances Research Center of University of Missouri, Columbia, was used for the most of the routine analyses. This procedure involved chromatographic separation of PCP on a C-18 reverse phase column (Supelco, length 25 cm, i.d. 4.6 mm, particle size 5 um) using acetonitrile containing 1 % v/v glacial acetic acid as mobile phase and peak detection using a Spectraflow 783 programmable UV detector at 254 nm (Kratos Analytical). The

flow rate of solvent was 0.5 ml/ min. A calibration curve was developed which was linear up to 100 mg/l PCP. The minimum concentration that could be detected with this method was 3.0 mg/l. This calibration curve was checked daily. ***EPA method 604*** was used for some of the samples. This involves extraction of PCP from liquid samples using methylene chloride followed by extraction and concentration in 2-Propanol. Analyses were conducted on a Perkin Elmer 3500 GC with capillary column (Altech, 15 m, 0.5mm i.d., coating RSL 200) with helium as carrier gas (15 ml/min) was employed. Other conditions were: injector 250 ^{o} C, oven temperature programmed between 75 ^{o} C (2 minute hold) and 180 ^{o} C (ramp rate 8 ^{o} C per minute). A good agreement was observed between the different methods.

Results and Discussions:

A number of experiments were conducted with different PCP concentrations ranging between 0-100 mg/l and a single glucose concentration of 4 g/l to observe the effect of PCP on the growth rate of cells. No significant lags were observed up to PCP concentrations of 50 mg/l. However, increasing the PCP concentration beyond 50 mg/l did produce long lag periods. Sequential acclimation of cells to higher PCP concentrations had little effect on the reduction of lag periods.

Typical profiles of cell dry weight, glucose and PCP for an experiment with an initial PCP concentrations of 50 mg/l and 100 mg/l are shown in figures 1 and 2. In both of these experiments, replicates were run and good reproducibility between the runs were observed. In either of these experiments glucose was not completely exhausted. The maximum specific growth rates were calculated for PCP concentrations ranging between 0 to 100 mg/l (Table 1) and these showed a definite inhibition as the PCP concentration increased. Figure 3 shows a plot in which the maximum specific growth rates were plotted against their respective initial PCP concentrations according to a model of non-competitive inhibition of growth by PCP

$$\mu = \mu^{*} \cdot \frac{K_I}{K_I + P} \qquad (1)$$

The inhibition parameter K_1 is 220 mg/l.

For the degradation of PCP, a non-growth associated first order kinetics was employed. Hence,

$$\frac{dP}{dt} = -a.P.X \qquad (2)$$

When coupled with the model for growth of cells, these two equations can be solved to reveal a relationship between the instantaneous concentration of PCP and cell dry weight in the broth. Accordingly,

$$\ln\left[\frac{P}{P_o}.\frac{K_I+P_o}{K_I+P}\right] = -\frac{a}{\mu^*}.(X-X_o) \qquad (3)$$

Figure 4 shows a plot of experimental data according to this equation. The data seemed to justify the model despite some bad data points. The degradation rate parameter "a" was calculated to be 0.4 l/hr.(g_{dw}).

Conclusions:

The kinetics of biodegradation of PCP by Pseudomonas cepacia has been studied. The PCP has been degraded as a cometabolite. The specific rate of PCP degradation is first order with respect to the concentration of PCP. PCP is also a non-competitive inhibitor of growth of cells.

Acknowledgements: Although the research described in this article has been funded in part by the U.S. Environmental Protection Agency under Assistance Agreement R-815709, to the University of Missouri-Columbia through Hazardous Substances Research Center for U.S. EPA Regions 7 and 8, headquartered at Kansas State University, it has not been subjected to the Agency's Peer and Administrative review and therefore may not necessarily reflect the views of the Agency and no official endorsement should be inferred.

References

1. Cirelli, D. P., "Patterns of PCP Usage in the United States - An Overview", in *Pentachlorophenol : Chemistry, Pharmacology, and Environmental Toxicology*. K. R. Rao (Ed). Plenum Press, New York, N. Y. 1978.

2. "Pentachlorophenol", Environmental Health Criteria 71, WHO Geneva, 1987.

3. Ahlborg, U. and Thunberg, T., CRC Crit. Rev. Toxicol., 7, 1 (1980).

4. Chu, J. P. and Kirsch, E. J., Appl. Microbial., 23, 1033 (1972).

5. Crawford, R. L. and Mohn, W. W., Enzyme Microbial Technol., 7, 617 (1985).

6. Saber, D. L. and Crawford, R. L., Appl. Environ. Microbiol., 50, 1512 (1985).

7. Stanlake, G. and Finn, R. K., Appl. Environ. Microbiol., 44, 1421 (1982).

8. Steiert, J. G. and Crawford, R. L., Biochem. Biophys. Res. Commun., 141, 825 (1986).

9. Edgehill, R. U. and Finn, R. K., Appl. Environ. Microbiol., 45, 1122 (1983).

10. Suzuki, T., J. Environ. Sci. Health, B12, 113 (1977).

11. Watenabe, J., Soil Sci. Plant Nutr., 19, 109 (1973).

12. Watanabe, I., Soil Biol. Biochem., 9, 99 (1977).

13. Ide, A., Niki, Y., Sakamoto, F., Watanabe, I, and Watanabe, H., Agr. Biol. Chem., 36, 1937 (1972).

14. Kuwatsuka, S. and Igarashi, M., Soil Biol. Plant Nutr., 21, 405 (1975).

15. Kilbane, J. J., Chatterjee, D. K., Karns, J. S., Kellogg, S. T., and Chakrabarty, A. ., Appl. Environ. Microbiol., 44, 72 (1982).

16. Tu, C. H., Jayanata, Y., Bajpai, R., Biotechnol. Bioeng. Symp. Ser., 15, 295 (1985).

17. Edgehill, R. U. and Finn, R. K., Eur. J. Appl. Microbiol. Biotechnol., 16, 179 (1982).

Table I

Initial PCP conc. (mg/L)	*Maximum sp. Growth rate* (hr^{-1})
0	0.36
20	0.33
50	0.29
100	0.25

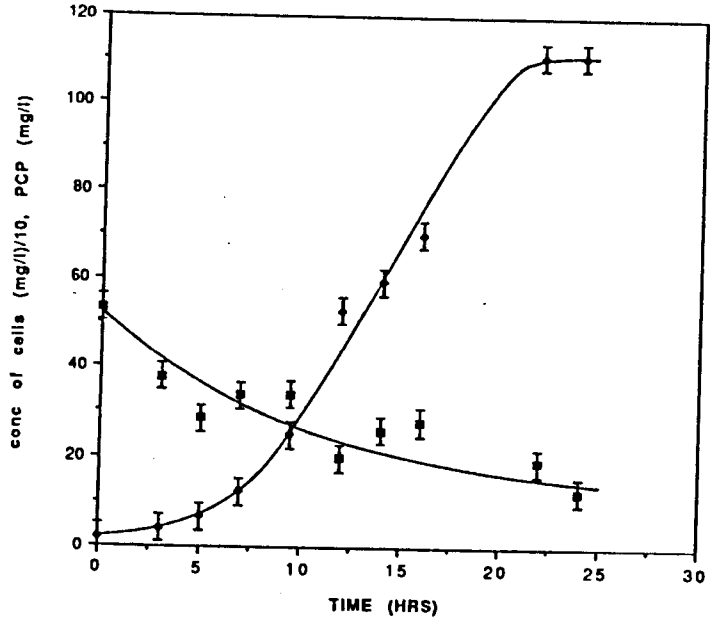

KINETICS OF GROWTH ON GLUCOSE IN PRESENCE OF 50 mg/l OF PCP

FIGURE 1

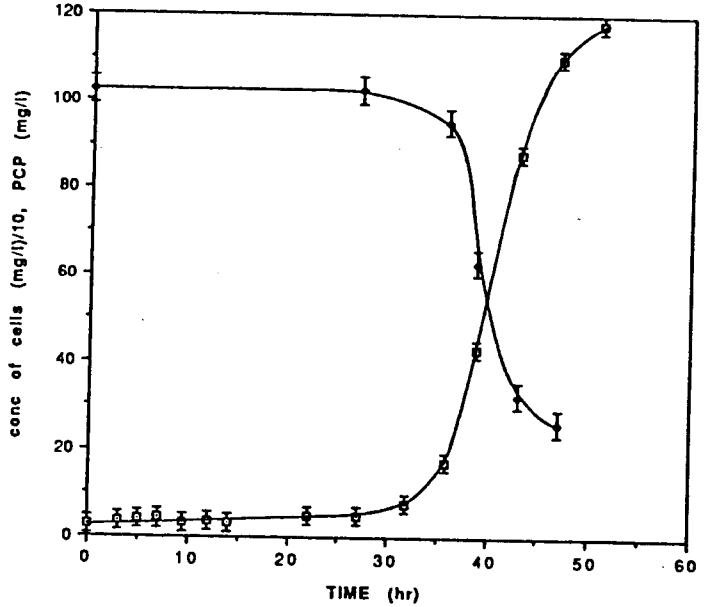

KINETICS OF GROWTH ON GLUCOSE IN PRESENCE OF 100 mg/l OF PCP

FIGURE 2

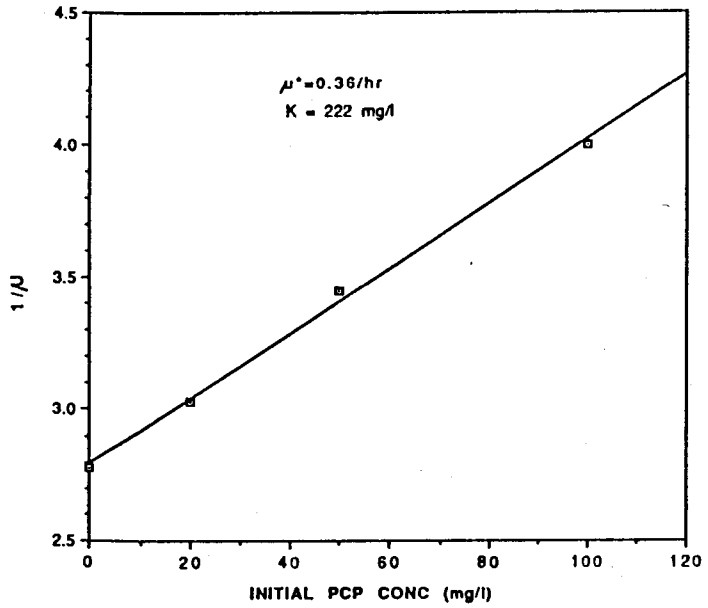

EFFECT OF PCP CONCENTRATION ON SP. GROWTH RATE OF CELLS.

FIGURE 3

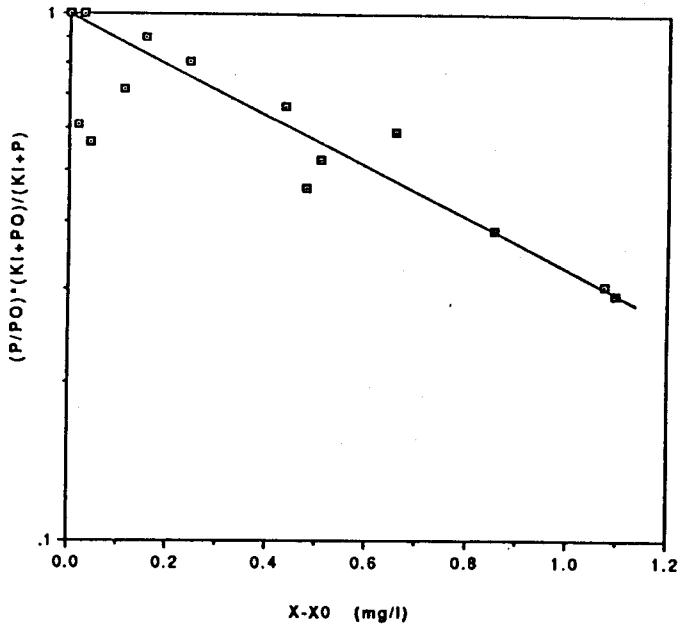

KINETICS OF DEGRADATION OF PCP BY CELLS GROWING ON GLUCOSE

FIGURE 4

MODELING THE BIOREMEDIATION OF CONTAMINATED SOIL AGGREGATES: A Phenomenological Approach

S. Dhawan, L.E. Erickson, and L.T. Fan

Department of Chemical Engineering
Durland Hall
Kansas State University
Manhattan, Kansas 66506

April 21, 1990

INTRODUCTION

The contamination of nature by accidental release of chemicals is a matter of growing concern. Pollutants released on the soil surface from improperly designed waste disposal facilities, underground storage tank leaks, and inadvertent chemical spills move to the groundwater through the aggregated-vadose zone. The contaminated vadose zone need be remediated to protect the groundwater. The complexity of various phenomena affecting the environmental fate of chemicals coupled with the lack of field and/or laboratory data makes the remediation of this zone extremely difficult.

The issues involved in the management of contaminated sites are fairly complex due to the interwined system of biotic and abiotic factors affecting the transformation and migration of chemicals in the environment (Donigian and Rao, 1986). The clean-up of such sites requires extensive resources. Nevertheless, the funds available for this purpose are rather limited. It is critically important, therefore, that we resort to effective measures to reduce the total cost of remediation (see, e.g., Boutwell *et al.*, 1986). Environmental models are increasingly being relied upon to facilitate evaluation and selection of the most suitable treatment scheme for remediation (see, e.g., Wood, 1982). It is difficult, however, to unequivocally take into account in such models the relative roles of all the processes affecting the behavior of chemicals in the environment; therefore, these models, essentially *caricatures of the real world*, include in them only the dominant factors. The use of site-specific rather than generic information in constructing such models, however, enables them to make fairly reliable predictions.

Environmental models can be classified into descriptive, physical, analogous, and mathematical models (see, e.g., Yeh, 1982). Of these, the mathematical models based on physical principles, axioms and reasonable assumptions, i.e., the mathematical-mechanistic models, offer promising means for predicting the spatial and temporal distributions of chemicals in the natural environment (see, e.g., Yeh, 1982). Such models provide a conceptual framework for objective assimilation and manipulation of the various mechanisms involved in the transport, transformation and accumulation of organic chemicals in soil; phenomenological estimates of the overall process based on these models supplemented by the best technical judgement would contribute to the clarification of the issues and ambiguities inherent in decision-making (see, e.g., Boutwell *et al.*, 1986). However, the existing modeling information is not adequate for large-scale field applications; the identification of dominant factors controlling the fate of pollutants in the natural environments remains elusive. An urgent need, therefore, exists for a concerted effort to develop and model new soil remediation technologies.

In-situ bioremediation, an innovative and cost effective treatment technology, has

been modeled by a number of researchers (Kosson *et al.*, 1987; Wu *et al.*, 1990). Much of the work can be found in the reviews by Weber and Smith (1987), Brusseau and Rao (1989), and Sims (1990). Most of the models have considered the soil phase to be homogeneous and isotropic (Grenny *et al.*, 1987; Wu *et al.*, 1990). Little attention has been focussed on the effect of aggregate size. The transport of solute without degradation in the porous media has been modeled by a number of researchers (Crittenden *et al.*, 1986; Goltz and Roberts, 1986; Fong and Mulkey, 1989). Only a few models incorporate the reaction term for contaminant degradation in the porous medium; the majority of these models contain linear first-order reaction terms (Pekdeger, 1984; Janssen *et al.*, 1990). In bioremediation, the organic contaminants are utilized by microorganisms as a carbon source in their metabolic process; hence, degradation can be better described by Monod kinetics (Bailey and Ollis, 1986).

The Contaminated Aggregates Bioremediation (CAB) model presented in this study describes the effect of some principal factors in the bioremediation of contaminated soil aggregates. The influence of aggregate radius, partition factor and initial substrate concentration has been investigated.

CAB MODEL

This model considers organic contaminants to be deposited uniformly in soil aggregates. Moreover, the microorganisms are present as suspended forms in the pore liquid and are also attached as microcolonies to the solid surface; they grow by consuming organic contaminants and oxygen.

The following major assumptions are imposed while deriving the model: (a) The bed is composed of spherical soil aggregates of a single size; (b) the aggregates are saturated, homogeneous and isotropic, and are made up of solid particles and stagnant water; (c) the temperature is constant in the bed; (d) the reaction rate depends only on the concentrations of three components, oxygen, biomass, and substrate; (e) transport in the aggregate is by diffusion only; (f) the transport resistances of substrate and oxygen to and through the microcolonies attached to the surface of soil particles are negligible; therefore, the microcolonies respond to the variations in the bulk concentrations in the pore liquid; and (g) the flow rate of oxygen-rich water having a zero concentration of substrate and a low value of biomass is sufficiently high in the macrovoids of the bed so that fixed concentrations of substrate, oxygen, and biomass are maintained at the exterior of the aggregate at $r = R$.

MODEL DERIVATION

The mass balance of component i in a spherical aggregate gives rise to

$$4\pi r^2 \Delta r \left[\epsilon_a \frac{\partial C_{i,p\ell}}{\partial t} + \rho \frac{\partial q_i}{\partial t} \right]$$

$$= 4\pi r^2 \left[- \frac{D_{i,p\ell} \epsilon_a}{\tau} \frac{\partial C_{i,p\ell}}{\partial r}\bigg|_r - D_{i,so} \rho \frac{\partial q_i}{\partial r}\bigg|_r \right]$$

$$- 4\pi r^2 \left[- \frac{D_{i,p\ell} \epsilon_a}{\tau} \frac{\partial C_{i,p\ell}}{\partial r}\bigg|_{r+\Delta r} - D_{i,so} \rho \frac{\partial q_i}{\partial r}\bigg|_{r+\Delta r} \right]$$

$$+ 4\pi r^2 \Delta r \epsilon_a r_i^{p\ell} + 4\pi r^2 \Delta r \rho r_i^{sf} \qquad (1)$$

where subscript i stands for substrate, oxygen, and biomass. Dividing both sides of Eq. 1 by $4\pi r^2 \Delta r$, and taking the limit as Δr approaches zero give

$$\epsilon_a \frac{\partial C_{i,p\ell}}{\partial t} + \rho \frac{\partial q_i}{\partial t} = \frac{D_{i,p\ell}\epsilon_a}{\tau r^2} \frac{\partial}{\partial r}\left[r^2 \frac{\partial C_{i,p\ell}}{\partial r}\right] + \frac{D_{i,so}}{r^2}\rho\left[r^2 \frac{\partial q_i}{\partial r}\right]$$

$$+ \epsilon_a r_i^{p\ell} + \rho r_i^{sf} \qquad (2)$$

The local adsorption-desorption equilibrium in the aggregate can be expressed as

$$q_i = K_{di} C_{i,p\ell} \qquad (3)$$

Substituting this equation into Eq. 2 leads to

$$(\epsilon_a + \rho K_{di}) \frac{\partial C_{i,p\ell}}{\partial t} = \frac{D_{i,p\ell}\epsilon_a/\tau + D_{i,so}\rho K_{di}}{r^2} \frac{\partial}{\partial r}\left[r^2 \frac{\partial C_{i,p\ell}}{\partial r}\right]$$

$$+ \epsilon_a r_i^{p\ell} + \rho r_i^{sf} \qquad (4)$$

Equation 4 is the general equation for component i in the aggregate. The reaction terms for substrate, oxygen and biomass are expressed in terms of the Monod model. The rate of substrate consumption by the microorganisms in the pore liquid, $-r_s^{p\ell}$, is expressed as

$$-r_s^{p\ell} = \frac{\mu_m}{Y_s} C_{b,p\ell} \left[\frac{C_{s,p\ell}}{K_s + C_{s,p\ell}}\right]\left[\frac{C_{o,p\ell}}{K_o + C_{o,p\ell}}\right] \qquad (5)$$

The rate of substrate consumption by the microcolonies attached to the surface of soil particles, $-r_s^{sf}$, is

$$-r_s^{sf} = \frac{\mu_m}{Y_s} q_b \left[\frac{C_{s,p\ell}}{K_s + C_{s,p\ell}}\right]\left[\frac{C_{o,p\ell}}{K_o + C_{o,p\ell}}\right] \qquad (6)$$

The rate of oxygen consumption in the pore liquid space, $-r_o^{p\ell}$, and that on the surface of soil particles, $-r_o^{sf}$, are expressed, respectively, as

$$-r_o^{p\ell} = \frac{\mu_m}{Y_o} C_{b,p\ell} \left[\frac{C_{s,p\ell}}{K_s + C_{s,p\ell}}\right]\left[\frac{C_{o,p\ell}}{K_o + C_{o,p\ell}}\right] \qquad (7)$$

$$-r_o^{sf} = \frac{\mu_m}{Y_o} q_b \left[\frac{C_{s,p\ell}}{K_s + C_{s,p\ell}}\right]\left[\frac{C_{o,p\ell}}{K_o + C_{o,p\ell}}\right] \qquad (8)$$

The rate of biomass growth in the form of suspended microorganisms in the pore liquid, $r_b^{p\ell}$, and that at the interface, r_b^{sf}, are expressed, respectively, as

$$r_b^{p\ell} = \mu_m C_{b,p\ell} \left[\frac{C_{s,p\ell}}{K_s + C_{s,p\ell}}\right]\left[\frac{C_{o,p\ell}}{K_o + C_{o,p\ell}}\right] - k_d C_{b,p\ell} \qquad (9)$$

$$r_b^{sf} = \mu_m q_b \left[\frac{C_{s,p\ell}}{K_s + C_{s,p\ell}}\right]\left[\frac{C_{o,p\ell}}{K_o + C_{o,p\ell}}\right] - k_d q_b \qquad (10)$$

Substituting the above kinetic expressions for substrate consumption, Eqs. 5 and 6, and the equilibrium relation, Eq. 3, into Eq. 4 gives rise to

$$(\epsilon_a + \rho K_{ds}) \frac{\partial C_{s,p\ell}}{\partial t}$$

$$= \frac{D_{s,p\ell}\epsilon_a/\tau + D_{s,so}\rho K_{ds}}{r^2} \frac{\partial}{\partial r}\left[r^2 \frac{\partial C_{s,p\ell}}{\partial r}\right]$$

$$-(\epsilon_a + \rho K_{db})\frac{\mu_m}{Y_s}C_{b,p\ell}\left[\frac{C_{s,p\ell}}{K_s+C_{s,p\ell}}\right]\left[\frac{C_{o,p\ell}}{K_o+C_{o,p\ell}}\right] \quad (11)$$

Oxygen adsorption in the solid phase is neglected; thus,

$$\epsilon_a \frac{\partial C_{o,p\ell}}{\partial t} = \frac{D_{o,p\ell}\epsilon_a}{\tau r^2}\frac{\partial}{\partial r}\left[r^2 \frac{\partial C_{o,p\ell}}{\partial r}\right]$$

$$-(\epsilon_a + \rho K_{db})\frac{\mu_m}{Y_o}C_{b,p\ell}\left[\frac{C_{s,p\ell}}{K_s+C_{s,p\ell}}\right]\left[\frac{C_{o,p\ell}}{K_o+C_{o,p\ell}}\right] \quad (12)$$

The surface diffusion of biomass is negligible, therefore, $D_{b,so} = 0$. Hence,

$$(\epsilon_a + \rho K_{db})\frac{\partial C_{b,p\ell}}{\partial t} = \frac{D_{b,p\ell}\epsilon_a}{\tau r^2}\frac{\partial}{\partial r}\left[r^2 \frac{\partial C_{b,p\ell}}{\partial r}\right]$$

$$+(\epsilon_a + \rho K_{db})\mu_m C_{b,p\ell}\left[\frac{C_{s,p\ell}}{K_s+C_{s,p\ell}}\right]\left[\frac{C_{o,p\ell}}{K_o+C_{o,p\ell}}\right]$$

$$-(\epsilon_a + \rho K_{db})k_d C_{b,p\ell} \quad (13)$$

Equations 11 through 13 are the governing equations for the CAB model. The effects of model parameters can be clarified further by transforming these equations into dimensionless forms. Thus, the following dimensionless variables and parameters are defined.

$$\bar{C}_{b,p\ell} = \frac{C_{b,p\ell}R_b}{C^o_{s,p\ell}R_sY_s}, \quad \bar{C}_{o,p\ell} = \frac{C_{o,p\ell}}{C^f_{o,p\ell}}, \quad \bar{C}_{s,p\ell} = \frac{C_{s,p\ell}}{C^o_{s,p\ell}}, \quad \bar{r} = \frac{r}{R},$$

$$\theta = \frac{t}{\theta_r}, \quad \phi_1 = \frac{R}{3}\sqrt{\frac{\mu_m\tau C^o_{s,pl}C^f_{o,p\ell}}{K_sK_oD_{s,p\ell}}}, \quad \phi_2 = \frac{R}{3}\sqrt{\frac{k_d\tau}{D_{s,p\ell}}},$$

$$\beta_o = \frac{C^f_{o,p\ell}}{K_o}, \quad \beta_s = \frac{C^o_{s,p\ell}}{K_s}, \quad R_b = 1 + \frac{\rho K_{db}}{\epsilon_a},$$

$$R_s = 1 + \frac{\rho K_{ds}}{\epsilon_a}, \quad \theta_r = \frac{R^2\tau}{D_{s,p\ell}}, \quad W = \frac{C^o_{s,p\ell}R_sY_s}{C^f_{o,p\ell}Y_o},$$

$$\bar{D}_s = \frac{D_{s,p\ell/\tau} + D_{s,so}(R_s-1)}{D_{s,p\ell/\tau}}, \quad \bar{D}_o = \frac{D_{o,p\ell}}{D_{s,p\ell}}, \quad \bar{D}_b = \frac{D_{b,p\ell}}{D_{s,p\ell}}$$

In these dimensionless expressions, $C^o_{s,p\ell}$ is the initial concentration of substrate in the bed, and $C^f_{o,p\ell}$ is the concentration of oxygen at the exterior of the aggregate. Substitution of the dimensionless variables into Eqs. 11, 12, and 13 yields, respectively,

$$\frac{\partial \bar{C}_{s,p\ell}}{\partial \theta} = \frac{\bar{D}_s}{R_s}\left[\frac{2}{\bar{r}}\frac{\partial \bar{C}_{s,p\ell}}{\partial \bar{r}} + \frac{\partial^2 \bar{C}_{s,p\ell}}{\partial \bar{r}^2}\right]$$

$$- 9\phi_1^2 \bar{C}_{b,p\ell} \left[\frac{\bar{C}_{s,p\ell}}{1+\beta_s \bar{C}_{s,p\ell}}\right]\left[\frac{\bar{C}_{o,p\ell}}{1+\beta_o \bar{C}_{o,p\ell}}\right] \tag{14}$$

$$\frac{\partial \bar{C}_{o,p\ell}}{\partial \theta} = \bar{D}_o\left[\frac{2}{\bar{r}}\frac{\partial \bar{C}_{o,p\ell}}{\partial \bar{r}} + \frac{\partial^2 \bar{C}_{o,p\ell}}{\partial \bar{r}^2}\right]$$

$$- 9\phi_1^2 W \bar{C}_{b,p\ell} \left[\frac{\bar{C}_{s,p\ell}}{1+\beta_s \bar{C}_{s,p\ell}}\right]\left[\frac{\bar{C}_{o,p\ell}}{1+\beta_o \bar{C}_{o,p\ell}}\right] \tag{15}$$

$$\frac{\partial \bar{C}_{b,p\ell}}{\partial \theta} = \frac{\bar{D}_b}{R_b}\left[\frac{2}{\bar{r}}\frac{\partial \bar{C}_{b,p\ell}}{\partial \bar{r}} + \frac{\partial^2 \bar{C}_{b,p\ell}}{\partial \bar{r}^2}\right]$$

$$+ 9\phi_1^2 \bar{C}_{b,p\ell} \left[\frac{\bar{C}_{s,p\ell}}{1+\beta_s \bar{C}_{s,p\ell}}\right]\left[\frac{\bar{C}_{o,pL}}{1+\beta_o \bar{C}_{o,p\ell}}\right] - 9\phi_2^2 \bar{C}_{b,p\ell} \tag{16}$$

The dimensionless numbers, ϕ_1 and ϕ_2, are the *Thiele moduli* for the growth and decay of biomass, respectively; β_o and β_s are the *saturation parameters* for oxygen and substrate, respectively; R_b and R_s are the *retardation factors* for biomass and substrate, respectively; and W is the *oxygen supply factor* (Wu *et al.*, 1990).

RESULTS AND DISCUSSION

The governing equations of the CAB model consist of a system of three coupled nonlinear partial differential equations. These equations have been numerically solved for simulation. Sensitivity analysis has been performed to study the mechanisms involved, and the effects of retardation factor, oxygen supply factor, and Thiele moduli on the total time of remediation, T_r. The initial and boundary conditions used for numerical simulation are as follows:

$$\text{At } \theta = 0,\ \bar{C}_{o,p\ell} = 0.05,\ \bar{C}_{s,p\ell} = 1.00,\ \bar{C}_{b,p\ell} = \bar{C}_b^o,\ \text{for } 0 \le \bar{r} \le 1$$

$$\text{At } \bar{r} = 0,\ \frac{\partial \bar{C}_{i,p\ell}}{\partial \bar{r}} = 0,\quad i = o, s, b,\quad \text{for } \theta \ge 0$$

$$\text{At } \bar{r} = 1,\ \bar{C}_{o,p\ell} = 1.00,\ \bar{C}_{s,p\ell} = 0,\quad \bar{C}_{b,p\ell} = \bar{C}_b^o,\ \text{for } \theta > 0$$

The results of simulation indicate that diffusion of oxygen into the aggregate and the retardation of contaminant transport in the aggregate affect significantly the remediation time in the aggregate. An increase in the aggregate radius, or equivalently, increase in the Thiele modulus transforms the overall remediation process from being reaction controlled to diffusion controlled. A small initial contaminant concentration requires a small oxygen supply factor, thus rendering the overall process to be reaction limited. A large initial contaminant concentration enhances the oxygen requirement. Under this circumstance, the saturation parameter, β_s, is also large, thereby indicating that the reaction is of

zero order with respect to substrate and is controlled by the rate of oxygen diffusion into the aggregate. An increase in the retardation factor decelerates the diffusion of substrate in the aggregate; the oxygen front moving through the aggregate by diffusion is the controlling mechanism for remediation. Furthermore, a low initial concentration of the substrate tends to prolong the time required for reducing the overall concentration of the organic contaminants to the drinking water standards due to low buildup of biomass. All simulations have been carried out till the concentration of adsorbed substrate at the center of the aggregate dropped below 1 ppb. Co-substrates, therefore, may be needed for the growth of biomass and subsequent faster degradation of organic contaminants. The bioremediation times in the aggregate obtained by varying the partition coefficient, radius of aggregate, and initial substrate concentration are listed in Tables 1 and 2, respectively. The values of the remaining parameters for simulation are summarized in Table 3.

CONCLUSIONS

The CAB model has been developed, and bioremediation in soil aggregates has been simulated based on this model. The numerical results demonstrate the influence of some of the limiting factors on the process of bioremediation in contaminated soil. Preliminary evaluations and screening may be performed by resorting to the phenomenological results obtained from this model.

ACKNOWLEDGEMENT

Although the research described in this article has been funded in part by the U.S. Environmental Protection Agency under assistance agreement R-815709 to the Hazardous Substance Research Center for U.S. EPA Regions 7 and 8 with headquarters at Kansas State University, it has not been subjected to the Agency's peer and administrative review and therefore may not necessarily reflect the views of the Agency and no official endorsement should be inferred. This research was partially supported by Kansas State University Center for Hazardous Substance Research.

NOTATION

$C_{i,p\ell}$ = concentration of component i in the pore liquid, M/L^3

$C^{f}_{o,p\ell}$ = concentration of oxygen at the exterior of the aggregate, M/L^3

$\bar{D}_i$ = dimensionless diffusion coefficient of component i

$D_{i,p\ell}$ = diffusion coefficient of component i in the pore liquid, L^2/T

$D_{i,so}$ = surface diffusion coefficient of component i in the solid phase, L^2/T

k_d = reaction rate constant for the decay of biomass, T^{-1}

K_o = saturation constant of oxygen, M/L^3

K_s = saturation constant of substrate, M/L^3

K_{di} = linear partition coefficient for component i, L^3/M

q_i = concentration of component i in the solid phase, M/M

r = radial position in the aggregate, L

R = radius of the aggregate, L

R_i = retardation factor for component i

$r_i^{p\ell}$ = reaction rate in the liquid phase, $M/L^3/T$

r_i^{sf} = reaction rate at the interface, M/M/T
t = time, T
T_r = time of remediation of the aggregate, T
W = oxygen supply factor
Y_o = yield factor of oxygen, M/M
Y_s = yield factor of substrate,M/M

Greek letters

β_i = saturation parameter of component i
ϵ_a = volumetric fraction of the liquid in the aggregate
μ_m = maximum specific growth rate of biomass, T^{-1}
ρ = bulk density of the aggregate particle, M/L^3
θ = dimensionless time
θ_r = characteristic time for diffusion, T
ϕ_1 = Thiele modulus for the growth of biomass
ϕ_2 = Thiele modulus for the decay of biomass
τ = tortuosity of pores in the aggregate

Superscripts and subscripts

i = b,o,s for biomass, oxygen, and substrate, respectively
$p\ell$ = pore liquid
sf = interface
so = solid phase

LITERATURE CITED

Bailey, J.E. and D.F. Ollis, Biochemical Engineering Fundamentals, pp. 373-456, Mcgraw-Hill, New York, 1986.

Boutwell, S.H., S.M. Brown, B.R. Roberts, and D.F. Atwood, Modeling Remedial Actions at Uncontrolled Hazardous Waste Sites, pp. 1-17, Noyes Publications, New Jersey, 1986.

Brusseau, M.L., and P.S.C. Rao, "Sorption Nonideality During Organic Contaminant Transport in Porous Media," Critical Reviews in Environmental Control, **19**(1), 33-99 (1989).

Crittenden, J.C., N.L. Hutzler, D.C. Geyer, J.L. Oravitz, and G. Friedman, "Transport of Organic Compounds with Saturated Groundwater Flow: Model Development and Parameter Sensitivity," Water Resources Research, **22**, 271-284 (1986).

Donigian, A.S. Jr. and P.S.C. Rao, "Overview of Terresterial Processes and Modeling," in *Vadose Zone Modeling of Organic Pollutants*, S.C. Hern and S.M. Melancon, eds., pp. 3-35, Lewis Publishers, Michigan, 1982.

Fong, F.K. and L.A. Mulkey, "Simulation of Solute Transport in Aggregated Media," AICHE J., **35**, 670-672 (1989).

Goltz, M.N. and P.V. Roberts, "Three-Dimensional Solutions for Solute Transport in an Infinite Medium With Mobile and Immobile Zones," Water Resources Research, **22**, 1139-1148 (1986).

Grenney, W.J., C.L. Caupp, R.C. Sims, and T.E. Short, " A Mathematical Model for the Fate of Hazardous Substances in Soil: Model Description and Experimental Results," Hazardous Waste & Hazardous Materials, **3**, 223-237 (1987).

Janssen, L.P.B.M., J. Prins, A.C. Hoffmann, R.J. De Meijer, and A.W.L. Veen, "Modeling the Migration of Contaminants in Soil," Chem. Eng. Comm., **89**, 37-47 (1990).

Kosson, D.S., G.C. Agnihotri, and R.C. Ahlert, "Modeling and Simulation of a Soil-based Microbial Treatment Process," J. of Hazardous Materials, **14**, 191-211 (1987).

Pekdeger, A., "Pathogenic Bacteria and Viruses in the Unsaturated Zone," in *Pollutants in Porous Media The Unsaturated Zone Between Soil Surface and Groundwater*, B. Yaron, G. Dagan, and J. Goldshmid, eds., pp. 195-206, Springer-Verlag, New York, 1984.

Sims, R.C., "Soil Remediation Techniques at Uncontrolled Hazardous Waste Sites A Critical Review," J. of the Air & Waste Management Association, **40**, 704-732 (1990).

Weber, W.J., Jr. and E.H. Smith, "Simulation and Design Models for Adsorption Processes," Environ. Sci. Technol., **21**, 1040-1050 (1987).

Wood, W.P., "Role of Environmental Transport and Fate Models in Implementing the Toxic Substances Control Act," in *Modeling the Fate of Chemicals in the Aquatic Environment*, K.L. Dickson, A.W. Maki, and J. Cairns, Jr., eds., pp. 49-58, Ann Arbor Science, Michigan, 1982.

Wu, J.C., L.T. Fan, and L.E. Erickson, "Modeling and Simulation of Bioremediation of Contaminated Soil," Environmental Progress, **9**(1), 47-56 (1990).

Yeh, G.T., "Modeling the Distribution of Chemicals in Aquatic Environments," in *Modeling the Fate of Chemicals in the Aquatic Environment*, K.L. Dickson, A.W. Maki, and J. Cairns, Jr., eds., pp. 35-48, Ann Arbor Science, Michigan, 1982.

Table 1. Effect of Partition Coefficient and Aggregate Radius on the Time Required for Bioremediation in the Aggregate

Case No.	Initial Substrate Concentration q_s^o, mg/kg	Radius of Aggregate R, cm	Partition Coefficient K_{ds}, cm^3/g	Bioremediation Time T_r, days
1	600	1	1.5	7.3
2	600	1	15	17.4
3	600	1	150	24.7
4	600	1	1500	41.3
5	600	0.1	15	2.2
6	600	10	15	1660.9

Table 2. Effect of Initial Substrate Concentration on the Time Required for Bioremediation in the Aggregate

Case No.	Initial Substrate Concentration q_s^o, mg/kg	Radius of Aggregate R, cm	Partition Coefficient K_{ds}, cm^3/g	Bioremediation Time T_r, days
1	15	1	15	4.0
2	150	1	15	6.5
3	600	1	15	17.4
4	1500	1	15	31.2
5	15000	1	15	83.9

Table 3. Parameter Values for Numerical Simulation

Parameter	Value
$C^{o}_{b,p\ell}$	1.0×10^{-7} g/cm^3
$C^{f}_{0,p\ell}$	8.0×10^{-6} g/cm^3
$D_{b,p\ell}$	1.0×10^{-6} cm^2/s
$D_{o,p\ell}$	2.0×10^{-5} cm^2/s
$D_{s,p\ell}$	4.0×10^{-6} cm^2/s
$D_{s,so}$	0
k_d	2.78×10^{-7} /s
K_o	1.0×10^{-8} g/cm^3
K_s	1.0×10^{-6} g/cm^3
K_{db}	30.0 cm^3/g
Y_o	1.0 g/g
Y_s	0.5 g/g
ϵ_a	0.37
μ_m	2.78×10^{-5} /s
ρ	1.72 g/cm^3
τ	1.4

BIOSPECIFIC ADSORPTION OF GLUCOAMYLASE-I FROM *ASPERGILLUS NIGER* ON RAW STARCH

Bipin K. Dalmia[1] and Zivko L. Nikolov[2]
Departments of Chemical Engineering[1] and
Food Science and Human Nutrition[2]
Iowa State University
Ames, IA 50011

INTRODUCTION

Glucoamylase (1,4-α-D-glucan glucohydrolase, EC 3.2.1.3) is an exo-acting carbohydrase that cleaves glucose units consecutively from the non-reducing end of starch molecules. Glucoamylase is produced naturally by many molds and yeasts [1]. Among the more common sources are *Aspergillus*, *Rhizopus* and *Endomyces* species. Glucoamylase frequently occurs in multiple forms with one form predominantly active in raw starch adsorption and digestion [2, 3, 4, 5]. The *A. niger* glucoamylase is produced in two main forms, glucoamylase I (GA-I) and glucoamylase II (GA-II). Svensson *et al.* [6] have determined the amino acid sequences of the *A. niger* glucoamylase forms and reported that GA-II is identical to residues 1 through 512 of the peptide chain of GA-I, which is 616 residues long. The active sites of both forms are identical in kinetic properties and subsite structure, therefore, the C-terminal 104 amino acids present in GA-I but lacking in GA-II do not affect the functioning of the active site [7]. It has been recently suggested that the 104 C-terminal amino acid residues of GA-I are involved in its binding to raw starch [8] because both GA-I and GA-II have similar activities towards soluble starch but only GA-I (the larger form) can bind and hydrolyze raw (insoluble) starch. Other studies with glucoamylase have also indicated that larger glucoamylase forms possess a specific domain, separate and independent of the active site, that allows reversible binding of the enzyme to raw starch [2, 3, 4, 5, 9, 10, 11, 12]. Previous studies on glucoamylase adsorption to raw starch have focussed on the differential binding of various forms and relatively little information is available on the parameters that affect the enzyme adsorption to starch.

In this study, starch adsorption properties of *A. niger* GA-I and GA-II were investigated as a function of pH, ionic strength, temperature, and enzyme concentration of the reaction mixture. Preliminary elution studies were also conducted using various substrates and buffers. A mathematical model describing the mechanism of GA-I and GA-II binding onto raw starch is proposed.

EQUILIBRIUM MODELS FOR ADSORPTION OF PROTEINS

Single Class of Binding Sites

The Langmuir model, originally devised for gas adsorption, is based on the assumption of hard, non-deformable spheres adsorbing at identical, independent and fixed sites on a homogeneous surface without lateral interactions between the adsorbing molecules [13]. It further

assumes that at most monolayer coverage could occur, that the adsorption is completely reversible and that the heat of sorption is constant with coverage [13, 14, 15].

The Langmuir model describing the equilibrium adsorption of proteins is given as

$$Q^* = \frac{Q_{max} K_a C^*}{1 + K_a C^*} \tag{1}$$

where,

Q^*	=	solid phase concentration of protein at equilibrium
Q_{max}	=	maximum adsorption capacity of the adsorbent
K_a	=	association constant
C^*	=	equilibrium protein concentration in bulk solution

The Langmuir model is hardly a realistic model for protein adsorption; for most systems the basic assumptions are not fulfilled and the equilibrium isotherm deviates to a greater or lesser extent from the ideal form [13, 15]. The ideal Langmuir model gives an approximate representation of the system behavior at low concentrations but breaks down in the saturation region where the effects of molecular interactions become more pronounced. Deviations can occur if any one or more of the postulates are not obeyed but in most cases they occur due to heterogeneity of sites or interaction between adsorbed protein molecules or both [15].

Takahashi *et al.* [5] assumed that the Langmuir model represents *Rhizopus* sp. $Gluc_1$ binding to starch and estimated the association constant to be $1.2 \times 10^5 M^{-1}$ at pH 5.0 and 4°C. Kyriacou and Neufeld [16] also used the Langmuir model to describe binding of fractionated *Trichoderma reesei* cellulase components to purified wood cellulose and obtained a good fit between the equilibrium adsorption data and the model.

Multiple Classes of Binding Sites

The deviation from ideal Langmuirian behavior is often determined by plotting a linearized form of Equation 1 as

$$\frac{Q^*}{C^*} = Q_{max} K_a - K_a Q^* \tag{2}$$

This plot of the ratio of the solid phase and the free protein concentration *versus* the solid phase concentration is usually referred to as the Scatchard plot [17]. For a single set of identical and independent binding sites the Scatchard plot is a straight line whose slope gives the K_a value and the intercept on the abscissa the Q_{max} value. However, very often the Scatchard plot is not a straight line but is curved upwards. This deviation is ascribed to the existence of multiple classes of independent binding sites and/or negative cooperativity [18]. Negative cooperativity is defined as the interference of an adsorbed molecule in the binding of another molecule at a nearby site.

When m classes of independent sites are present on the adsorbent surface, the total protein bound is equal to the sum of the amount bound for each class of sites [15, 19]

$$Q^*_{total} = \sum_{i=1}^{m} Q^*_i = \sum_{i=1}^{m} \frac{Q_{maxi} K_{ai} C^*}{1 + K_{ai} C^*} \tag{3}$$

For two sets of independent sites ($m = 2$) Equation 3 reduces to

$$Q^*_{total} = \frac{Q_{max1} K_{a1} C^*}{1 + K_{a1} C^*} + \frac{Q_{max2} K_{a2} C^*}{1 + K_{a2} C^*} \tag{4}$$

The same mathematical form as given in Equation 4 describes binding to a single class of independent sites with negative cooperativity. Therefore, from binding data alone it is not possible to distinguish between the two models, one in which deviations from ideal Langmuir behavior are attributed to protein–protein interactions and the other in which the deviations are ascribed to energetic heterogeneity of binding sites [15]. The two–site model has been frequently applied in modelling heterogeneous protein–ligand interactions, e.g., fusicoccin binding on plasmalemma–enriched membranes of maize coleoptiles [20], binding of testosterone to late–pregnancy plasma proteins [21], caprylic acid and tolbutamide binding with serum albumin [22], vitamin–receptor binding [23], and binding of amphetamine in rat brain [24]. Bremner and Chase [25] used a three–site model to explain antigen–antibody binding. Starch surface is known to be heterogeneous and the presence of multiple classes of binding sites is highly likely.

For $K_{a2} C^* \ll 1$, the two site model reduces to

$$Q^*_{total} = \frac{Q_{max1} K_{a1} C^*}{1 + K_{a1} C^*} + Q_{max2} K_{a2} C^* \tag{5}$$

This is a special case of Equation 4 when one class of sites has low affinity for the adsorbate, i.e., a small K_a value. Anderson and Walters [26] applied this model to describe the binding of various sugars on immobilized concanavalin A. They assumed two sets of binding sites: one with high affinity for sugar molecules and another with low specificity and weak binding energy. Equation 5 predicts a linear increase in the amount bound at high sugar concentrations, as was observed by Anderson and Walters, and was used to fit their experimental data, resulting in excellent agreement between the curve fit and the data points.

MATERIALS AND METHODS

Analytical Techniques

GA-I and GA-II were purified from a commercial glucoamylase preparation (Takamine Diazyme 160, Miles Laboratories, Clifton, NJ) by ion-exchange chromatography on DEAE-Toyopearl 650S column using a linear salt gradient [27]. Lowry protein assay [28] was used for determining protein concentration with bovine serum albumin as a standard. Vertical 7.5% SDS-PAGE gels were run as described by Hames [29]. Coomassie Brilliant Blue G-250 and/or silver staining were used to verify the purity of the enzyme preparations.

Adsorption Equilibrium

Equilibrium adsorption data were obtained as follows. Raw starch aliquots of 0.2 g were washed twice with 0.05 M acetate buffer of the appropriate pH and NaCl concentration. Three mL of enzyme solution of various concentrations were added to each tube containing 0.2 g of washed starch and the suspension was shaken at 250 rpm for 1 h. The starch was separated by centrifugation and the supernatant assayed for free protein and glucose

content. The protein concentration in the supernatant gave the equilibrium bulk protein concentration and the difference in the initial and the supernatant concentrations gave the amount of protein bound on starch. NaCl was present in the buffer only when the effect of ionic strength was studied. NaCl was always included in the washing buffer at the same concentration as in the binding experiments.

Enzyme Elution

Elution of the adsorbed protein from starch was achieved by first washing the starch pellet twice with 3 mL of 0.05 *M* acetate buffer of pH 4.5 for 15 min to remove all loosely bound protein. Then, after centrifugation, 3 mL of eluant were added to the starch pellet and the mixture was shaken for 15 min followed by centrifugation. The supernatant was assayed for eluted protein. Various ligands (glucose, maltose, acarbose, maltodextrin, and soluble starch) were used to desorb GA-I. Glucose, maltose, and corn starch were purchased from Sigma. A maltodextrin sample of DE 5 (Star-Dri 5) was donated by A. E. Staley (Decatur, IL). Acarbose was obtained from Dr. P. J. Reilly of Iowa State University. All procedures were performed at 4°C unless otherwise specified.

RESULTS AND DISCUSSION

Proposed Model

GA-II adsorption isotherms at various binding conditions (pH and ionic strength) were all of similar shape. They were best represented by a linear isotherm and will be shown in the next two sections.

The adsorption of GA-I was more difficult to model since the shape of the experimental binding isotherm did not resemble any of the five types of adsorption isotherms [15]. The Scatchard plot of GA-I equilibrium binding data curved upwards, suggesting presence of heterogeneous binding sites on the starch surface [17, 30]. Heterogeneous sites rather than negative cooperativity was assumed because of the heterogeneous structure of the starch granule, which consists of amorphous and crystalline phases [31]. The two-site model given by Equation 4 was applied to our system, assuming two classes of independent binding sites on the starch surface. The four parameters K_{a1}, K_{a2}, Q_{max1} and Q_{max2} were determined by curve fitting of GA-I experimental data using a nonlinear least squares Marquardt regression fit (PROC NLIN, SAS Institute Inc.). The standard deviations (errors) for K_{a1} and K_{a2} were very high (±100–200%), suggesting a poor fit. The two-site model (Equation 4) also predicts that the adsorption isotherm would level off at saturation ($Q_{max1} + Q_{max2}$) after both sets of sites are fully occupied by GA-I. The experimental binding isotherm of GA-I even at high initial concentrations did not level off, reaching a very high binding level of over 10 mg/g of starch (data not shown).

Since this model failed to explain the linear increase of the enzyme bound to the starch surface at high concentrations, we tested and subsequently used the three-parameter model (Equation 5) to estimate the adsorption constants. The model is rewritten as

$$Q^* = \frac{Q_{max} K_a C^*}{1 + K_a C^*} + KC^* \tag{6}$$

The definitions of K_a and Q_{max} correspond to those of K_{a1} and Q_{max1}, respectively,

with the same physical meaning. The third constant (K) is used in the model to lump the effects of various not-so-well defined protein-protein and/or protein-starch interactions such as lateral and vertical protein-protein interactions in the adsorbed layer as well as binding of the protein on the edges, cracks, and depressions of the starch granule.

Because of the difference of adsorption models, affinities of GA-I and GA-II for starch binding sites were compared using initial slopes of equilibrium adsorption isotherms. In general, the initial slope of an adsorption isotherm is a measure of the affinity of the adsorbate for the adsorbent and could be considered as a Henry's law constant. Initial slopes (α) of the adsorption isotherms of GA-I were obtained by differentiating Equation 6 with respect to C^* and setting $C^* = 0$. Thus

$$\alpha = \left.\frac{dQ^*}{dC^*}\right|_{C^*=0} = K_a Q_{max} + K \tag{7}$$

The constant used to characterize GA-II binding is the slope of the adsorption isotherm (α), defined as

$$\alpha = \frac{Q^*}{C^*} \tag{8}$$

There were two main reasons for adapting the three–parameter equation to model the binding of GA-I on raw starch. First, washing of the starch granule with buffer (after GA-I adsorption) revealed that the amount of loosely bound protein desorbed from starch increased linearly with protein concentration (data not shown). The tightly bound protein calculated as a difference between the total bound and the loosely bound GA-I when plotted against equilibrium protein concentration gave an adsorption curve of Langmuirian type. Therefore, the total bound GA-I could be described with a composite adsorption isotherm by combining the Langmuir term for the tightly bound protein and the linear term for the loosely bound protein. Such a composite isotherm has been used before in liquid chromatography systems to model the binding of ethyl acetate on silica gel, where it was concluded that the linear increase was due to the formation of a bilayer [32]. Secondly, the proposed model accounts for the linear increase in bound protein observed at high protein concentrations. The linear and the three–parameter models fitted the data for GA-II and GA-I very well, respectively, and adsorption constants were calculated for various experimental conditions.

Effect of pH

The effect of pH on adsorption of GA-I and GA-II to raw starch is illustrated in Figure 1. The highest solid phase concentrations of GA-I at various protein concentrations were measured at pH 3.5, the isoelectric point of the enzyme [7]. As the pH of the starch–enzyme mixture was increased the GA-I adsorption to starch decreased progressively. Such behavior of a binding maximum near the isoelectric point has been observed before with other proteins at solid–liquid interfaces [33].

When binding of GA-II was studied in the same pH range, no significant difference in the amount bound were observed, although GA-II has a similar pI value as GA-I (pI=3.6) [7]. The shape of the GA-I isotherms changed with pH, indicating that adsorption constants were also affected. The effect of pH on the apparent adsorption constants was determined by fitting the three–parameter model (Equation 6) to GA-I adsorption data and a linear

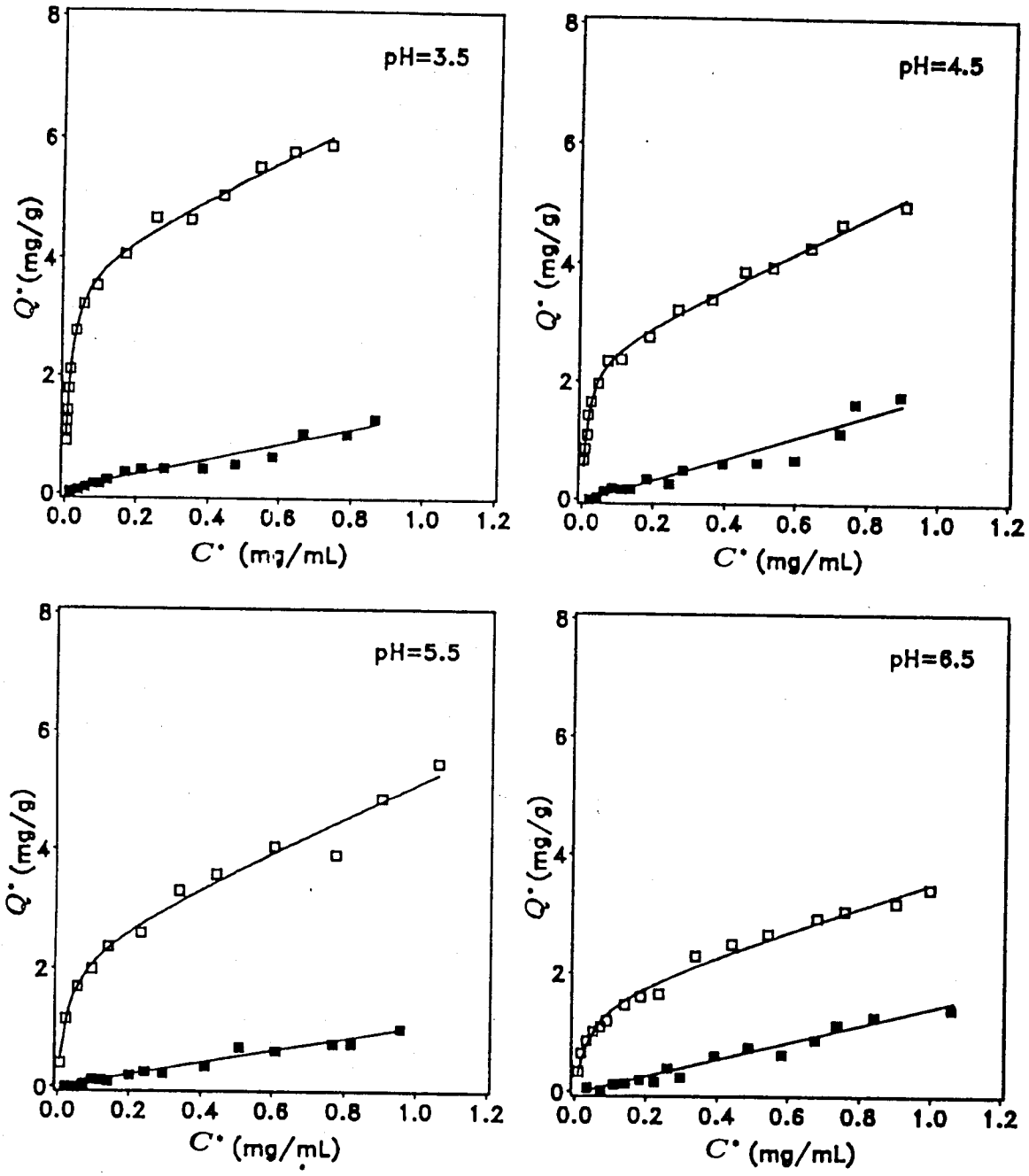

Figure 1: Effect of pH on binding of GA-I (□) and GA-II (■) at 4°C. (Solid lines are model fits)

regression to GA-II adsorption data. The resulting adsorption constants and initial slopes are presented in Tables 1 and 2. The apparent association constant (K_a) for GA-I reached a maximum at pH 4.5 and the lowest value of K_a was obtained at pH 6.5. The maximum binding capacity (Q_{max}) for GA-I decreased monotonically in the direction away from the isoelectric point, reaching a minimum value at pH 6.5. The K values, describing the 'loosely' bound GA-I, showed no consistent trend with pH.

Table 1: Effect of pH on apparent adsorption constants for GA-I

pH	$K_a(\times 10^6)$ (M^{-1})	K (mL/g)	Q_{max} (mg/g)
3.5	3.9±0.55[a]	2.6±0.46	4.3±0.23
4.5	5.4±0.61	2.9±0.14	2.5±0.09
5.5	2.7±1.05	2.8±0.33	2.4±0.27
6.5	2.0±0.55	2.0±0.19	1.6±0.16

[a]Standard error.

The effect of pH on GA-I adsorption is very typical of proteins binding on solid surfaces. The amount of adsorbed GA-I reached a maximum at the isoelectric point (pI) of the enzyme and reduced as pH was moved further from the pI (Figure 1 and Table 1). Such behavior of a binding maximum at the isoelectric point has been observed before with other proteins [33]. This indicates that charge repulsion is a dominant factor. Since at the isoelectric point the intramolecular electrostatic repulsions are at a minimum, the enzyme molecules are more compact and also repulsions between adsorbed molecules is reduced, allowing them to assemble more closely on the starch surface [33]. Both these effects contribute to accommodate more protein on the surface at the isoelectric point.

Table 2: Effect of pH on initial slopes (α) of adsorption isotherms

	α (mL/g starch)		
pH	GA-I	GA-II	BSA
3.5	214	1.28±0.09[a]	-
4.5	170	1.82±0.15	1.06±0.14
5.5	82	1.03±0.05	1.60±0.23
6.5	43	1.47±0.08	0.65±0.08

[a]Standard error.

The overall affinity of GA-I for starch dropped almost five times from pH 3.5 to 6.5 (Table 2). On the other hand, GA-II isotherm initial slopes did not change between pH 3.5 and 6.5 and were about 200 to 50 times lower than those for GA-I, depending on the pH. These much higher initial slope values for GA-I indicate a higher affinity of GA-I for the starch surface than GA-II. The initial slopes of bovine serum albumin (BSA) isotherms were determined by a linear regression analysis based on four experimental points.

GA-II binding, as noted above, is unaffected by pH and the bound protein levels are the same as those of bovine serum albumin (BSA) binding on raw starch, which too binds independently of pH. A possible explanation is that the solid–phase concentrations of both GA-II and BSA are pretty low, and hence the enzyme molecules are spaced sparsely on the surface so that electrostatic repulsion does not play a role. The apparently similar behavior of two completely unrelated proteins, GA-II and BSA, on starch, indicates that their binding is not specific but is a result of some non-specific interactions. This is also indicated by the low α values for GA-II and BSA given in Table 2.

Effect of Ionic Strength

The effect of ionic strength on the binding of GA-I and GA-II to raw starch at pH 6.5 is shown in Figure 2. Because the lowest adsorption capacity of GA-I was observed at pH 6.5, presumably due to electrostatic repulsions, this particular pH was chosen to make the effect of ionic strength on the binding capacities easily detectable. As expected, the binding capacity at various protein concentrations increased with increasing ionic strength and at an ionic strength of 0.35 M reached the same level as those observed at pH 3.5 and an ionic strength of 0.05 M (see Figure 1). GA-II binding, however, was not affected by increasing the ionic strength from 0.05 M to 0.35 M. As before, the effect of ionic strength on the apparent adsorption constants was determined by fitting GA-I and GA-II adsorption data to the respective models. The apparent adsorption constants were estimated as before and are shown in Table 3. The apparent association constant, K_a, was not affected by ionic strength while the Q_{max} value increased with ionic strength, reflecting that the enzyme molecules bound more closely by virtue of higher salt concentration reducing the electrostatic repulsions between them. The K value, again, did not change significantly with ionic strength as with pH and neither did the initial slopes of GA-II isotherms.

Table 3: Effect of ionic strength on apparent adsorption constants for GA-I

pH	I (M)	$K_a(\times 10^6)$ (M^{-1})	K (mL/g)	Q_{max} (mg/g)
3.5	0.05	3.9±0.55[a]	2.6±0.46	4.3±0.43
3.5	0.35	6.4±1.24	6.5±0.52	3.5±0.23
6.5	0.05	2.0±0.55	2.0±0.19	1.6±0.16
6.5	0.15	1.9±0.73	2.2±0.56	2.8±0.42
6.5	0.35	2.0±0.40	3.1±0.52	4.4±0.38

[a]Standard error.

Table 4 lists the numerical values of the initial slopes. At pH 3.5, increasing the ionic strength from 0.05 M to 0.35 M changed minimally the Q_{max} value, indicating that electrostatic repulsion did not play a role in the binding at pH 3.5, the isoelectric point of GA-I. The slopes did not change significantly for GA-II but increased for GA-I, reflecting the increase in the Q_{max} value with ionic strength.

Increasing the concentration of NaCl, in view of the charge shielding effect of salt, de-

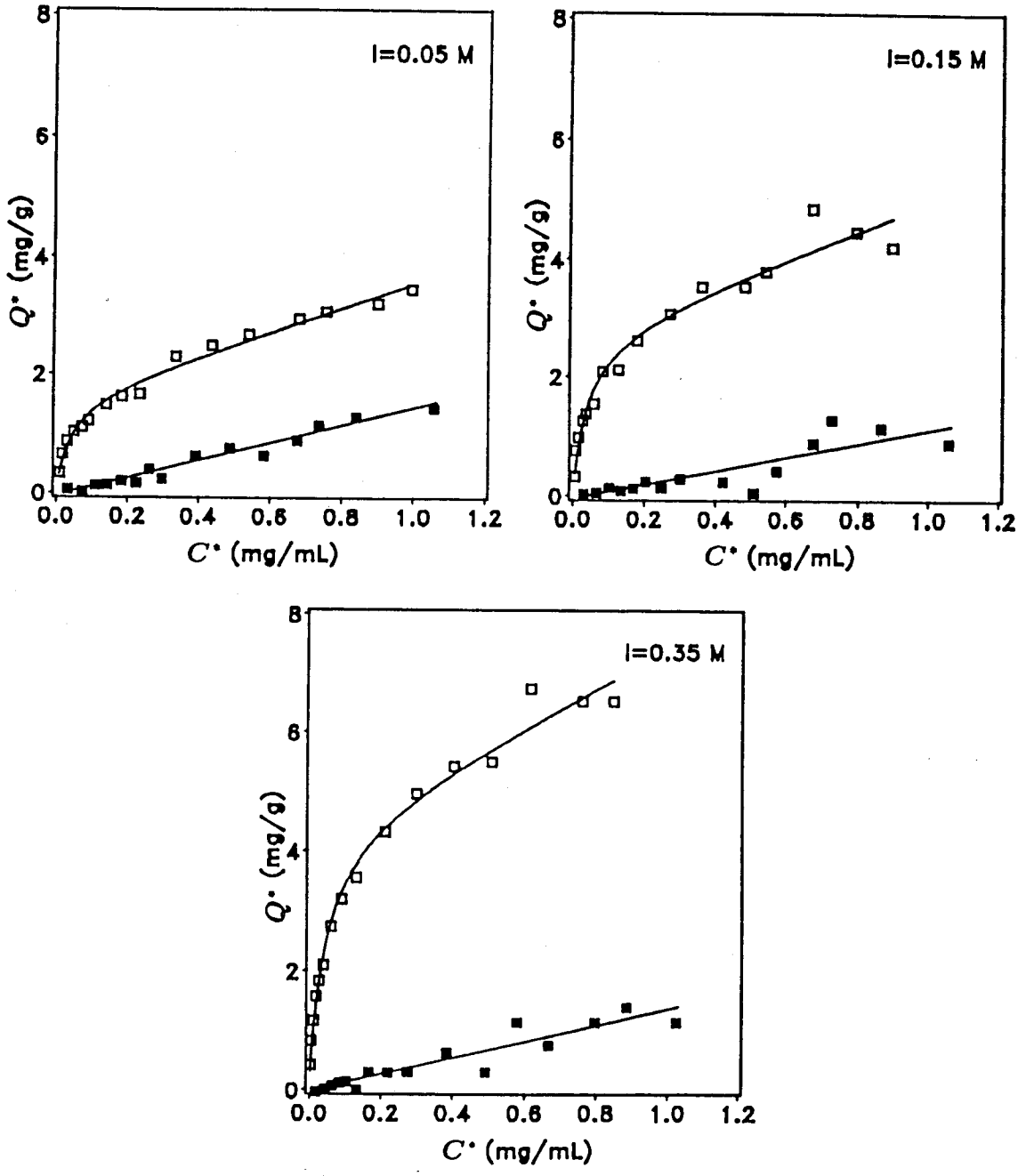

Figure 2: Effect of ionic strength on binding of GA-I (□) and GA-II (■) at pH 6.5 and 4°C. (Solid lines are model fits)

Table 4: Effect of ionic strength on initial slopes (α) of adsorption isotherms

		α (mL/g starch)	
pH	I (M)	GA-I	GA-II
3.5	0.05	214	1.28±0.09[a]
3.5	0.35	280	-
6.5	0.05	43	1.47±0.08
6.5	0.15	70	1.14±0.20
6.5	0.35	113	1.37±0.14

[a]Standard error.

creases the size of the 'double layer' surrounding the enzyme molecule [34]. The reduction in the thickness of the 'double layer' diffuses the charge repulsions between molecules in solution as well as on the starch surface, allowing them to come more closer and consequently increasing the level of binding. This explains the increase in binding observed at high ionic strengths at pH 6.5 and no significant change in binding at pH 3.5 (the pI of GA-I) at high ionic strength. At pH 3.5 the intermolecular repulsions are already at a minimum by virtue of the zero net charge on the enzyme molecule. GA-II binding was not affected by increasing the ionic strength, because GA-II surface concentrations are low and the enzyme molecules are probably spaced sparsely on the starch surface. Therefore, a reduction of intermolecular repulsion is inconsequential.

Effect of Temperature

The effect of temperature was not studied in detail due to excessive hydrolysis of the raw starch by the enzyme during binding at temperatures above 4°C. The adsorption of GA-I on raw starch at two different temperatures, 4°C and 20°C, was studied at pH 4.5 and 6.5 with and without acarbose, respectively. At pH 6.5 glucoamylase activity is reduced by 50% [35] and excessive degradation of the starch granule can be avoided. In the presence of 109 mol acarbose/mol GA-I the activity of GA-I is almost completely suppressed [36]. Estimated adsorption constants are given in Table 5.

Table 5: Effect of temperature on apparent adsorption constants for GA-I

Temp. (°C)	pH	$K_a(\times 10^6)$ (M^{-1})	K (mL/g)	Q_{max} (mg/g)
4	4.5	1.7±0.40[a]	1.9±0.22	2.0±0.18
20	4.5	1.0±0.66	1.1±0.81	2.4±0.76
4	6.5	2.0±0.55	2.0±0.19	1.6±0.16
20	6.5	1.0±0.70	1.4±0.39	1.6±0.48

[a]Standard error.

The K_a and K values were affected the most by the temperature increase while Q_{max} did not change significantly. In both cases, K_a decreased about 50% while the second adsorption constant, K, was reduced 30% at pH 6.5 and almost 50% at pH 4.5 in the presence of acarbose. The decrease of the association constant of GA-I at both pH 4.5 and pH 6.5 should be expected because higher thermal energy breaks more H-bonds, thereby reducing the net affinity of the molecule for the starch surface.

Elution

Since the binding of GA-I to starch was inhibited by soluble starch and a maltodextrin with an average degree of polymerization of 20 glucosyl residues (Star-Dri 5) (data not shown), it seemed that they would also be effective in eluting bound GA-I from starch. GA-I was bound to raw starch at pH 4.5 and 4°C and then the starch was washed twice to remove loosely bound protein. Various displacement ligands were used to desorb the specifically bound GA-I from starch. Acetate buffer solutions of 2% and 4% soluble starch and of 5% and 10% Star-Dri 5 at pH 4.5 were equally effective in completely eluting the bound GA-I. A 2% maltose solution prepared similarly eluted about 90% of the bound GA-I. An eluant containing 2% glucose, also prepared in the same buffer, eluted only about 27%, while 0.1% acarbose solution eluted about 50% of the bound GA-I. In general, the larger the substrate the more effective it was in desorbing the bound enzyme from its raw starch complex. The successful and complete elution of adsorbed GA-I with starch–like ligand is an evidence of the biospecific nature of its interaction with raw starch.

References

[1] Saha, B. C. and Zeikus, J. G. *Starch/Stärke* 1989, **41**, 57.

[2] Hayashida, S., Kunisaki, S., Nakao, M. and Flor, P. Q. *Agric. Biol. Chem.* 1982, **46**, 83.

[3] Ueda, S. and Saha, B. C. *Enzyme Microb. Technol.* 1982, **5**, 196.

[4] Tanaka, Y., Ashikari, T., Nakamura, N., Kiuchi, N., Shibano, Y., Amachi, T. and Yoshizumi, H. *Agric. Biol. Chem.* 1986, **50**, 1737.

[5] Takahashi, T., Kato, K., Ikegami, Y. and Irie, M. *J. Biochem.* 1985, **98**, 663.

[6] Svensson, B., Larsen, K. and Svendsen, I. *Carlsberg Res. Commun.* 1983, **48**, 529.

[7] Meagher, M. M., Nikolov, Z. L. and Reilly, P. J. *Biotechnol. Bioeng.* 1988, **34**, 681.

[8] Svensson, B., Jespersen, H., Sierks, M. R. and MacGregor, E. A. *Biochem. J.* 1989, **264**, 309.

[9] Medda, S., Saha, B. C. and Ueda, S. *J. Ferment. Technol.* 1982, **60**, 261.

[10] Saha, B. C. and Ueda, S. *J. Ferment. Technol.* 1983, **61**, 67.

[11] Hayashida, S., Nakahara, K., Kuroda, K., Miyata, T. and Iwanaga, S. *Biol. Chem.* 1989, **53**, 135.

[12] Hayashida, S., Nakahara, K., Kanlayakrit, W., Hara, T. and Teramoto, Y. *Agric. Biol. Chem.* 1989, **53**, 143.

[13] Brash, J. L. and Horbett, T. A. in *Proteins at Interfaces* (Brash, J. L. and Horbett, T. A., eds.), ACS Symp. Series **343**, 1986, pp. 1–33.

[14] Liapis, A. I. *J. Biotechnol.* 1989, **11**, 143.

[15] Ruthven, D. M. *Principles of Adsorption and Adsorption Processes*, John Wiley and Sons, New York, 1984, pp. 86–91.

[16] Kyriacou, A. and Neufeld, R. J. *Enzyme Microb. Technol.* 1988, **10**, 675.

[17] Scatchard, G. *Ann. N. Y. Acad. Sci.* 1951, **51**, 660.

[18] Norby, J. G., Ottolenghi, P. and Jensen, J. *Anal. Biochem.* 1980, **102**, 318.

[19] Glasel, J. A. and McKelvy, J. F. *J. Biol. Chem.* 1976, **251**, 2929.

[20] Aducci, P., Coletta, M. and Marra, M. *Plant Sci. Lett.* 1984, **33**, 187.

[21] Weder, H. G., Schildknecht, J., Lutz, R. A. and Kesselring, P. *Eur. J. Biochem.* 1974, **42**, 475.

[22] Yamamoto, M., Aki, H. and Wakabayashi, T. *Yakugaku Zasshi* 1981, **101**, 443.

[23] Shultz, T. D., Bollman, S. L. and Kumar, R. *Proc. Workshop Vitam. D, 5th(Vitam. D: Chem., Biochem. Clin. Endocrinol. Calcium Metab.)* 1982, 105.

[24] Light, K. E. *Science* 1984, **223**, 76.

[25] Bremner, W. S. and Chase, G. D. *Ligand Q.* 1980, **3**, 21.

[26] Anderson, D. J. and Walters, R. R. *J. Chromatogr.* 1986, **376**, 69.

[27] Dalmia, B. K., M. S. Thesis 1990, Iowa State University, Ames, Iowa.

[28] Lowry, O. H., Rosebrough, N. J., Farr, A. L. and Randall, R. J. *J. Biol. Chem.* 1951, **193**, 265.

[29] Hames, B. D. in *Gel Electrophoresis of Proteins: A Practical Approach* (Hames, B. D. and Rickwood, D., eds.), IRL Press Limited, Washington, DC, 1981, pp. 23–49.

[30] Edsall, J. T. and Gutfreund, H. *Biothermodynamics*, John Wiley & Sons, New York, 1983, pp. 161–165.

[31] French, D. in *Starch: Chemistry and Technology* (Whistler, R. L., BeMiller, J. N. and Paschall, E. F., eds.), 2nd ed., Academic Press, Inc., Orlando, 1984, pp. 184–247.

[32] Scott, R. in *HPLC* (Brown, P. R. and Hartwick, R. A., eds.), John Wiley & Sons, New York, 1989, p. 132.

[33] Andrade, J. D. in *Surface and Interfacial Aspects of Biomedical Polymers* (Andrade, J. D., ed.), Plenum Press, New York, 1985, pp. 1–80.

[34] Hughes, M. A. in *Solid-Liquid Separations* (Svarovsky, L., ed.), 2nd ed., Butterworths, London, 1981, pp. 68–71.

[35] Lineback, D. R., Russell, I. J. and Rasmussen, C. *Arch. Biochem. Biophys.* 1969, **134**, 539.

[36] Nikolov, Z. L., Ph. D. Dissertation 1986, Iowa State University, Ames, Iowa.

OVEREXPRESSION IN RECOMBINANT MAMMALIAN CELLS: EFFECT ON GROWTH RATE AND GENETIC INSTABILITY

Jeffrey A. Kern and Dhinakar S. Kompala
Department of Chemical Engineering
University of Colorado
Boulder, Colorado 80309-0424

July 2, 1990

Abstract

Overexpression of foreign protein is obtained in recombinant Chinese hamster ovary cells through dihydrofolate reductase(*dhfr*) gene amplification. In the absence of selective pressure, the amplified genes may be unstable and loss in productivity of the foreign protein will result. Several amplified cell lines were examined for stability of the *dhfr* genes after removal of selective pressure.Through flow cytometric measurements of dihydrofolate reductase it appears that the cells lost *dhfr* copy number at an exponential rate. An examination of cell growth rates showed that cells which had lost *dhfr* copy number had an increased growth rate. The relationship between cell growth rate and rate of loss of *dhfr* is discussed.

1 Introduction

Recombinant mammalian cells are being widely used for the production of complex therapeutic proteins. These proteins require post-translational modifications such as glycosylation or proteolytic processing to attain full biological activity. This processing is not performed by bacterial cells.

A common technique to obtain very high expression levels of recombinant proteins is through the use of dihydrofolate reductase (*dhfr*)[1] gene amplification. In this technique Chinese Hamster Ovary(CHO) cells deficient in *dhfr* are transfected with an expression vector carrying a selectable *dhfr* cDNA and a nonselectable expression cassette containing the desired gene. The cells are grown in the presence of methotrexate, a folate analog which is a

[1]**Abbreviations: β-IFN, beta interferon; CHO, Chinese hamster ovary; DHFR, dihydrofolate reductase; *dhfr*, dihydrofolate reductase gene; FBS, fetal bovine serum; HSRs, homogeneous staining regions; MeT, metallothionein; MTX, methotrexate; MTX-F, fluorescein methotrexate.**

direct inhibitor of dihydrofolate reductase. Only those cells which have an increased copy number of *dhfr* are able to survive. Stepwise increases in methotrexate concentration leads to very high amplification of the *dhfr*. Units of DNA amplified are much larger than just the *dhfr* thus the desired gene is co-amplified along with the *dhfr*. This amplification procedure has been reported to lead to as much as a 1000-fold increase in gene copy number and expression[1].

Amplified genes have been found to exist in two forms. Amplified units can exist in small acentromeric chromosomes called "double minutes". Double minutes are highly unstable and are lost rapidly in the absence of selective pressure. More stably amplified genes exist in tandem in long segments of chromosomes known as homogeneously staining regions(HSRs). CHO cells tend to form amplified units primarily as HSRs[1]. Weidle *et al.*[7] demonstrated for three amplified CHO cell lines that HSR regions are gradually lost in absence of selective pressure. The mechanisms for gene amplification and genetic instability which lead to loss of foreign gene copy number is not well understood.

One factor which may contribute to the loss of productivity is the effect of expression level of foreign protein on cell growth rate. From previous results obtained with bacterial cells, we propose that cells which produce a lower level of foreign protein have a lesser metabolic burden and thus are able to grow faster. These lower producing cells would thus overtake the higher producing, slower growing cells in a bioreactor. Bentley and Kompala[3] developed a structured kinetic model which could predict the effect of foreign protein expression on bacterial cell growth rates. We intend to examine the possibility of applying a similar modeling approach to recombinant mammalian cell cultures. A goal of this modeling is the development of optimal induction strategies to minimize loss of productivity in recombinant mammalian cell cultures. As an initial step towards this goal, we have quantified the rate at which amplified cells lose their productivity and have begun to relate this to cell growth rate.

2 Materials and Methods

2.1 Cell Lines and Culture

The Chinese hamster ovary(CHO) cell lines used in the experiments were kindly given to us by Dr.Martin Page at Wellcome Biotechnology Limited (United Kingdom). The five cell lines which were received are M1-7, M1-62, M1-65, M1-52, and M1-59.

The M1 cells are CHO which were transfected with the expression plasmid pSVdMIF shown in figure 1 [2]. The two gene components which are of importance here are the gene coding for human β-interferon(β-IFN) and the *dhfr* gene. The expression of the human β-IFN cDNA is under the control of the inducible human metallothionein (MeT) II_A promoter [6]. This promoter causes the expression of β-IFN to be induced by the addition of heavy metals such as cadmium or zinc. The *dhfr* cDNA allows for the selection of cells containing the expression vector and also for amplification in the presence of methotrexate. The linkage of the expression cassette β-IFN and the selection cassette *dhfr* on the same plasmid should

ensure co-amplification of these two components. Cell line M1-7 had been amplified to a level of 10^{-7} M MTX, M1-62 and M1-65 to 10^{-6} M MTX, and M1-52 and M1-59 to 10^{-5} M MTX. Table 1 shows levels of β-IFN produced by the M1 cell lines with and without induction with 1 μM cadmium[2].

The M1 cell lines were maintained in Iscove's Modified Dulbecco's Medium (IMDM) obtained from GIBCO (PN 430-2200) supplemented with 10% fetal bovine serum (FBS), 100 U/ml penicillin, 100 μg/ml streptomycin, and the above mentioned concentrations of methotrexate. The CHO cells, which are anchorage dependant, were grown in polystyrene tissue culture flasks. When the cells reached confluency they were detached by trypsinization, counted with a hemocytometer, and passed to a fresh tissue culture flask at a seeding density of 12,000 cells/cm^2. From the cell count the number of cell doublings since the previous passage was calculated. Every two or three days the cells were either passaged or the old media was removed and fresh media was added. Healthy growing cells required passage every 4 or 5 days.

2.2 MTX-F Labeling and Flow Cytometry

In flow cytometric analysis cells are directed single file in a stream which intersects a laser beam. As cells flow through the laser they scatter light in all directions and emit fluorescence from fluorescent probes which label specific cellular components. The amount of light emitted at various wavelengths is then measured electronically and the results are displayed in the form of histograms which show the distribution of fluorescence in the cell population.

Using fluorescein-conjugated methotrexate (MTX-F) to label DHFR, the flow cytometer was used to measure the level of DHFR in individual cells. The cells were incubated with 30 μM of MTX-F for 24 hours and were prepared for flow cytometric analysis as described by Kaufman *et al*[4]. Cells were analyzed by using a Coulter model Epics 541 flow cytometer with laser power set at 1000 mW and photomultiplier voltage at 425 volts. Fluorescent beads were used to check the alignment and calibrate the flow cytometer. When cells are analyzed with forward angle and 90° light scatter the viable population of cells can be distinguished from the non-viable cells. Using this distinction, the non-viable population was gated out electronically so that only viable cells were analyzed. The MTX-F labeled DHFR emits green light which is then measured and displayed as a histogram showing the distribution of fluorescence in the cell population.

3 Results

It was assumed that there was a direct correlation between the fluorescein units per cell, the level of DHFR enzyme, and the copy number of the amplified *dhfr* gene. These correlations were shown to exist by Kaufman *et al.*[4, 5]. They showed that there was a linear correlation between mean fluorescence per cell and DHFR specific activity. They also found a direct correlation of DHFR enzyme content to *dhfr* gene copy number, as measured using DNA

hybridization methods.

Cell lines M1-65 and M1-59 were examined for stability in the absence of selective pressure. The cells were grown with and without methotrexate and examined every two weeks with the flow cytometer to measure the DHFR level. The fluorescence distributions for the M1-65 and M1-59 cells are shown in figure 2. Each histogram represents the results from an analysis of 25,000 cells. Figure 2A and 2E are the fluorescence distributions of M1-65 and M1-59 respectively before removal of MTX. Figures 2B, C, and D, and 2F, G, and H show the fluorescence distributions for M1-65 and M1-59 at 17, 32, and 45 days after removal of selective pressure. As the cells lose *dhfr* copies the cell population on the histogram moves to the left. The increased fluorescence shown for M1-59 after 17 days is unexpected and may be due to some unknown phenomenon or merely experimental error. Re-analysis of M1-59 cells continually maintained in 10^{-5} M MTX for 4 weeks showed that they remained stable at the same mean fluorescence as obtained from the fluorescence distribution shown in figure 2E. The mean fluorescence of the MTX^+ M1-59 cells was actually lower than the MTX^+ M1-65 cells but when compared to the level of uninduced β-interferon expression shown in Table 1, this is not unexpected.

A further amplification step was performed on M1-59 by growth in 10^{-4} M MTX to produce the M1-4 cell line. After growing the M1-4 cells for only 20 days after amplification, the MTX selective pressure was removed from some of the cells and flow cytometric analysis was used to monitor the stability of the amplified gene.

In figure 3 the mean fluorescence obtained from the fluorescence distributions is plotted versus time for each of the cell lines examined. All three cell lines experienced a loss in mean fluorescence. The level of *dhfr* in M1-65 and MTX^- M1-4 appears to decrease exponentially initially at a specific rate of -0.024 and -0.027 inverse days respectively (corresponding to *dhfr* half lives of 29 and 26 days). A surprising result was that the M1-4 cells maintained in 10^{-4} M MTX also lost *dhfr* at about the same rate as the MTX^- M1-4 cells. Apparently the newly amplified M1-4 cells have not yet reached a stable steady state. It appears that the *dhfr* was initially amplified to a high level and is now decreasing. It is expected that the *dhfr* level will plateau at a steady state which is higher than the *dhfr* level of the M1-59 cells from which the M1-4 cells were derived.

At each cell passage of the M1-65, M1-59, and M1-4 cells the number of doublings since removal of MTX was calculated and is plotted versus time in figure 4. This graph shows that removal of selective pressure does cause the cells to grow faster, as the difference in the number of doublings of the MTX^- and the MTX^+ cells of each cell line increases over time. The graph also shows that the more highly amplified cell lines grow slower than the less amplified cells. It should be noted that the number of doublings may not correlate directly with cell growth rate because cell growth is inhibited when the cells reach confluency. Also, if cells are allowed to become too confluent before passing this seems to cause a stress on the cells which may cause a longer lag phase and/or slower growth rate after passage.

4 Discussion

The flow cytometry results revealed that the degree of instability of the amplified expression vectors was relatively high in the M1 cells. The results here were very similar to results obtained by Weidle et al.[7] in which they examined the stability of HSRs in amplified CHO cells. They showed that the *dhfr* copy number decreased steadily for about 50 days and then appeared to reach a plateau in which a new stable state or much slower rate of *dhfr* loss was seen. The last analysis for M1-65 and M1-59 shown in figure 3 shows that the rate of *dhfr* loss has decreased noticeably from the early loss rates. Further analysis of the these cells will reveal whether or not a new steady state has been achieved.

We have shown that the growth rate of the M1 cells does increase after removal of selective pressure. More quantitative growth rate studies are needed in order to correlate *dhfr* level with growth rate. There are two effects which may be responsible for increased growth rate. First, in the presence of MTX, cells which have lost *dhfr* copies are unable to survive. Thus MTX causes an increased death rate, proportional to rate of *dhfr* loss, which results in a lower overall growth rate. Secondly, cells which have lost *dhfr* copies produce lower levels of foreign protein. This results in a lower metabolic burden, thus allowing a faster growth rate. Careful growth rate studies of cells containing various levels of *dhfr* with and without selective pressure could be used to determine which of these effects is of greater importance.

Growth rate measurements are more easily obtained for cells growing in suspension. We have been able to adapt the M1 cells to growth in suspension after a several week adaptation period. Thus, further work will include using suspension cultures to determine more precisely the effect of foreign protein expression level on cell growth rate. The suspension cultures will also be useful to study the effect of cadmium or zinc induction on the cell growth rate and expression of β-IFN.

References

[1] L.A. Weymouth and J. Barsoum, "Genetic Engineering in Mammalian Cells". in *Mammalian Cell Technology*, W. G. Thilly (ed.) (Butterworth Publishers, MA, 1986)

[2] M. J. Page, (1985) "Expression of amplified human beta interferon genes using heavy metal induction in Chinese hamster ovary cells." *Gene* **37**, 139-144

[3] W.E. Bentley and D.S. Kompala, (1989) "A novel structured kinetic modeling approach for analysis of plasmid instability in recombinant bacterial cultures." *Biotech. Bioeng.* **33**, 49-61

[4] R. J. Kaufman, J. R. Bertino, and R. T. Schimke, (1978) "Quantitation of dihydrofolate reductase in individual parental and methotrexate-resistant murine cells." *J. of Biol. Chem.* **253**, 5852-5860

[5] R. J. Kaufman and R. T. Schimke,(1981) "Amplification and loss of dihydrofolate reductase genes in a chinese hamster ovary cell line." *Mol. and Cell. Biol.* **1**, 1069-1076

[6] M. Karin, G. Cathala, and M. C. Nguyen-Huu, (1983) "Expression and regulation of a human metallothionein gene carried on an autonomously replicating shuttle vector." *Proc. Natl. Acad. Sci. USA*, **80**, 4040-4044

[7] U. H. Weidle, P. Buckel, and J. Wienberg, (1988) "Amplified expression constructs for human tissue-type plasminogen activator in Chines hamster ovary cells:instability in the absence of selective pressure." *Gene*, **66**, 193-203

Figure 1: Amplifiable β-interferon expression plasmid pSVdMIF.

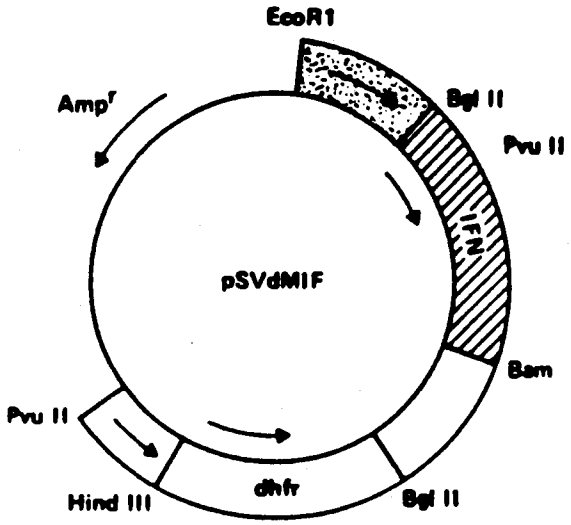

Table 1: Levels of β-IFN produced from the M-7, M-6, and M-5 series of cell lines as reported by Page[2].

Cell line	Units β-IFN/10^6 cells/24 hr	
	No Induction	Induction w/ 1 μM $CdSO_4$
M1-7	3400	N.D.
M2-7	4300	N.D.
M1-62	15900	94100
M1-63	14800	52500
M1-64	13800	34600
M1-65	34300	108400
M1-52	46300	213700
M1-54	103700	284900
M1-57	260300	325400
M1-59	29600	319200

Figure 2: Fluorescent histograms of M1-65 and M1-59 cells.

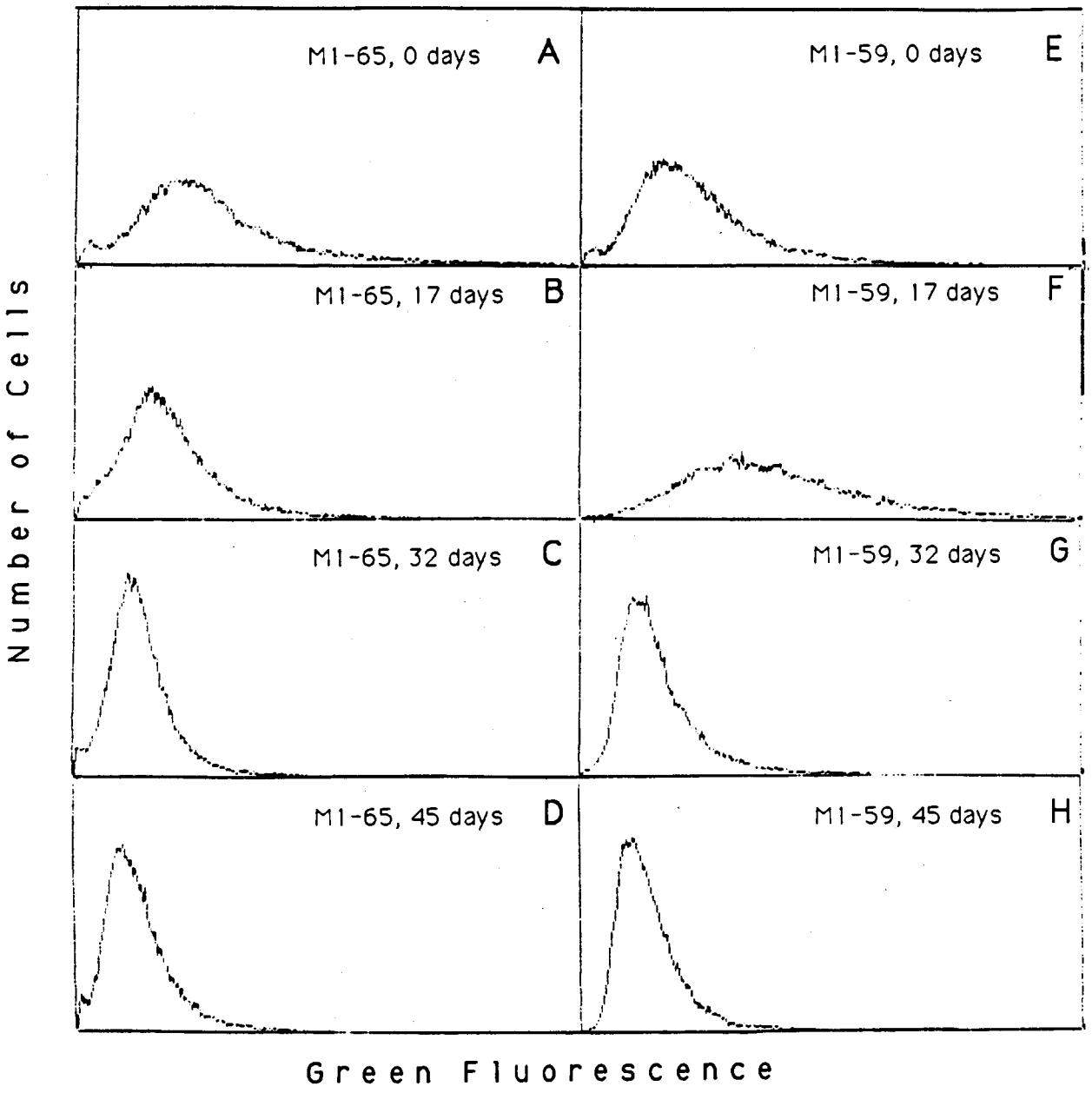

Figure 3: Instability of Amplified CHO Cells

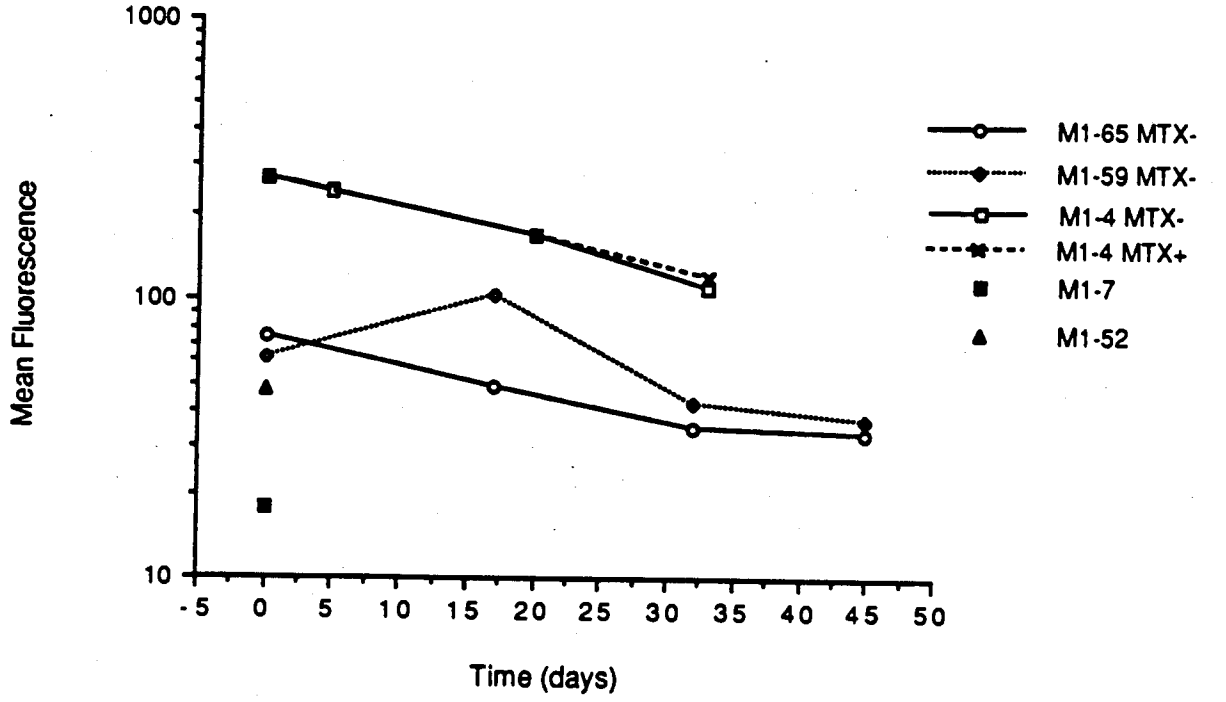

Figure 4: Doublings of M1 Cells After MTX Removal

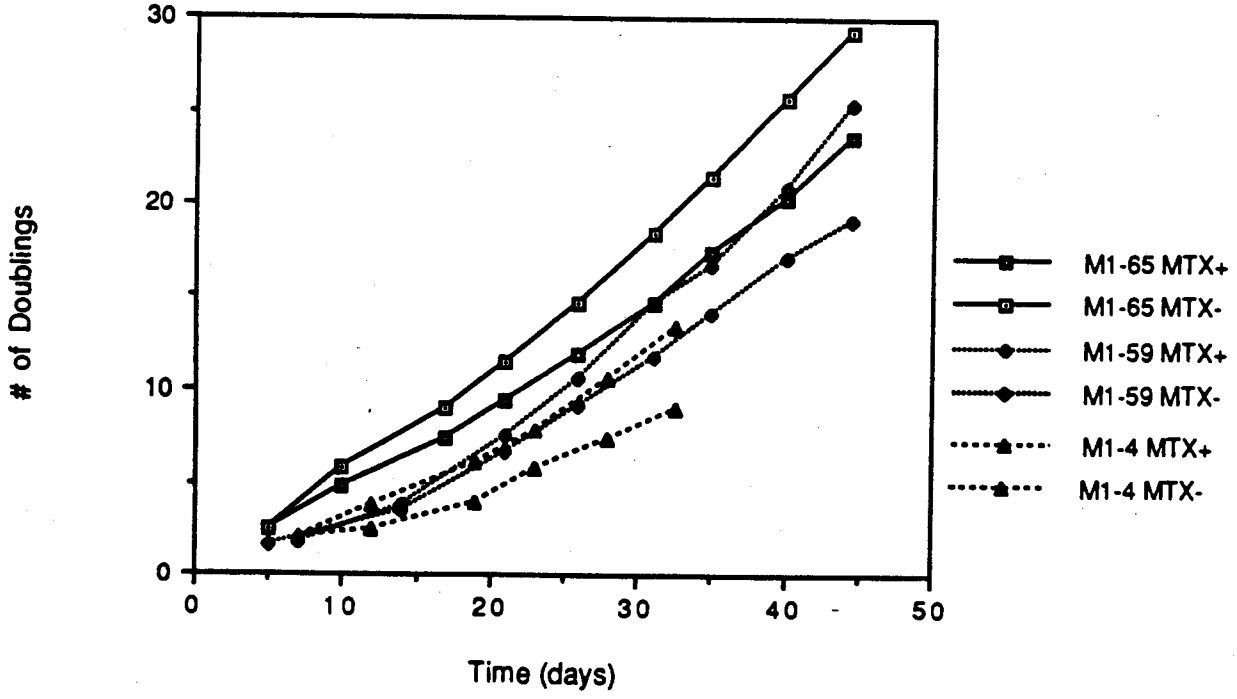

STRUCTURED MATHEMATICAL MODELING OF XYLOSE FERMENTATION

A.K. Hilaly, M.N. Karim, J.C. Linden and S. Lastick
Department of Agricultural and Chemical Engineering
Colorado State University
Fort Collins, CO 80523

ABSTRACT

A structured mathematical model for xylose fermentation using recombinant E.coli has been developed. The model is able to predict the production of alcohol and organic acids. The model takes into account plasmid replication, plasmid instability and transcription and translation of cloned gene. The model predictions were consistent with the experimental data.

INTRODUCTION :

The concern about the future availability of petroleum and natural gas has generated much interest in processes which utilize the vast natural renewable resource of plant biomass for the production of liquid fuel. The major component of plant biomass are cellulose, hemicellulose and lignin. A number of processes have already been investigated for conversion of cellulose, starch and sugars to produce fuels. However, less attention has been given towards utilization of pentose sugars which represent a third or more of total carbohydrate content of biomass.

Bacteria were the first organisms found that carry out xylose fermentation. In bacterial fermentation, xylose is converted to xylulose, which then flows through the glycolytic pathway to form ethanol. However, due to the presence of other side pathways, bacteria produce substantial amounts of lactic acid, acetic acid, glycerol etc. and hence main product yield is poor. Therefore interest was focussed towards yeasts, which have higher yields and ethanol tolerance level compared to bacteria. Recently, Ingram et al (2) genetically modified the bacterium Escherichia coli to produce large amounts of ethanol from xylose. The genes coding for pyruvate decarboxylase and alcohol dehydrogenase from Zymmomonas mobilis were inserted into E coli and placed under the control of a single enteric promoter to produce an artificial operon for production of ethanol. High levels of gene expression were obtained resulting in large amounts of ethanol production.

This work concentrates on modeling of the batch fermentation of xylose. A structured mathematical model has been developed for the fermentation system. The model predicts the production of different metabolites as well as plasmid instability.

MODEL DEVELOPMENT :

The model takes into consideration the following vital cellular processes :

(i) Plasmid replication
(ii) Plasmid loss during cell division
(iii) Transcription of cloned gene
(iv) Translation of cloned gene
(v) Ethanol production from translated enzyme

The plasmid pLOI297 developed by Dr. L. Ingram is a derivative of ColE1 plasmid. The replicon of pLOI297 consists of three elements : (i) an origin of replication, (ii) a gene for synthesis of initiator (RNAII) ribonucleic acid molecules by RNA polymerase, (ii) another gene for repressor RNA (RNAI) synthesis. In ColE1 plasmids, RNAII transcript forms a persistent hybrid with the template DNA near the replication origin. The hybridized RNAII is then cleaved by the enzyme RNAase. The cleaved RNAII acts as a primer for DNA systhesis by DNA polymerase I. The initiation of DNA replication may be inhibited by RNAI which binds with RNAII and prevents hybridization and primer formation.

The equations for the plasmid replication process are based on the work done by Satyagal and Agrawal (6). The synthesis of the transcripts RNAI and RNAII follow first order kinetics. The complex formation between RNAI and RNAII is a second order reaction. The model assumes the rate of plasmid replication is limited by the availability of the initiator molecules and is affected by host-plasmid inteaction.The rate for repressor,initiator and plasmid synthesis are given by equations (1), (2) and (3) in Table 1. The factor F_h accounts for host plasmid interaction. Replication of a foreign plasmid requires different host proteins as well as other necessary precursors. Therefore, the host cell has a strong influence on the plasmid synthesis rate which depends on the physiological state of the host cell.

There are two kinds of plasmid instability : (i) structural and (ii) segregational. Structural instability arises due to the fact that the cloned genes undergo spontaneous insertions, deletions and substitutions which may render the cloned gene product non functional. Segregational instability is due to the improper partitioning of the plasmids during cell divisions. Usually high copy number plasmids lack the 'par' gene system which ensures equal partitioning. The rate of structural instability may be calculated from spontaneous mutation rate. Probability analysis gives the rate of segregational instability. The model developed by Seo and Bailey (7) was used in the present work. Equations (5) - (10) describe the structural and segregational instability of plasmid.

The expression of the cloned gene in pLOI297 is under the control of lac operon. The lac operon is negatively regulated by lac repressor protein. An inducer can bind to the repressor protein and prevent it from putting off the transcription of the structural genes. Catabolite activator protein (CAP) binds slightly upstream of the promoter region and positively regulates the transcription. CAP protein needs to form a complex with cAMP prior to its binding with DNA. The model assumes no control in the level of translation. The transcription and translation reaction are assumed to follow first order kinetics. The degradation rate of mRNA and translated enzyme are also first order. Equations (11) and (12) describe the transcription and translation process. The transcription efficiency is calculated by the model proposed by Lee and Bailey(5).

The enzyme,alcohol dehydrogenase, catalyzes the formation of ethyl alcohol from acetaldehyde. By pseudo steady state hypothesis, it is reasonable to assume that the intracellular concentration of acetaldehyde remains unaltered with respect to time. However, the flux of ethanol production will change with time depending upon the uptake rate of xylose and production rate of the enzyme. In this model,it is assumed that the reaction catalyzed by ADH II, obeys the two substrate kinetic model of Daiziel (1). Product inhibition occurs when sufficient amounts of alcohol has been formed. A parameter for ethanol inhibition has been added to the Daiziel model. Equation (28) gives the rate of reaction producing ethanol. Equation (29) shows the dependence of maximum reaction velocity on product (ethanol) concentration. The parameter A_E, which accounts for the modulation of enzymatic activity, has been expressed as a function of substrate (xylose) utilization flux (equation 30).

The fermentation of xylose also produces substantial amounts of organic acids, such as, lactic acid, acetic acid and succinic acid. Experimental data shows that these organic acids are produced at rates proportional to the rate of ethanol production. Equations (25)-(27) describe the rate of production of organic acids.

The model assumes the existence of three kinds of cells in the population. X_3 type of cells contain the functional plasmid and due to segregational instability, plasmid free cells (X_1) are generated. X_2 type of cells contain the antibiotic genes (genetic marker) but the cloned gene of interest is inactive due to mutations. Equations (19)-(21) describe the rate of change of these three kinds of cells. The specific growth rate of plasmid containing cells is a function of plasmid concentration, enzyme concentration and xylose (substrate) concentration (equation 24). The specific growth rate of plasmid free cells depends only on substrate concentration. For X_2 type of cells, the specific growth rate depends on both substrate and plasmid concentration. These are shown in equations (25) and (26).

TABLE 1

$$dR/dt = k_2[P] - k_3[R] - k[I][R] - \mu_3[R] \quad (1)$$

$$dI/dt = k_4[P] - k_5[I] - k[I][P] - \mu_3[I] \quad (2)$$

$$dP/dt = k_1[I].F_h - \mu_3[P] \quad (3)$$

$$F_h = V_h.\mu_3/(K_h + \mu_3) \quad (4)$$

$$\beta = \xi.[P]/t_D \quad (5)$$

$$t_D = \ln(2)/\mu_3 \quad (6)$$

$$\sigma = (1/\Sigma C_i)\{[f(N_m;N_m) + f(0;N_m)]\Sigma C_i + \Sigma [f(I;I) + f(0;I)] C_{I-k}\} \quad (7)$$

$$C_x = [1/(2 - \sigma)]\{[f(x;N_m) + f(N_m-x;N_m)]\Sigma C_I + \Sigma [f(x;I) + f(I-x;I)] C_{I-k}\} \quad (8)$$

$$f(x;N) = [N!/\{x!(N-x)!\}.\gamma^x.(1-\gamma)^{N-x} \quad (9)$$

$$\phi = \mu_1\sigma/\mu_3 \quad (10)$$

$$d[mRNA]/dt = k_m.\eta.[P] - k_d[mRNA] - \mu_3[mRNA] \quad (11)$$

$$d[ENZ]/dt = k_p.[mRNA] - k_{dp}.[ENZ] - \mu_3[ENZ] \quad (12)$$

$$\eta = (1-\psi_1)(1-\psi_2)\psi_3 + \delta_2(1-\psi_1)\psi_2.\psi_3 \quad (13)$$

$$\psi_j = 1/2[(1 + \rho_j/\theta_j + 1/\alpha_j\theta_j) - \{(1 + \rho_j/\theta_j + 1/\alpha_j\theta_j)^2 - 4\rho_j/\theta_j\}^{1/2}] \quad (14)$$

$$\alpha_j = (K'_{Aj} + K'_{Cj}.K'_{Dj}[e_j])/(1 + K'_{Cj}[e_j]) \quad (15)$$

$$K'_{Aj} = K_{Aj}/(1 + K_{Bj}[\theta_j]) \quad (16)$$

$$K'_{Cj} = K_{Cj}(1 + K_{Ej}[\theta_j])/(1 + K_{Bj}[\theta_j]) \quad (17)$$

$$K'_{Dj} = K_{Dj}/(1 + K_{Ej}[\theta_j]) \quad (18)$$

TABLE 1 (Continued)

$$dX_3/dt = \mu_3.X_3(1 - \beta - \phi)(1 - X_3/X_{max}) \quad (19)$$

$$dX_2/dt = \mu_2.X_2(1 - \phi) + \mu_3.X_3.\beta \quad (20)$$

$$dX_1/dt = \mu_1.X_1 + \mu_2.X_2.\phi + \mu_3.X_3 \quad (21)$$

$$\mu_1 = \mu_0.[xyl]/(K_s + [xyl]) \quad (22)$$

$$\mu_2 = \mu_0.(1 - [P]/P_{max})([xyl]/(K_s + [xyl])) \quad (23)$$

$$\mu_3 = \mu_0.(1 - [P]/P_{max})(1 - [ENZ]/ENZ_{max})([xyl]/(K_s+[xyl]) \quad (24)$$

$$d[LAC]/dt = f_L.d[ETH]/dt \quad (25)$$

$$d[SUC]/dt = f_S.d[ETH]/dt \quad (26)$$

$$d[ACET]/dt = f_A.d[ETH]/dt \quad (27)$$

$$V = V_m/(1 + K_{ma}/[NADH] + K_{mb}/[CH_3CHO] + K_{mb}.K_i/[NADH][CH_3CHO]) \quad (28)$$

$$Vm = K_{cat}.[ENZ].A_E.(1 - [ETH]/ETH_{max}) \quad (29)$$

$$A_E = \alpha_1.\upsilon/(\alpha_2 + \upsilon) \quad (30)$$

$$\upsilon = d[xylose]/dt \quad (31)$$

$$d[xylose]/dt = -(1/Y_{XS})(\mu_1.X_1 + \mu_2.X_2 + \mu_3.X_3) \quad (32)$$

SOLUTION OF THE DIFFERENTIAL EQUATIONS :

The set of simultaneous differential equations were solved by the fourth order Runge-Kutta method. Due to problems of stiffness, a small step size was necessary for stable solution. The model predictions were compared with the experimental data obtained from Dr. S. Lastick of the Solar Energy Research Institute (Golden, Colorado).

RESULTS AND DISCUSSIONS :

The time course of substrate (xylose) and cell concentration are shown in figure 1 and 2. The model predictions agreed quite well with the experimental data. In the model, the cell yield coefficient was varied during the course of fermentation. This was done in accordance with the experimental observation.

Figure 3 shows the concentration profile of ethanol. Good agreement can be seen between model prediction and experiment. The constants α_1 and α_2 in the enzyme activity parameter was found by trial and error. Without the activity parameter, the deviation between model prediction and experiment increases significantly. The rationale of incorporation of the activity parameter in the enzyme kinetic equation is to account for the sharp increase of intracellular metabolite fluxes with the uptake of substrate.

The concentration profiles of organic acids produced in the fermentation are shown in figure 4. Only the final concentrations of the organic acids were measured experimentally. Hence, time course predicted by the model could not be verified. However, the final concentrations of the acids predicted by the model agreed quite well with the experimental values.

Figure 5 shows the model prediction of average plasmid copy number. Due to lack of experimental data, the prediction could not be compared. However, Ingram and Alterthum (3) reported very high levels (98-100%) of plasmid stability. The model predicts 5% loss of plasmid at the end of fermentation.

The kinetic parameters for plasmid replication were taken from the work of Satyagal and Agrawal (6).However, the parameters k1, k2 and k4 were fine-tuned in the present model. The rate constants and other binding parameters for transcription and translation reaction were taken from the work of Lee and Bailey (5). The work of Kinoshita *et. al* (4) provided the enzyme kinetics parameters. The rate constant K_{cat} was calculated and fine-tuned. The criterion for the adjustments of the parameters was to minimize the error between the predicted and experimental values of the measured variables.

CONCLUSIONS :

1. Good agreement has been obtained between model predictions and experimental data.

2. Need more experiments to measure the plasmid content of the cells and expression level of the cloned gene enzymes during the course of fermentation.

3. Need chemostat studies to see the effect of dilution rate and other environmental conditions (pH, T etc.) on the overall productivity of ethanol.

4. On-line optimization using 'ARMAX' type of model needs to be examined.

ACKNOWLEDGEMENT

This work was partially supported by Colorado State University Experiment Station. Thanks are also due to Dr. L. Ingram (University of Florida) for providing the recombinant E.coli cells and to Dr. S. Lastick for supplying the experimental data.

REFERENCES:

1. Daiziel, K., In : Boyer PD (ed) The Enzyme, vol 11, Academic Press, New York, pp 1-60, 1975.

2. Ingram, L. O., Conway, T., Clark, D. P., Sewell, G. W. and Peterson, J. F., Applied and Environmental Microbiology, 53 : 2420-2425,1987.

3. Ingram, L.O. and Alterthum, F., Applied and Environmental Microbiology, 55 : 1943-1948, 1989.

4. Kinoshita, S., Kakizono, T., Kadota, K., Das, K. and Taguchi, H., Applied Microbiology and Biotechnology, 22 : 249-254, 1985.

5. Lee, S. B. and Bailey, J. E., Biotechnology and Bioengineering, 26 : 1383-1389, 1984

6. Satyagal, V. N. and Agrawal, P., Biotechnology and Bioengineering, 33 : 1135-1144, 1989.

7. Seo, J. and Bailey, J. E., Biotechnology and Bioengineering, 27 : 156-165, 1985

NOMENCLATURE

[R] = CONCENTRATION OF REPRESSOR
[I] = CONCENTRATION OF INITIATOR
[P] = CONCENTRATION OF PLASMID
μ_3 = SPECIFIC GROWTH RATE OF PLASMID CONTAINING CELLS
F_h = FACTOR ACCOUNTING FOR HOST PLASMID INTERACTION

β = RELATIVE RATE OF STRUCTURAL INSTABILITY
ξ = SPONTANEOUS MUTATION RATE
t_D = CELL DOUBLING TIME

σ = PROBABILITY OF BIRTH OF PLASMID FREE CELLS
ϕ = RELATIVE RATE OF SEGREGATIONAL INSTABILITY
f(x;N) = BINOMIAL DISTRIBUTION

[mRNA] = CONCENTRATION OF MESSENGER RNA
[ENZ] = CONCENTRATION OF ENZYME
η = TRANSCRIPTION EFFICIENCY
ψ_i = BINDING PROBABILITY OF REGULATORY ELEMENTS

X3 = CONCENTRATION OF PLASMID CONTAINING CELLS
X2 = CONCENTRATION OF CELL WITH INACTIVE CLONED GENE
X1 = CONCENTRATION OF PLASMID FREE CELLS
μ_j = SPECIFIC GROWTH RATE
f_j = PROPORTIONALITY CONSTANT
[LAC] = CONCENTRATION OF LACTIC ACID
[SUC] = CONCENTRATION OF SUCCINIC ACID
[ACET] = CONCENTRATION OF ACETIC ACID
[ETH] = CONCENTRATION OF ETHANOL
[ENZ] = CONCENTRATION OF ENZYME

A_E = ENZYME ACTIVITY PARAMETER
υ = SUBSTRATE UTILIZATION FLUX
α_1, α_2 = CONSTANTS
[ENZ] = CONCENTRATION OF ENZYME

k_j = FIRST ORDER RATE CONSTANTS
Ci = PROBABILITY CONSTANTS
ρ_j = REGULATORY PROTEINS
θ_j = BINDING SITES
KAj, KBj, KCj, KDj, KEj = BINDING PARAMETERS

XYLOSE CONCENTRATION VS TIME

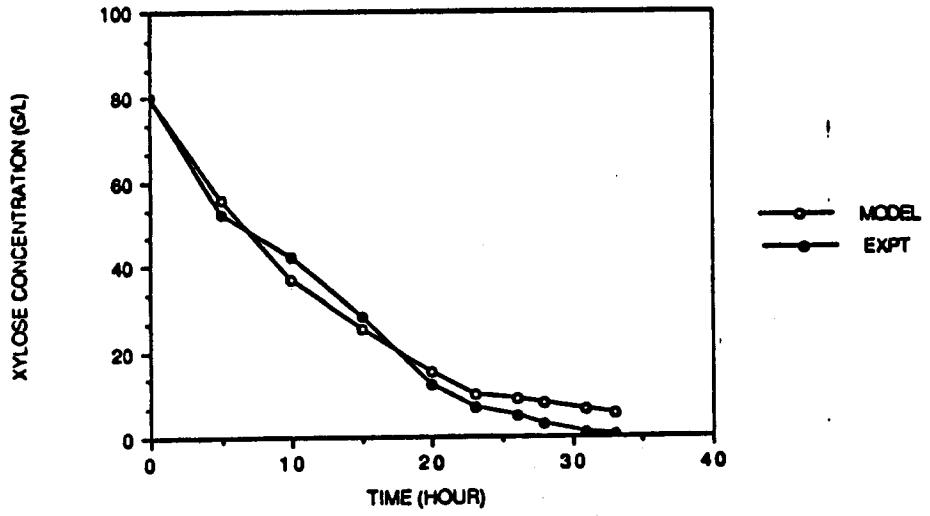

FIGURE 1

CELL CONCENTRATION VS TIME

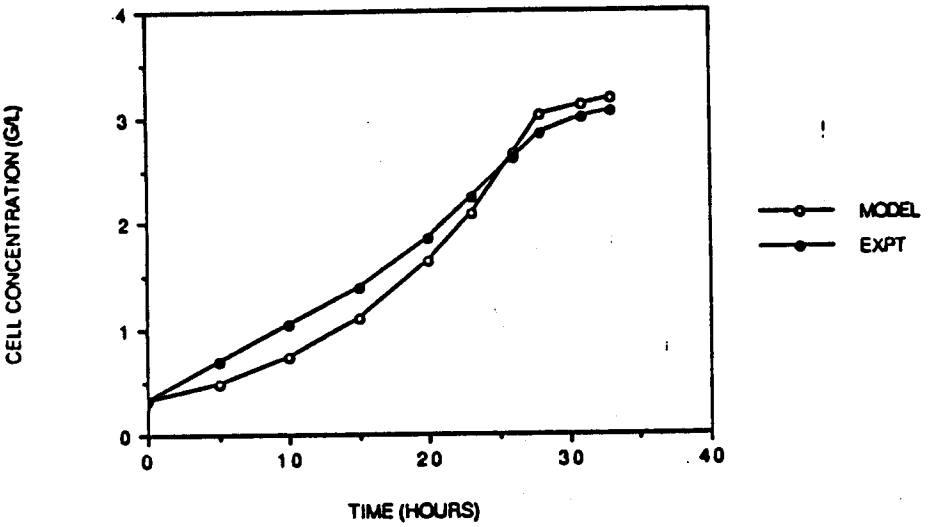

FIGURE 2

ETHANOL CONCENTRATION VS TIME

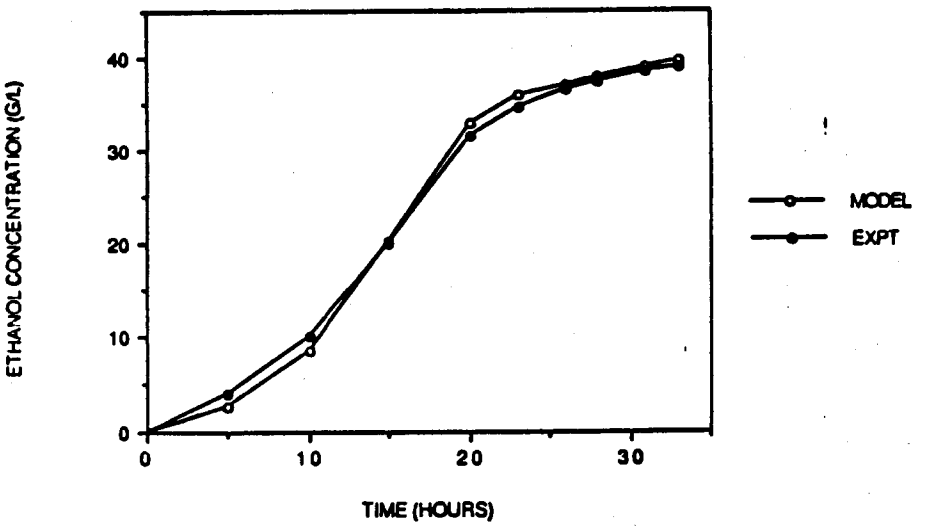

FIGURE 3

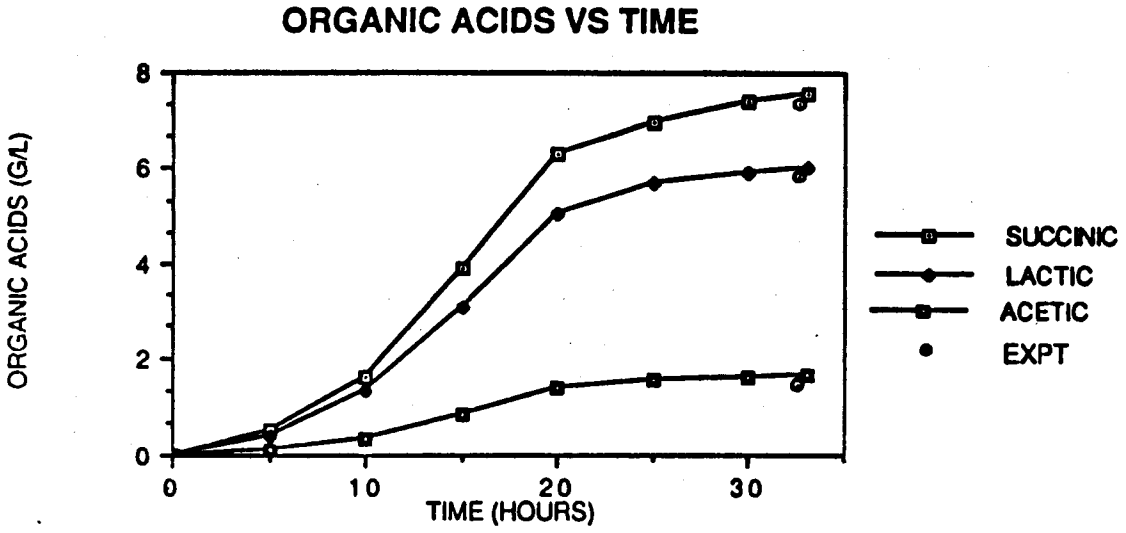

FIGURE 4

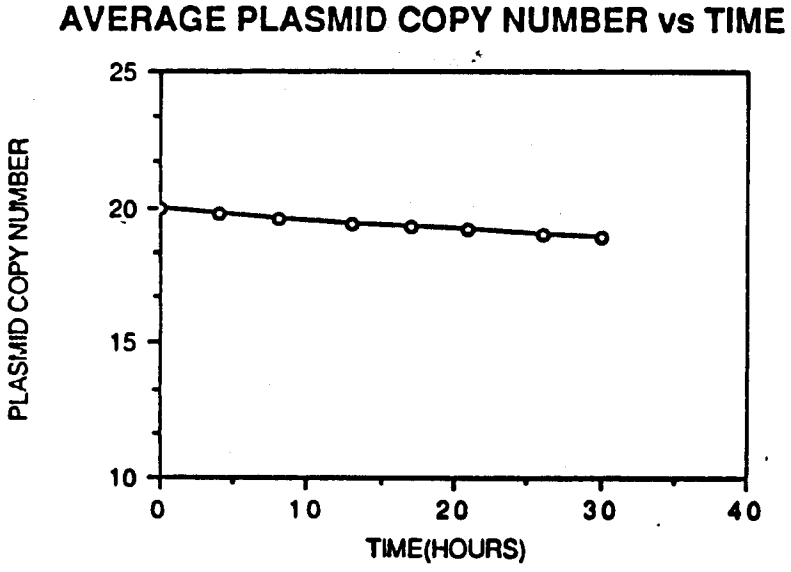

FIGURE 5

A NEW CULTURE MEDIUM FOR CARBON-LIMITED GROWTH OF *BACILLUS THURINGIENSIS**

W. -M. Liu and R. K. Bajpai

Department of Chemical Engineering
University of Missouri-Columbia
Columbia, MO 65211

Abstract

A culture medium for batch production of δ-endotoxin by *Bacillus thuringiensis* has been modified for use in fed-batch operation. Through the studies involving batch and continuous cultivation, the original medium was diagnosed to be limited in organic nitrogen. Corn steep liquor was found to be an excellent source for the organic nitrogen and its addition resulted in significant increases in the amount of cells produced as well as in the extent of sporulation. The results of bioassays are also shown.

Introduction

Bacillus thuringiensis forms spores when the environment becomes unfavorable for vegitative growth. During sporulation, it also produces a proteinacious toxin named δ-endotoxin. The toxin in a sporulating cell aggregates to form a dimond-shaped particle commonly known as crystal. The endotoxin crystals possess insecticidal activity specifically against many kinds of insects in the categories of *Lepidoptera* and *Diptera*. Yet, they are not harmful to human beings or useful insects such as honey bees. Nor do they cause pollution problems. Consequently, preparations of *B. thuringiensis* crystals are now widely used in biological pest control plans[1-4].

Many investigators have studied the cultivation of *B. thuringiensis*. Sakharova *et al.*[5] studied crystal formation under various nutrient limitations. The growth kinetics of *B. thuringiensis* was investigated by Sakharova *et al.*[6]. A two-stage continuous cultivation was attempted by Khovrychev *et al.*[7]. Scherrer *et al.*[8] looked into the effect of glucose concentration on crystal production. Nickerson and Bulla[9] studied the minimal nutrient requirements of *B. thuringiensis*. Yousten and Rogoff[10] related metabolism of *B. thuringiensis* to spore and crystal formation. Foda *et al.*[11] noticed that aeration and pH control were important during cultivation. Goldberg *et al.*[12] modified a medium by

*Paper presented at the Twentieth Annual Biochemical Engineering Symposium held in the Kansas State University, Manhattan, KS on April 21, 1990.

continuous cultivation for a high yield production of spore-crystal preparation. Arcas *et al.*[13] showed that yeast extract in the medium could be substituted with malt sprout extract for crystal production. Arcas *et al.*[14] recently reported some data of a fed-batch fermentation, but LC_{50} values of the crystal preparations were not included.

The long-term objective of this research is to understand the process of sporulation so as to control it in the direction of extending the stage of toxin-formation. The first part of this research is to obtain a high cell concentration during the vegitative growth phase and then shift to sporulation in order to get a large amount of crystals. A computer-controlled fed-batch fermentation will be used to achieve the goal, but an adequate medium to be used in the fed-batch process must be developed beforehand. It has been indicated in the literature[5] that carbon, nitrogen or mineral mutrient limitations would all trigger the onset of sporulation. In this research a medium limited in carbon source is desired because carbon-source limitation reportedly induces massive sporulation[5] and also because the carbon sources can be monitored and controlled more easily.

Materials and Methods

Bacillus thuringiensis var. *kurstaki* HD-1 was obtained from the Bacillus Genetic Stock Center, Ohio State University (stock no. 4D6). This strain was kept on slants of Schaeffer's sporulation medium. The composition of the medium is listed in Table 1. Shake flask cultivations with 50 ml medium in baffled Erlenmeyer flasks were performed at 200 rpm and 30 °C. Unless otherwise specified, the medium composition in shake flasks is listed in Table 2. A loopful of spores from slant culture was used to inoculate the shake flasks unless otherwise mentioned. pH in shake flasks was adjusted to 7.5 before autoclaving. There was no pH control during shake flask cultivations.

Batch and continuous cultivations were performed in a Virtis Omni-culture fermentor (working volume: 1 liter) operated at 900 rpm, 2 liter air/min and 30 °C with pH controlled above 6.5. The medium composition in the fermentor will be disscussed in the Results and Discussions section. The inoculum for the fermentor consisted of 50 ml culture (11-hr old) from shake flasks. During continuous operation, the dilution rate was set at 0.3.

Glucose concentration was determined by using an HPLC with an RI detector. A Brownlee Labs polypore H 10 µm column was used at room temperature. The eluent was double-distilled water adjusted to pH 2 by using sulfuric acid and the flow rate was 0.2 ml/min.

Cell dry weight was measured by filtering broth sample through a preweighed 0.2 µm filter paper, washing the cells with distilled water and then drying the paper, along with the wet cells on it, in a 750 W microwave oven for 5 minutes. The drying procedure has been standardized in this lab.

Total crystal protein in the broth was analyzed by using Lowry's method. The reagents used in the analysis were obtained from Sigma Chemical Co.. The samples were prepared by

centrifuging at 10,000 rpm for 10 min. The sedimented pellet containing spores, crystals and cell debris was washed twice with distilled water, dried in a 80 °C oven and then redispersed in 0.1 N NaOH solution[8,15]. The last step took advantage of the fact that crystals are soluble in alkaline solutions but not in neutral or acidic ones. The final solution was votexed for 20 min for total dissolution of the crystals and then centrifuged at 10,000 rpm for 10 min. The supernatant containing dissolved crystal protein was used in total protein analysis; dilutions of the supernatant with 0.1 N NaOH solution were made if necessary. 1 ml modified Lowry's reagent dissolved in distilled water was added to 1 ml crystal protein solution. The mixture was votexed well. After 10 minutes, 0.5 ml Folin's phenol reagent in distilled water was added to the mixture with rapid votexing, . The final mixture was allowed to stand at room temperature for 20 min to allow the characteristic blue color to develop. Absorbence of the mixture at 700 nm against 0.1 N NaOH solution was measured and protein concentration was calculated by using a calibration curve prepared from the absorbence of protein standard solutions treated in the same way as the crystal protein solution.

Potency of the crystals in the broth sample taken at the end of a fermentation was analyzed by calculating the LC_{50} obtained from bioassays conducted on *Trichoplusia ni* (cabbage looper) according to a method standardized by Dulmage[16]. Eggs of *T. ni* for the first generation were obtained from the SEA Biocontrol Lab, USDA, Columbia, MO. By following a guideline of rearing provided by that lab, we have been able to keep *T. ni* successfully for score of generations in our lab. A semisynthetic diet with the composition listed in Table 3 was used to feed larvae of *T. ni*. For each generation the majority of larvae were used in bioassays while the rest were kept to produce the next generation. A control consisting of standard *B. thuringiensis* crystal preparation was used in all bioassays. This standard, HD-1-S-1980 was provided by Institut Pasteur, Paris, France and had potency of 16,000 IU/mg formula. For the comparison group in a bioassay, solutions of various concentrations of the standard preparation were blended with the diet. For the test group, a broth sample taken at the end of a fermentation was centrifuged, the pellet containing crystals was washed and redispersed in distilled water, and solutions of various concentrations of the sample preparation were blended with the diet as in the case of the standard preparation. Blanks, which were prepared in the same manner as the test or comparison group except no crystal was blended in the diet, always accompanied a bioassay in order to check the validity of this bioassay[16]. Four-day old larvae were transferred onto the bioassay diet. The mortality of the larvae was checked five days later and the LC_{50}'s of the test and comparison groups were calculated by using a computer Probit procedure in the SAS package. The potency of the crystal preparation from the fermentation sample was calculated via the following equation:

$$\text{Potency of sample (IU)} = \frac{LC_{50} \text{ of comparison group} \times \text{Potency of standard (IU)}}{LC_{50} \text{ of test group}}$$

Results and Discussions

The medium composition listed in Table 2 was found best from literature[14] and was used as the starting point in this research. It was noted that the sole source of iron in this medium came from yeast extract. Fig. 1 shows a batch fermentation with this medium composition. Repeated batch fermentations showed the same results as in Fig. 1. It was found that cells stopped growing at about the seventh hour after inoculation while glucose was still abundant at that moment. This implied that carbon source was not limiting in the medium. It was suspected that some other nutrient was limiting to initiate the stationary phase. A modification of the medium was then studied in order to find out the limiting factor and the nutrient requirements of *B. thuringiensis*. The methed used in this study was continuous cultivation technique[12]. It was believed that a nutrient could be identified to be limiting if that nutrient was added to a fermentor operated at steady state during continuous cultivation and then a transcient change in cellular metabolism as reflected by variations in cell concentration, glucose concentration or dissolved oxygen in the broth was observed.

From an elemental analysis of the composition of general bacterial cells, it was found that the amounts of inorganic nitrogen (NH_4^+), iron, calcium and manganese were relatively small compared to the other nutrients in the medium; therefore, solutions of the four nutrients were added to a continuous culture first. The concentration of each nutrient solution tested was such that 5 ml solution would provide the same amount of the particular nutrient as 1 L medium with composition listed in Table 2. A sterile syringe was used to add the 5 ml solution to the fermentor under continuous operation. However, after the four nutrients were added, no variation in dissolved oxygen or increase in cell concentration was observed. Yeast extract was tested next. The results of yeast extract test shown in Fig. 2(a) indicated that organic nitrogen ($-NH_2$ or -NH-) was limiting in the medium.

Because yeast extract was considered an expensive source of organic nitrogen, corn steep liquor, which is abundant in organic nitrogen content, was used next. Corn steep liquor showed the same effect as yeast extract as indicated in Fig. 2(b). Successive additions of corn steep liquor were also tested to realize how much of it could be added to increase cell concentration. The results are shown in Fig. 2(c). By taking dilution effect into consideration, a rough estimation of the final corn steep liquor concentration after the fourth addition was 4 g/L. It should be noted that 1 g/L glucose still remained in the broth after the fourth addition. This was considered owing to the nature of continuous operation because glucose was being fed into the fermentor continuously.

Next, a test was designed with some shake flask cultures to demonstrate how glucose could be made limiting in the medium. Table 4 shows the medium compositions used in the shake flasks. Arcas'[14] medium (Table 2) was used as the control. Each flask received as inoculum a 5 ml aliquot of broth from a 11-hr old shake flask culture with medium composition same as that in the control flask. Fig. 3 shows the concentration profiles in the flasks. When the cultures reached the stationary phase, glucose was used up only in flask 2 while there was still plenty of that in the control flask. In effect, we shifted organic nitrogen limitation present in the control flask to carbon limitation present in flask 2 by changing the medium composition according to Table 4. Other results of the shake flask cultivations are also summerized in Table 4. It was observed that maximum cell concentrations corresponded to the variations in the medium compositions, with corn steep liquor being the major factor and glucose the secondarily important one. Glucose and corn steep liquor had approximately the same effect on the amount of crystal protein and crystal potency. It was understood that not all protein in the crystals shows insecticidal activity[2,3,4]. The specific potency, obtained by dividing crystal potency by the amount of crystal protein in Table 4, can serve as an index of the "quality" of the crystals. Good-qualitied crystals were obtained in flask 1 and 2 with that in flask 2 slightly better. On the other hand, the control flask had poor-quality crystals compared to flask 1 or 2. The medium composition in flask 2 will be used in the subsequent study of fed-batch fermentation of *B. thuringiensis*.

Conclusions

Two important points can be drawn from this study:

1. Continuous cultivation technique was used to diagnose the original medium and it was found that organic nitrogen was limiting in the medium.
2. When 4 g/L corn steep liquor was added to the medium, glucose would become limiting if its concentration dropped below 8 g/L.

References

1. Rowe, G. E. and A. Margaritis, *CRC Crit. Rev. Biotechnol.*, **6**, 87(1987).
2. Bulla, L. A., Jr., D. B. Bechtel, K. J. Kramer, Y. I. Shethna, A. I. Aronson and P. C. Fitz-James, *CRC Crit. Rev. Microbiol.*, 147, October 1980.
3. Bulla, L. A., Jr., R. M. Faust, R. Andrews and N. Goodman, Ch. 7 in *The Molecular Biology of The Bacilli, Vol. II*, D. A. Dubnau, ed., Academic Press, New York(1985), p. 185.
4. Carlton, B. C. and J. M. Gonzalez, Jr., Ch. 8 in *The Molecular Biology of The Bacilli, Vol. II*, D. A. Dubnau, ed., Academic Press, New York(1985), p. 211.
5. Sakharova, Z. V., Yu. N. Ignatenko, M. P. Khovrychev, V. P. Lykov, I. L. Rabotnova and V. V. Shevtsov, *Mikrobiologiya*, **53**, 279(1984).

6. Sakhrova, Z. V., Yu. N. Ignatenko, F. Shchul'ts, M. P. Khovrychev and I. L. Rabotnova, *ibid*, **54**, 604(1985).
7. Khovrychev, M. P., Z. V. Sakharova, Yu. N. Ignatenko, T. P. Blokhina and I. L. Rabotnova, *ibid*, **55**, 983(1986).
8. Scherrer, P., P. Luthy and B. Trumpi, *Appl. Microbiol.*, **25**, 644(1973).
9. Nickerson, K. W. and L. A. Bulla, Jr., *ibid*, **28**, 124(1974).
10. Yousten, A. A. and M. H. Rogoff, *J. Bacteriol.*, **100**, 1229(1969).
11. Foda, M. S., H. S. Salama and M. Selim, *Appl. Microbiol. Biotechnol.*, **22**, 50(1985).
12. Goldberg, I., B. Sneh, E. Battat and D. Klein, *Biotechnol. Letters*, **2**, 419(1980).
13. Arcas, J., O. Yantorno, E. Arraras and R. Ertola, *ibid*, **6**, 495(1984).
14. Arcas, J., O. Yantorno and R. Ertola, *ibid*, **9**, 105(1987).
15. Milne, R., D. Murphy and P. G. Fast, *J. Invertebr. Pathol.*, **29**, 230(1977).
16. Dulmage, H. T., O. P. Boening, C. S. Rehnborg and G. D. Hansen, *ibid*, **18**, 240(1971).
17. Schaeffer, P., J. Millet, and J.-P. Aubert, *Proc. Natl. Acad. Sci. USA*, **54**,704(1965)

Table 1: Composition of The Schaeffer's Sporulation Medium[17].

Component	Concentration (g/L)
Agar	15
Nutrient broth	8
$MgSO_4 \cdot 7H_2O$	0.25
KCl	1
$FeSO_4 \cdot 7H_2O$	2.78×10^{-4}
$MnCl_2$	1.98×10^{-3}
$CaCl_2$	0.147

Table 2: Medium Composition for Shake Flask Cultures[13].§

Component	Concentration (g/L)
Glucose	10
Yeast extract	4
$(NH_4)_2SO_4$	1
KH_2PO_4	3
K_2HPO_4	3
$MgSO_4 \cdot 7H_2O$	4
$CaCl_2 \cdot 2H_2O$	0.041
$MnSO_4.H_2O$	0.030
$FeSO_4 \cdot 7H_2O$	0

§ Glucose and $MgSO_4 \cdot 7H_2O$ were autoclaved separately from the others.

Table 3: Composition of The Diet Larvae of *Trichoplusia ni* Feed on.¶

Ingredient	Amount
Water	3000 ml
Agar	95 g
Casein	126 g
Sucrose	135 g
Wheat germ (raw)	175 g
Salt mix (Wesson)	36 g
Alphacel	25 g
Potassium sorbate (dissolved in a small amount of water)	4 g
Methyl paraben (dissolved in a small amount of ethanol)	5.4 g
Linseed oil (raw)	26 ml
Vitamin mix	36 g
Aueromycin	4 g
KOH (45%)	9 ml
Formalin (40%)	3 ml

¶ When the diet is being prepared, linseed oil, vitamin mix and aueromycin are added to the diet after the temperature of the diet has dropped to 50 °C.

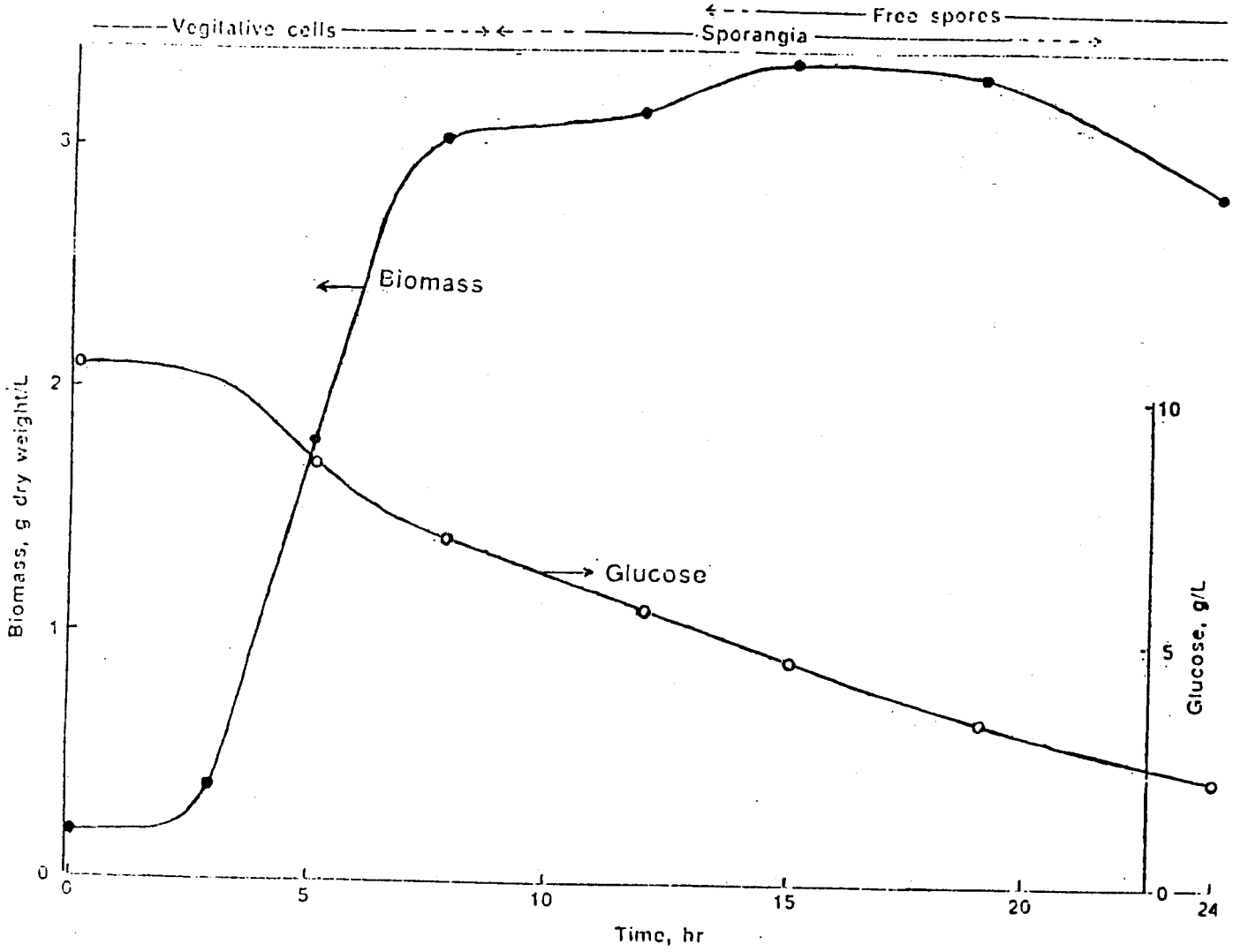

Fig. 1: Concentration Profiles of A Batch Fermentation with Arcas' Medium (Table 2).

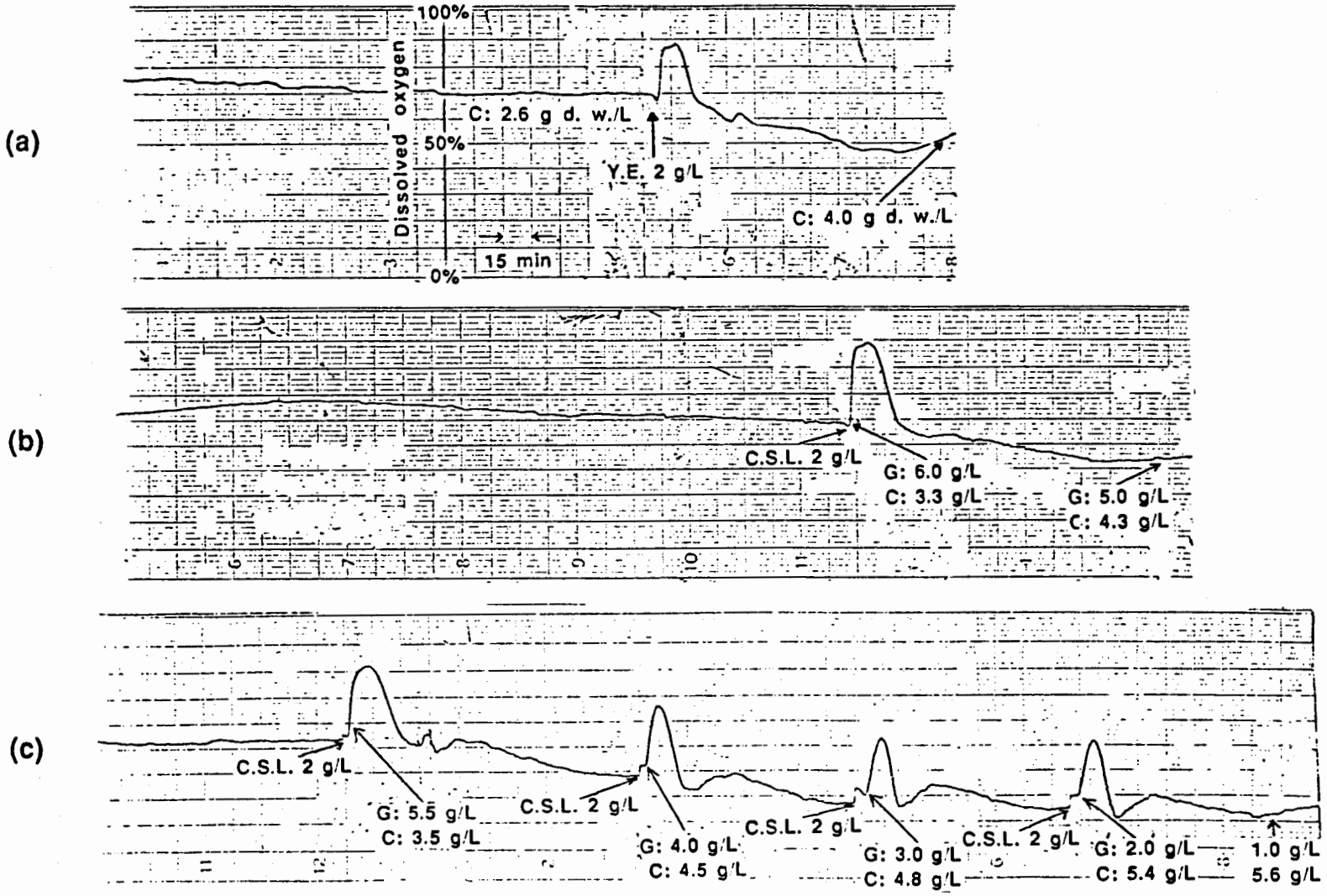

Fig. 2: Transcient Responses of Nutrient Additions to A Continuous Fermentation; (a): Single Addition of Yeast Extract, (b): Single Addition of Corn Steep Liquor, (c): Consecutive Additions of Corn Steep Liquor. Y.E.: Amount of Yeast Extract Added, C.S.L.: Amount of Corn Steep Liquor Added, C: Cell Concentration, G: Glucose Concentration.

Table 4: Effects of Medium Compositions on Shake Flask Cultures.[1]

Flask	Control	#1	#2	#3
Glucose, g/l	10	10	8	12
Yeast Extract, g/l	4	4	4	4
Corn Steep Liquor, g/l	--	4	4	4
maximum cell concentration, g dry weight/l	4.21	5.98	5.80	6.10
crystal protein, µg/ml broth	491.84	1258.02	824.19	ND[2]
potency, x10^3 IU/ml broth	145	814	559	ND[2]
specific potency, IU/µg crystal protein	294.5	646.8	678.1	ND[2]

[1]The mineral concentrations in each flask are the same as those listed in Table 2.

[2]Not determined.

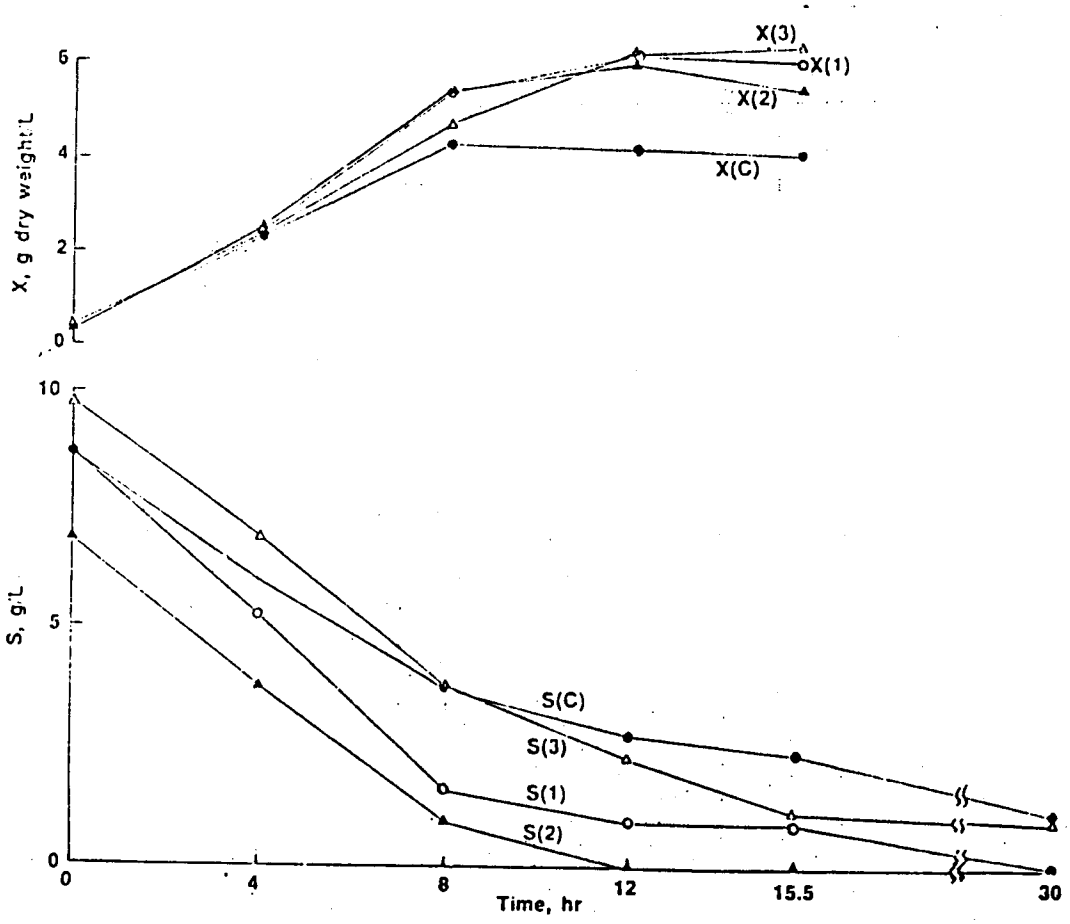

Fig. 3: Concentration Profiles of Shake Flask Cultures with Medium Compositions Listed in Table 4. S: Glucose Concentration, X: Cell Concentration; Numbers in Parentheses refer to Flask Numbers.

DETERMINATION OF SUGARS AND SUGAR ALCOHOLS BY HIGH PERFORMANCE ION CHROMATOGRAPHY

Thomas J. Paskach[1], Hans-Peter Lieker[2], Peter J. Reilly[1], and Klaus Thielecke[2]
[1]*Department of Chemical Engineering, Iowa State University, Ames, IA 50011 and*
[2]*Institute for Agricultural and Sugar Technology, Technical University of Braunschweig, D-3300 Braunschweig, Federal Republic of Germany*

ABSTRACT

High-performance ion chromatography (HPIC) was used to separate sugars and sugar alcohols on a quaternary ammonium-bonded column near pH 13. After separation, peaks were detected with a differential refractometer at Iowa State University and with a pulsed amperometric detector at the Technical University of Braunschweig. Separation occurs by the differential deprotonation of the sugars at the high pH's used. The retention times of 93 substances (mono- to tetrasaccharides and sugar alcohols) were determined. These were correlated with the molecular structure of the monosaccharides and with the glycosidic bond type and glycosyl residue of the homologous oligosaccharide series separated.

INTRODUCTION

Analysis of sugar mixtures is achieved chiefly by gas chromatography (GC) and by various types of high-performance liquid chromatography (HPLC). HPLC methods often have poor selectivity[1,2], and often more than one method must be used in combination to achieve reliable results. Even though good separations are obtainable in one step[3,4], GC requires a preliminary derivatization of the sample. Furthermore, GC and HPLC separations can be time-consuming.

Recently developed is separation of carbohydrates by high-performance ion chromatography (HPIC)[5]. This method overcomes many of these problems and is the subject of this paper, which is based on a cooperative effort carried out at the Technical University of Braunschweig and Iowa State University. Some of the work reported here, chiefly that conducted in Braunschweig, has already appeared[6].

EXPERIMENTAL

Chromatography was conducted with a Dionex model HPIC-AS6 column. This is a strong-base column with a quaternary ammonium group bonded to a strong nondeformable polystyrene matrix, made into very small nonporous beads attached to the surface of neutral nonporous beads of 10 μm diameter. The nonporous nature of the beads ensures the absence of pore diffusion limitation, and this leads to very sharp chromatographic peaks. The quaternary ammonium structure maintains most of its positive charge even up to pH 13. The column shell is an epoxy resin, which limits column pressure to about 135 atm. Usual pressure drops were about half this.

The separation is based on the particular pK_a of the sugars being analyzed, which lie

between 12 to 14. Under these strongly alkaline conditions, the sugar is deprotonated, and the anion formed is attracted to the positively charged quaternary ammonium group in the stationary phase.

The separation conditions were a flow rate of 1.0 mL/min, a sample injection size of 20 μL, and sample concentration of 0.1 g/L (Braunschweig) or 2.8 m*M* (Iowa State). This gives good detection and a large signal-to-noise ratio. The eluent used was 0.1*N* sodium hydroxide solution, which gives a pH of about 13.

RESULTS

The retention times of 93 substances were determined, and they are reported in Table 1 in the form of capacity factors

$$k_p' = (t_r - t_o)/t_o$$

where t_r is the observed retention time of the sugar and t_o is the dead time, which is the retention time of an unretained tracer. The capacity factor represents the dimensionless normalized retention time, which can be used for comparison with other systems.

In all cases, the capacity factors obtained in Braunschweig are larger. The results of the two groups are plotted against each other in Figure 1. A linear correlation with a slope of 1.5 and a correlation coefficient, r^2, of 0.996 results.

Figures 2-4 show the relationship between structure and capacity factor for the aldoses, ketoses, and sugar alcohols of one glycosyl residue. It is readily apparent that the capacity factors of aldoses and ketoses vary sufficiently from each other so that they can by easily separated by this technique. Also, for this reason, the identification of the peaks is quite easy. The sugar alcohols are much harder to deprotonate since they are already in the reduced form. They therefore have much higher pK_a's and much shorter retention times, and are not easily separated from each other. Capacity factor increases with number of carbons among the sugar alcohols, but this relationship does not hold for aldoses and ketoses.

Figure 5 shows the relationship between ln k_p' and the chain length in several homologous series of oligosaccharides. Each plot is extremely linear, with correlation coefficients of 0.999 or better. The intercept at unit chain length is the parent capacity factor, k_p', while the slope is the substituent parameter, τ_j, and these are summarized in Table 2.

This type of relationship has been shown before for other chromatographic systems and is based on a linear free-energy relationship, where the logarithm of the capacity factor is proportional to the free energy change associated with the chromatographic process

$$\ln k_{pi}' = \text{const.} - \Delta G_i/RT.$$

CONCLUSIONS

Several conclusions can be drawn from this research. First, separations are very fast, with monosaccharides and sugar alcohols eluting in less than 5 min and disaccharides and trisaccharides usually eluting in less than 30 min. The plots of the ln k_p' vs. chain length

can be easily extrapolated to predict the retention times of longer molecules. Because of the nonporous nature of the column beads, chromatographic peaks are very sharp, leading to high selectivity, even between sugars with similar retention times. As seen in Figures 2-4, generally retention times vary sufficiently between different sugars for easy identification.

Carbohydrates in alkaline solution, even in the absence of oxygen or other oxidizing reagents, undergo diverse fragmentation and rearrangement reactions, yielding initially isomeric sugars and eventually complex mixtures of acidic and stable adehydic compounds. For this reason it may seem implausible to use chropmatography at pH 13 for sugar analysis. These degradation reactions, however, are slow compared to the time required for chromatography, so in nearly all cases no adverse effects were noticed. The exception to this was seen in the short-chain ketoses, which degraded quite rapidly.

No sugar derivatization is required for this technique. This is a major advantage over previous techniques.

A final conclusion from this research is the establishment of a quantitative structure-retention relationship for several homologous oligosaccharide series. This relationship is also seen in other chromatographic systems, but this research is the first to demonstrate it for the strong-base HPIC of sugars.

Acknowledgements

This project was supported in part by the U. S. Department of Agriculture through the Biotechnology Bioproducts Consortium, composed of Iowa State University, the University of Iowa, and the City of Cedar Rapids, Iowa, and also by the Engineering Research Institute of Iowa State University. The authors would like to thank Südzucker AG, Pfeifer & Langen, and Drs. H. D. Scobell and Bent Stig Enevoldsen for their gifts of carbohydrates.

References

1. Nikolov, Z. L. and P. J. Reilly. *J. Chromatogr.*, **254**, 157 (1983).
2. Nikolov, Z. L., M. M. Meagher, and P. J. Reilly. *J. Chromatogr.*, **319**, 51 (1985).
3. Nikolov, Z. L., M. M. Meagher, and P. J. Reilly. *J. Chromatogr.*, **321**, 393 (1985).
4. Selosse, E. J.-M. and P. J. Reilly. *J. Chromatogr.*, **328**, 253 (1985).
5. Edwards, W. T., C. A. Pohl, and R. Rubin, *TAPPI J.*, **70**, 138 (1987).
6. Thielecke, K., H.-P. Lieker, and T. Paskach, *Zuckerind.* (December 1989).

Table I. Capacity factors of carbohydrates measured with two Dionex HPIC-AS6 columns eluted with NaOH.

Carbohydrate	*Capacity factor*		*Carbohydrate*	*Capacity factor*	
	*TU Braun-schweig**	*Iowa State Univ.***		*TU Braun-schweig**	*Iowa State Univ.***
D-Allose		2.01	Lactulose	4.14	2.92
D-Altrose		2.78	Laminaribiose***		4.63
D-Arabinose	1.57	1.13	Leucrose	3.36	
L-Arabinose		1.13	D-Lyxose		1.38
D-Arabitol	0.43		Maltitol	2.00	
L-Arabitol		0.35	Maltose	11.4	6.87
Cellobiose	7.00	4.15	Maltotriitol	7.79	
3-O-β-Cellobiosyl-D-glucose		4.82	Maltotriose		25.5
			Maltulose		2.87
Cellotetraose		30.7	D-Mannitol	0.71	0.56
Cellotriose		12.3	D-Mannose		1.44
Chloralose		7.13	L-Mannose		1.43
2-Deoxy-D-galactose		0.97	Melezitose	7.50	4.51
2-Deoxy-D-glucose		1.15	Melibiitol		0.62
2-Deoxy-D-ribose	1.00	0.75	Melibiose		2.01
D-Digitoxose		0.68	α-Methyl-D-mannoside	0.21	
Dihydroxyacetone***			3-Methyl-D-glucose		0.92
D,L-Dithiothreitol		1.61	Nigerose***		6.32
Dulcitol	0.57	0.44	Palatinose	6.79	4.82
meso-Erythritol	0.21	0.21	Panose		6.26
D-Erythrose		1.99	D-Psicose		1.82
D-Erythrulose***			Raffinose	8.07	5.54
D-Fructose	2.50	1.73	L-Rhamnose	1.07	0.90
D-Fucose	0.86	0.65	Ribitol		0.44
L-Fucose		0.65	D-Ribose	2.79	1.85
Galactinol	0.43		D-Ribulose***		
D-Galactose	2.07	1.50	Sedoheptulose		0.23
L-Galactose		1.52	Sophorose		8.86
Gentiobiose		3.92	Sorbitol	0.57	0.45
D-Glucoheptose		3.03	D-Sorbose	2.36	
D-Glucoheptulose		3.03	L-Sorbose		1.80
6-O-α-D-gluco-pyranosyl-mannitol	1.21		Stachyose		6.29
			Sucrose	4.43	3.30

D-Glucose	2.14	1.51	D-Tagatose		1.50
L-Glucose		1.50	D-Talose		3.02
D,L-Glyceraldehyde	0.93	0.84	D,L-Threitol		0.20
Glycerol		0.17	D-Threose		1.82
D-Gulose		1.94	α,α-Trehalose	0.86	0.63
L-Iditol		0.40	α,β-Trehalose		3.13
D-Idose			β,β-Trehalose		1.15
meso-Inositol	0.21		α,α-Trehalulose	4.57	
myo-Inositol	0.21	0.18	Turanose***	6.29	4.29
Isomaltitol	0.86		Xylitol		0.30
Isomaltose	3.93	2.94	Xylobiose		3.23
Isomaltotriose		5.96	D-Xylose	2.21	1.59
3-Ketosucrose***			Xylotetraose		11.5
Kojibiose***		3.43	Xylotriose		5.70
Lactose	4.21	2.69	D-Xylulose		3.26

* Dead time: 1.40 min, eluent flow rate: 1 mL/min; NaOH concentration: 0.102*N*, temperature: 25°, sample concentration: 0.1 g/L, sample volume: 20 μL; detector: Dionex pulsed amperometric detector with gold electrode.

** Dead time: 1.42 min, eluent flow rate: 1 mL/min; NaOH concentration: 0.095*N*, temperature: 23°, sample concentration: 2.8m*M*, sample size: 20 μL; detector: Knauer differential refractometer.

*** Degradation in alkaline solution caused multiple peaks.

Table 2. Values of substituent parameter (τ_j) and capacity factor of parent compound (k_p') for homologous oligosaccharide series chromatographed with Dionex HPIC-AS6 columns eluted with 0.1*N* NaOH.

Oligosaccharide series	Substituent	Parent compound	τ_j	k_p' (calc.)	k_p' (meas.)
Cello-	4-O-β-D-glucopyranosyl	D-Glucose	1.01	1.52	1.51
Isomalto-	6-O-α-D-glucopyranosyl	D-Glucose	0.69	1.49	1.51
Maltitol-	4-O-α-D-glucopyranosyl	Sorbitol	1.26	0.44*	0.45*
Malto-	4-O-α-D-glucopyranosyl	D-Glucose	1.42	1.55	1.51
Xylo-	4-O-β-D-xylopyranosyl	D-Xylose	0.65	1.61	1.59

* Converted to Iowa State University basis by use of Fig. 1.

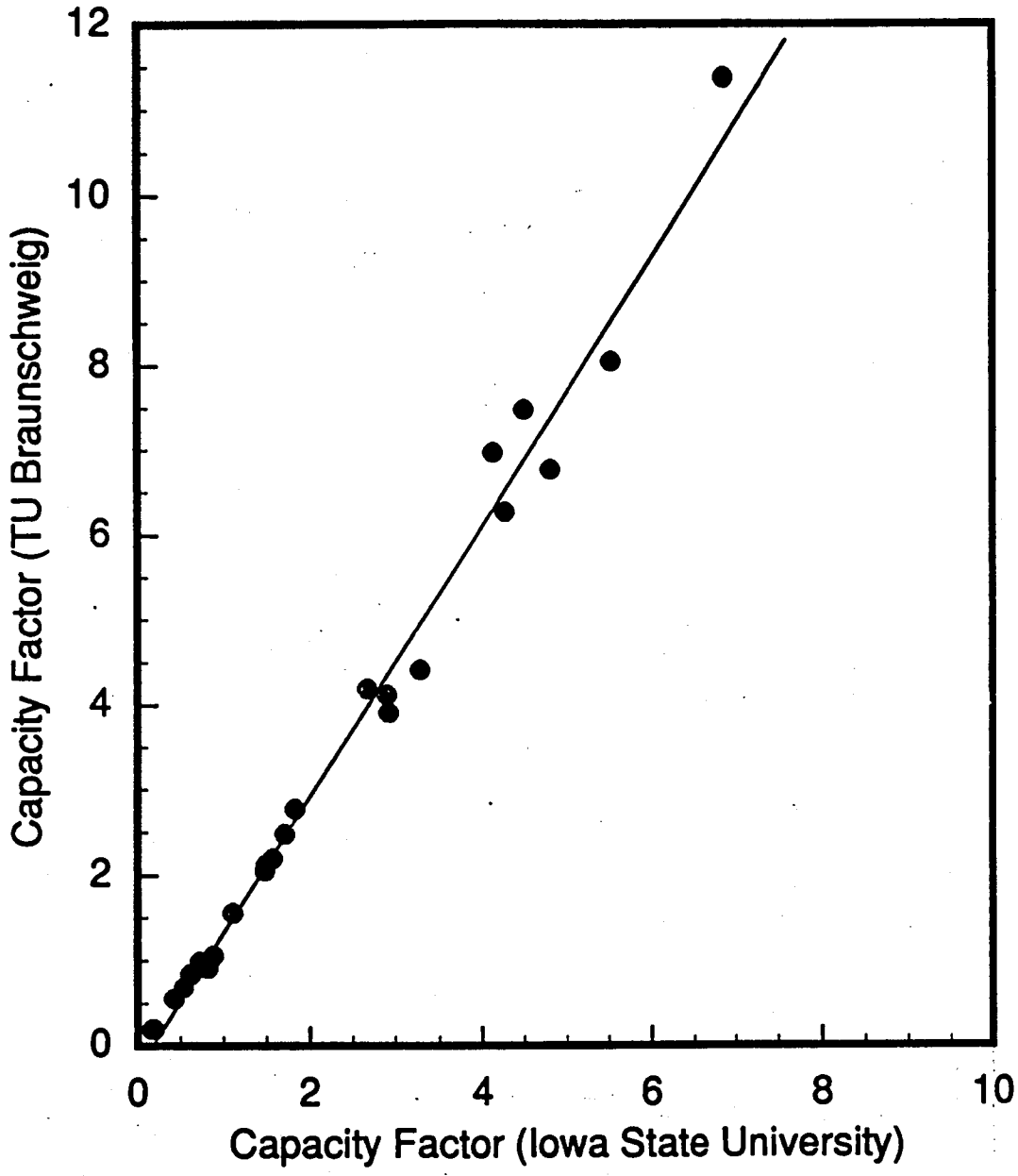

Figure 1. Comparison of capacity factors of identical substances measured with two different Dionex HPIC-AS6 columns.

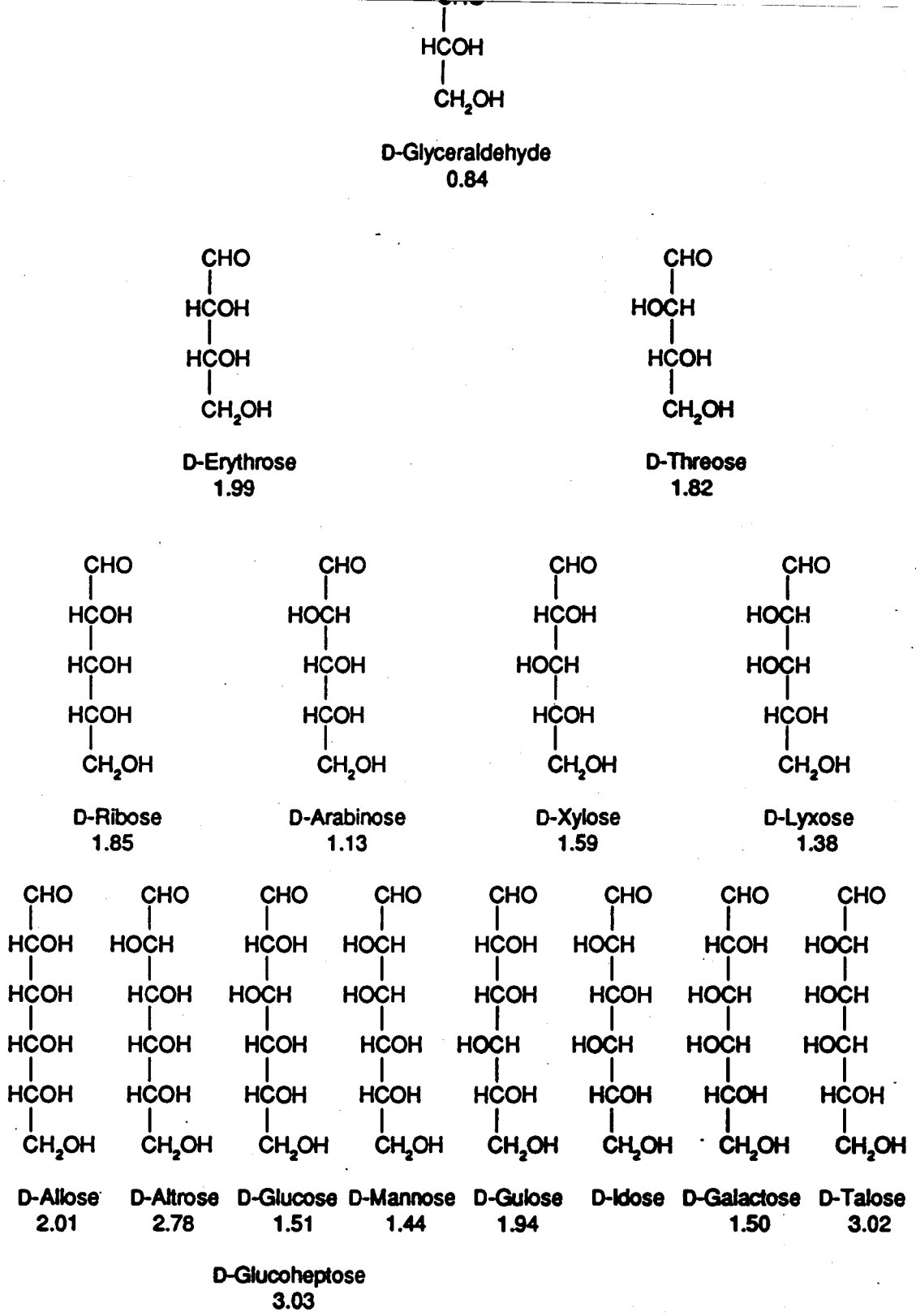

Figure 2. Effect of structure on capacity factors of aldoses measured at Iowa State University.

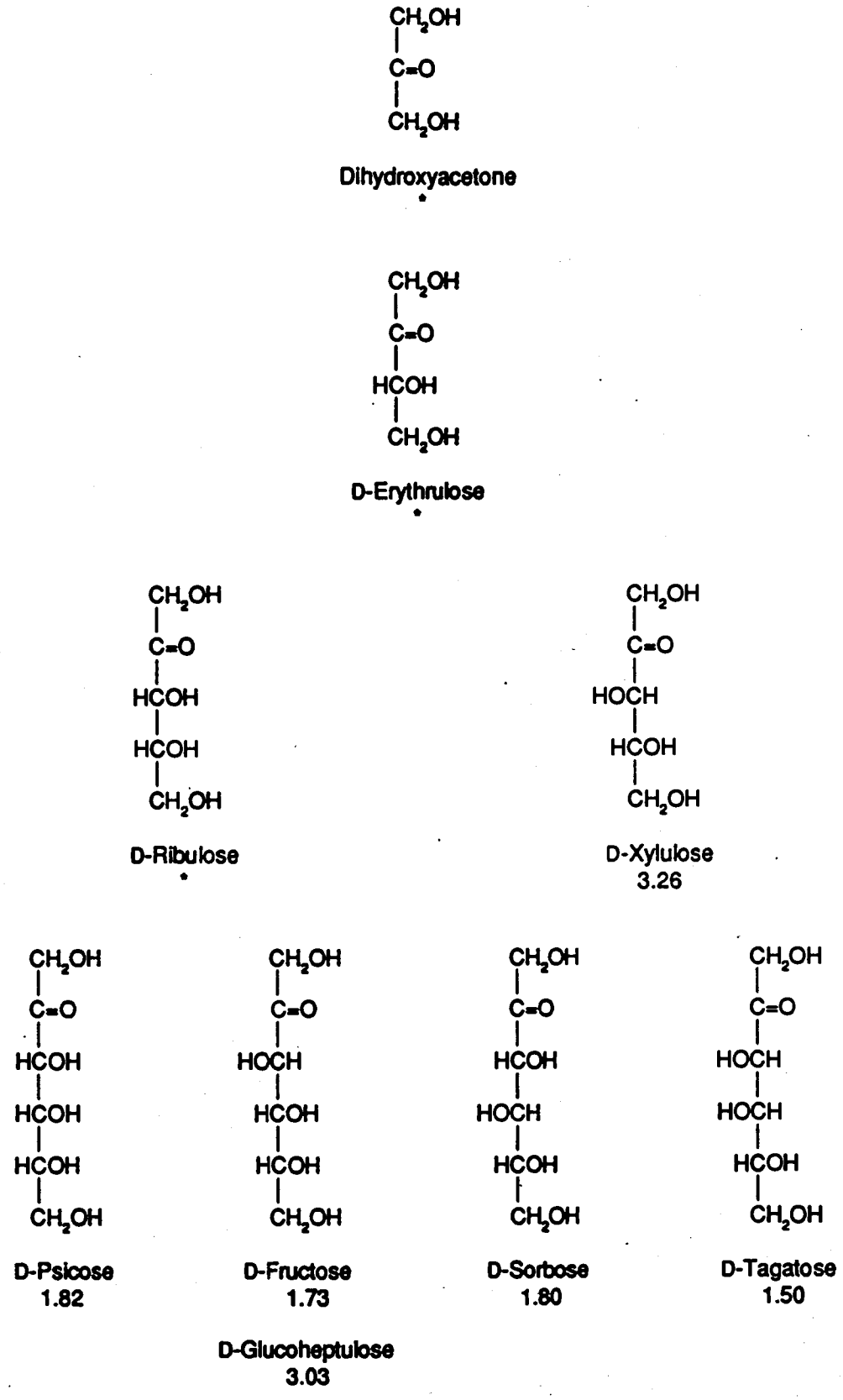

Figure 3. Effect of structure on capacity factors of ketoses measured at Iowa State University. *: Degradation in alkaline solution caused multiple peaks.

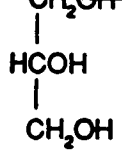

Glycerol
0.17

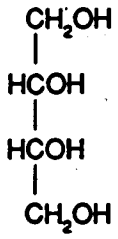

meso-Erythritol
0.21

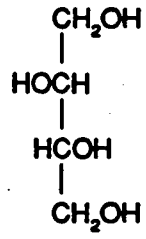

D-Threitol
0.20

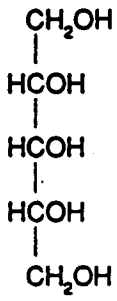

Ribitol
0.44

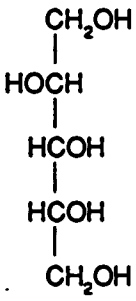

D-Arabitol
0.35

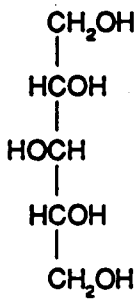

Xylitol
0.30

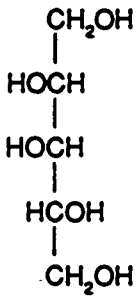

D-Lyxitol

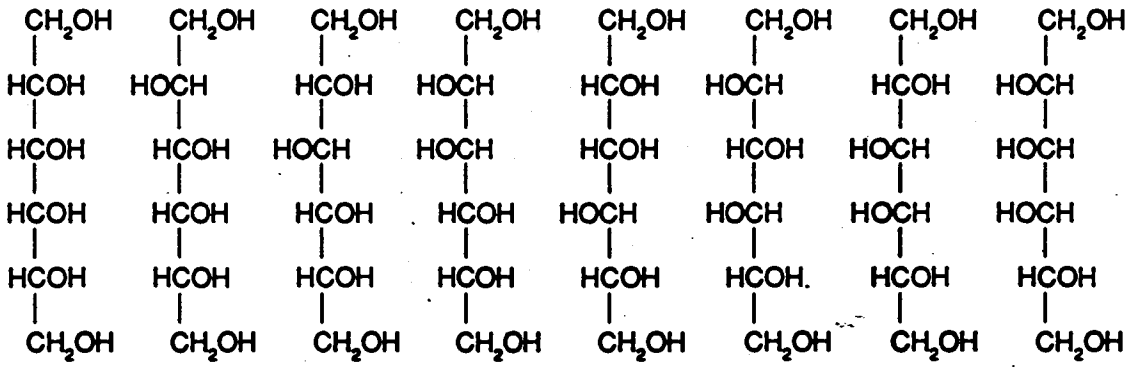

Allitol | D-Altritol | Sorbitol 0.45 | D-Mannitol 0.56 | D-Gulitol | D-Iditol 0.40 | Dulcitol 0.44 | D-Talitol

Figure 4. Effect of structure on capacity factors of sugar alcohols measured at Iowa State University.

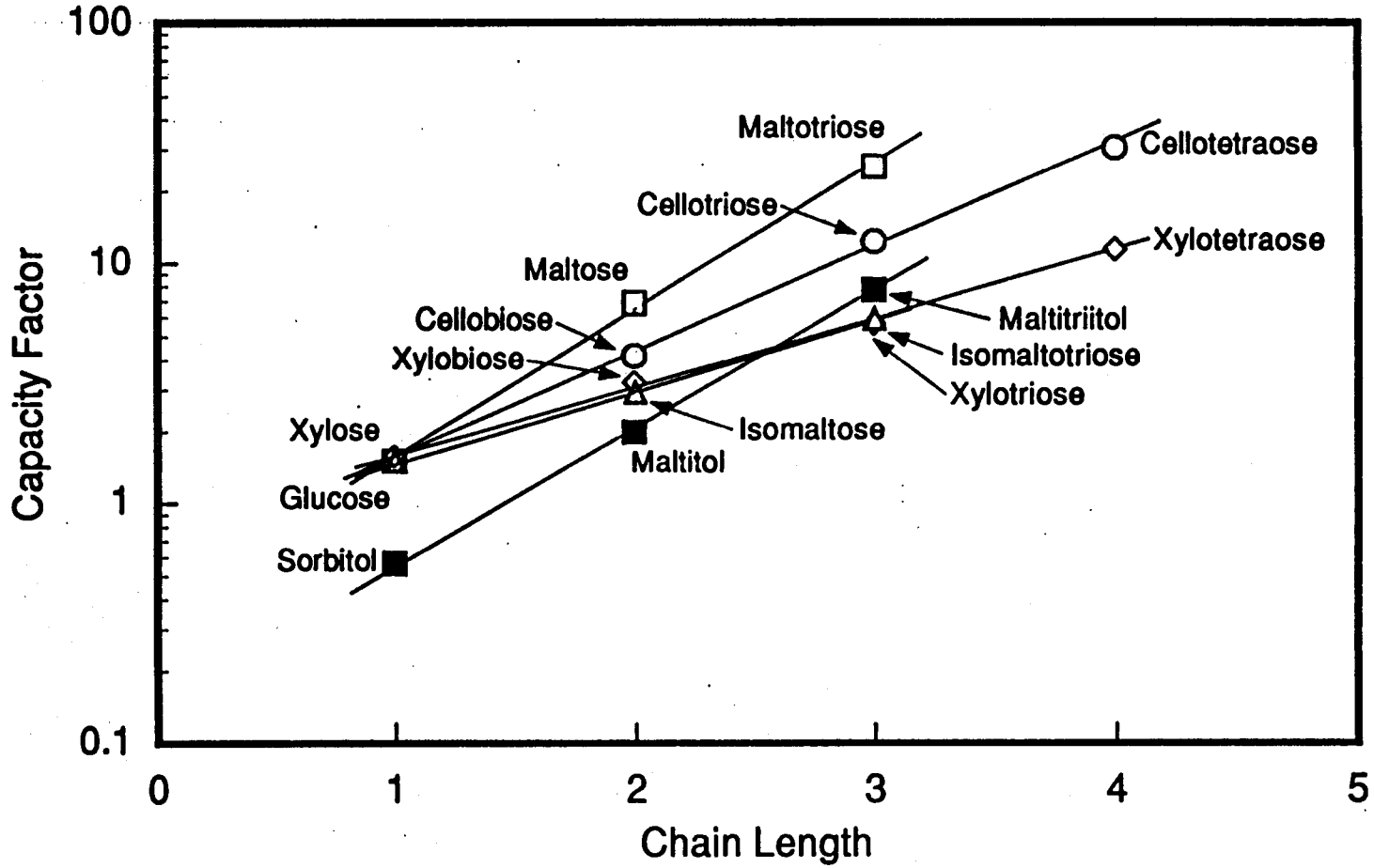

Figure 5. Effect of chain length on capacity factors of members of homologous series of oligosaccharides. Closed symbols: measured at TU Braunschweig; open symbols: measured at Iowa State University.

CHARACTERIZATION OF POLY-ASP TAILED ß-GALACTOSIDASE

M.Q. Niederauer and C.E. Glatz
Department of Chemical Engineering

I.A. Suominen and C.F. Ford
Department of Genetics

M.A. Rougvie
Department of Biochemistry and Biophysics

Iowa State University, Ames, IA 50010

Introduction

The downstream processing of enzymes is often the most expensive part of enzyme production. The improvement of the separation characteristics of an enzyme will result in reduced purification costs. The aim of this project is to improve the separation characteristics of enzymes through genetic manipulation[1]. This project concentrates on the addition of a charged poly-amino acid tail to either end of the enzyme. The study being presented here restricts itself to the addition of tails to the carboxyl terminus of β-galactosidase. Although the primary focus of research has been on the addition of negatively charged poly-aspartic acid tails, this study also includes one positively charged poly-arginine tail. The characterization of these genetically engineered enzymes is necessary to understand and model their behavior in various methods of separations and is the focus of this presentation.

β-galactosidase from E. coli is a tetrameric enzyme which catalyzes the conversion of lactose to galactose and glucose. An analog, o-nitrophenol-β-D-galactopyranoside (ONPG), is converted by β-galactosidase to o-nitrophenol and galactose, the former of which is yellow, making the enzyme easily assayable[2]. Each wild-type monomeric unit consists of 1023 amino acids and has a molecular weight of 116.4 kDa. The wild-type enzyme is fairly well characterized, yet the 3D structure is not known. The DNA and amino acid sequences of the genetically engineered enzymes are given below (Fig. 1) to show the primary structure of the tails. The genetic sequence has been verified using automated sequencing at the ISU Nucleic Acid Facility, yet the amino acid sequence of the tails has yet to be verified by sequencing.

Materials and Methods

The following is a short description of the materials and methods used in characterizing the enzymes.

SDS-PAGE: Sodium dodecyl sulphate polyacrylamide gel electrophoresis (SDS-PAGE) was performed using 7.5% acyrlamide in the resolving gel. Electrophoresis was conducted under a constant current of 25mA and the gel stained with Coomassie Blue[3].

HPGPC: High performance gel permeation chromatography (HPGPC) was performed using a variety of columns[4,5]. The types of columns and the operating conditions for the experiments are listed below.

Column
Synchrom Synchropak GPC300 0.1M $NaPO_4$/0.0-0.3M NaCl, pH 7.3
Beckman Spherogel TSK5000PW 0.1M KPO_4/0.0-0.3M NaCl, pH 7.3
Beckman Spherogel TSK3000SW 0.1M KPO_4/0.0-0.3M NaCl, pH 7.3

HPIEC: High performance ion exchange chromatography (HPIEC) was performed using the Supelco Toyopearl TSK DEAE 5PW weak anion exchange column in several buffer systems[6]:

10mM Tris-HCl pH 8.0 with 0.5M NaCl gradient
0.1M $NaPO_4$ pH 6.0 with 0.5M NaCl gradient
0.1M $NaPO_4$ pH 5.7 with 0.5M NaCl gradient
0.1M KPO_4 pH 5.7 with 0.5M K_2SO_4 gradient
0.1M KPO_4 pH 5.7 with 0.5M NaCl gradient

Results and Conclusions

SDS-PAGE: From the SDS-PAGE gel (Fig. 2) it can be seen that the purified β-galactosidase from the affinity column is not entirely free from contaminants. Four other protein bands appear at approximate molecular weights of 106, 93, 89 and 56 kDa. These bands are usually present after the affinity column purifications and are most probably due to non-specific interactions of the matrix with these proteins.

HPGPC: All of the experiments performed on the various columns and their associated buffers yielded very similar results: increasing tail length resulted in shorter elution times, corresponding to an increased effective molecular diameter (Fig. 3). The result is significant in that the additional amino acids do not contribute significantly to the overall size of the enzyme: in the case of the largest tail, this only corresponds to an increase in size of 1.5%. These results indicate that the tails are indeed accessible to the surface and protrude into the surrounding fluid. Another interesting result is that CD16 eluted before CD11 only on the Beckman TSK3000SW column. On the two other columns, it consistently eluted between CD11 and CD5 (not pictured here). It is proposed that this effect is due to the folding back of the tail onto an adjacent positively charged region on the surface of the enzyme, hence reducing its interaction with the surrounding fluid. Other explanations for this effect may be that the tail is shearing off at various lengths in the fluid during purification, or that the tail is being folded back into the protein. These possibilities are currently under study.

HPIEC: The separation of the various tailed enzymes by ion exchange yielded a much higher degree of resolution than either of the above methods (Fig. 4). Notably, however, the longer tailed CD16 does not elute as would be predicted by the elution patterns of the other enzymes. From the calibration of net estimated tetramer charge versus NaCl concentration (Fig. 5), it can be seen that the relationship is linear for the

shorter tailed versions, including the positive CR5 tail, yet CD16 elutes at a much lower ionic strength than would be predicted. The elution pattern of CD16 is also notably different in that it displays a high degree of bandspreading. From these results the conclusion from the gel permeation experiments is reinforced. The effect of the tail folding back onto the surface of the enzyme would result in lower accessability of the tail to binding ligands on the column. This would in turn result in a lowered binding strength of the enzyme to the column. Furthermore, taking into consideration that the tail could fold back at various lengths, the result would be a wider distribution of net charge accessable to the column matrix, explaining the bandspreading present for CD16.

Current and Future Research

In order to investigate some of the above mentioned anomalies and further characterize the enzyme, the following experiments are either currently being conducted or are being planned for the future.

Cleavage of the Tail: Current experiments are being conducted using different methods to attempt to cleave the tail from the enzyme for sequencing. This would verify whether the tail structure was actually being produced as predicted by the genetic sequence and surviving the purification procedures intact. Two methods are currently being used to cleave the tail: CNBr and formic acid cleavages. CNBr is known to specifically cleave methionine residues at their carboxy terminus[7], whereas formic acid cleaves aspartic acid/proline peptide bonds, yet at a lower frequency than CNBr cleavage[8,9].

Sequencing of the Tail: The purified tails from the cleaved β-galactosidase will be sequenced by the Protein Facility at ISU to verify the structure of the tail.

Binding Constant Determination: Polyamino acid peptides identical to the tail segments are to be constructed at the ISU Protein Facility for use in determining the binding coefficients of the tails. This information would facilitate more accurate modeling of the behavior of the modified proteins in precipitation reactions.

Acknowledgments

The authors would like to thank the National Science Foundation (Grant No. EET-87 12347) for its support of this research project. Additional thanks goes to John Luther of the Department of Chemical Engineering at ISU for the production and purification of the C-Ctrl and CR5 tailed enzymes used in these studies.

References

1) Brewer, S.J. and H.M. Sassenfeld. *Engineering Proteins for Purification.* Monsanto Co., Corporate Research & Development,

St. Louis, MO, and Immunex Corp., 51 Univ. St., Seattle, WA (1987).

2) Sigma Chemical Co. product note. *Enzyme Assay Procedure using ONPG as Substrate.* Sigma Chemical Co., P.O. Box 14508, St. Louis, MO (1987).

3) Maniatis, T., E.F. Fritsch, and J. Sambrook. Molecular Cloning: A Laboratory Manual. Cold Spring Harbor Laboratory Press, Cold Spring Harbor, NY (1983).

4) Huang, J. and G. Guiochon. *Application of Preparative HPLC to Peptides and Proteins.* BioChromatography **3**(4):140-148.

5) Kato, Y. *The Toyo Soda TSK-SW Column.* CRC Handbook of HPLC for the Separation of Amino Acids, Peptides, and Proteins: Vol. II. CRC Press, Boca Raton, FL (1984).

6) Ladisch, M.R., R.L. Hendrickson, and K.L. Kohlmann. *Correlation of Protein Equilibria at High Concentrations for an Anion Exchange Resin.* American Chemical Society Convention, Miami Beach, FL (1989).

7) Robyt J.F., and B.J. White. Biochemical Techniques - Theory and Practice. Brooks/Cole Publ. Co., Monterey, CA (1987).

8) Landon, M., *Cleavage at Aspartyl-Prolyl Bonds.* Methods in Enzymology **47**:145-149 (1977).

9) Piszkiewicz, D., M. Landon, and E.L. Smith. *Anomalous Cleavage of Aspartyl-Prolyl Peptide Bonds during Amino Acid Sequence Determinations.* Bioch. & Bioph. Research Comm. **40**(5):1173-1178 (1970).

Fig. 1: Genetic and Amino Acid Sequence of Engineered β-Galactosidase

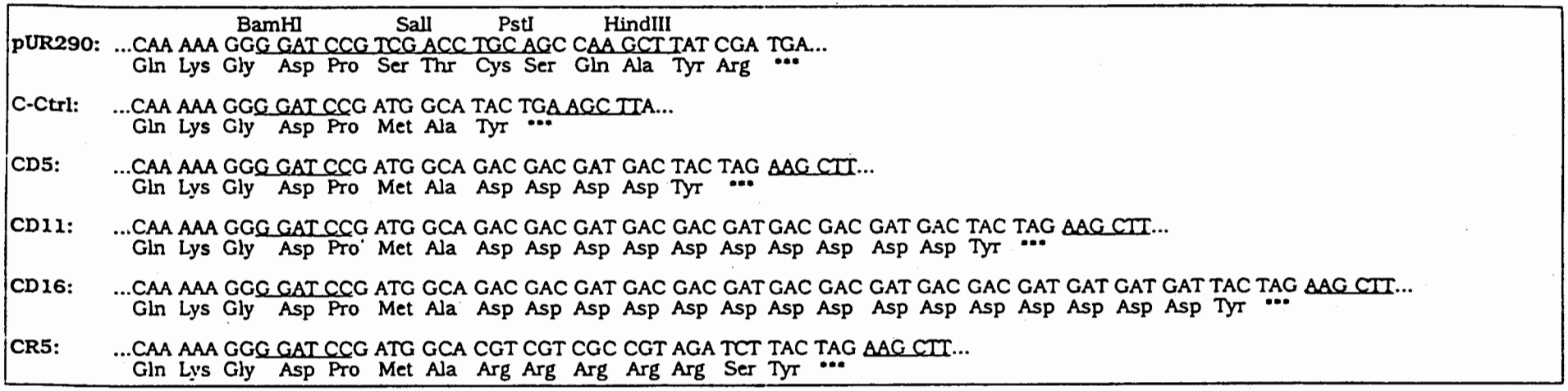

Fig. 2: SDS-PAGE of β-Galactosidase

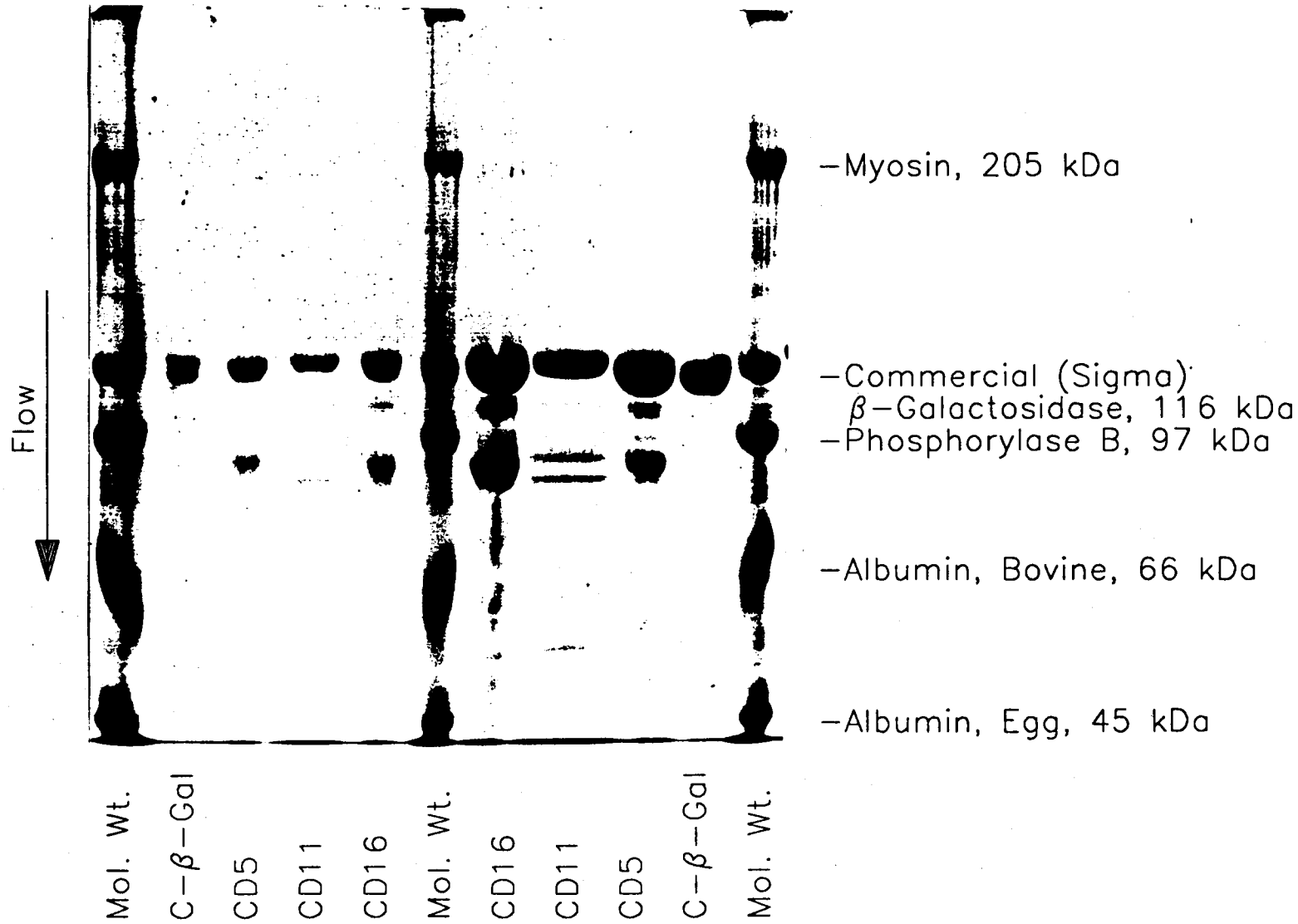

Fig. 3: Effect of Tail Length on Size Exclusion

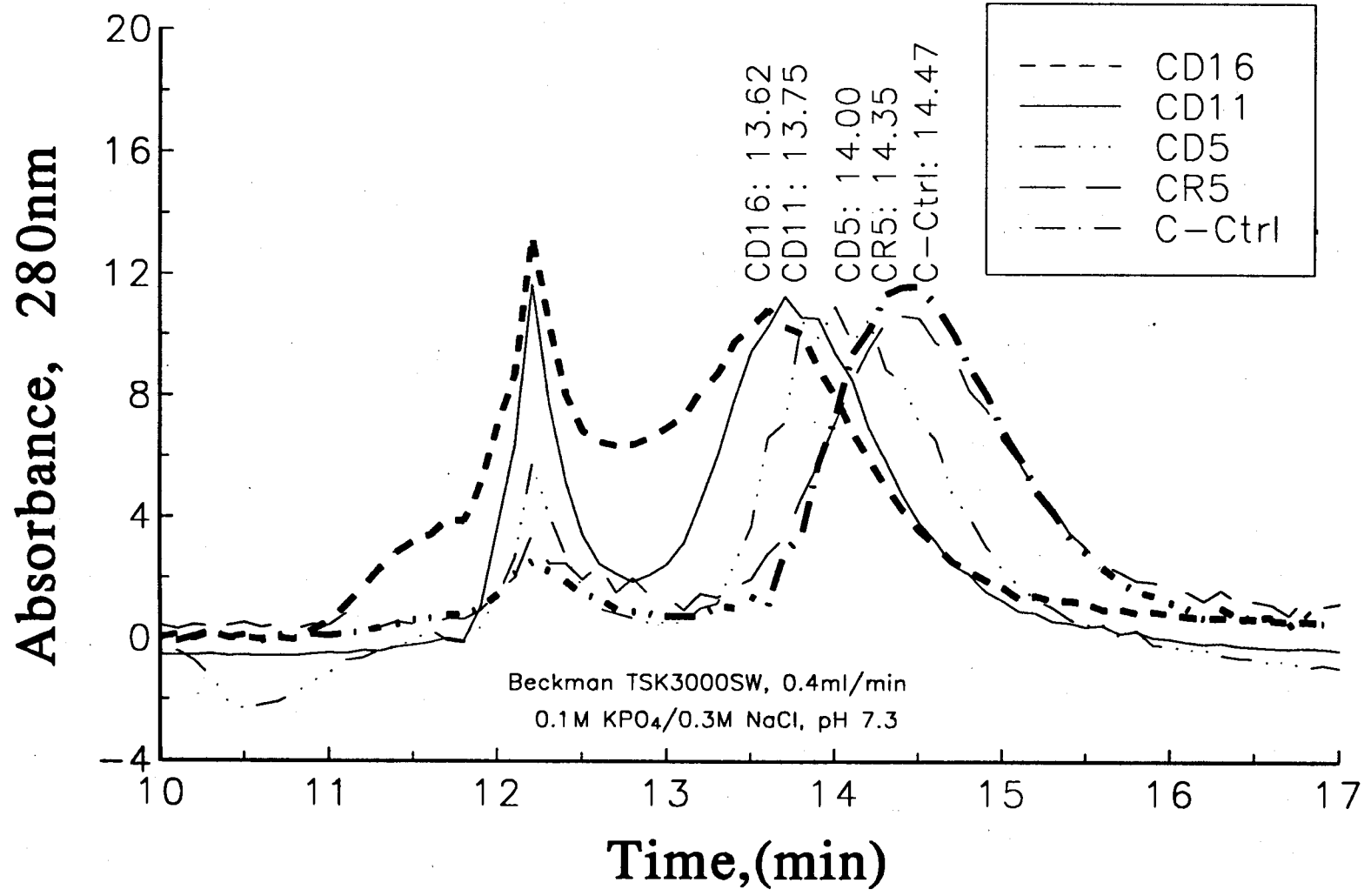

Fig. 4: Effect of Charged Tail Length on HPIEC Elution

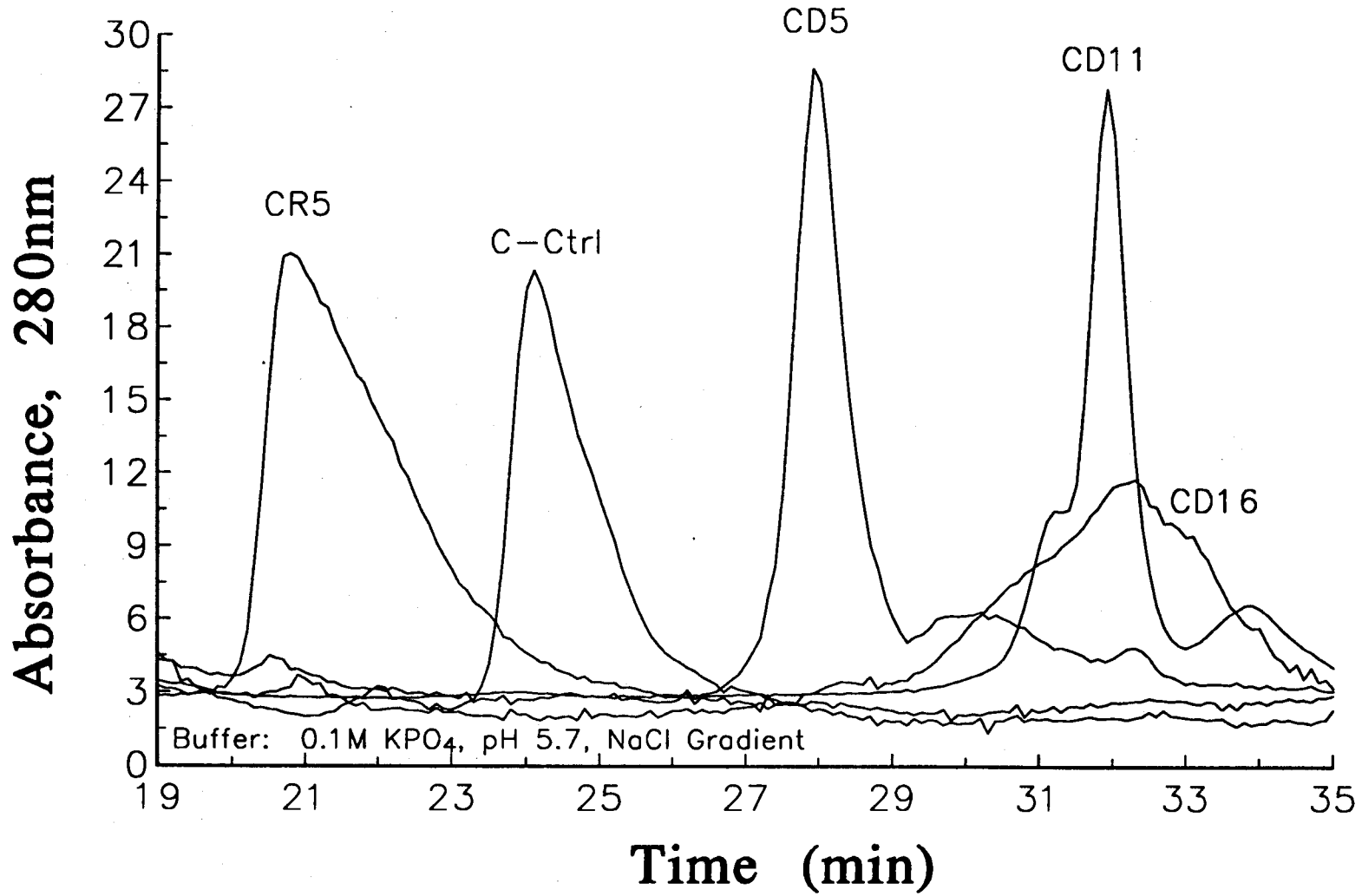

Fig. 5: Effect of Net Charge on Elution Strength

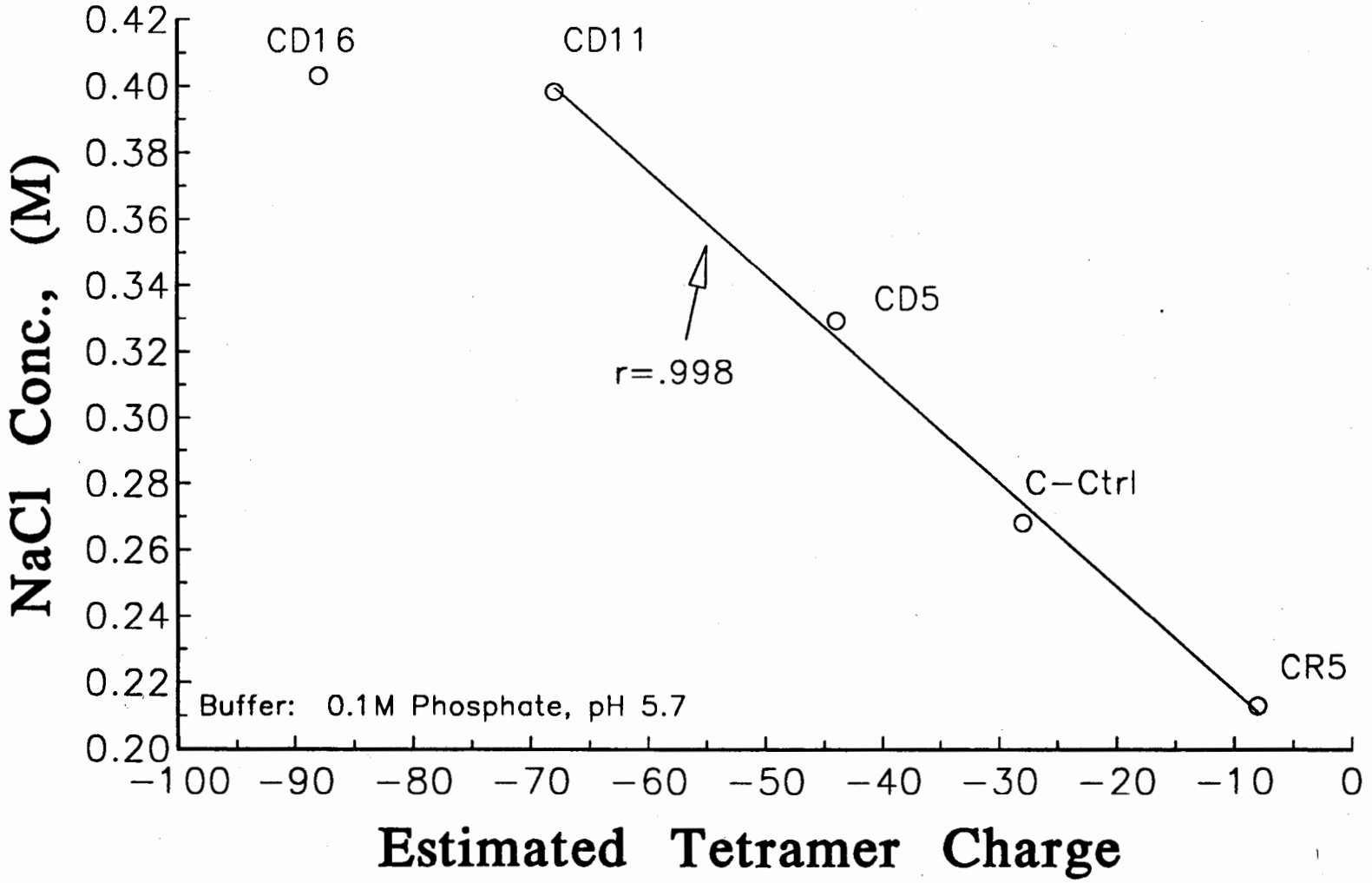

COMPUTATION OF CONFORMATIONS AND ENERGIES OF α-GLUCOSYL DISACCHARIDES

Jing Zeng, Michael K. Dowd, and Peter J. Reilly

Department of Chemical Engineering
Iowa State University
Ames, IA 50011

1. Introduction

Molecular mechanics techniques using a force field or potential function have developed into an important tool for predicting the structures and energies of molecules. Much of the early work in the carbohydrate area was aimed at determining polysaccharide structure. The pyranose ring has been studied extensively and the techniques have successfully predicted chair conformations (Sundararajan and Rao, 1968) and anomeric distributions (Angyal, 1968). Several researchers have reported on aspects of the modelling of maltose and cellobiose, the dimer units of the important polysaccharides, amylose and cellulose (Melberg and Rasmussen, 1979, 1980; French, 1988; Tran and Buleon, 1988; Ha *et al.*, 1988). Only limited work has been reported for most other disaccharides.

Studying saccharide and oligosaccharide structures with these methods has proven quite demanding. Because of the conformational complexity of saccharide monounits, a complete characterization of the conformational space is not yet obtainable. Consequently, simplifying assumptions are necessary to approach these problems. In general these involve either forcing some parts of the molecules to be rigid (typically the ring structures) or neglecting some of the possible rotational conformers.

We have previously worked on the HPLC, GC, NMR, and anomeric and general equilibria of the five α-linked glucosyl disaccharides: α,β-trehalose, kojibiose, nigerose, maltose, and isomaltose. Stick diagrams of these molecules are given in Figure 1. Here we report on the conformations and energies of these disaccharides as obtained by molecular modelling. Both the α– and β–conformers have been studied. In principle, the energies obtained using molecular mechanics can be used to determine anomeric equilibria after accounting for the populations of different conformers, entropic effects, and solvation. By making simple assumptions about the entropy, we have calculated anomeric distributions for maltose, nigerose, and kojibiose and have compared the results with reported experimental values.

2. Computational Procedures

The molecular mechanics program MMP2(85), developed by Allinger (1977) and distributed by the Quantum Chemistry Program Exchange (Department of Chemistry, Indiana University, Bloomington, IN 47405), was used to obtain

steric energy contour maps of α,β-trehalose, β-kojibiose, β-nigerose, and β-maltose. The maps were obtained by using the driver option of MMP2 to rotate the Φ and Ψ bonds between the two glucosyl rings in 10-15° intervals. Torsional angles (Φ, Ψ and ω) are defined as ∠(A-B-C-D) with the sign being taken as positive if the direction taken by bond A-B when rotated around B-C to cover C-D is clockwise. Because the maps only generate optimized structures relative to the fixed Φ and Ψ torsional angles, the low-energy conformers from these plots were further optimized by relaxing Φ and Ψ. Energy variations about the hydroxymethyl groups were then accounted for by optimizing each minimum about each *trans* orientation. The exocyclic torsional angles associated with the hydroxyl ligands were not optimized because the number of conformers quickly becomes overwelming (3^9 optimizations for each of the 3^2 *trans* orientations of each minimum). Hence, each minimum reported should be thought of as a manifold of minima relative to the neglected exocyclic torsion angles.

A full map for β-isomaltose was not generated because the MMP2 driver is capable of handling only two rotatable bonds. We found the minima for this disaccharide by optimizing selected initial conformations about the Φ, Ψ, and ω bonds. The initial conformations were chosen from the possible *trans* orientations as well as from other favorable conformations determined with the aid of stick models. Initial conformations for all structures were calculated with a program MINP (QCPE #543).

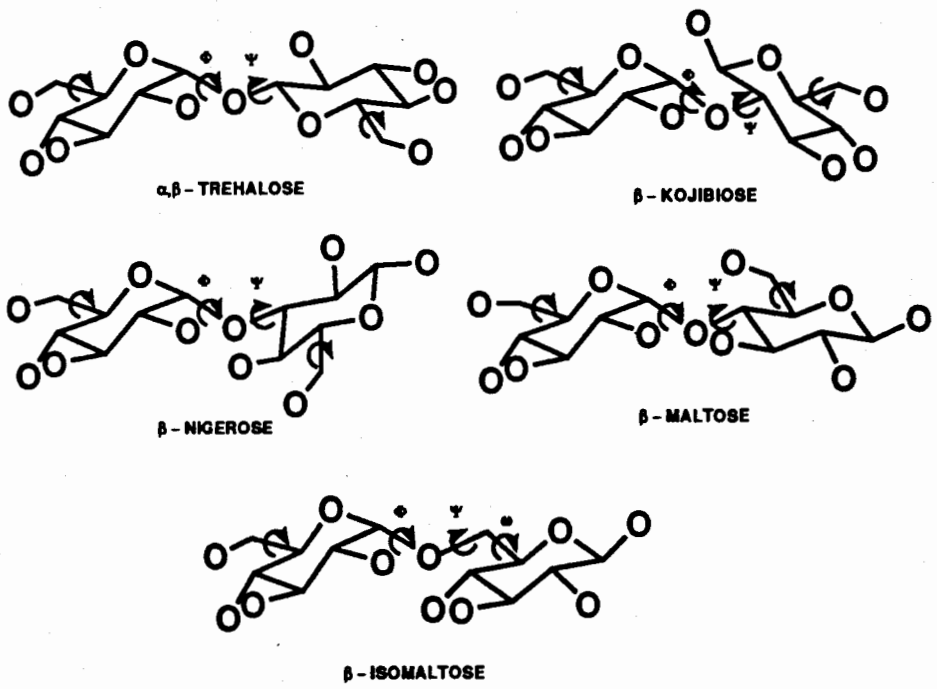

Figure 1. Stick figures of α,β-trehalose, β-kojibiose, β-nigerose, β-maltose and β-isomaltose

Average gas-phase energies were calculated by using Boltzmann's energy distribution with the assumption that the entropic differences between the the α-and β-anomers are negligible. A simple solution model that accounts for dielectric effects was used to determine the energies of the disaccharides in solvents:

$$E_{solution} = E_{steric} + E_s$$

where E_s represents the energy of solvation. For a polarizable dipole, this energy is given by

$$E_s = -\frac{1}{2}\frac{f\mu^2}{(1 - f\alpha)}$$

where μ is the dipole moment of the solute, f is the field factor and α is the molecular polarizability. The field factor and polarizability factor are given as

$$f = \frac{2}{a^3}(1 - \varepsilon^{-1/3})$$

and

$$\alpha = a^3 (n_d^{2/3} - 1)$$

respectively, where a represents the cavity radius and is taken as the average of the solvent and solute molecular radii, ε represents the dielectric constant, and n_d is the solute refractive index. We used the program MOLSV (QCPE #509) to calculate the disaccharide molecular radii. For the solvents the radii used were 138.5 pm for water and 214.0 pm for pyridine. The dielectric constants for these solvents were 78.3 for water and 12.4 for pyridine. For all calculations n_d was taken as 1.56 (Tvaroska, 1982). The hydrogen bonding contributions were taken as being identical for each anomer pair since the number of hydroxyl groups does not change.

3. Results

Contour plots for α,β-trehalose, β-kojibiose, β-nigerose, and β-maltose are given in Figure 2. Also shown on each map are the locations and energies of optimized minima within 5 kcal of the lowest minimum. In general, the process of relaxing the torsional angles did not affect the locations of the low-energy minima. Only minima with higher relative energies moved appreciable. In addition, we found that the second optimization step did not greatly lower the conformational energies.

The map and locations of the minima for β-maltose are in good agreement with previous work by Melberg and Rasmussen (1979) and Ha et al. (1988). Both groups report five β-maltose minima that are in agreement with our results. Melberg and Rasmussen also found that the conformations of the lowest two minima are in agreement with NMR work and X-ray structures.

One point about these maps should be noted. During the optimizing procedure, the driver starts a new map point with the optimized conformation generated at the previous point. This can cause problems when passing through the high-energy regions of the map, where the basic geometry of the pyranose rings can become distorted. These distorted structures can then be propagated through other optimized points, generating non-global minima. In this work we have restarted the optimization process when we found this problem, but some of the high energy regions in our maps may exhibit this feature. French *et al.* (1990) have recently presented a procedure for correcting for this problem. Their procedure starts each optimization from a single optimized point and then compares the results from a few initial configurations.

For β-isomaltose the minima we found are shown in Figure 3 together with the contours generated with the simpler force field used by Tvaroska *et al* (1978). In this earlier work the rings were held rigid and not allowed to flex with the optimization. Because they are generating maps, each of the rotatable bonds between the two rings was also fixed. The minima found with MMP2 are in reasonable agreement with their contours, although some of our minima are considerable outside the *trans* ω orientations (i.e. 180°, 60°, or -60°) that Tvaroska's structures are restricted to. These minima are associated with values of Ψ around -60°. Crystal conformations of oligosaccharides with α-(1→6) linkages were in close agreement with our lowest minima in the ω = 180° and -60° planes. A minimum was found in the ω = 60° plane with a much lower energy than had been found previously.

For all the disaccharides studied, the low-energy conformers lie in a narrow range of Φ values from -60° through 0° to 60°, and over a much wider range for Ψ. An average *gauche* orientation of Φ is preferred for all the disaccharides. This may be necessary to keep the rings separated or may be related to the exo-anomeric effect. In all the disaccharides but β-isomaltose, the favored range for Ψ is between -180° through 0° to 45°, with the lowest energies centered around the range of -45° to 45°. Additional minima are found at larger values of Ψ, but they are relatively high energy. For isomaltose the range extends from -60° through -180°(180°) to 60°, with the minima being clustered at the three *trans* orientations. The lowest minima tend to be clustered around Φ = 0. Energy minima were also a lower for β-isomaltose, as expected, because the third rotatable bond separates the rings further (Fig. 1). A larger number of minima were generated for this disaccharide and the the molecule is found to occupy a larger proportion of conformational space confirming a greater degree of conformational flexibility consistent with the larger distances between the two rings. For all the disaccharides the low-energy conformations had their ring separated and were slightly bent or twisted.

Values of the calculated anomeric distributions in solvents are given in Table 1. In water, the results are in reasonable agreement with the work of Toba and Adachi (1977). In particular for maltose and kojibiose the favored α-forms in the gas phase become less favored in water. For nigerose the β anomer is favored in either case, although it is less favored in the water. The changes with solvation are all in the correct direction, as expected from the experimental data. In pyridine, the results are not in as good agreement. The experimental results of Nikolov and Reilly (1983) in pyridine are close to the results in water, even though the solvents are chemically quite different. The solution model used in this work has a much smaller effect on the energies in

pyridine, causing an undercorrection of the energies. In general a more comprehensive model may be required to adequately describe the solvation effects.

4. References

Allinger, N. L. (1977) *Conformational Analysis. 130. MM2. A Hydrocarbon Force Field Utilizing V1 and V2 Torsional Terms.* J. Am. Chem. Soc. 99: 8127-8134.

Angyal, S. J. (1968) *Conformational Analysis in Carbohydrate Chemistry. I. Conformational Free Energies. The Conformations and α : β Ratios of Aldopyranoses in Aqueous Solutions.* Aust. J. Chem. 21: 2737-2756.

French, A. D. (1988) *Rigid- and Relaxed-Residue Conformational Analysis of Cellobiose Using the Computer Program MM2.* Biopolymers 27: 1519-1525.

French, A. D., V. H. Tran, and S. Perez (1990) *Conformational Analysis of a Dissacharide (Cellobiose) with the Molecular Mechnics Program, MM2.* in Computer Modeling of Carbohydrate Molecules. ACS Symposium Series. edited by French & Brady 430pp.

Ha, S. N., L. J. Madsen, and J. W. Brady (1988) *Conformational Analysis and Molecular Dynamics Simulations of Maltose.* Biopolymers 27: 1927-1952.

Melberg, S. and K. Rasmussen (1979) *Conformations of Disaccharides by Empirical Force-Field Calculations: Part I. β-Maltose.* Carbohydrate Res. 69: 27-38.

Melberg, S. and K. Rasmussen (1979) *Conformations of Disaccharides by Empirical Force-Field Calculations: Part II. β-Cellobiose.* Carbohydrate Res. 71: 25-34.

Nikolov, Z. L. and P. J. Reilly (1983) *Isothermal Capillary Column Gas Chromatography of Trimethylsilyl Disaccharides.* J. Chromatogr. 254: 157-162.

Sundararajan, P. R. and V. S. R. Rao (1968) *Theoretical Studies on the Conformation of Aldopyranoses.* Tetrahedron 24: 289-295.

Toba, T. and S. Adachi (1977) *Gas-Liquid Chromatography of Trimethylsilylated Disaccharide Oximes.* J. Chromatogr. 135: 411-417.

Tran, V. and A. Buleon (1988) *Relaxed Potential Energy Surfaces of Maltose.* Biopolymers 28: 679-690.

Tvaroska, I. (1982) *Theoretical Studies on the Conformation of Saccharides. IV. Solvent Effect on the Stability of β-Maltose Conformers.* Biopolymers 21: 1887-1897.

Tvaroska, I., S. Perez, and R. H. Marchessault (1978) *Conformational Analysis of (1→6)-α-D-Glucan.* Carbohydrate Research 61: 97-106.

Table 1. Energies and distributions of α-glucosyl disaccharides.

		maltose		nigerose		kojibiose		α,β-trehalose
		α	β	α	β	α	β	
In vacuo	E_{ave}	31.75	32.67	33.14	32.36	32.66	33.46	31.75
	x	82.5	17.5	21.1	78.9	79.4	20.6	
In water	E_{ave}	26.78	26.45	29.17	29.02	31.06	30.70	28.19
	x	36.4	63.6	43.7	56.3	35.3	64.7	
Toba & Adachi (1977)	x	44	56	56	44	47	53	
In pyridine	E_{ave}	29.92	30.44	31.63	31.52	32.04	32.47	30.48
	x	70.6	29.4	45.4	54.6	67.4	32.6	
Nikolov & Reilly (1983)	x	44.8	55.2	60.3	39.7	33.8	66.2	

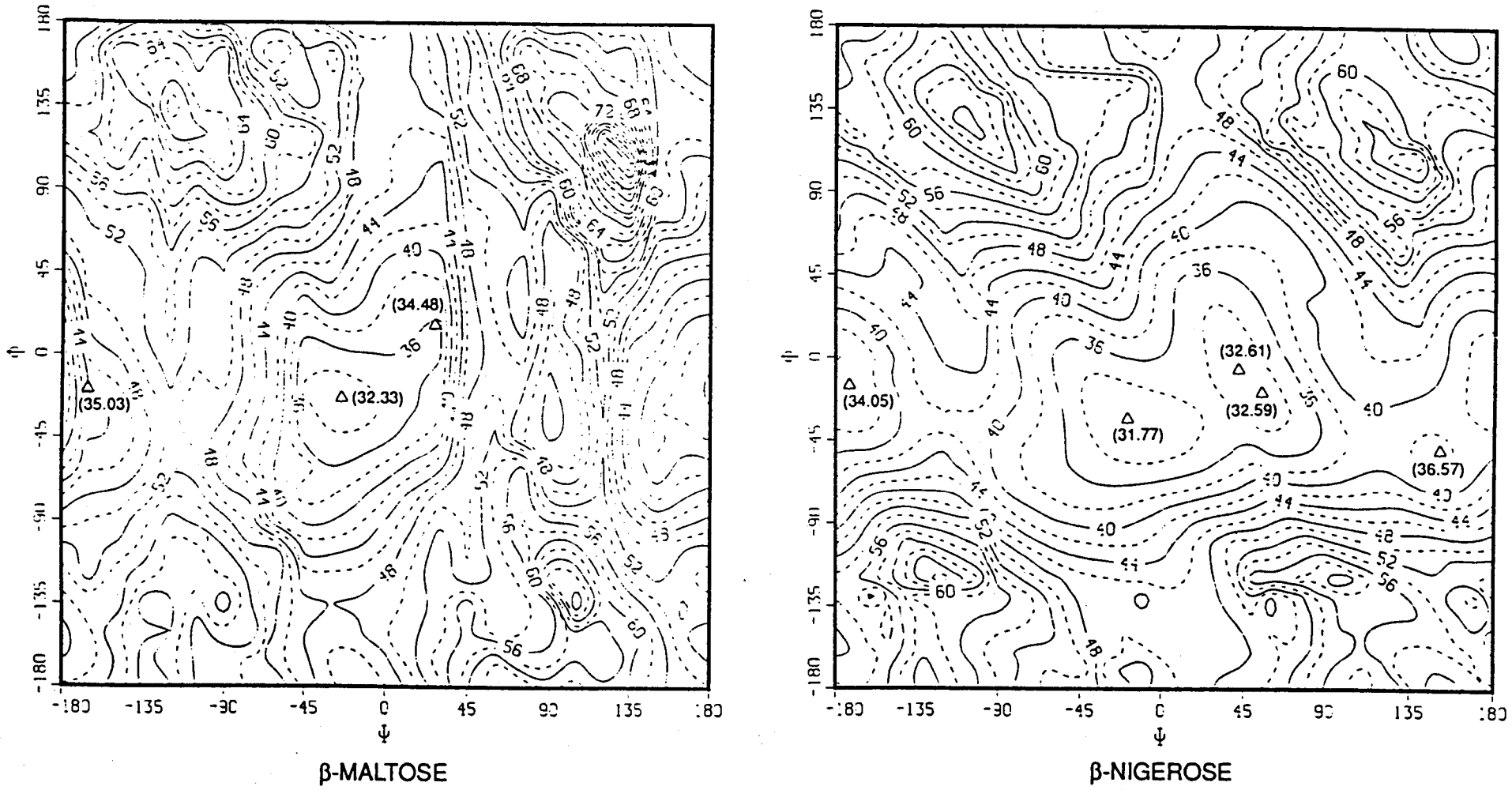

Figure 2. Isoenergy contour maps for β-maltose, β-nigerose, β-kojibiose, and α,β-trehalose.

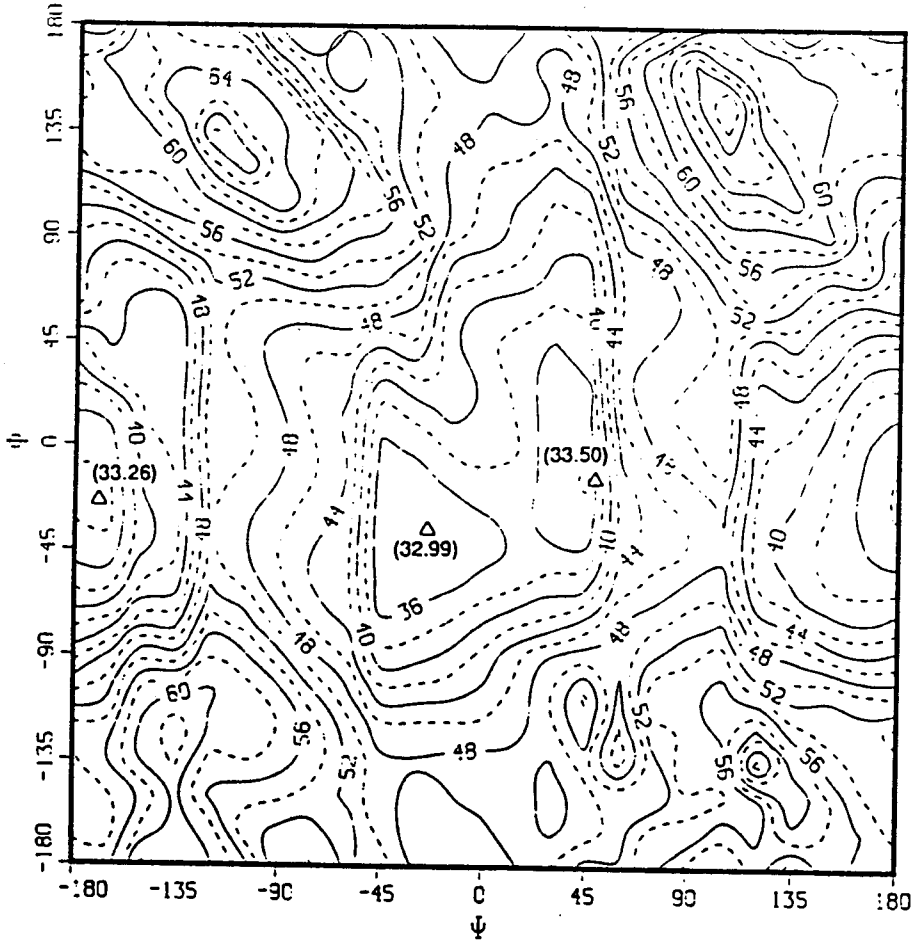

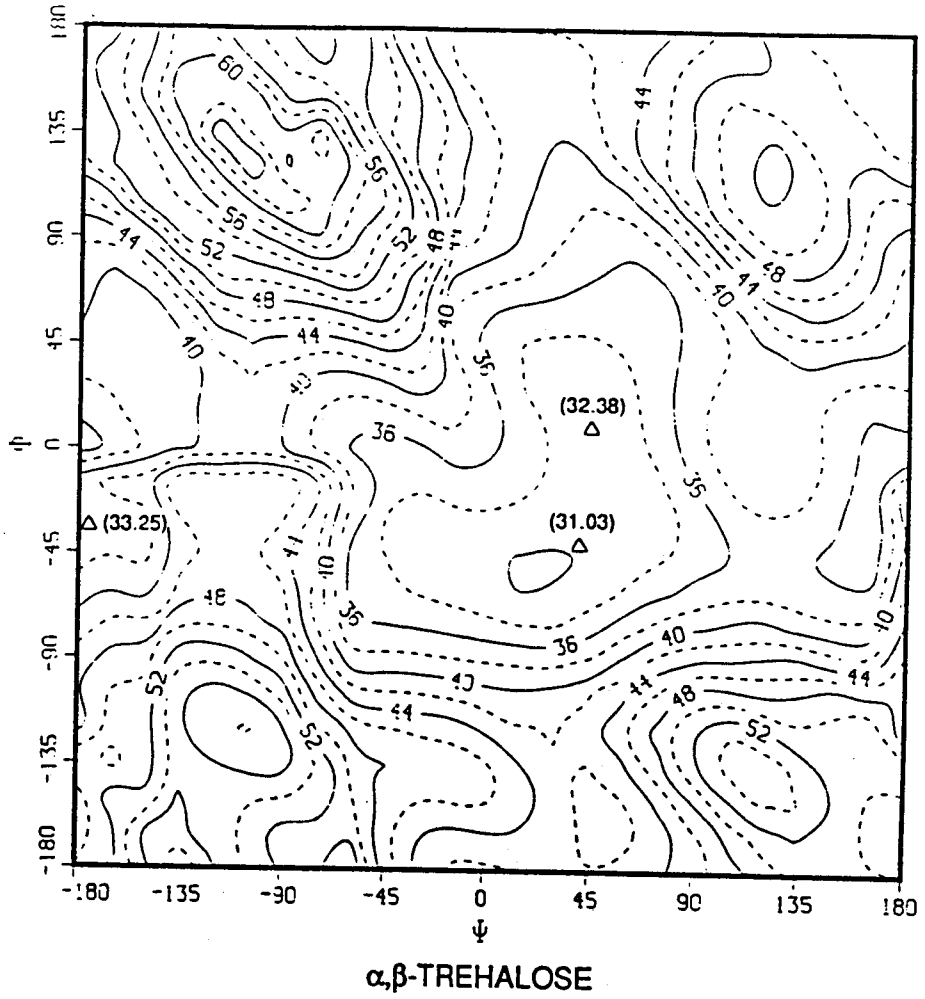

Figure 2. **(continued)**

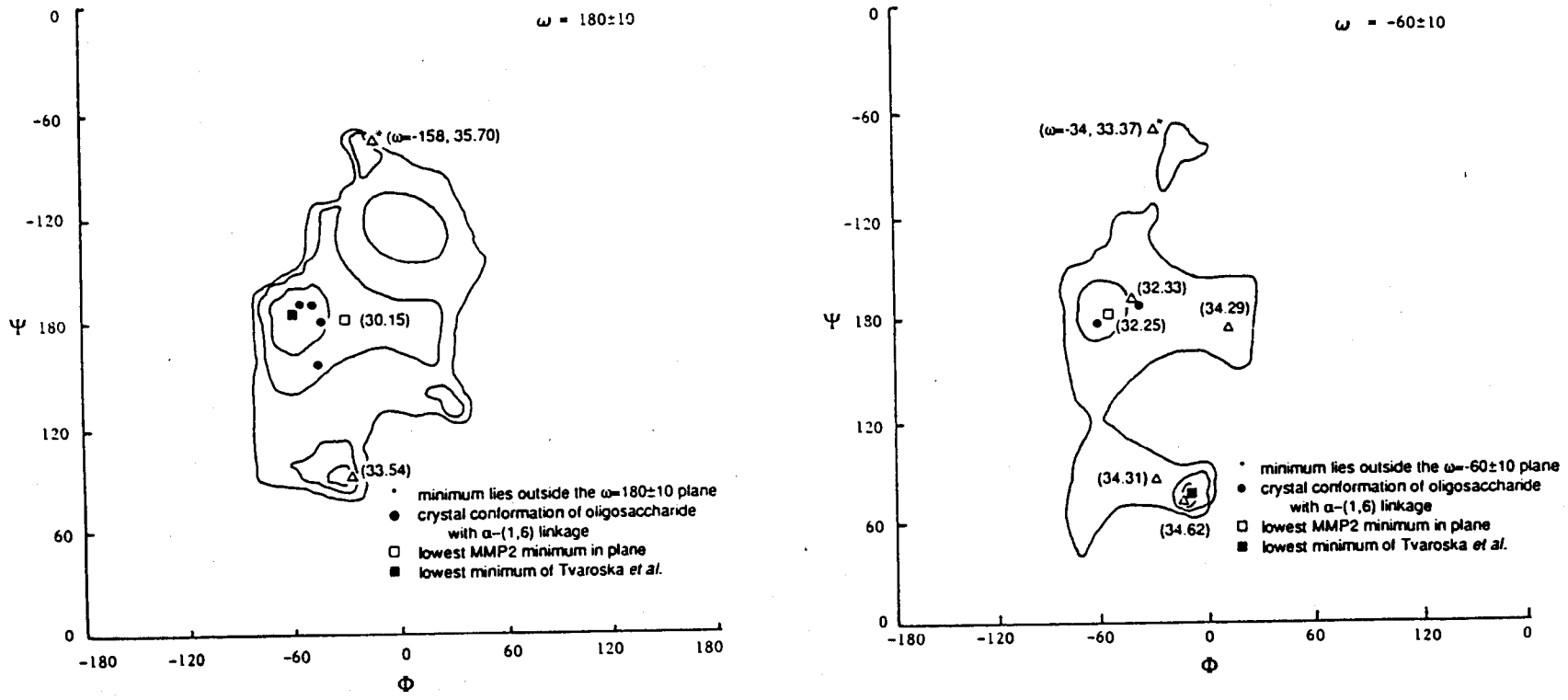

Figure 3. MM2(85) minima for β-iomaltose. Contour lines are from Tvaroska *et al.* (1978).

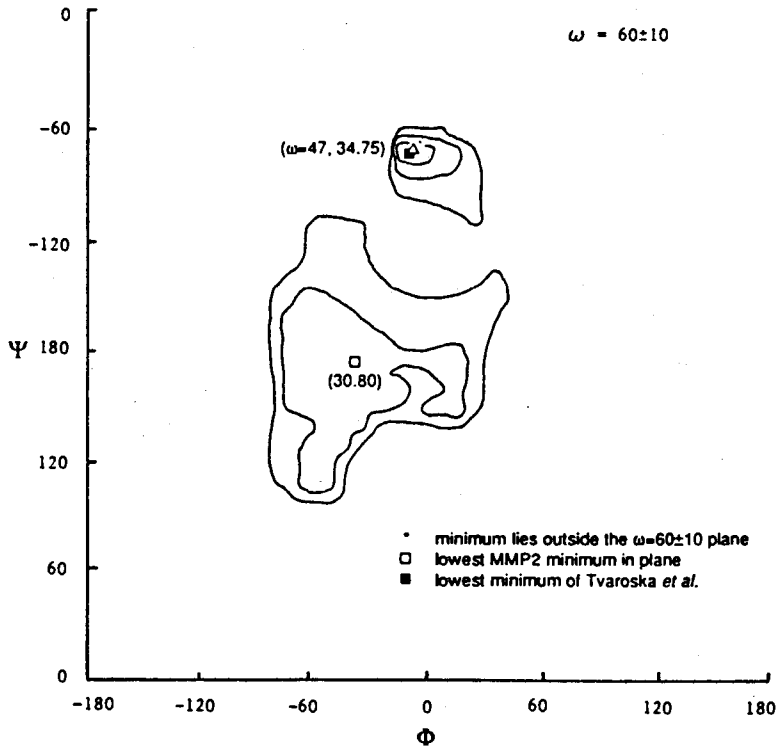

Figure 3. (continued)

PENTACHLOROPHENOL INTERACTIONS WITH SOIL

Shein-Ming Wei
Shankha K. Banerji
Rakesh K. Bajpai*
Department of Civil Engineering
University of Missouri
Columbia, MO 65211

ABSTRACT:

Pentachlorophenol (PCP) adsorption and desorption was studied with two Menfro silt loam soils -- upper horizon and lower horizon. For the adsorption studies the variables were: temperature (10° and 30°C) and the amount of organic matter. The variables for the desorption studies confirmed the importance of soil organic matter for adsorption of PCP on the soils. The adsorption data at different temperatures indicated the physical nature of the adsorption process. The desorption data produced non-singularity and some PCP was irreversibly adsorbed onto the soil despite repeated washings. Increased pH increased the desorption of PCP from the soil. The anionic surfactant, sodium dodecylbenzene sulfonate (SDS) was able to desorb significant amounts of PCP from the soil at doses equal to critical micelle concentration (CMC). But, the nonionic surfactant, Triton X-405 required a much higher dose, twice the CMC to cause a significant desorption of PCP from the soil.

INTRODUCTION:

Pentachlorophenol (PCP) has been used extensively in the past as a wood preservative, pesticide and herbicide (1). As such, many sites exist in the U.S. and other parts of the world where the soil and aqueous environment has been contaminated with this compound (2). Presently, the use of PCP as a wood preservative has been restricted by the U.S. EPA due to its toxic properties (3).

The primary aim of the study was to determine the interactions (adsorption/desorption) of PCP with soils under different environmental conditions. Temperature, and presence of organic matter in the soils were the variables studied. Desorption of the PCP from the soil was determined at different temperatures, pH and in the presence of surfactant molecules.

MATERIALS & METHODS:

Soils: The soils chosen were two Menfro series fine silt loam, one upper horizon and the other lower horizon soil, obtained from a site near Columbia, Missouri. The Menfro series consists of deep, well drained soils on uplands. These soils formed in silty loess deposits 6 to 20 feet thick. The permeability of the soil is moderate.

---

* Department of Chemical Engineering, University of Missouri- Columbia

Chemicals: The PCP used in the study was obtained from Sigma Chemical Company, St. Louis, Missouri. It was 99.3% pure.

Powdered humic acid was also obtained from Sigma Chemical Company. It was purified by washing with 0.01N NaOH and subsequent precipitation with H_2SO_4. Humic acid was used to increase the organic content of the soils.

Two surfactants were used to aid in the desorption of the PCP from the soil. The first one was an anionic surfactant dodecylbenzene sulfonate (80% aqueous solution) obtained from Pfaltz and Bauer, Inc., Stamford, CA. The second one was a nonionic surfactant Trition X-405 (t-octylphenoxypolyethoxyethanol) (70% aqueous solution) obtained from Sigma Chemical Company, St. Louis, Missouri.

Analytical Methods:

Aqueous PCP samples were measured by extraction with methylene chloride and concentrated, 2-propanol was added to the mixture and heated to remove methylene cholride. The PCP in 2-propanol was injected into a gas chromatograph (GC) in accordance with EPA Method 604. The temperature of program started at 75°C for 12 min., increased to 180°C at 8°C/min., and carrier gas flow rate was 15 ml/min. Helium was used as carrier gas in this method. A flame ionization detector was used for PCP detection.

In addition, High Pressure Liquid Chromatograph (HPLC) was also used to determine aqueous PCP samples using a 100:1 mixture of acetonitrile/acetic acid as the solvent at the flow rate of 0.5 ml/min. UV detector was used for PCP detection.

RESULTS AND DISCUSSIONS:

Equilibrium Adsorption and Desorption Kinetics: Figure 1 shows the kinetics of adsorption of PCP on the upper horizon soil at pH 6.5 and temperature of 30°C. It can be seen that equilibrium was reached in 24-30 hours. Similar results were obtained at 10°C. Lee, et al. (6) found that with the different soil systems the PCP adsorption equilibriums were reached in 4 hours. Karickhoff, et al. (7) observed that for compounds with low solubility, soil adsorption equilibrium was generally attained after 24 hours. Therefore, the results obtained for PCP adsorption kinetics are generally in line with the observations made by other. For all subsequent adsorption experiments the equilibration time was taken as 48 hours.

Figure 1 also shows the desorption kinetics. It is evident that after about 24 hours equilibrium was reached. The rate of desorption was found to be approximately the same as the adsorption rate. Voice and Weber (8) reported that the kinetics of desorption were generally slow, but did not indicate the time involved in the process. Isaacson and Frink (9) studied the adsorption/desorption of phenol, 2-chlorophenol and 2,4-dichlorophenol on sediments. They, also found that desorption of these phenols was much slower than the adsorption on sediments.

Equilibrium Adsorption Isotherm: Freundlich isotherm equation is given by:

$$X/M = K\,Ce^{1/n} \quad (1)$$

where: X/M = Concentration of sorbate (PCP) on the soil (mg/kg soil)
Ce = Equilibrium concentration of the sorbate, (mg/L)
K & n = Constants characteristics for the system

$$X/M = Kp\,Ce \quad (2)$$

where:
Kp = Equilibrium Partition coefficient.

In the logarithmic form Equation 1 becomes:

$$\log\ X/M = \log\ K + 1/n \log\ Ce \quad (3)$$

A log-log plot of X/M vs Ce, provides a method for determining constants K and n. Figures 2 and 3 show the log-log plot of X/M vs Ce for the two soils at 30°C and 10°C, respectively. The K and n values are tabulated in Table 1. It can be seen that the upper horizon soil had higher values of K at both temperatures compared to the lower horizon soil, which indicated a higher capacity to adsorb PCP in aqueous solution. This was clearly evident from Figures 2 and 3; also, the equilibrium adsorption values for upper horizon soil at all concentrations were higher than that of lower horizon soils. The n values were fairly close 1.0 except for the upper horizon soil at 30°C, which was 1.45.

The K values observed here were in the same range as observed by Lee et al. (6) for PCP adsorption on different soils. However, Schellenberg et al. (10) reported Kp values for PCP sorption to be much higher (200-3670 cm 3/g) in river and lake sediments. These adsorptions were carried out at different pH values and the sediments had different amounts of organic matter.

The effect of temperature on the adsorption of PCP on the two soils is evident by looking at the values of K in Table 2. At lower temperatures (10°C) the PCP adsorption (K value) was always higher for both soils, which indicated that chemisorption was not a factor here. The adsorption of PCP on these soils was a physical process rather than a chemical process.

The Koc values for the two soils were also calculated and are shown in Table 1. It can be seen that upper horizon soil having a larger organic carbon content had Koc value much higher than the lower horizon soil. The soil constituent properties (% clay, etc.) played an insignificant role in the adsorption of PCP on these soils. The lower horizon soils having a larger clay content, presumably larger surface area per unit mass had a lower adsorption capacity compared to the upper horizon soil. The Koc values shown in Table 1 are comparable to values reported in the literature for PCP at pH 6.5 (7). The Koc values reported by Schellenberg et al. (10) were much higher than reported herein. The difference could be that Koc values were being measured by these investigators at lower pH values than 6.5, which would increase the partitioning of PCP on the soils.

Effect of Organic Carbon:

As shown in Table 2 the presence of organic matter in the upper horizon soil increased the PCP adsorption to a great extent. Humic acid was added to the upper horizon soil to further increase the amount of organic carbon in the soil. In addition, sodium hydroxide treatment was done to a sample of the upper horizon soil to remove as much of the natural organic matter of the soil as possible. The results of the adsorption studies with different organic carbon levels are shown in Table 3. It is evident again that increasing the organic content of the soil increased the amount of PCP retained on the soil. The relationship between PCP adsorbed and % organic carbon of the soil was linear (Figure 4). If linear adsorption isotherm is assumed for the PCP adsorption on this soil (Equation 2), the Kp and Koc values for the adsorption data can be calculated i.e., Kp = X/M/Ce and Koc = Kp/foc. Table 3 also shows the Kp and Koc values, which were comparable to that reported in Table 2. The Koc value for these soils remained fairly constant, as expected, with different organic content of the soils.

Equilibrium Desorption Isotherm:

The equilibrium PCP desorption data are shown in Figures 5 and 6 at 30°C and 10°C. The desorption data at 10°C were somewhat erratic (Figure 5), which indicated that the desorption equilibrium did not follow the Freundlich equation. The data reported in Table 4 for 10°C were obtained with lines of best fit through the plotted data.

The upper horizon soil desorbed more PCP than the lower horizon soil. This was unexpected, since the upper horizon soil had a higher organic carbon content and was expected to retain higher amounts of the PCP. Presumably, the interaction between PCP and the organic matter was quite weak and easily reversible. The K values for desorption were generally lower than that obtained for adsorption (Table 2). There was some nonsingularity observed during desorption (i.e. hysteresis). This would indicate that some PCP was irreversibly adsorbed on the soil. others have reported such an irreversible adsorption of chlorophenols (9) and hysteresis with other compounds (11) (12). This finding is quite significant from the point of view of biological treatment of contaminated soil in a slurry reactor or in a land farm operation. If the adsorbed PCP cannot easily be desorbed in a reasonable amount of time, the microbial degradation may not be feasible. This concern has been mentioned by several investigators (4) (13).

Effect of pH on Desorption Equilibrium:

Table 5 shows the results of an experiment in which upper horizon soils were equilibrated with PCP solution at 30°C and pH 6.5, and a desorption experiment (as described in Material and Methods Section) was run at different pH values after the soil was separated from the equilibrium test, the soil samples were washed with 2-propanol to further recover more difficult to desorb PCP molecules. It can be seen that the increase of pH allowed higher recovery of the PCP molecule. At higher pH, PCP was present as a phenolate ion whose soil interaction would be expected to be weak, causing a larger fraction to be easily desorbed. The lower soil PCP adsorption at high pH was also reported by Lee et al. (6). They suggested that at higher pH in addition to phenolate ion, ion pairs of neutral cation-pentachlorophenolate are present in solution. The relative contribution

of sorption of ionized PCP to the total sorption of PCP is a function of pH and ionic strength.

The 2-propanol washing recovered variable amounts of PCP absorbed, but the total recovery was far short of the total adsorbed PCP. This would further indicate that a certain amount (25-50%) of PCP was irreversibly bound to the soil.

Surfactant Desorption Studies:

The use of surfactants has been proposed to improve the solvent characteristics of recharge water, to emulsify nonsoluble organics and to enhance the removal of hydrophobic organics sorbed onto soil particles (14). Much of the earlier experience with surfactants was achieved with tertiary oil recovery in the petroleum industry. Portier (15) applied a nonionic surfactant (Triton X-100) in a soil slurry reactor treating hydrophobic polyaromatic-hydrocarbon compounds (PAHs) to improve the solubilization of the compounds.

The results of desorption of PCP with sodium dodecylbenzene sulfonate (SDS) from the upper horizon soil at 30°C and pH 6.5 are shown in Figure 7. It can be seen that the desorption with SDS was the same as control (Distilled water) until the concentration of the SDS was increased to critical micelle concentration (CMC) (0.0012M, 418 mg/L)(5). At that level the desorption of PCP was significant, i.e. amount of PCP remaining on the soil was much lower. Higher than CMC concentration did not improve the desorption behavior. SDS is an anionic surfactant with an hydrophobic alkyl chain and a hydrophilic end containing the sulfonate ion. The effect of SDS on desorption of PCP cannot be explained on direct interaction between the molecules since both are anionic in nature. But, at CMC the surfactant molecules form an aggregate (micelle) in which PCP could be "trapped" inside (16).

The results of desorption of PCP with the nonionic surfactant Triton X-405 from the upper horizon soil at 30°C and pH 6.5 are shown in Figure 8. It can be seen that no significant desorption occurred until the concentration of the surfactant reached twice the CMC (0.0015M, 3000 mg/L)(5). It could be that Triton X-405 was also adsorbed on the soil and after the adsorption was completed, the surfactants are often used with herbicides and pesticides nonionic surfactants are often used with herbicides and pesticides to improve the action of these compounds in soil environment. Huggenberger et al. (16) reported the contrasting effects of surfactant concentration on herbicide adsorption on soil. Below the CMC of the surfactant concentrations, the adsorption of herbicide was reduced. This presumably was caused by the sorption of the herbicide by the surfactant micelles. The PCP desorption data with Triton X-405 followed a somewhat similar pattern.

ACKNOWLEDGEMENT:

Although the research described in this article has been funded in part by the U.S. Environmental Protection Agency under Assistance Agreement R-815709, to the University of Missouri-Columbia through the Hazardous Substances Research Center for U.S. EPA Regions 7

and 8, headquartered at Kansas State University, it has not been subjected to the Agency's Peer and Administrative review and therefore may not necessarily reflect the views of the Agency and no official endorsement should be inferred.

REFERENCES:

(1) Cirelli, D.P. "Patterns of Pentachlorophenol Usage in the United States of America." In "Pentachlorophenol: Chemistry, Pharmacology andEnvironmental Toxicity," Ed. Rao, K.R., P. 13, Plenum Press, New York (1978).

(2) Sittig, M. "Handbook of Toxic and Hazardous Chemicals," Noyes Publications, Park Ridge, N.J. (1981).

(3) Federal Register, 49, 28666 (July 1984).

(4) Smith, J. R. et al. "Application of Biodegradation Screening Protocol toContaminated Soils from Manufactured Gas Plant Sites." Proceedings IGT Symposium on Gas, Oil, Coal and EnvironmentalTechnology, New Orleans, La. (Dec. 1989).

(5) "Critical Micelle Concentration of Aqueous Surfactant System, U. S. Department of Commerce, National Bureau of Standards (1971).

(6) Lee, L. S., et al., "Influence of Solvent and Sorbent "Characteristics on Distribution of Pentachlorophenol in Octanol-Water and Soil-Water System," Environ. Sci. and Tech., 24, 5, 654 (1990).

(7) Karickhoff, S. W., Brown, D.S. and Scott, T.S., "Sorption of Hydrophobic Pollutants on Natural Sediments, "Water Res., 13, 241 (1979).

(8) Voice, T. C., and Weber, W. J., "Sorption of Hydrophobic Compounds by Sediments, Soils and Suspended Solids - I. Theory and Background," Water Res., 17, 1433 (1983).

(9) Isaacson, P. J. and Frink, C. R., "Nonreversible Sorption of Phenolic Compounds by sediment Fractions: The Role of Sediment Organic Matter,"Environ. Sci. and Tech., 18, 1, 43 (1984).

(10) Schellenberg, K. et al., "Sorption of Chlorinated Phenols by Natural Sediments and Aquifer Materials,"Environ. Sci. and Tech., 18, 9, 652 (1984).

(11) Vaccari, D. A. and Kaouris, M., "A Model for Irreversible Adsorption Hysteresis," Jour. Environ. Sci, Health, A23, 8, 797 (1988).

(12) Raman, S., et al., "Adsorption-Desorption of Atrazine of Four Soils of Hyderabad," Water, Air and Soil Pollution, 40, 177 (1988).

(13) Doyle, R. and Piotrowski, M., "In-situ Bioremediation of Wood Treating Compounds in Groundwater," Proceedings 10th National Conference on Superfund, Washington, D.C., Hazardous Materials Control Research Institute, Silver Spring, MD. (Nov. 1989).

(14) Amonette, J. and O'Connor, G. A. "Noionic Surfactant Effects on Adsorption and Degradation of 2,4-D" Soil Sci. Soc. Am. Jour., 44, 540 (1980).

(15) Portier, R. J., "Bioremediation Using Adapted Bacterial Cultures. Topic 1. Examination of Site Data and Discussion of Microbial Physiology with Regards to Site Remediation,j" Proceedings 10th National Conference on Superfund, Washington, D.C., Hazardous Materials Control Research Institute, Silver Spring, MD. (Nov. 1989).

(16) Huggenberger, F. et al., "Effect of Two Nonionic Surfactants on Adsorption and Mobolity of Selected Pesticides in a Soil-System, " Soil Sci. Soc. Am. Proc., 37, 215 (1973).

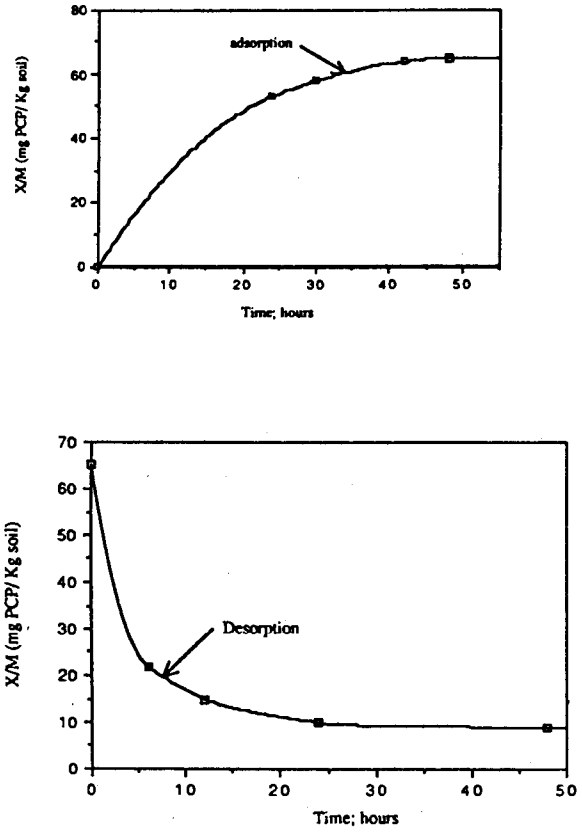

Fig. 1 Kinetics of adsorption and desroption of PCP in the Menfro Series Soil; pH=6.5, 30°C

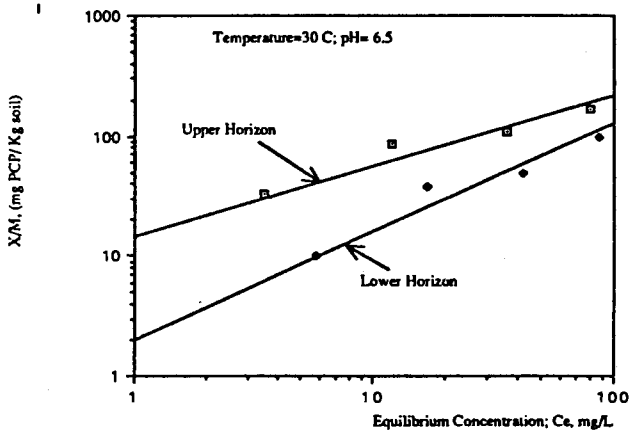

Fig. 2 Equilibrium Adsorption of PCP on the Menfro series Soil

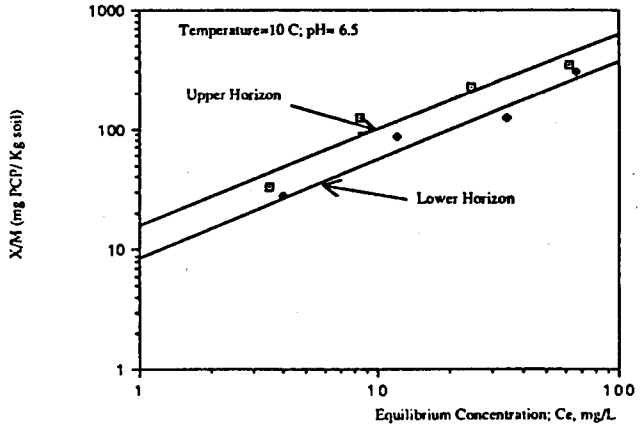

Fig. 3 Equilibrium Adsorption of PCP on the Menfro Series Soil

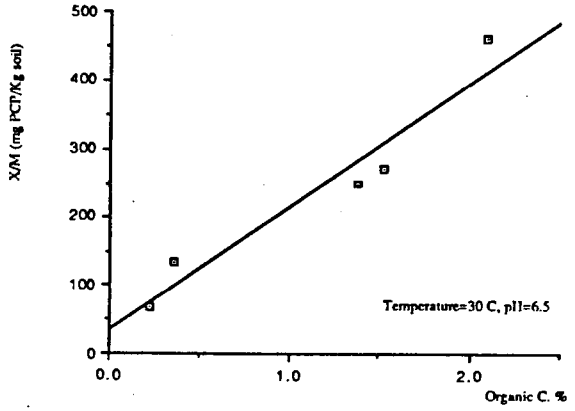

Fig. 4 Effect of Organic Carbon Content of the Menfro Series Soil on PCP Adsorption

	X/M (mg PCP/Kg soil)				
	adsorbed	desorbed			
		pH	desorbed by D.I. water	desorbed by 2-propanol	recovered (%)
sample A	846	5.0	225	175	50.8
sample B	846	6.5	480	4.8	57.3
sample C	846	9.0	592.5	24.3	72.9
sample D	846	11.0	620	5.2	73.9

TABLE 5 The Effect of pH on PCP Desorption & Rcorvery Upper Horizon Soil, temperature=30°C

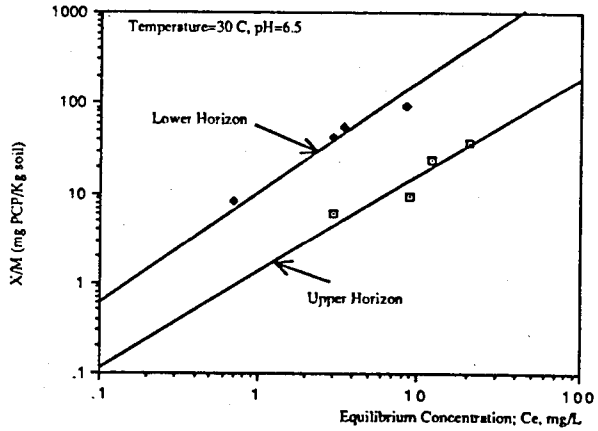

Fig. 5 Equilibrium Desorption of PCP on the Menfro Series Soil

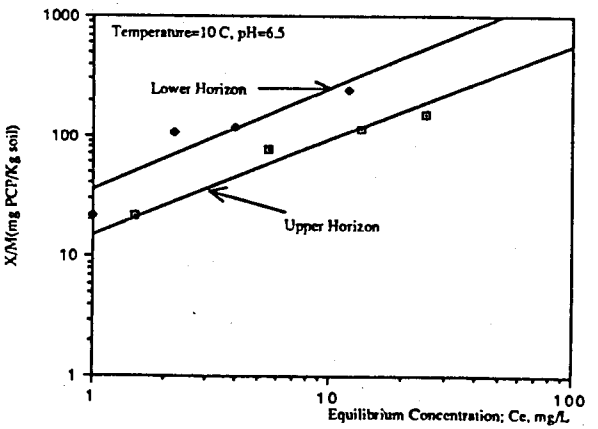

Fig. 6 Equilibrium Desorption of PCP on the Menfro Series Soil

Fig. 7 The Effect of Surfactant SDS on Desorption of PCP

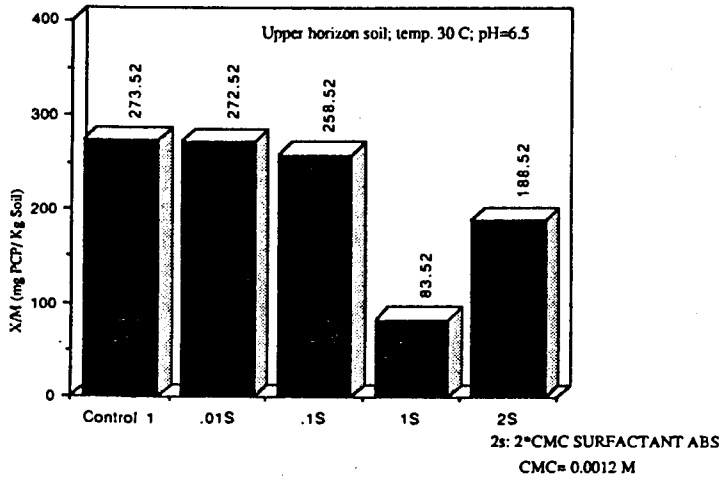

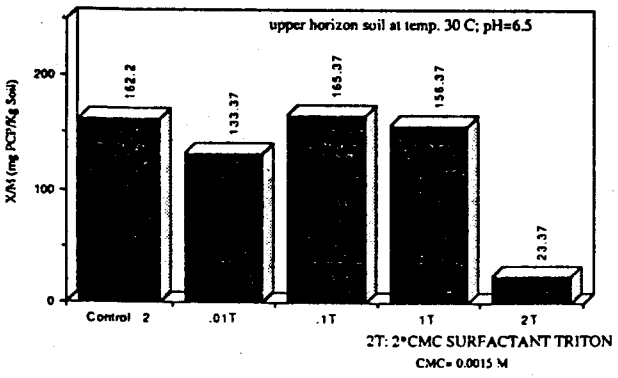

Fig. 8 The Effect of Surfactant Triton X-405 on Desorption of PCP

TABLE 1 Porperties of the Menfro Silt Loam Soil

SAMPLE	DEPTH	---SIZE DISTRIBUTION --- clay <.002(mm)	silt .002-.05.	sand .05-2	------pH------- $CaCl_2$ 0.01M	H2O	ORG. C %
upper horizon	0-5 cm	10.9	80.4	8.7	5.5	6.1	2.1
lower horizon	25-30 c	24.2	68.8	7.0	5.8	6.5	0.5

Adsorption equilibrium isotherm

CONSTANTS	UH-30 C	UH-10 C	LH- 30 C	LH-10 C
n	1.45	1.30	1.024	1.13
k	11.87	17.25	2.035	8.19
k oc	860	1250	565.3	227.5
Org. C	1.38	1.38	0.36	0.36

Freundlich equation:

$$X/M = k^* Ce\ Exp(1/n)$$

$$X/Moc = koc\ ^*Ce\ Exp(1/n)$$

TABLE 2 Freundlich Equilibrium Adsorption Data for PCP with the Menfro Silt Loam

TABLE 3 Effect of Organic Matter on the Adsorption of PCP on the Menfro Silt Loam Soil; pH=6.5, temperature=30°C

	ORG. C (%)	C_o (mg/L)	C_e (mg/L)	X/M (mg/Kg)	Kp	Koc
UH + HUMIC ACID I	2.1	100	54	460	8.5	405
UH + HUMIC ACID II	1.53	100	73	270	3.7	241
UH	1.38	100	75	250	3.3	241
LH	0.36	100	86.5	135	1.56	433
TREATED UH	0.22	100	93	70	0.75	342

Desorption Equlibrium Isotherm

constants	UH-30 C	UH-10 C	LH- 30 C	LH-10 C
n	1.1	1.38	1.14	1.33
k	2.1	15.5	2.035	8.19
Org. C	1.38	1.38	0.36	0.36

Freundlich equation:

$$X/M = k^* Ce\ Exp(1/n)$$

TABLE 4 Freundlich Equilibium Desorption Data for PCP with the Menfro Silt Loam Soil

OXYGEN TRANSFER TO VISCOUS LIQUID MEDIA IN THREE-PHASE FLUIDIZED BEDS OF FLOATING BUBBLE BREAKERS†

Y. Kang* and L.T. Fan
Department of Chemical Engineering
Kansas State University
Manhattan, Kansas 66506-5102

B.T. Min
Department of Chemical Engineering
Chungnam National University
Taejon, 302-764, Korea

S.D. Kim
Department of Chemical Engineering
Korea Advanced Institute of Science and Technology
Seoul, 136-791, Korea

March 5, 1990

ABSTRACT

The rates of oxygen transfer from air bubbles to viscous liquid media were promoted by floating bubble breakers in three-phase fluidized beds operated in the bubble coalescing regime. The liquid-phase volumetric oxygen transfer coefficient has been recovered by fitting the axial dispersion model to the resultant data, and its dependence on the experimental variables, such as the gas and liquid flow rates, particle size, concentration of bubble breakers, and liquid viscosity, has been examined. The results indicate that the liquid-phase volumetric oxygen transfer coefficient can be enhanced up to 20 ~ 25%. The coefficient exhibits a maximum with respect to the volume ratio of the floating bubble breakers to the fluidized solid particles; it increases with increases in the gas and liquid flow rates and size of fluidized particles, while it decreases with an increase in the liquid viscosity. An expression has been developed to correlate the liquid-phase volumetric oxygen transfer coefficient with the experimental variables.

INTRODUCTION

The objective of this work was to investigate the volumetric rates of oxygen transfer in the liquid phase in three-phase fluidized beds with viscous non-Newtonian liquid media operated in the bubble coalescence regime. Furthermore, an attempt was made to enhance the volumetric oxygen transfer rates by means of floating bubble breakers.

The three-phase fluidized bed can serve as a biofilm reactor for the selection of a mixed culture for the aerobic degradation of phenol using activated carbon (Tang and Fan, 1987), coal (Worden and Donaldson, 1987) or sand (Etzenspenger *et al.*, 1989) as a support. It has also been adopted as bioreactors for immobilizing existing xenobiotic

---

† Presented at the Twentieth Annual Biochemial Engineering Symposium, Manhattan, KS, April 21, 1990.

* To whom all correspondence should be addressed; on leave from Department of Chemical Engineering, Chungnam National University, Taejon, 302-764, Korea.

strains (Tang and Fan, 1987). The successful design of a three-phase fluidized-bed bioreactor requires knowledge of the rate of oxygen transfer. The rates of mass transfer in three-phase fluidized beds (Nguyen-Tien *et al.*, 1985; Chang *et al.*, 1986; Tang and Fan, 1990) and fluidized-bed bioreactors (Tang and Fan, 1987; Sun and Funusaki, 1988) have been evaluated in terms of the volumetric mass transfer coefficients. It has been generally known that the volumetric mass transfer coefficients in a three-phase fluidized bed of relatively small particles are lower than those in a comparable bubble column (Nguyen-tien *et al.*, 1985; Chang *et al.*, 1986; Sun and Funrusaki, 1988). This arises from the fact that the bubbles in the former are larger than those in the latter. Apparently, the size of bubbles should be reduced by some means or other, e.g., resorting to the bubble breakers, if we wish to enhance the rate of mass transfer in the three-phase fluidized bed and bubble column. Floating bubble breakers have been successfully used in a bubble column (Kang *et al.*, 1990) and three-phase fluidized beds (Kim and Kim, 1990); they have been found to substantially increase the gas holdup and rate of mass transfer by decreasing the bubble size without appreciably increasing the pressure drop in the bed or column (Kim and Kim, 1987). Various bioprocess systems utilizing three-phase fluidized beds involve viscous liquid media exhibiting non-Newtonian flow behavior; nevertheless, there has been little attention paid to the effect of liquid viscosity on the volumetric mass transfer coefficient in the three-phase fluidized beds (Patwari *et al.*, 1986; Schumpe *et al.*, 1989).

EXPERIMENT

Experiments were carried out in a column with an ID of 0.15m and a height of 2m, as illustrated in Figure 1. A perforated plate containing 147 evenly spaced round holes, each with a diameter of $3x10^{-3}$m, served as the liquid distributor; it was overlaid by a screen. The distributor of air was made of four perforated feed pipes with an ID of $6.35x10^{-3}$m. Each pipe had 30 holes, each with a diameter of $1.0x10^{-3}$m drilled horizontally through the grid. The pipes were evenly spaced across the liquid distributor plate. This arrangement allowed gas and liquid to enter the column separately. The distributor was situated between the test section of the column proper and a stainless steel distributor box with a height of 0.5 m and a diameter of 0.15 m. For measuring the pressure drop through the column, thirteen pressure taps, connected to liquid manometers, were mounted flush with the wall of the column along the axial direction at an interval of 0.15 m between adjacent taps.

The liquid sampling taps connected to solenoid valves were located at five axial positions along the column (0, 0.11, 0.36, 0.61 and 0.81 in the dimensionless axial coordinate). A liquid tank with a gas distributor at the bottom was employed as the purge tank; a temperature control system was installed in it to maintain the liquid temperature within the desired range.

Compressed filtered air served as the gas phase, and tap water or an aqueous solution of carboxy methyl cellulose (CMC) as the liquid medium. Characteristics of the pseudoplastic behavior of CMC solutions are listed in Table 1. The fluidized solid particles were glass beads with a density of 2500 Kg/m^3. The average diameter of these beads was either $1.0x10^{-3}$ or $3.0x10^{-3}$m. The floating bubble breakers, fabricated from a cylindrical acrylic tube, had an OD of 0.015m and a height of 0.019m. A copper rod was inserted in the acrylic tube to adjust the bulk density of the floating bubble breakers to 1450 Kg/m^3.

To determine the liquid-phase volumetric oxygen transfer coefficient, the holdup of each phase and the axial concentration profile of dissolved oxygen in the liquid phase were measured under each set of experimental conditions. Sampling of the liquid

medium was repeated at three radial positions at the dimensionless radial coordinates, r/R, of 0, 0.5, and 1.0 for a given set of operating conditions. The sampled liquids were well stirred with a magnetic stirrer and maintained at a constant temperature. Recycled liquid from the weir at the top of the column was fed to the purge column, where the dissolved oxygen in the liquid was desorbed by pure compressed nitrogen gas. In the purge column, the temperature was maintained at 20±0.5°C, and the dissolved oxygen concentration in the liquid medium was maintained below 1.0×10^{-4}mol/ℓ. The volumetric ratio of the floating bubble breakers to the fluidized solid particles was in the range between 0 and 0.15.

ANALYSIS OF DATA

The holdups of individual phases can be determined by means of the following equations from the knowledge of pressure drop through the column and amounts of solid particles and floating bubble breakers.

$$\epsilon_g + \epsilon_L + \epsilon_p + \epsilon_B = 1 \tag{1}$$

$$-\frac{\Delta P}{L} = (\epsilon_g\rho_g + \epsilon_L\rho_L + \epsilon_p\rho_p + \epsilon_B\rho_B)g \tag{2}$$

$$\epsilon_p = \frac{W_p}{AL\rho_p} \tag{3}$$

$$\epsilon_B = \epsilon_p R_B \tag{4}$$

The viscous liquid medium, CMC solution, exhibits pseudoplastic behavior; thus, the effective shear rate due to multi-phase contacting has to be considered in evaluating its effective viscosity. The relationship between the effective viscosity and shear rate of non-Newtonian liquid ($0.72 \le n \le 1$) can be written as follows (Kawase and Moo-Young, 1986; Schumpe *et al.*, 1989):

$$\mu_{eff} = K(\dot{\gamma}_{eff})^{n-1} \tag{5}$$

In an upward gas-liquid concurrent continuous operation, the effective shear rate can be described as (Schumpe *et al.*, 1989; Kang *et al.*, 1990)

$$\dot{\gamma}_g = 2800\left[v_g - v_L\frac{\epsilon_g}{\epsilon_L}\right] \tag{6}$$

The additional shear due to the fluidized solid particles and floating bubble breakers can be estimated based on the capillary flow model (Mishra *et al.*, 1975; Schumpe *et al.*, 1989).

The shear rate induced by the flow of a pseudoplastic liquid in a cylindrical tube can be written as

$$\dot{\gamma} = \frac{8v_{Li}}{D_{eff}}\left[\frac{3n+1}{4n}\right] \tag{7}$$

In a three-phase fluidized bed with floating bubble breakers, D_{eff} can be written as follows:

$$D_{eff} = \frac{4\epsilon_L}{\frac{6\pi d_p^2 \epsilon_P}{\pi d_p^3} + \frac{6\pi d_B^2 \epsilon_B}{\pi d_B^3}} = \frac{2/3\ \epsilon_L}{\frac{\epsilon_P}{d_p} + \frac{\epsilon_B}{d_B}} \tag{8}$$

Consequently, Eqs. 7 and 8 yield collectively the contribution of fluidized solid particles and floating bubble breakers to the shear rate which is experienced by a viscous liquid medium; the resultant expression is

$$\dot{\gamma}_{P+B} = \frac{12V_L}{\epsilon_L^2}\left[\frac{\epsilon_P}{d_p} + \frac{\epsilon_B}{d_B}\right]\left[\frac{3n+1}{4n}\right] \tag{9}$$

Thus, the effective shear rate in a three-phase fluidized bed containing floating bubble breakers is the sum of shear rate due to rising bubbles and those due to fluidized solid particles and floating bubble breakers; thus,

$$\begin{aligned}\dot{\gamma}_{eff} &= \dot{\gamma}_g + \dot{\gamma}_{P+B} \\ &= 2800\left[V_g - V_L\frac{\epsilon_g}{\epsilon_L}\right] \\ &\quad + \frac{12V_L}{\epsilon_L^2}\left[\frac{\epsilon_S}{d_p} + \frac{\epsilon_B}{d_B}\right]\left[\frac{3n+1}{4n}\right]\end{aligned} \tag{10}$$

Hence, the effective viscosity of a pseudoplastic liquid medium can be determined from Eqs. 5 and 10.

Based on the steady-state axial dispersion model (Deckwer *et al.*, 1974, 1983; Kang *et al.*, 1990; Kim and Kim, 1990), the oxygen balance around a differential volumetric section of the bed yields

$$\frac{1}{Pe}\frac{d^2C}{dx^2} - \frac{dC}{dx} + St(C^*-C) = 0 \tag{11}$$

The appropriate boundary conditions are

$$\text{at } x = 0,\ C = C_0 + \frac{1}{Pe}\left.\frac{dC}{dx}\right|_{x=0} \tag{12}$$

$$\text{at } x = 1,\quad \left.\frac{dC}{dx}\right|_{x=1} = 0 \tag{13}$$

In these equations,

$$Pe = \frac{V_L L}{D_Z \epsilon_L}, \quad St = (k_L a)\ \frac{L}{V_L} \text{ and } x = \frac{Z}{L} \tag{14}$$

$$C^* = a + bx \tag{15}$$

In the above expressions, C^* is the equilibrium concentration of oxygen, and the constants, a and b, can be written as (Deckwer *et al.*, 1974)

$$a = \frac{Y}{H}\ (P_T + \rho_L g \epsilon_L L) \tag{16}$$

$$b = -\frac{Y}{H}\ \rho_L g \epsilon_L L \tag{17}$$

The volumetric oxygen transfer coefficients have been estimated by fitting the analytical solution of Eq. 11 to the concentration profiles of dissolved oxygen in the axial direction of the column (Kang *et al.*, 1990; Kim and Kim, 1990).

RESULTS AND DISCUSSION

Effects of the gas flow rate on the volumetric oxygen transfer coefficient, $k_L a$, in three-phase fluidized beds can be seen in Figure 2; the parameters are the particle size, liquid flow rate and viscosity, and amount of floating bubble breakers. The figure indicates that the volumetric oxygen transfer coefficients were enhanced by an increase in the gas flow rate in all cases studied. This was due to the increases in the gas holdup and intensity of turbulence.

The values of oxygen transfer coefficients obtained are compared with those of Patwari *et al.* (1986) and Schumpe *et al.* (1989) in Figure 2. While the former data are the origional ones, the latter are the values estimated from the correlation,

$$k_L a = 2988\ D_L^{0.5}\ V_g^{0.44}\ \mu_{eff}^{-0.34}\ V_t^{0.71} \tag{18}$$

where D_L and V_t are the molecular diffusivity of oxygen and the particle terminal velocity, respectively. Note that the data of Patwari *et al.* (1986) are slightly lower and those of Schumpe *et al.*(1989) are somewhat higher than those of the present study. The difference between the results of the present study and those of Patwari *et al.*(1986) may be due to the difference in the liquid flow rate.

Figure 2 also indicates that the oxygen transfer coefficients in three-phase fluidized beds of glass beads, either 1.0×10^{-3} or 3.0×10^{-3}m in diameter, are generally lower than those in the bubble columns of viscous liquid media. This can be attributed to the bubble coalescence in the beds of relatively small glass beads. The values of the oxygen transfer coefficient in the bubble columns have been calculated from the following correlation of Kang *et al.* (1990) under similar experimental conditions;

$$k_L a = 4.47 \times 10^{-2}\ V_g^{0.782}\ V_L^{0.160}\ \mu_{eff}^{-0.407}\ (1+\epsilon_B)^{2.820} \tag{19}$$

where ϵ_B is the volume fraction of floating bubble breakers in the column. It has been known that the bubble coalescence causes decreases in heat (Kang *et al.*, 1985; Kim *et al.*, 1986) as well as mass (Nguyen-Tien *et al.* 1985; Chang *et al.*, 1986; Kim and Kim, 1990) transfer coefficients in three-phase fluidized beds.

One of the convenient and efficient methods to break down rising bubbles in a three-phase fluidized bed is the use of floating bubble breakers; this method does not require additional power or expensive material and does not generate appreciable pressure drop in the bed. The effects of floating bubble breakers on the oxygen transfer coefficients in three-phase fluidized beds of viscous liquid media are illustrated in Figure 3. Note that the coefficients are enhanced by the addition of floating bubble breakers. Also note that the breakage of bubbles can result in increases in both the gas-liquid contact area and the intensity of turbulence in the bed. The liquid-phase volumetric oxygen transfer coefficient, however, attains its maximum at a certain volume ratio of the bubble breakers to the fluidized solid particles in each case (Figure 3). This appears to imply that the optimum amount of floating bubble breakers may exist in a three-phase fluidized bed for the maximum oxygen transfer coefficient. Moreover, the higher the volume fraction of floating bubble breakers over the optimum value, the lower the gas-liquid contact area in the bed (Kim and Kim, 1990). The optimum volume ratio of bubble breakers to the fluidized solid particles has been found to be approximately 0.12 in all experimental runs. As can be seen in Figure 3, the volumetric oxygen transfer coefficient has been enhanced as much as 25% by adding the floating bubble breakers in the bubble coalescence regime. The liquid-phase volumetric oxygen transfer coefficients have been correlated with the experimental variables as shown below.

$$k_La = 0.256\ v_g^{0.56}\ v_L^{0.41}\ \mu_{eff}^{-0.52}\ d_p^{0.47}\ (1 + R_B)^{1.68} \qquad (20)$$

It has yielded a correlation coefficient of 0.9765.

CONCLUDING REMARKS

The liquid-phase volumetric oxygen transfer coefficient increases with increases in the gas and liquid flow rates; while the coefficient decreases with an increase in the liquid viscosity in the bubble coalescence regime. The volumetric oxygen transfer coefficient is enhanced as much as 25% by adding the floating bubble breakers to the bed, and the oxygen transfer coefficient exhibits a maximum value with increasing the volume ratio of floating breakers to the fluidized solid particles.

NOTATION

A = cross-sectional area of the column, m^2
a,b = constant in Eq. 15, mol/l
C = oxygen concentration, mol/l
C^* = equilibrium oxygen concentration, mol/l
D_L = oxygen diffusivity in the liquid media, $m^2 \cdot s$
D_{eff} = effective hydraulic column diameter, m
D_z = axial dispersion coefficient of the liquid phase, m^2/s
d_B = equivalent hydraulic diameter of bubble breaker, m
d_p = fluidized particle diameter, m
g = gravitational acceleration, m/s^2
H = Henry's constant, atm · l/mol

K = fluid consistency index, $Pa \cdot s^n$
K_La = volumetric oxygen transfer coefficient, 1/s
L = column height, m
n = flow behavior index, dimensionless
Pe = Peclet number defined in Eq. 14, dimensionless
P_T = pressure at the top of the column, Pa
Δp = pressure drop in the column, Pa
R_B = volume ratio of floating bubble breaker to the fluidized particles defined in Eq. 4, dimensionless
St = Stanton number defined in Eq. 14, dimensionless
V = flow rate, m/s
V_{Li} = interstitial flow rate of the liquid phase, m/s
W = weight of particles, Kg
x = dimensionless distance defined in Eq. 14, dimensionless
y = partial pressure, atm
z = axial distance, m

Greek letters

ϵ = phase holdup, dimensionless
ρ = density, Kg/m^3
μ = viscosity, $Pa \cdot s$
$\dot{\gamma}$ = shear rate, 1/s
σ = surface tension, N/m

Subscripts

B = bubble breaker
eff = effective
g = gas
L = liquid
O = initial
P = fluidized particle
t = terminal

LITERATURE CITED

Chang, S.K., Y. Kang and S.D. Kim, "Mass Transfer in Two- and Three-Phase Fluidized Beds," J. Chem. Eng. Japan, **19**, 524-530 (1986).

Deckwer, W.D., B. Burckhart and G. Zoll, "Mixing and Mass Trasnfer in Tall Bubble Columns," Chem. Eng. Sci., **29**, 2177-2188 (1974).

Deckwer, W.D., K. Nguyen-Tein, G.B. Kelkar and Y.T. Shah., "Applicabilty of Axial Dispersion Model to Analyze Mass Transfer Measurements in Bubble Columns," AIChE J., **29**, 915-922 (1983).

Etzensperger, M., S. Thoma, S. Petrozzi and I.J. Dunn, "Phenol Degradation in a Three-Phase Biofilm Fluidized Sand Reactor," Bioprocess Eng., **4**, 175-181 (1989).

Kang, Y., I.S. Suh and S.D.Kim, "Heat Transfer Characteristics of Three-Phase Fluidizied Beds," Chem. Eng. Commun., **34**, 1-13 (1985).

Kang, Y., B.T. Min, J.B. Nah and S.D. Kim, "Mass Transfer in Bubble Columns of Continuous Operation with Floating Bubble Breaker," Proc. of The Second Asian Conference on Fluidized-Bed and Three-Phase Reactors, pp. 299-309, Feb. 18-20 (1990); also accepted for publication in AIChE J. (1990).

Kawase, Y. and M. Moo-Young, "Influence of Non-Newtonian Flow Behavior on Mass Transfer in Bubble Columns With and Without Draft Tubes," Chem. Eng. Commun., **40**, 67-83 (1986).

Kim, J.O. and S.D. Kim, "Bubble Characteristics in Three-Phase Fluidized Beds of Floating Bubble Breakers, Particulate Sci. Technol, **5**, 309-321 (1987).

Kim J.O. and S.D. Kim, "Mass Transfer Characteristics in Two-and Three-Phase Fluidized Beds of Floating Bubble Breakers," Can. J. Chem. Eng., in press (1990).

Kim, S.D., Y. Kang and H.K. Kwan, "Heat Transfer Characteristics in Two- and Three-Phase Slurry Fluidized Beds," AIChE J., **32**, 1397-1400 (1986).

Mishra, P., D. Singh and I.M. Mishra, "Momentum Transfer to Newtonian and Non-Newtonian Fluids Flowing Through Packed and Fluidized Beds," Chem. Eng. Sci., **30**, 397-405 (1975).

Nguyen-Tien, K., A.N. Patwari, A. Schumpe and W.D. Deckwer, "Gas-Liquid Mass Transfer in Fluidiized Particle Beds," AIChE J., **31**, 194-202 (1984).

Patwari, A.N., K. Nguyen-Tien, A. Schumpe and W.D. Deckwer, "Three-Phase Fluidized Beds with Viscous Liquid: Hydrodynamics and Mass Transfer," Chem Eng. Commun., **40**, 49-65 (1986).

Schumpe, A., W.D. Deckwer and K.D.P. Nigam, "Gas-Liquid Mass Transfer in Three-Phase Fluidized Beds with Viscous Pseudoplastic Liquids," Can. J. Chem. Eng., **67**, 873-877 (1989).

Sun, Y. and S. Furusadi, "Mean Bubble Diameter and Oxygen Transfer Coefficient in a Three-Phase Fluidized Bed Bioreactor," J. Chem. Eng. Japan, **21**, 20-24 (1988).

Tang, W.T. and L.S. Fan, "Steady State Phenol Degradation in a Draft-Tube, Gas-Liquid-Solid Fluidized-Bed Bioreactor," AIChE J., **33**, 239-249 (1987).

Tang, W.T. and L.S. Fan, "Gas-Liquid Mass Transfer in a Three-Phase Fluidized Bed Containing Low Density Particles," Ind. Eng. Chem. Res., **29**, 128-133 (1990).

Wordon, R.M. and T.L. Donaldson, "Dynamics of a Biological Fixed Film for Phenol Degradation in a Fluidized-Bed Bioreactor," Biotech. Bioeng., **30**, 398-412 (1987).

Table 1. Physical Properties of Liquid Media and Ranges of Fluid Flow Rates

Liquid Medium	ρ_L (Kg/m^3)	$Kx10^3$ ($Pa \cdot s^n$)	n	$\sigma_L x10^3$ (N/m)	$V_g x10^2$ (m/s)	$V_L x10^2$ (m/s)
Water	1000	1.000	1.000	72.9	2.2-9.5	3.5-10.5
CMC(1) Solution	1001	21.69	0.882	73.2	2.2-9.5	3.5-10.5
CMC(2) Solution	1002	43.82	0.847	73.3	2.2-9.5	3.5-10.5
CMC(3) Solution	1003	71.64	0.825	73.6	2.2-9.5	3.5-10.5

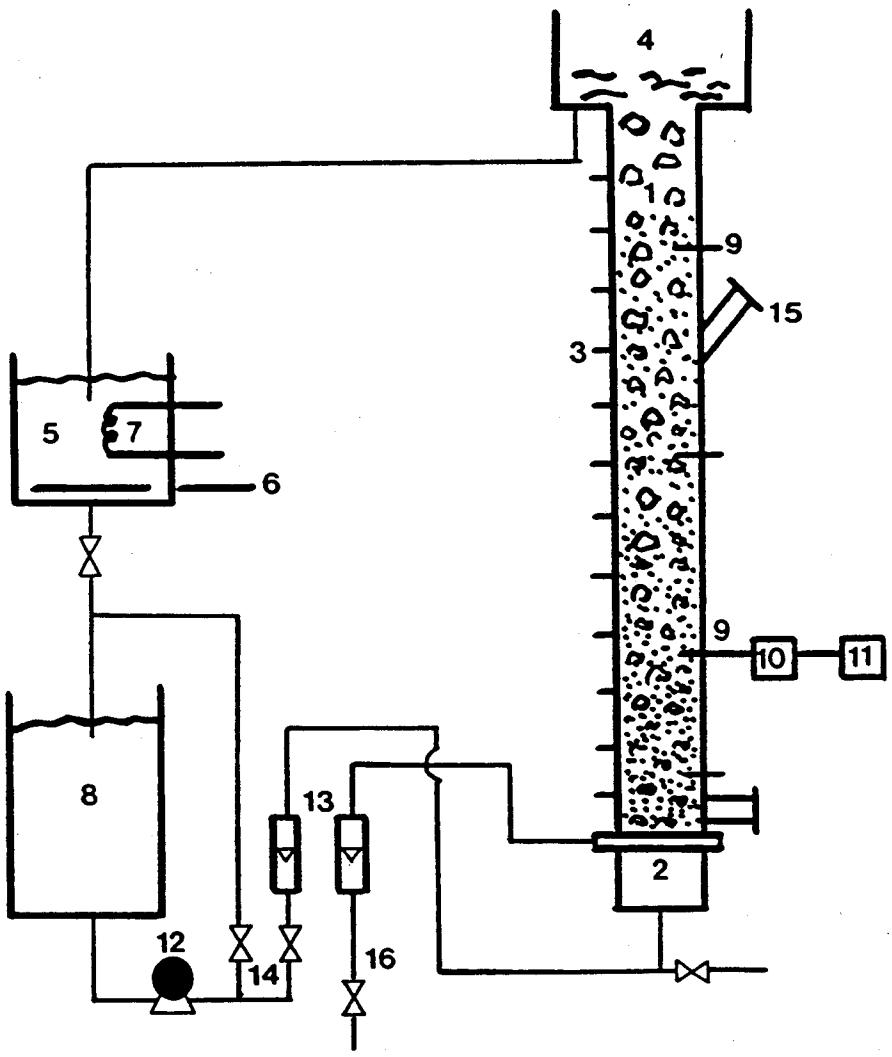

Figure 1. Experimental apparatus:

1.	Main column	9.	Liquid sampling tap
2.	Distributor	10.	Solenoid valve
3.	Manometer	11.	O_2 analyzer
4.	Weir	12.	Pump
5.	Purge tank	13.	Rotameter
6.	N_2 gas injection	14.	Valve
7.	Temperature controller	15.	Loading port
8.	Liquid reservoir	16.	Air filter and regulator

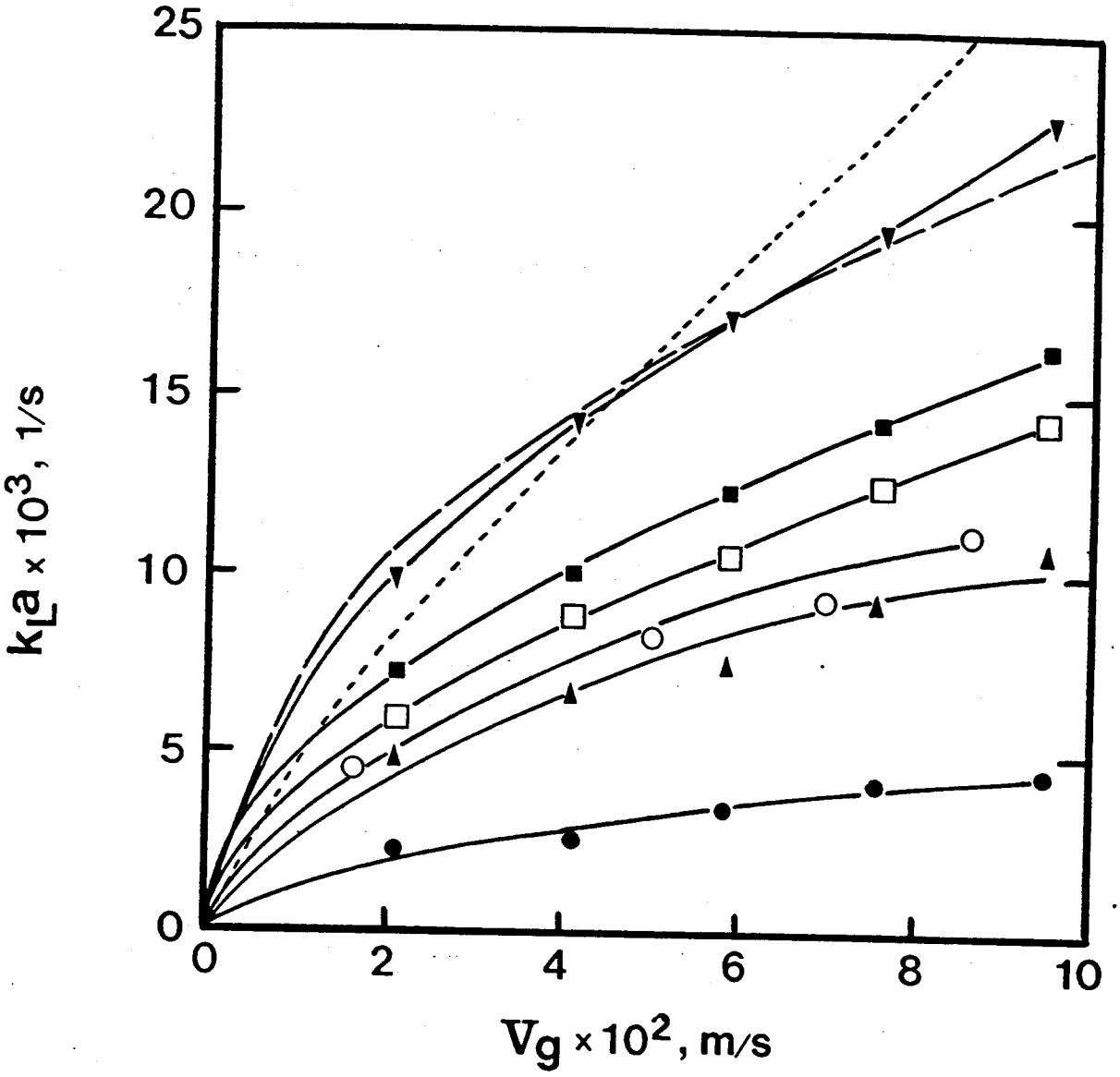

Figure 2. Effects of V_g on k_La in beds of glass beads fluidized by CMC solution and air:

Key:	●	▲	■	▼
d_p (m):	0.001	0.001	0.003	0.003
V_L (m/s):	0.035	0.056	0.085	0.105
Liquid:	CMC(3)	CMC(1)	CMC(2)	CMC(1)
R_B:	0	0.06	0.09	0.12
Source:	this study			

Key:	□	○	-----	— — —
d_p (m):	0.003	0.003	0	0.003
V_L (m/s):	0.085	0.041	0.085	0.085
Liquid:	CMC(2)		CMC(2)	CMC(2)
R_B:	0	0	0	0
Source:	this study	Patwari et al.* (1986)	Kang et al. (1990)	Schumpe et al. (1989)

* CMC Solution (K = 3.3, n = 0.905)

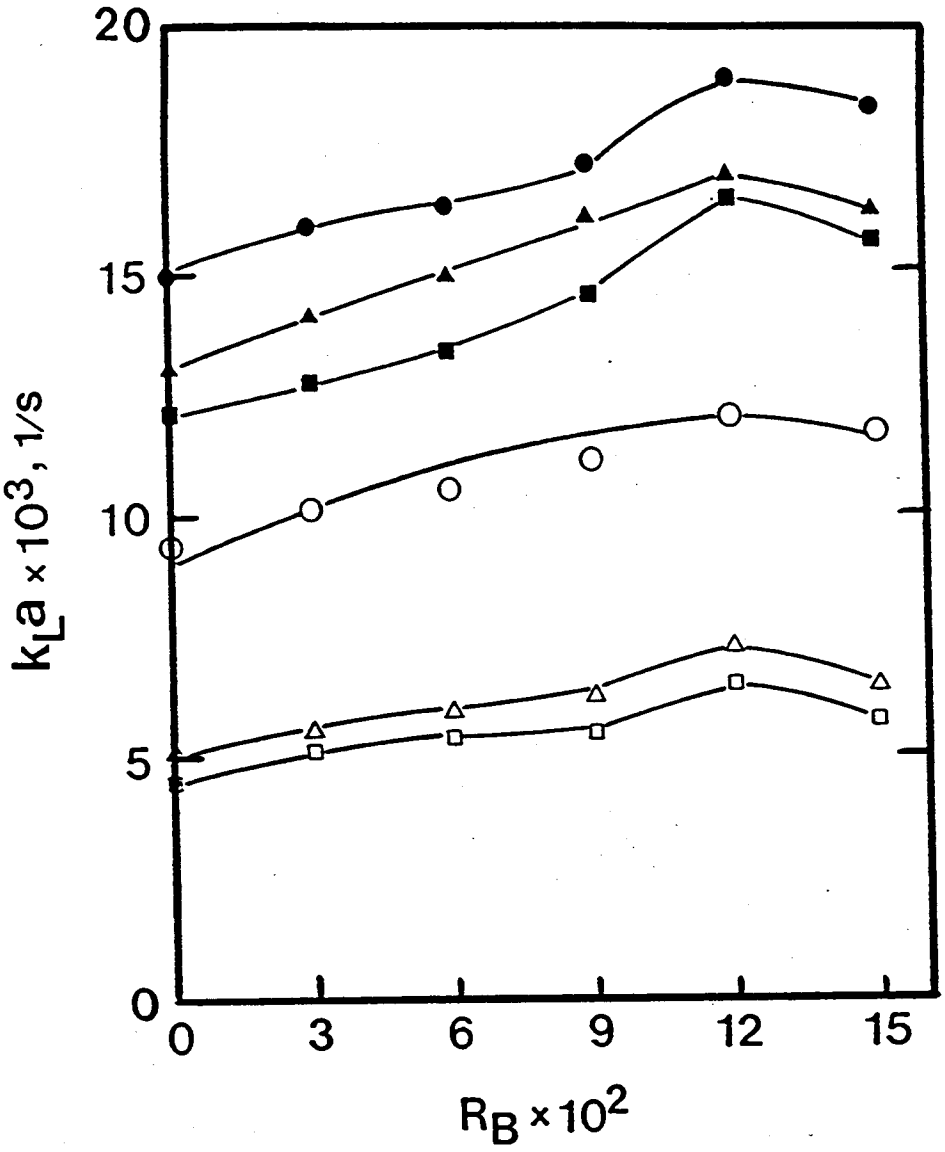

Figure 3. Effects of R_B on k_La in beds of glass beads fluidized by CMC solution and air:

Key:	o	Δ	□	●	▲	■
d_p(m):	0.001	0.001	0.001	0.003	0.003	0.003
V_g(m/s):	0.095	0.058	0.095	0.076	0.076	0.095
V_L(m/s):	0.056	0.056	0.035	0.085	0.105	0.105
Liquid:	CMC(1)	CMC(2)	CMC(3)	CMC(1)	CMC(2)	CMC(3)

STUDIES ON THE *INVITRO* DEVELOPMENT OF CHICK EMBRYO

A. Venkatraman

Department of Chemical Engineering
Durland Hall
Kansas State University
Manhattan, Kansas 66506-5102

and

T. Panda

Department of Chemical Engineering
Indian Institute of Technology
Madras, India-600036

ABSTRACT

A detailed analysis of the growth of chick-embryo in an artificial growth medium was undertaken to determine the conditions of growth that gave the maximum rate of development of chick-embryo. It was found that the rate of invitro development of embryo was dependent on the age of the incubated egg at the time of transfer to the cultivation medium. The physiological changes in the development of the embryo were observed during the entire period of development. In all cases, the maximum increase in weight was observed after the fourteenth day of incubation.

INTRODUCTION

The propagation of animal cells in artificial medium can be the basis for the large scale biosynthesis of commercial animal proteins. This technique is, generally, effected by dissection of the tissue, mincing, enzymic digestion, centrifugation and washing and finally transferring the cells to a suitable growth medium. For the large scale cultivation of such cells that adhere to surfaces, one of the most promising techniques is to grow the cells on the surface of micro-carriers in a growth medium.[1] However, in addition to this, the growth of the chick embryo is difficult, because many of the cell types of interest exist as a dense packing of similar cells. The challenge faced in the submerged cultivation of these cells is to provide an acceptable environment for the growth of cells.[5] So it is necessary to determine the cultivation conditions which allow growth of cells to the maximum density in the shortest possible time. Again, quantitative analysis on the development of chick-embryo is practically non existent.[3]

MATERIALS AND METHODS

Fertilized chicken egg: This was obtained from M/s Futnani poultry farm, Madras, India.

Cultivation medium: The medium used for promoting the growth of the chick-embryo was developed in the author's laboratory, with the following composition for the chick-embryo development:[4]

Chick ringer solution -50mL, Fresh egg albumin -30mL

Trace quantities of streptomycin and penicillin-G were also added to the growth medium. All operations were performed under strict aseptic conditions.

Culture conditions: The incubated egg was placed in a particular position and the shell was chipped away. The vitelline membrane was removed with minimal damage to the blood vessels. The embryo was carefully transferred to the growth medium. The top end of reactor was cleaned thoroughly to avoid any contamination of the cotton plug upon insertion. The process was carried out at 38°C and 65% humidity was maintained throughout the development of the embryo.

RESULTS AND DISCUSSION

It was observed that when the reactor was maintained under stirred conditions the growth of the chick-embryo was negligible. Hence, the experiments were carried out under unstirred conditions. Different changes were observed for the yolk and the embryo, depending on the age of the fertilized egg at the time of transfer to medium. It is important to mention here that the basic kinetic analysis of chick-embryo requires knowledge of characteristic changes with time, of the embryo and associated yolk.

It was observed, for a one day old incubated egg, that the shape of the yolk changed from a spherical and compact mass to a flattened globule. After the fourth day, a blood vessel network appeared on the top half of the yolk. The thickening of the network continued till the ninth day wherein a scaly fibrous matter made it's presence. The yolk size diminished rapidly after the fifteenth day of cultivation. The changes in the embryo followed the following pattern:[4]

The red spot that was seen on top of the yolk just after transfer increased in size as the time of cultivation progressed. A pale shaped body was seen after the fourth day on the same spot. On the growing embryo with the primary optic vesicles, the forelimbs and hindlimbs made their presence after the eighth day. The beak, body hair and the prominent long neck were seen after the eleventh day on the embryo. The embryo attained its maximum size after the fifteenth day of cultivation.

The invitro growth of the five day old fertilized egg on transfer showed a thickening of a blood vessel network on the bottom of the yolk, followed by a rapid change in the shape and size of the translucent lower half after the fifth day.

In the case of the ten day old fertilized egg, after transfer, the condition of the yolk was very different from all the other cases. The yolk has broken up into tiny globules and only half of it was in a coherent mass attached to the embryo. The embryo after transfer to the reactor was fully developed and no growth in quantitative terms was observed.

It must be mentioned that in all cases the rate of growth of the chick embryo invitro was slower than the growth within the unbroken shell. It was also observed that the transfer operation became very difficult when the age of the fertilized egg was more than six days, just before transfer to the medium. The growth curve for the four day old fertilized egg was compared with the nine day old fertilized egg, as shown in Figure 1. The four day old fertilized egg had the maximum change in embryo weight with time when compared to all other fertilized eggs. The goodness of fit between the observed change in embryo weight with time and the modeled growth curve (eqn. 1) was the best for this class of eggs as seen in Figure 2.

Thus it was observed that the development of chick-embryo was dependent on the age of the fertilized egg on transfer. The maximum change in the weight was 1.8g/d, 1.19g/d, 1.11g/d, 0.8g/d and 0.7g/d for the four day, seven day, nine day, ten day and eleven day old fertilizer eggs respectively as shown in Figure 3. Further, it was found in all embryos, irrespective of the age of incubation, that the maximum change in the weight of the embryo occurred from the fourteenth day onwards, inclusive of the time of incubation.

The generalized equation that fits the experimental data was found to be:

$$V_w = \frac{K_1}{\sqrt{\theta}} \exp \frac{-(1-\theta)^2}{K_2 \theta} \qquad (1)$$

where V_w = change in weight of embryo (g/d)
θ = *observation time/av. time for maximum change in weight*
K_1, K_2 = constants

The values of the constants (Table 1) were found to be higher for those fertilized eggs which had a shorter incubation time (at the time of transfer). This was in concordance with the observed qualitative aspect of the growth of the chick embryo.

CONCLUSION:

The cultivation of chick-embryo invitro depends on the conditions of growth including the efficiency of transfer operations and these factors play an important role in the growth of the embryo in a well defined cultivation medium. The kinetic analysis showed that fertilized eggs, having an age less than five days, had the highest growth rates (The change in weight of the embryo with time) relative to all other classes of fertilized eggs.

REFERENCES

1. W.S. Hu and T.C. Dodge: Biotechnology Progress, 1, (4), 209, 1985.
2. D. Perlman: Process Biochem. 42, 1967.
3. W.S. Hu and D.I.C Wang: Biotechnol Bioeng., 30, 548, 1987.
4. A. Venkatraman: Bachelor of technology project, Indian Institute of Technology, Madras, India, 600036, 1989.
5. J.P.Tharakan and P.C.Chau:Biotechnol. Bioeng., 29, 657, 1987.

Table 1: Effect of chick-embryo age during transfer on the values of K_1 and $1/K_2$.

Age of transferred embryo	K_1	$1/K_2$
4	0.571	0.24
7	0.381	0.30
9	0.347	0.32
10	0.38	0.33
11	0.282	0.34

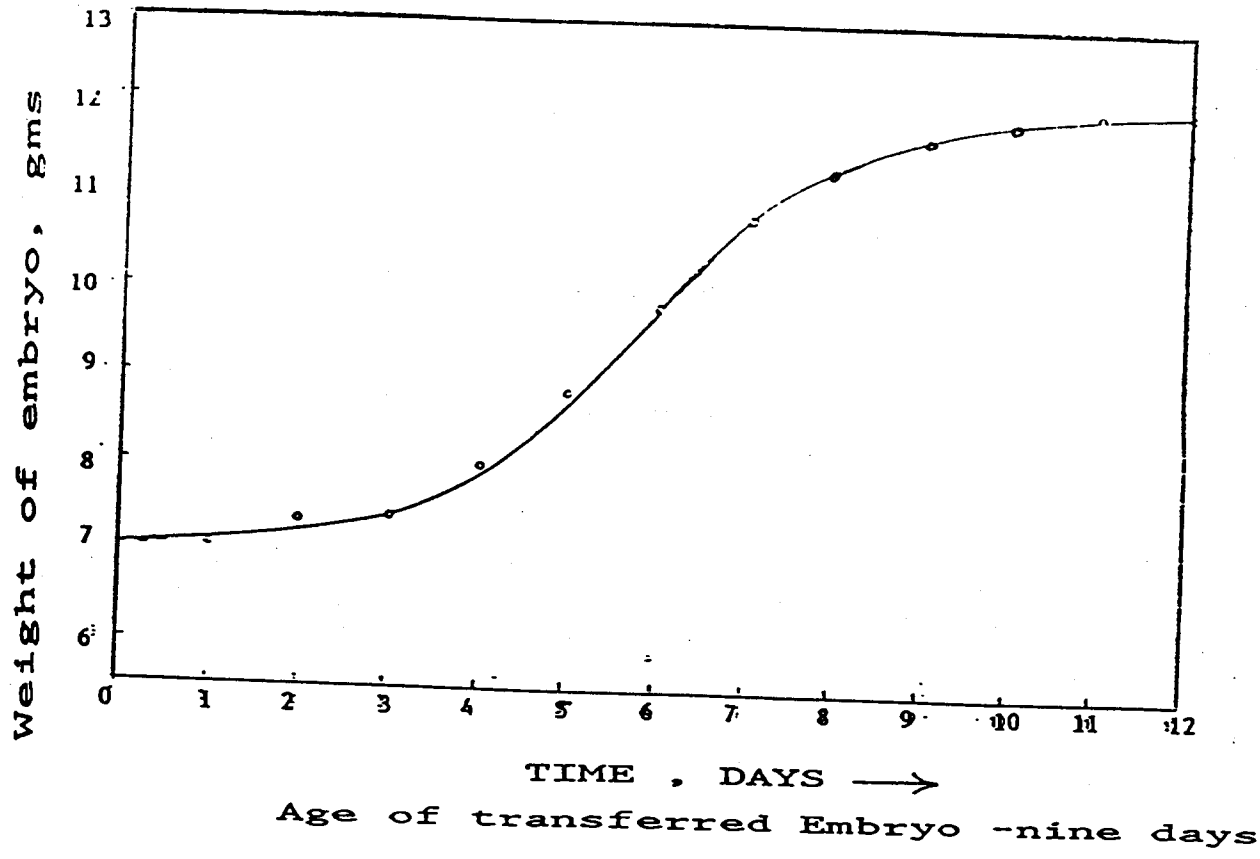

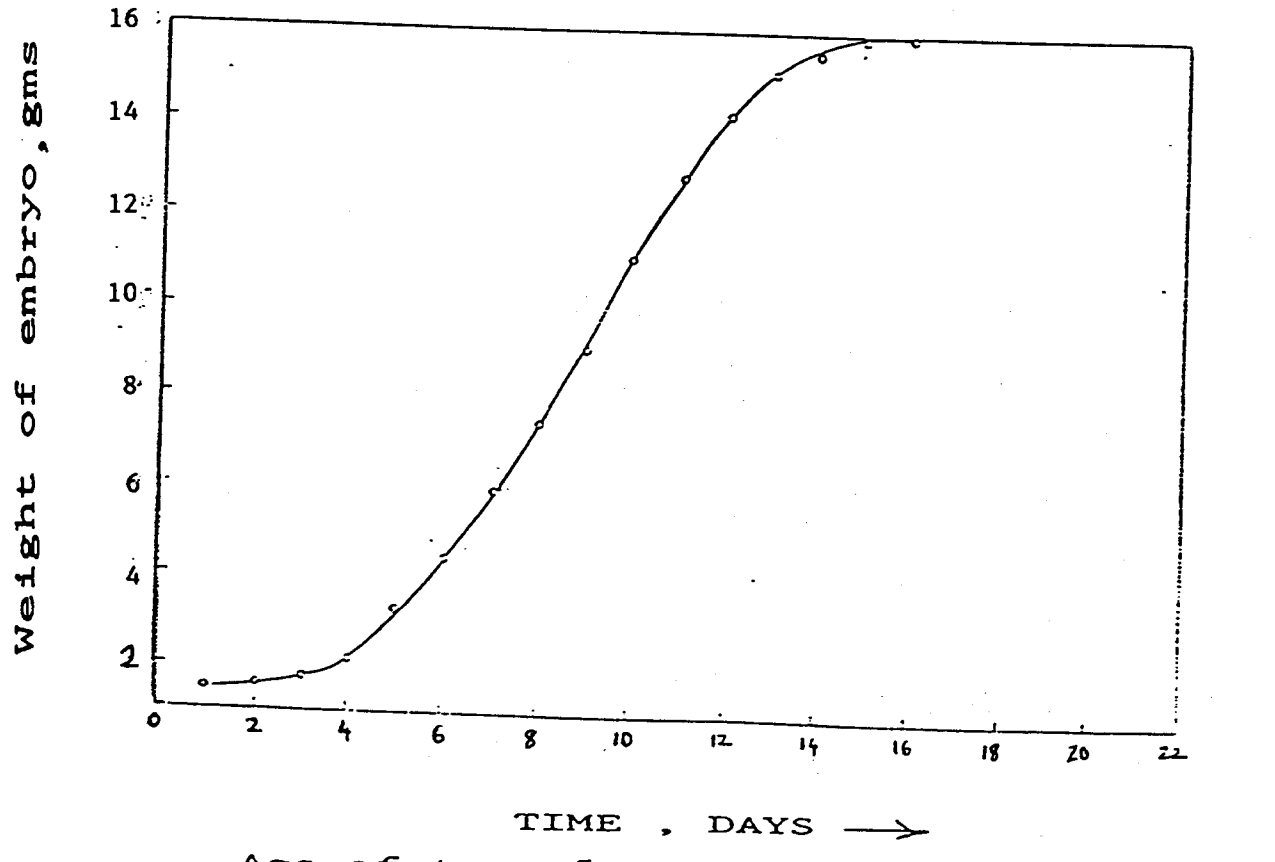

Fig 1. A comparison of the growth curves of the four day and nine day old fertilized eggs.

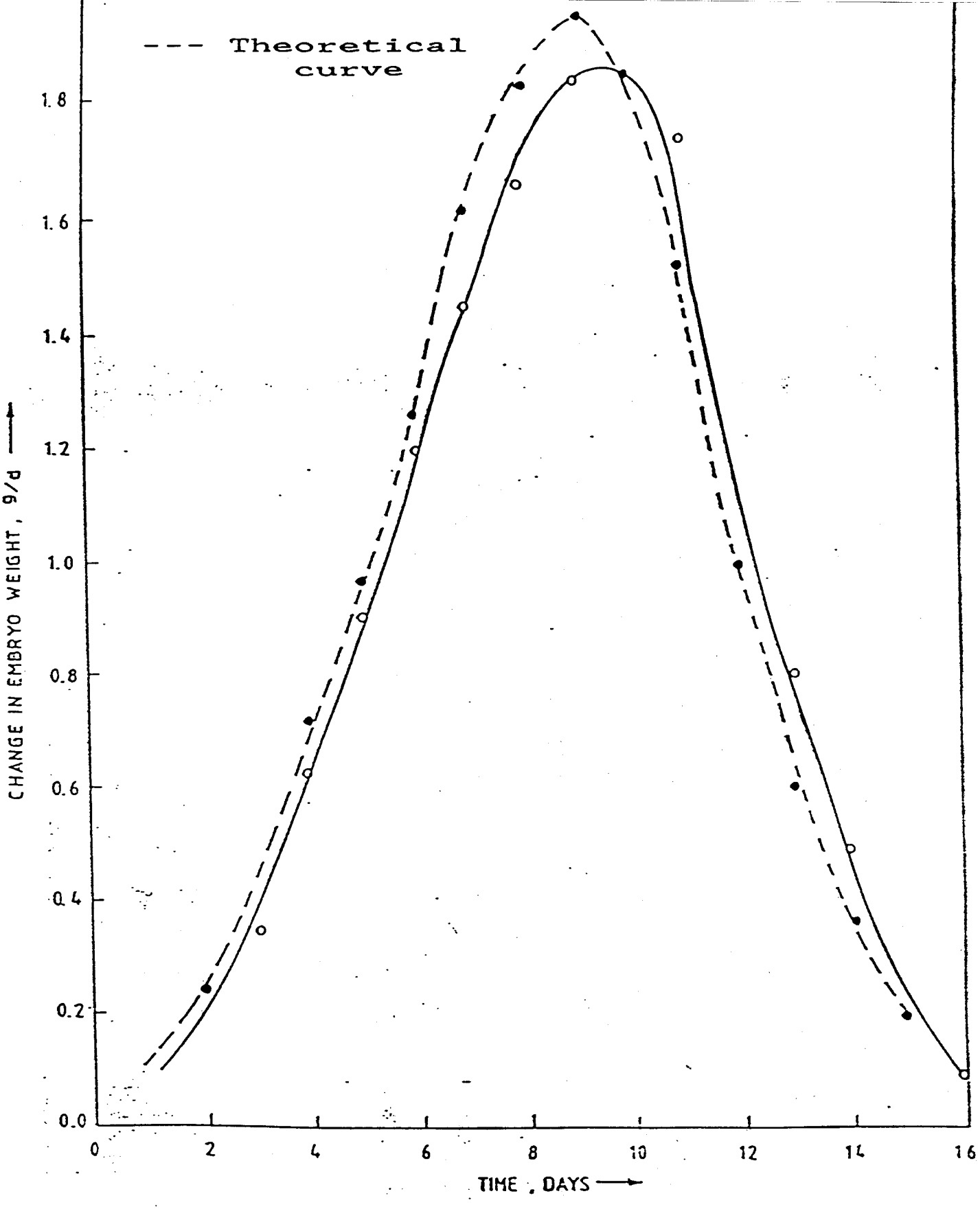

Fig. 2. AGE OF TRANSFERRED EMBRYO - four days

GROWTH OF EMBRYO DURING IN-VITRO CULTIVATION

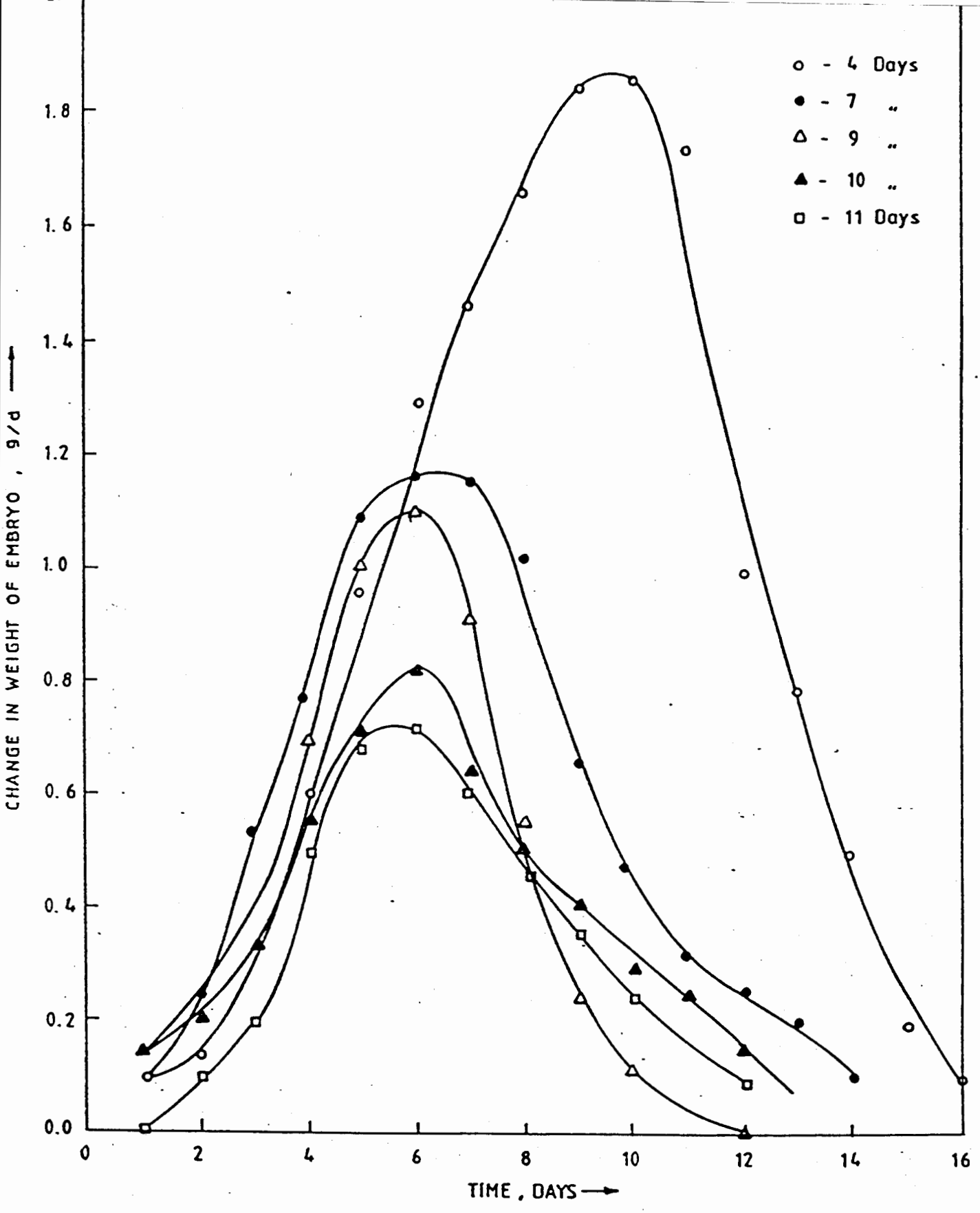

FIG. 3 - COMPARISON OF THE CHANGE IN EMBRYO WEIGHT DURING THE IN VITRO STUDY

THE EVOLUTION OF A SILICONE BASED PHASE-SEPARATED GRAVITY-INDEPENDENT BIOREACTOR

Peter E. Villeneuve
Eric H. Dunlop

Colorado State University
Dept of Chem Engineering
Fort Collins, Co
80523

ABSTRACT

The evolution of phase-separated gravity-independent bioreactor is described. Initial prototypes consisted of a silicone tube zero headspace fermenter, i.e., a manifold reactor. Fermentation media passes across oxygen-containing silicone tubing. This design was found to lead to inherent fluid mechanic problems. Large boundary layers resistances prevent efficient transfer of oxygen to the media. Three reactors, all of which resemble heat exchangers, have been built and tested terrestrially. The Mark I, II and III developed higher transfer intensities when compared to the manifold reactor. The Mark III reactor stands out as the most efficient design. Oxygen transfer intensities of 232 mmolO_2/1/h and high economies are achieved in this particular reactor configuration. Phase inversion, water internal and air external to the tubing, is the main contribution to the high intensities and economies.

INTRODUCTION

Food supplies ultimately determine the length of space travel. Long excursions in space are not presently obtainable, without replenishing food reserves. If long term space travel is to become a reality an onboard carbon recycle system must be engineered. Recycling a fixed organic carbon supply ensures a constant food supply. Earth has a fixed amount of carbon that is recycled by microorganisms on a slow but continuous basis. The same logic must be applied in space.

Growing microorganisms in space offers many challenges. Oxygen containing gas bubbles injected into liquid media do not rise in microgravity environments. Bubbles coalesce resulting in two completely separate nonmixing phases.

Presently, we have no knowledge of a functional gravity independent bioreactor designed to grow microorganisms in space. We are aware of the cell culture mammalian bioreactor currently being tested at Johnson Space Center and the JPL reactor constructed at the Jet Propulsion Laboratory. However, low oxygen delivery capacities of these reactors will not allow growth of high oxygen demanding aerobic carbon recycling microorganisms.

Apparatus and Methods

Phase separated bioreactors have the distinct advantage of operating under bubble free conditions. This circumvents gas-liquid disengagement problems that develop in microgravity environments /1/. However, designing a silicone based phase separated bioreactor with high oxygen transferring capabilities, suited for oxygen intensive microbial growth, has proven to be a challenge. Large boundary layer resistances and channeling have plagued most design schemes.

JPL Reactor

Petersen, Sheshan and Dunlop designed and constructed a phase separated membrane bioreactor /2/. The reactor was built at the Jet Propulsion Laboratory (JPL). The reactor consisted of a silicone tube laced zero head- space fermenter i.e. a manifold fermenter. Conclusions drawn from the study are:

i) At infinite stirrer speed the mass transfer coefficient becomes infinite implying that the external fluid resistances are extremely high compared to which any resistance from the oxygen diffusion across the membrane is negligible.

ii) Oxygen limitation dominate under most conditions and should thus be the focus of future studies.

Colorado State University Reactors

The development of the three CSU phase separated bioreactors were based on conclusions derived from the JPL study. Oxygen transfer intensities became the focus of design. We felt that by lowering fluid resistances higher oxygen transfer intensities would follow. In order to lower fluid resistances a different design approach seemed appropriate. CSU reactors are modeled on heat exchanger design.

Experimental apparatus

Gassing-out and sulphite oxidation techniques are the traditional means by which the follow parameters are determined in a

fermenter: Kl, Kla, oxygen transfer intensities, flux and economy. Unfortunately both techniques posses major draw backs. Bell and Gallo (1971) /3/ demonstrated that minor amounts of surface active contaminants (such as amino acids, proteins, fatty acids, esters, lipids, ect.) could have an major effect on the accuracy of the sulphite oxidation technique. The accuracy of a gassing out experiment is completely dependent of the response time of the dissolved oxygen probe. Discussions by Taguchi and Humphrey (1966) /4/, Heinekin (1970,1971) /5/ and Wernau and Wilke (1973) /6/, point out a necessary incorporation of a probe response correction factor.

A solution to these problems can be found by conducting a steady state experiments that do not utilize sulphite oxidation or depend on dissolved oxygen probe response time. This is achieved by passing deoxygenated water through a reactor at constant velocities and monitoring relative changes in dissolved oxygen before and after the water is exposed to the reactor; refer to figure (1). This allows one to calculate the important parameters listed earlier.

CSU REACTORS

Mark I and Mark II

Both the Mark I and Mark II reactors mimic the design illustrated in fig (2). The geometry of the two reactors is essentially the same. Working volume of Mark II is 14.5X greater then Mark I. It also has 3X more tubing per volume. Both reactors were constructed out of plexiglass and silicone tubing.

Mark III

The geometry of the Mark III does not resemble either the Mark I or II reactors. The geometry resembles the JPL reactor. However, in the Mark III the phases are inverted, air is run external and the water is run internal with respect to the tubing. Construction material consisted of steel and silicone tubing.

Table (1) gives the tubing specification for the different reactors.

RESULTS AND DISCUSSION

MARK I

Small working volume made evaluation of the Mark I reactor extremely difficult. Under nearly all experimental conditions the dissolved oxygen probe was forced to function at very low concentrations. The low membrane surface area contributed to

this observation. However, experimental data collected from this reactor revealed oxygen transfer intensities 10X higher than prevously reported /2/.

MARK II

Increasing total volume and percent tubing while holding geometry constant seemed to be a logical step in design development. The percent tubing was increased 3X in order to increase membrane surface area while geometry was maintained. This increased dissolved oxygen concentrations well above the detectable range the of the probe.

Initial evaluations indicated that massive channeling predominated the Mark II reactor. This was evidenced by the decreasing intensities as water velocities increase. Mass transfer should increase as a function of turbulence. However, the inverse of this is seen. if channeling persists. Subsequent dye injection studies substantiated initial channeling predictions. Dye rushed passed either side of the tubes, refer to figure (3). In order to minimize channeling the sides of the reactor were packed with foam. This reduced channeling. However, the data still indicated channeling. This promoted a total tubing enclosure with foam. The foam enclosed membrane reactor exhibited substantially less channeling. Now as the external water velocities increase oxygen transfer intensities increase. From a biological point of view this reactor has major draw backs.

Growing yeast or any other microbe in a silicone/foam packed plexiglass reactor presents two major problems.

i) Cells would accumulate and adhere to the foam.
ii) Sterilization is quite difficult if not impossible.

The above mentioned problems combined with relatively poor oxygen transfer intensities prompted construction of the mark III reactor.

MARK III

Unlike other CSU reactors the Mark III operates under inverted phases. This system has tremendous advantages, refer to table (2).

ADVANTAGES

i) Stagnant liquid boundary layers can be minimized by increasing water velocities.

ii) Channeling is no longer an issue.

iii) Sterile conditions are readily obtainable.

Relatively high intensities of 232 mmolO_2/l/h obtained in this reactor are attributed to a lack of channeling and a very small liquid boundary layer.

Three major resistances effect the mass transfer of oxygen into the liquid phase.

RESISTANCES

1) Stagnant liquid layer
2) Stagnant vapor layer
3) Membrane

Liquid resistances are smallest if turbulent conditions are maintained inside the tubing. Typically, this condition in pipes is achieved at Reynolds numbers greater than 2300. However, in small diameter smooth silicone tubing the transition between turbulent and laminar flow is not seen at Reynolds number of 4560. This was determined experimentally by plotting friction factor versus Reynolds number (figure 4). In order to promote the transition from laminar to turbulent, larger diameter tubes and high flow rates are necessary.

Experimental data reveals a nondetectable stagnant boundary layer on the vapor side of the membrane. Water flow rate was held constant as air velocities fluctuated from a Reynolds number of 89 to 3450. Increases in dissolved oxygen were nondetectable. A logical explanation of this observation lies in the diffusivities of oxygen in air, silicone and water, refer to figure (5).

$$1/Kl = 1/kg + 1/kl + \text{membrane resistance}$$

Both the reciprocal of kg and kl are very small under correct conditions. Membrane resistance is equal to the oxygen permeability in silicone which is 6.86X higher than oxygen in water at 25°C. This magnifies the importance of minimizing the liquid stagnant boundary layer which is the determining factor of the over all mass transfer coefficient.

Percent gas utilization was not measured. However, the Mark III has the inherent potential of utilizing a large percentage of the gas entering the reactor. Because of the importance of this parameter it will receive more attention in future studies.

CONCLUSIONS

1. First attempts at building a silicone phase separated gravity independent bioreactor were accompanied with large liquid stagnant boundary layers and channeling.

2. Large differences in oxygen diffusivities between air and water results in a very small gas boundary layer.

3. Oxygen permeabilities are 6.8X greater in silicone relative to water. Under circumstances of large kg and low oxygen water permeabilities Kl is basicly equal to kl.

4. Both the boundary layers and channeling are minimized to a great extent through inversion i.e. liquid is run inside the tube. This improves the economy, intensity, Sherwood, Kl, Kla, flux, and gas utilization.

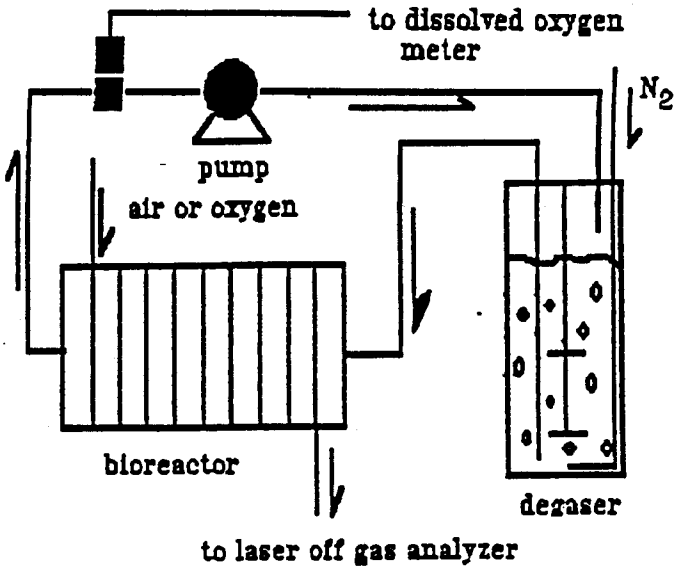

Figure (1) Steady state experimental apparatus. Kl, Kla, intensities, flux and economy can be calculated from this apparatus.

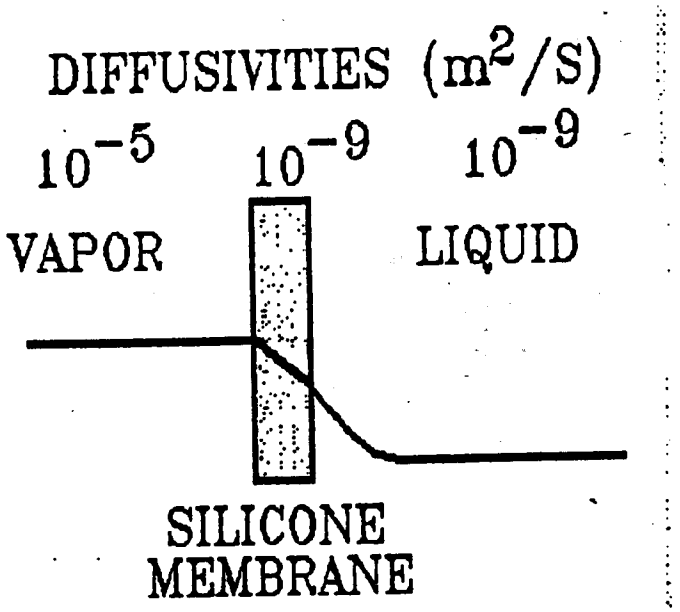

Figure (2) Diffusivities of oxygen in different materials.

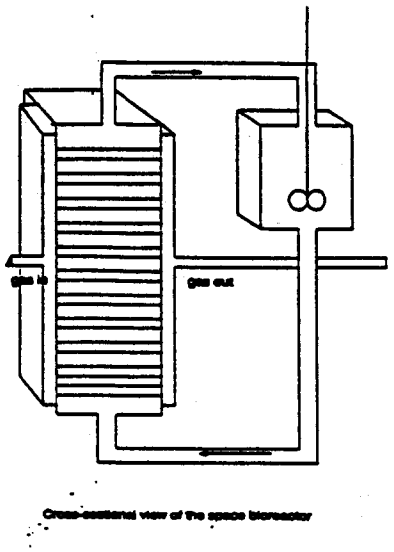

Figure (3) Heat exchanger design of Mark I and Mark II.

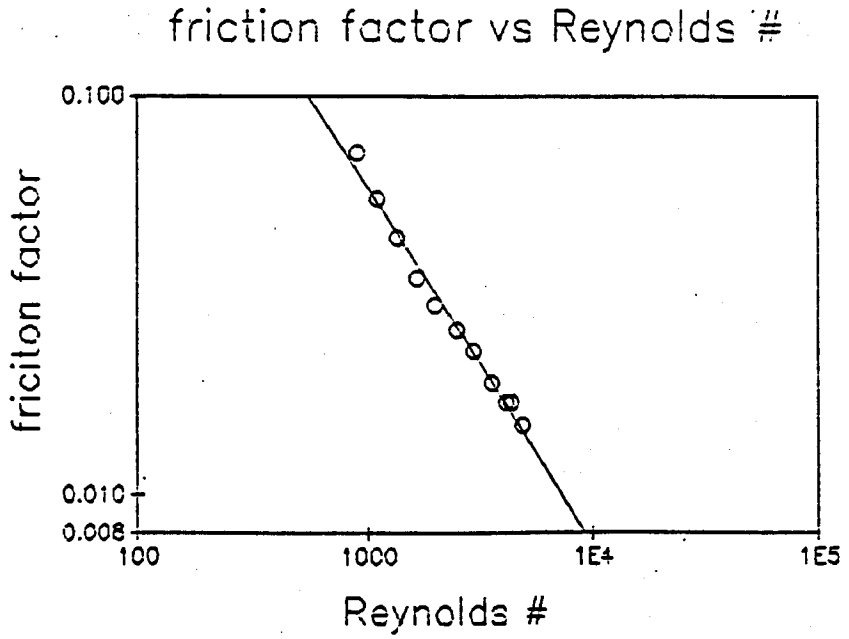

Figure (4) Friction factor versus Reynolds number.

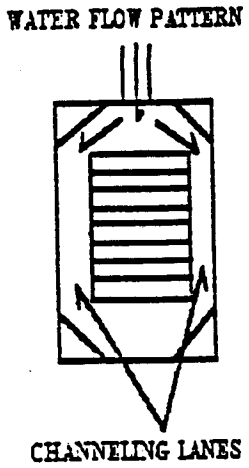

Figure (5) Channeling lanes found in the mark II reactor.

TABLE OF TUBING SPECS

	Mark I	Mark II	Mark III
tubing ID mm	0.5	1.57	3.35
tubing OD mm	0.93	3.17	4.65
tubing wall thickness mm	0.215	0.80	0.65
tubing length cm	30	1101	1400
cm^2/reactor volume 1/cm	0.32	5.46	3.03

Table (1) Tubing specifications

SUMMARY OF RESULTS

	Ref /2/	mark I	mark II	mark III
Intensity (mmolO2/l/h)	0.22	3.33	2.57	232
Kl (m/h)	0.0619	0.0199	0.776	0.6919
Kla (1/h)	8.1	0.0199	0.131	9.4
flux (mmolO2/h/cm^2)	1.74e-3	0.0033	0.0131	0.01705
Sherwood No.	16.5	10.6	133	257.5
economy (mmolO2/watt h)	0.376	2.27	1.0	136
% tubing	7.5	5.0	17.4	30%
intensity/%tubing (mmol/l/h/%tubing)	0.293	0.666	0.147	7.73

Table (2) Summary of results

References

1. Seshan, P.K., Petersen, G.R., Beard, B.J., And Dunlop, E.H. "Design Concepts for Bioreactors in Space in CELSS" NASA Technical Manual 88215 (1986).

2. Petersen, G.R., Seshan, P.K., And Dunlop E.H. "Phase Separated Membrane Bioreactor: Results From Model System Studies" Adv. Space Res. Vol. 9, No. 8, pp. (8) 185-(8) 193, 1989.

3. Bell, G.H. And Gallo, M. (1971) "Effect of Impurities on Oxygen Transfer." Process Biochem. 6(4), 33-35.

4. Taguchi, H. And Humphrey, A.E. (1966) "Dynamic Measurement of Volumetric Oxygen Transfer Coefficient in Fermentation Systems." J. Ferm. Tech. 44(12), 881-889.

5. Heineken, F.G. (1971) "Oxygen Mass Transfer and Oxygen Respiration Rate Measurements Utilizing Fast Response Oxygen Electrodes." Biotech. Bioeng. 13, 599-618.

6. Wernau, W.C. And Wilkie, C.R. (1973) "New Method for Evaluation of Dissolved Oxygen Probe Response for K_{La} Determination." Biotech. Bioeng. 15, 571-578.

BIODEGRADATION OF DIETHYL PHTHALATE

Guorong Zhang, Kenneth F. Reardon and Vincent G. Murphy
Department of Agricultural and Chemical Engineering
Colorado State University, Fort Collins, CO 80523

ABSTRACT

Several aerobic and facultative strains capable of degrading diethyl phthalate were isolated from wastewater treatment plant sludge. The effects of temperature, dissolved oxygen, initial primary substrate concentration, secondary substrates, and organic and inorganic nutrients were investigated under both aerobic and anaerobic conditions. At high concentrations, DEP inhibited all of the strains under both aerobic and anaerobic conditions. Low dissolved oxygen levels and low temperatures decreased the rate of DEP degradation and the growth rate. The addition of casamino acids stimulated anaerobic cell growth and increased the overall DEP degradation rate. Yeast extract increased the aerobic cell growth but inhibited DEP degradation.

INTRODUCTION

Diethyl phthalate (DEP), a phthalic acid ester, is widely used as a plasticizer. DEP is also a suspected teratogen and carcinogen [1], and has been listed as a priority pollutant by the U. S. Environmental Protection Agency [2]. DEP is widespread in soil and water systems, persists in soils, and rapidly penetrates through soil into groundwater [3]. Several investigations into the pathways of DEP biodegradation have been reported [4-7].

As a preliminary study in a project on soil bioremediation, the effects of several environmental factors such as initial primary substrate concentration, secondary substrates, temperature, and organic and inorganic nutrients (including dissolved oxygen) were studied under both aerobic and anaerobic conditions with several microorganisms.

MATERIALS AND METHODS

Microorganisms

These experiments utilized aerobic strains A and X and facultative strains B and G, which were isolated from wastewater treatment plant sludge by enrichment culture using DEP as the sole carbon source.

Medium

The basic medium used in these investigations consisted of 6 g/L Na_2HPO_4, 3 g/L KH_2PO_4, 0.5 g/L NaCl, 1 g/L NH_4Cl, 0.11 g/L $CaCl_2$, 0.247 g/L $MgSO_4 \cdot 7H_2O$, 69.2 mg/L $ZnSO_4 \cdot 7H_2O$, 270 mg/L $FeCl_3 \cdot 6H_2O$, 80 mg/L $MnSO_4$, 7.4 mg/L $CuCl_2$, 28.1 mg/L $CoSO_4 \cdot 7H_2O$, 3 mg/L H_3BO_3, and 10 mg/L yeast extract.

Shake Flask Experiments

The effects of different strains, initial primary substrate concentration, inorganic and organic nutrients other than dissolved oxygen, and secondary substrates on the biodegradation of DEP were studied in shake flask cultures. Preculture 5% (v/v) was inoculated into 100 mL of medium in 500 mL flasks. These flasks were kept in a shaker-incubator during the experiments.

Fermenter Experiments

The effects of dissolved oxygen and temperature on the biodegradation of DEP were studied in a 2 L fermenter with dissolved oxygen and temperature control. Each of these fermenter runs was started by adding 5% (v/v) preculture to 1.5 L medium.

Analytical Methods

DEP and a degradation intermediate, phthalic acid, were assayed using a gas chromatograph equipped with a flame ionization detector. Cell growth was estimated by measuring optical density at 660 nm.

RESULTS

1. AEROBIC DEGRADATION

1.1 DEP Degradation by Different Strains

The DEP degrading abilities of both aerobic and facultative microorganisms were studied under aerobic conditions. The initial DEP concentrations were about 100 mg/L, the temperature was 25 °C, and the cultures were grown in shake flasks. It was found that aerobic strains worked better than anaerobic strains and that aerobic strain A worked best among the four

strains. Facultative strain G degraded DEP faster than facultative strain B under aerobic conditions.

1.2. Effects of the Initial DEP Concentration

Figure 1 presents the results of experiments in which strain A (aerobic) was exposed to different initial DEP concentrations in shake flasks. At higher DEP concentrations, the microorganisms exhibited extended lag times. DEP inhibited not only aerobic strain A but also all of the other strains studied.

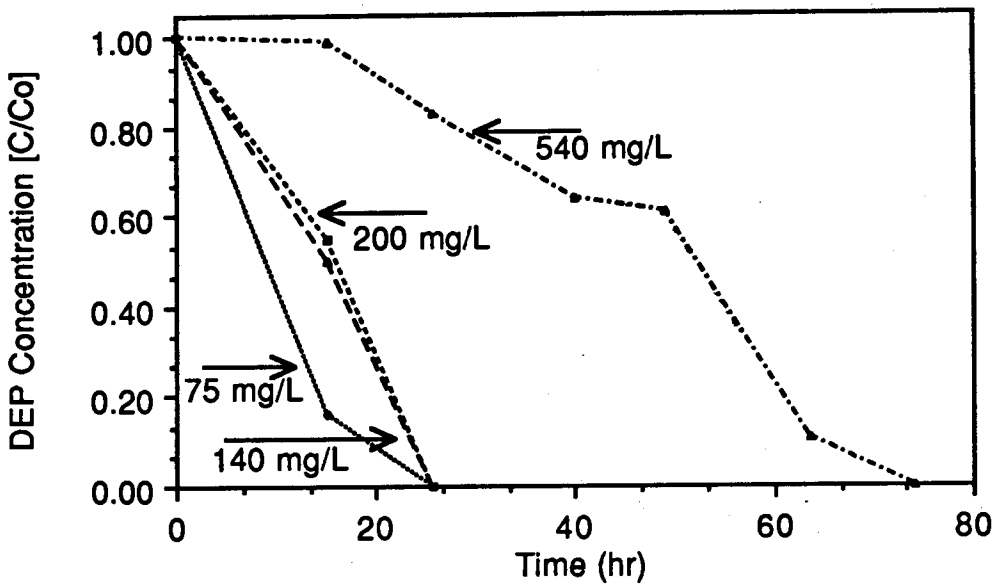

Figure 1. Effects of Initial DEP Concentration Degradation by Aerobic Strain A (Co is the initial DEP concentration)

1.3. Effects of Medium Components and Alternative Substrates

The effects of medium components and some secondary substrates on DEP degradation rates were investigated in shake flask cultures of strain A. The compounds tested and their concentration ranges are:

Yeast Extract	10-1,000 mg/L (1-100 times base level)
Nitrogen	1.9-190 mM (0.1-10 times base level)
Phosphorus	214-1,286 mM (0.33-2 times base level)
Potassium	22-2,200 mM (0.1-10 times base level)
Dextrose	250-1,000 mg/L
Ethanol	125-500 mg/L.

No significant effects were found except in the case of yeast extract, which increased the cell growth but inhibited DEP degradation.

1.4. Effects of Dissolved Oxygen

Figures 2, 3 and 4 show the effects of dissolved oxygen on the growth and the rate of DEP degradation by strain A. The experiments were done in a fermenter at a temperature of 25 °C. At this temperature, the saturation concentration of oxygen is about 3.16 cm^3/100 cc water [8]. At 100% dissolved oxygen, a three-step growth pattern occurred. The primary degradation rate was so fast that the primary substrate (DEP) was completely degraded before the microorganisms attacked a new substrate (a DEP degradation product). At 50% dissolved oxygen, a two-step growth curve was seen, while only one growth curve was observed at 10% dissolved oxygen. At those lower dissolved oxygen conditions, the microorganisms grew more slowly and had more time to adapt to growth on new metabolites.

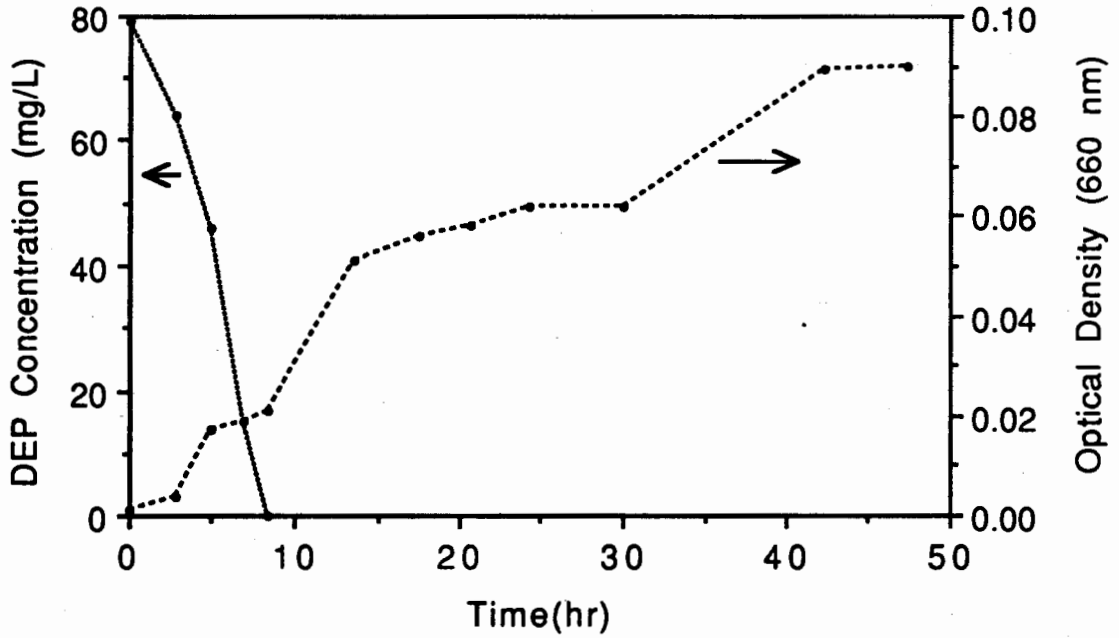

Figure 2. Growth and Degradation by Strain A at 100% Dissolved Oxygen

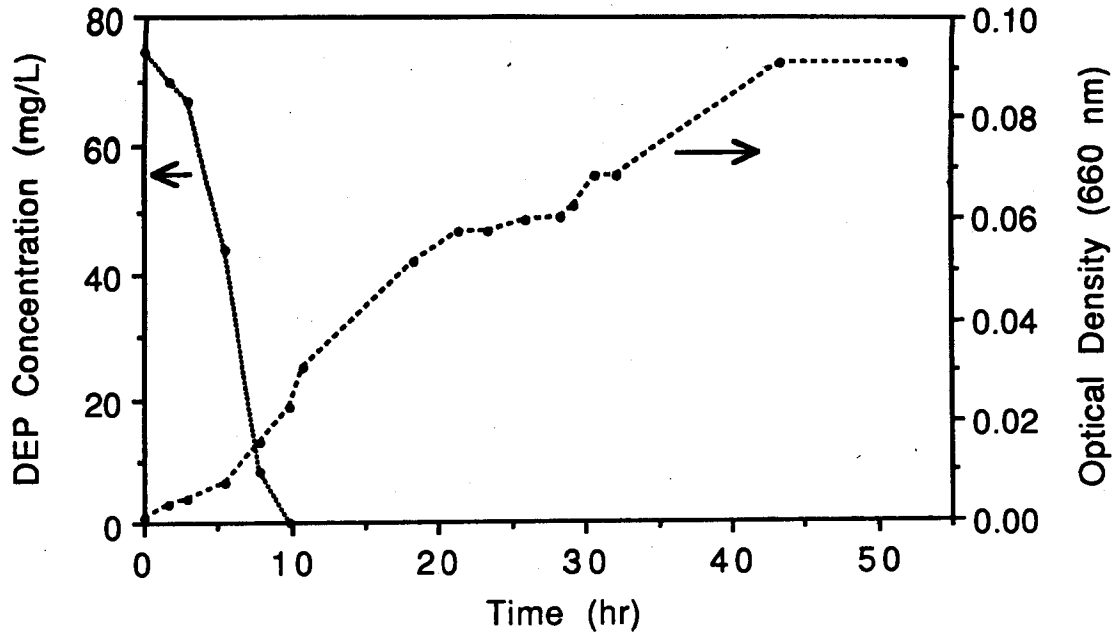

Figure 3. Growth and Degradaton by Strain A at 50% Dissolved Oxygen

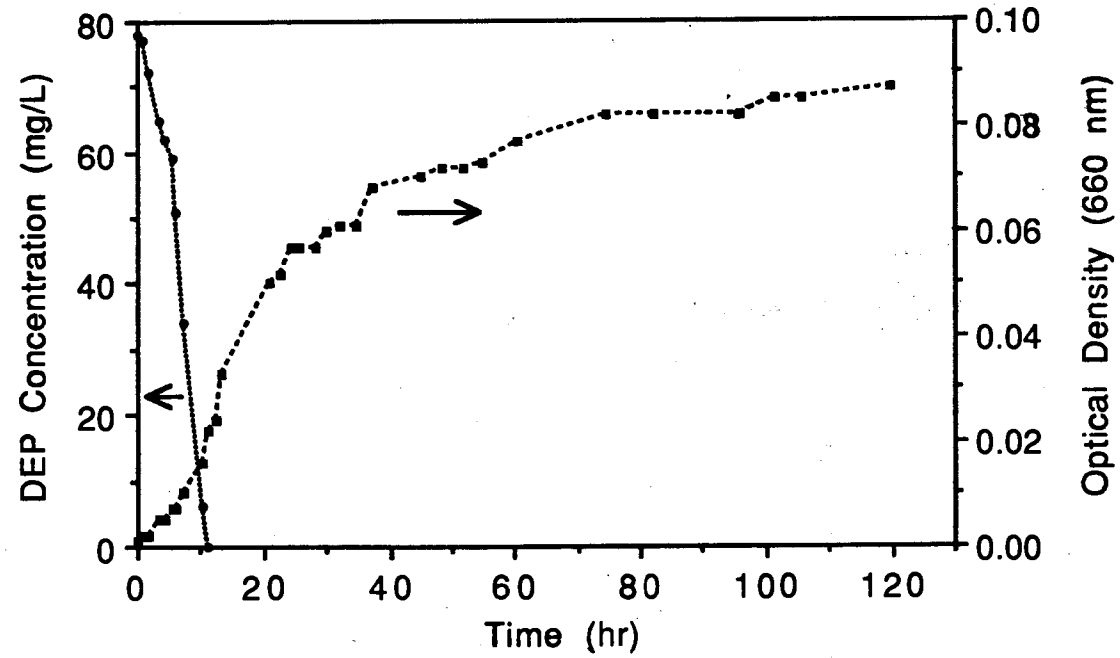

Figure 4. Growth and Degradation by Strain A at 10% Dissolved Oxygen

Figure 5 shows the effects of dissolved oxygen on the rate of DEP degradation by facultative strain B. Lowering the dissolved oxygen concentration affected degradation by the facultative strain much less than the aerobic strain.

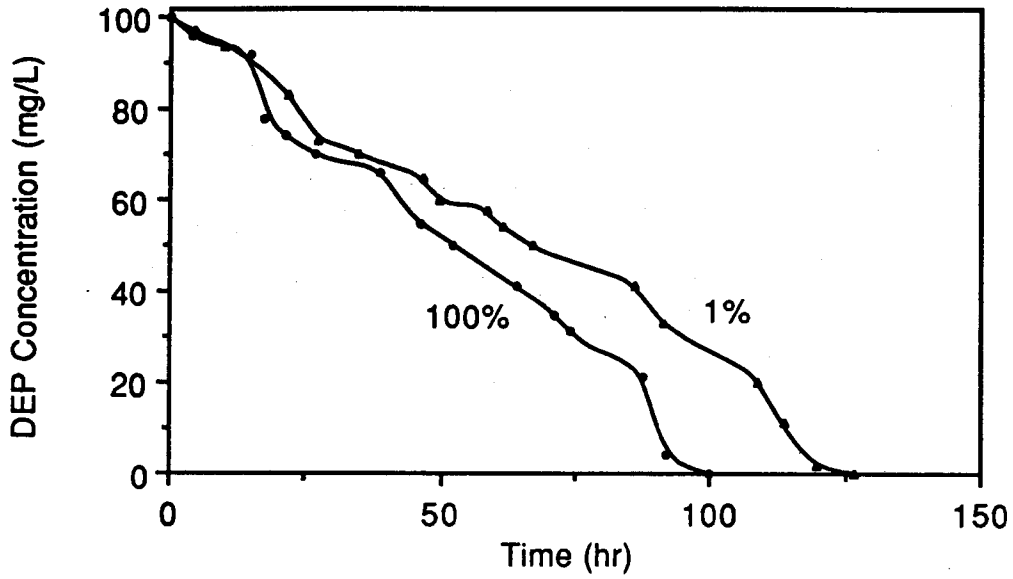

Figure 5. Effects of Dissolved Oxygen Level on Degradation by Facultative Strain B

1.5. Effects of Temperature

The results of fermentation studies under aerobic conditions (100% D.O.) at different temperatures is shown in Figure 6. In the temperature range of 15-25 °C, the degradation rates didn't change significantly. However, the degradation rate at 5 °C was much lower than that at 15 or 25 °C.

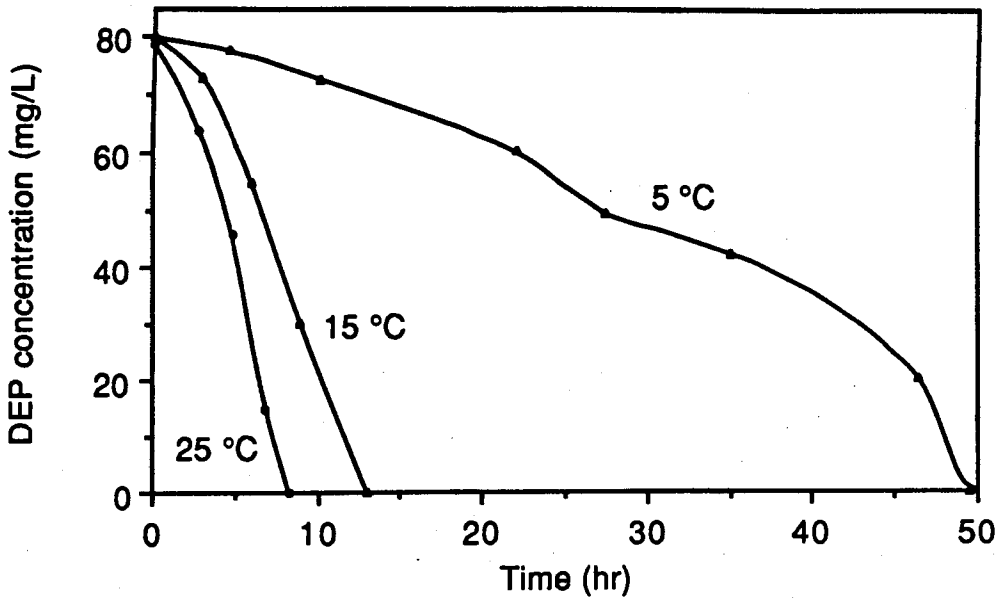

Figure 6. Effects of Temperature on Degradation by Aerobic Strain A

2. ANAEROBIC DEGRADATION

2.1. DEP Degradation by Different Strains

DEP degradation was studied under anaerobic conditions using facultative strains B and G. The initial DEP concentrations were about 50 mg/L, the temperature was 25 °C, and the cultures were grown in an anaerobic hood. It was found that the degradation rate of strain B was faster than that of strain G under anaerobic conditions; the reverse is true in aerobic systems.

2.2. Effects of Initial DEP Concentration

Figure 7 shows the effects of initial DEP concentration on strain B. Clearly, DEP also increased the lag time for facultative strains under anaerobic conditions.

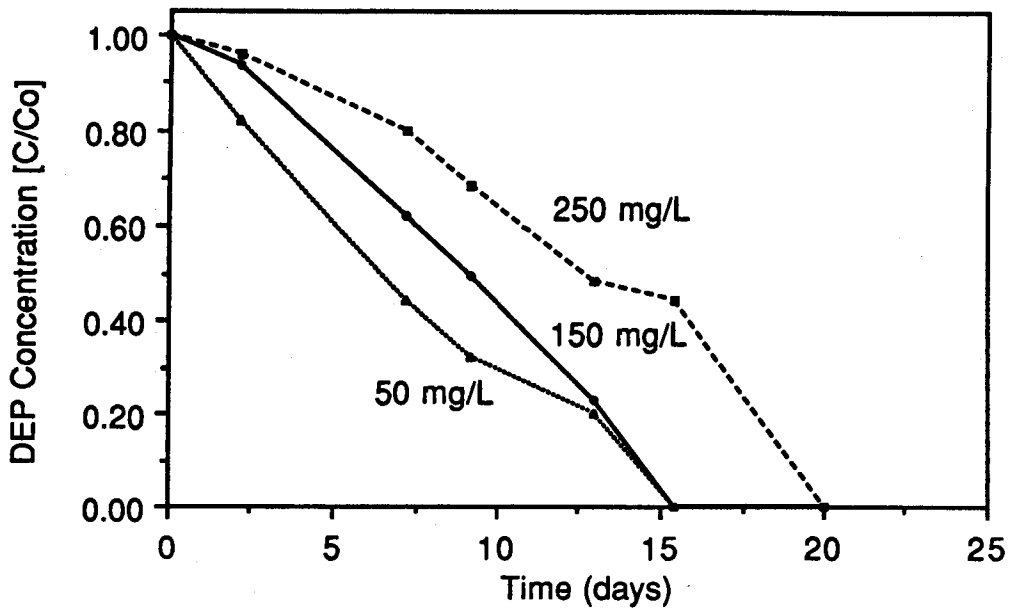

Figure 7. Effects of Initial DEP Concentration on Anaerobic Degradation by Facultative Strain B

2.3. Effects of Medium Components and Alternative Substrates

The effects of one of the medium components (yeast extract) and some secondary substrates on the DEP degradation rates of strain B were investigated under anaerobic conditions. These compounds and their concentration ranges were:

Yeast extract	10-1,000 mg/L (1-100 times base level)
Dextrose	100-1,000 mg/L
Ethanol	10-100 mg/L
Casamino acids	250-2,000 mg/L.

No significant effects were found except in the case of casamino acids. The addition of casamino acids increased the degradation rate at all concentrations studied. The optimal casamino acids concentration was about 1,000 mg/L.

SUMMARY

Aerobic strains A and X and facultative strains B and G, isolated from wastewater treatment plant sludge, have good diethyl phthalate-degrading abilities.

DEP increased the lag time for all of the strains isolated under both aerobic and anaerobic conditions. The higher the concentration, the longer the acclimation phase.

Low dissolved oxygen levels decreased the rate of DEP degradation and the growth rate, especially at higher cell concentrations. Dissolved oxygen affected degradation rates by aerobic strains much more than facultative ones.

Although the degradation rate at 15 °C was not much slower than the rate at 25 °C, lowering the temperature from 15 to 5 °C dramatically slowed the degradation of DEP.

Under anaerobic conditions, the addition of casamino acids stimulated cell growth and increased the overall DEP degradation rate. Under aerobic conditions, yeast extract increased the cell growth but inhibited DEP degradation.

REFERENCES

1. N. Irving Sax. 1987. Hazardous chemicals desk reference. Van Nostrand Reinhold, New York.

2. Natural Resources Defense Council, Inc. v. Train, 8 ERC 2120, 2122-2129. (D.D.C. 1976).

3. T. F. Jenkins, D. C. Leggett, L. V. Parker and J. L. Oliphant. 1985. Toxic organics removal kinetics in overland flow land treatment. Water Res. 19:707-718.

4. Richard H. Sugatt, Dean P. O'Grady, Sujit Banerjee, Philip H. Howard, and W. E. Gledhill. 1983. Shake flask biodegradation of 14 commercial phthalate esters. Appl. Environ. Microbiol. 47:601-606.

5. R. Kurane. 1986. Microbial degradation of phthalate esters. Microbiol. Sci. 3:92-95.

6. Daniel R. Shelton, Stephen A. Boyd, and James M. Tiedje. 1984. Anaerobic biodegradation of phthalic acid esters in sludge. Environ. Sci. Technol. 18:93-97.

7. Dean P. O'Grady, Philip H. Howard, and A. Frances Werner. 1985. Activated sludge biodegradation of 12 commercial phthalate esters. Appl. Environ. Microbiol. 49:443-445.

8. Robert C. Weast. 1984-1985. Handbook of physics and chemistry. CRC Press, Inc., Boca Raton, Florida.

MICROCOSM TREATABILITY OF SOIL CONTAMINATED WITH PETROLEUM HYDROCARBONS

P. Tuitemwong, B.M. Sly, S. Dhawan
L.E. Erickson and J.R. Schlup

Department of Chemical Engineering
Kansas State University
Durland Hall
Manhattan, KS 66506

ABSTRACT

Microcosm studies were carried out to evaluate the microbial treatability of petroleum contaminated soil. The effects of water content, inorganic nutrient addition, and inoculation on the biodegration of hydrocarbons in soil were investigated using small laboratory bioreactors. The evolution of carbon dioxide and the consumption of oxygen were monitored for signs of microbial activity. Dilution plate counts were performed to determine microbial cell number. The concentration of petroleum hydrocarbons was measured with a Fourier transform infrared (FTIR) spectrometer. The maximum extent of biodegradation was attained when the moisture content was at 75% of the water holding capacity (WHC) and when both nutrient and inoculum were added to soil samples in which the moisture content was at 60% of the WHC.

INTRODUCTION

Treatability studies for sites contaminated with organic wastes can provide useful information regarding the potential rate and extent of bioremediation of soil. Several methods have been used to study the treatability of soils, the laboratory microcosm being one such method (Sims *et al.*, 1989). It has been used to study biodegradation in contaminated water, saline water, and soil (Atlas, 1981; Wilson *et al.*, 1983; Russo *et al.*, 1986; Dhawan *et al.*, 1989; Sims *et al.*, 1989). The rate and extent of treatability of soil contaminated with petroleum hydrocarbons can be established in laboratory bioreactors containing microcosms.

Treatability studies validate technology and generate useful data on the rate and extent of biodegradation. Normally, such studies are conducted under nearly optimum conditions with respect to mixing, contact of soil particles with contaminants and microorganisms, and homogeneity throughout the microcosm (U.S. EPA, 1988; Sims, 1990). Therefore, these treatability studies provide an estimate of the maximum level of bioremediation that can be expected from the field scale process.

Literature Review

The major factors which influence biodegradation processes in land treatment are: the chemical compounds in the waste, the physical availability of the waste, the types of microorganisms, the amount of microbial mass, the concentration of waste, and the availability of oxygen and water.

Oxygen transfer. Oxygen can be a limiting factor for biodegradation in microcosms (Dhawan *et al.*, 1989). The availability of oxygen for biodegradation in soil is a function of the gas phase void fraction, partial pressure of oxygen in the soil gases, rate of

oxygen transfer from the gas phase (in the soil) to the aqueous phase, and the rate of oxygen utilization by the microorganisms (Huddleston *et al.*, 1986). The microcosms may reflect the limitations of oxygen transfer and contaminant transport to microorganisms which occur under field conditions. Erickson *et al.* (1990) have developed a model which takes into account the effects of the size and void fraction of the soil aggregate on the growth of biomass, and the transport of oxygen and contaminants through the soil.

Water Content. Biodegradation in the unsaturated soil zone depends on the water content in the soil. Water is necessary not only for the biological processes of the microorganisms, but is also required for the transport of nutrients and substrate to the organisms and of the organisms to the substrate. The water content of soil also affects the diffusion of gases to and from the organism.

The soil water content is measured as the weight fraction of water in a sample; however, it is usually expressed in terms of soil moisture constants such as "saturation capacity" (SC), "water holding capacity" (WHC), and "field capacity" (FC) as upper limits and "permanent wilting percentage" (PWP) as a lower limit. Moisture levels are then established relative to these limits (e.g. 3/4 FC, 60% WHC) (Papendick and Campbell, 1981).

Water holding capacity (WHC) or saturation content (SC) is usually taken as the water content at saturation. Typically, the water content in soil ranges from 25 to 100% WHC which is equivalent to about 7 to 28 volume percent. Microbial activity is usually optimum at a moisture level equal to 60% WHC (Griffin, 1981; Harris, 1981; Linn and Doran, 1984), but a recent study has found that a value of 75% WHC in the field provided optimal conditions for biodegradation (Hinchee *et al.*, 1989).

Inorganic nutrients. Microorganisms use available inorganic nutrients in soil for biodegradation of hydrocarbons; however, the nitrogen and phosphorous in soil are not sufficient for shock loading of hydrocarbons and are depleted rapidly (McGill, 1980; Overcash and Pal, 1979). Fertilizer has been used to supply essential nutrients, basically N and P, to the contaminated soil. The C/N ratio reported to be effective for biodegradation is 25 or lower; a higher C/N ratio (over 38) is considered to be an indication of nitrogen depletion (Routson and Wildung, 1970; Huddleston et al., 1986).

Microbial biomass. A high starting cell number leads to a high rate of biodegradation when nutrients and oxygen are available (Huddleston *et al.*, 1986). In many circumstances, the initial number of microorganisms in contaminated soil is low. Moreover, microorganisms need a certain period of time to acclimatize themselves to the new environment. Addition of specific microorganisms for hydrocarbon degradation increases the chance to remove the hydrocarbon more rapidly (Solmar, 1989).

Objectives

A treatability study was conducted using soil microcosms to examine the effects of soil water content, inorganic nutrient additions, and microbial supplements on the biodegradation of petroleum hydrocarbons in soil. The main objective of the study was to examine the effect of soil water content on hydrocarbon biodegradation. Other objectives of the study were:

a. to study the effects of inorganic nutrient and microbial supplements on the extent of biodegradation of the petroleum hydrocarbons in the soil samples;

b. to develop microcosm methods for evaluating the treatability of petroleum hydrocarbons in soil samples;

c. to develop solvent extraction methods and FTIR quantitative analysis techniques for measuring hydrocarbons in soil samples.

MATERIALS AND METHODS

Sampling Methodology

Soil samples were collected from each of the two stockpiles of petroleum contaminated soil at the project site. The soil samples were mixed together manually for 20 minutes, divided into jars, and kept in a refrigerator.

Microcosm Study

Sample preparation. Microcosm samples were prepared by adding 150 g of soil to each 250 mL Erlenmeyer flask. To study the effect of soil water content, deionized water was added to obtain samples with moisture levels equal to 25, 60, 75, and 100% WHC. To investigate the effects of nutrients and inoculum, samples with the inorganic nutrients as indicated by Chiu *et al.* (1972) and microbial powder obtained from Solmar company (strain L104) were prepared individually and in combination; water was added to obtain samples with 60% WHC. Control samples containing only soil with nothing added were also prepared. A rubber stopper with a hypodermic needle inserted was placed over the opening of each Erlenmeyer flask. The stopper and needle were covered with heavy duty aluminum foil which was held in place with a rubber band placed around the neck of the flask to limit the leakage of gases. Duplicates for all samples were prepared.

Mixing. Samples were mixed by manually shaking the flasks without opening them each day for the first month; however, the mixing was not very effective because of aggregate formation. Samples supplemented to 60% WHC with deionized water were prepared and used as controls to study the case of no mixing.

Head space gas analysis. The activity of the microorganisms was monitored by measuring carbon dioxide and oxygen. Head space gases expressed as peak fraction of CO_2 and O_2 were analyzed by a computerized Dycor mass spectrometer. The capillary probe of the mass spectrometer was inserted through the hypodermic needle in the flask on a daily basis. The capillary probe was left for 0.5 to 1.0 min. before the gas composition was analyzed with the mass spectrometer and the resulting data were stored in the computer. A second set of data was obtained 10 seconds later.

Dilution plate counts. The bacterial numbers were evaluated by dilution plate count (Urban, 1977); samples were taken at the time the flasks were opened to let oxygen into the system.

Analysis of hydrocarbons. Hydrocarbons in the soil were analyzed by a Fourier transform infrared (FTIR) spectrometer. The modified ASTM standard method D3921-85, designed for detecting hydrocarbons in water and waste water, was used (ASTM, 1989). In this method, the determination of the fluorocarbon-extractable substances is used to estimate the combined hydrocarbon content in a water sample. Hydrocarbons in a soil sample were extracted using 1,1,2-trichloro-1,2,2-trifluoroethane (Fluorocarbon 113, Aldrich Chemical); the clear liquid portion was analyzed. One hundred and fifty grams of a soil sample were weighed and acidified to pH less than 2.0 with 6N hydrochloric acid (HCl). The sample was placed in a 500 mL separatory funnel with teflon

stopcock. Four 50 mL extractions were performed. The mixture was left standing for at least 1 min; then it was vigorously shaken for 2 min. After again standing for 1 min, the solvent was drained from the separatory funnel. The solvent was filtered through number 40 Whatman filter paper and collected into a 200 mL volumetric flask. The tip of the separatory funnel, the filter paper, and the funnel were rinsed with a total of 5-10 mL solvent; this solvent was collected in the volumetric flask. The extract was diluted when it was suspected to contain greater than 1000 mg/L of hydrocarbon. Five to ten mL of the final liquid were discarded, and 3 g silica beads (grade 923, 100-200 mesh, Aldrich Chemical) were added to the extracted portion. The flask was closed and stirred for 5 min with a magnetic stirrer.

The hydrocarbon content of the clear liquid portion was measured using FTIR spectroscopy as per ASTM standard method D3921-85. The infrared data were acquired on a Mattson Instruments Nova Cygni 120 spectrometer with a triglycine sulfate (TGS) detector. Each spectrum was acquired by co-adding 32 scans at 4 cm^{-1} resolution. A 10 mm cell with potassium bromide (KBr) windows was used. The results were obtained from the maximum peak absorbance at about 2930 cm^{-1} using a two point corrected absorbance. The maximum absorbance was obtained from the distance between this connecting line and the apex of the 2930 cm^{-1} peak.

The calibration curve was obtained by measuring the absorption of the infrared spectrum of the serial dilutions (20 to 400 mg/L) of 15mL/15mL n-hexadecane and isooctane in the solvent 1,1,2-trichloro-1,2,2-trifluoroethane. A plot of the absorbance against the hydrocarbon concentration (mg/kg) was prepared. The concentrations of the hydrocarbons in the samples were obtained from this calibration curve.

Total organic carbon analysis. Soil samples obtained from the sites were mixed manually for 20 minutes and divided into jars. Five samples were drawn from each of three jars for total organic carbon analysis. The soil samples, each weighing 7 to 12 mg, were placed directly into the "boat" of the Total Organic Carbon analyzer (Dohrmann DC-180). The data obtained was analyzed statistically to evaluate the homogeneity of hydrocarbons in the mixed soil sample.

Moisture content. Several ten gram samples of soil were dried in an oven at 105°C for 24 hours. The samples were weighed after they were cooled to room temperature in a desiccator.

RESULTS

Water Content and Soil Analyses

The moisture contents of the soil samples were 14.02% (w/w) for the original soil sample and 16.16, 19.57, 24.52, and 30.50% for samples with water added to obtain 25, 60, 75, and 100% of the water holding capacity, respectively. An unmodified soil sample contained phosphorus, nitrate nitrogen, ammonia nitrogen, and sulfur (SO_4-S) of 24, 1, 12.5, and 120 mg/L, respectively.

Cell Number

Cell numbers in the soil samples are tabulated in Tables 1 and 2. The initial numbers of microorganisms in the uninoculated samples were about the same, 1.0 to 1.2 x 10^6 per gram soil; the inoculated samples contained 1.2 x 10^7 cells per gram soil. The recommended amount of cell powder was 50 g powder per 1000 cubic yards of soil which corresponds to the 1.6 mg per 150g soil used in this experiment. The initial number of cells in 1 gram of cell powder was 1.3 x 10^9. The powder consisted of dry cells and filler; it was

recommended to soak the powder in warm water for 4-6 h before use (Solmar, 1989). The cell number obtained from the microbial count of the inoculated soil was larger than the calculated value; this may be due to cell reproduction during the time the powder was soaked in warm water. The results in Tables 1 and 2 indicate that the number of microorganisms increased during the first 45 days for each of the microcosm experiments. The cell numbers measured at 220 days were less than those reported at 45 days.

Gas Phase Measurements

The peak fractions of oxygen and carbon dioxide in the head space of soil samples having different water contents were measured. After 28 days of incubation, the samples were opened to replenish the oxygen supply. There are differences in oxygen consumption between low water content (25% WHC) and high water content (60 to 100% WHC).

Hydrocarbon Measurements

The results obtained using ASTM method D3921-85 (FTIR hydrocarbon analysis) are presented in Figures 1 and 2. This analysis measures the hydrocarbon compounds based on the absorbance at 2930 cm^{-1}. The absorbance at 2930 cm^{-1} represents the C-H stretching of aliphatic hydrocarbons (George and McIntyre, 1987). George and McIntyre (1987) point out that CH_2 groups in alkanes have absorbance peaks at 2926 and 2853 cm^{-1} and that CH_3 groups in alkanes exhibit two peaks at 2962 and 2872 cm^{-1}. The peaks obtained indicate that the original samples contain hydrocarbon compounds. The concentrations of hydrocarbons determined by this method indicate maximum biodegradation at a water content equal to 75% WHC (Figure 1) and when nutrient and inoculum are added to samples with 60% WHC (Figure 2).

DISCUSSION

The numbers of microorganisms appeared to be relatively stable at about 10^6 to 10^7 per gram of soil; lower numbers were obtained after 220 days of incubation. The results at 45 days indicated that microbial reproduction had occurred; the production of carbon dioxide and consumption of oxygen and the reduction of hydrocarbon concentration in the soil also provided evidence of biodegradation. The gas phase measurements were continued after 220 days of bioremediation; however, they showed no evidence of oxygen consumption and carbon dioxide production.

In Figure 1, the sample with the water content equal to 75% WHC has the lowest final hydrocarbon concentration. This could be due to the effect of water content on substrate diffusion. The availability of the hydrocarbons to the microorganisms may be greatest at a water content of 75% WHC. The diffusion of oxygen to the microorganisms may limit growth rates in soils with high water contents; however, the extent of bioremediation should not be limited by the availability of oxygen. Inorganic nutrients were not added to the samples described in Figure 1. The results in Figure 2 clearly indicate that inorganic nutrient addition increased the extent of bioremediation.

The addition of the inoculum solution improved the extent of bioremediation. Since the inoculum solution contained some inorganic nutrients, the results in Figure 2, where the inoculum solution was added and the nutrient solution was not added, are superior to those where only the nutrient solution was included. The best results were obtained when both the inorganic nutrient solution and the inoculum solution were added. The inoculum was a commercially produced microorganism especially made for hydrocarbon degradation.

The soil samples were collected at several locations at the project site which contained two stockpiles of petroleum contaminated soil. Manual methods were used to blend the samples; several experimental results suggest that the samples were not completely mixed during the 20 minutes of manual mixing. Hydrocarbon analyses on the original soil samples showed a mean concentration of 421 mg/kg and a standard deviation of 261 mg/kg. This standard deviation is much larger than that expected as a consequence of the analytical technique alone. These results were obtained from three samples with each sample taken from a different jar of the blended soil.

A total organic carbon analyzer was also used to investigate the variation in carbon content of several of the original soil samples after blending. The sample size for the total organic carbon analyzer ranged from 7.0 to 12.6 mg of soil; each sample was placed directly into the boat of the instrument. The mean value of the total organic carbon from 15 samples was 15.2 g/kg. However, for each of the three jars with 5 samples per jar the results were as follows: 8.26 g/kg $\pm$ 2.26, 20.86 $\pm$ 7.50, and 16.51 $\pm$ 11.98 where the mean and standard deviation are presented for each jar. These results show that the 20 minutes of manual mixing was not sufficient to obtain a uniformly blended mixture. Differences in the results reported in this work may be due, in part, to variations in the initial hydrocarbon concentration among samples because of inadequate mixing.

CONCLUDING OBSERVATIONS

Petroleum hydrocarbons were not completely degraded by microorganisms over a period of 220 days. Among the samples containing moisture equal to 60% of the water holding capacity, the ones to which inorganic nutrients and inoculum had been added resulted in the greatest extent of biodegradation. Based on experiments conducted at several different soil moisture contents, the greatest extent of biodegradation was observed when the soil moisture was at 75% of the water holding capacity. The number of microorganisms in the microcosms was larger after 45 days than at the start of the experiment; however, the numbers had declined after 220 days.

FTIR analysis (as per ASTM method D3921-85) is very applicable for the determination of hydrocarbons in soil samples once suitable procedures have been developed for their extraction. While the standard test method provides information regarding aliphatic hydrocarbons, current FTIR spectroscopic techniques simultaneously provide information concerning aromatic hydrocarbons as well.

ACKNOWLEDGEMENT

Although the research described in this article has been funded in part by the U.S. Environmental Protection Agency under assistance agreement R-815709 to the Hazardous Substance Research Center for U.S. EPA Region 7 and 8 headquartered at Kansas State University, it has not been subjected to the Agency's peer and administrative review and therefore may not necessarily reflect the views of the Agency and no official endorsement should be inferred. This research was partially supported by the Kansas State University Center for Hazardous Substance Research. The authors thank Nancy Berry and L. T. Fan.

REFERENCES

American Society for Testing Materials Test D3921-85, "Standard Test Method for Oil and Grease and Petroleum Hydrocarbons in Water," 1989 Annual Book of ASTM Standards 11.02, pp. 42-46 (1989).

Atlas, R.M.,"Microbial Degradation of Petroleum Hydrocarbon: Microbial Perspective," Microbiological Review, 45:180-209 (1981).

Campbell, G.S., "Soil Water Potential Measurement: An Overview," Irrig. Sci., 9:265-273 (1988).

Chiu, S.Y., L.E. Erickson, L.T. Fan, and I.C. Kao, "Kinetic Model Identification in Mixed Population Using Continuous Culture Data," Biotechnol. Bioeng., 14:207-231 (1972).

Dhawan, S., L.E. Erickson, L.T. Fan, P. Tuitemwong, and R. Mahadevaiah, "Microcosm Techniques for Investigating the Biodegradation Potential of Light-Non Aqueous Phase Liquids and Dense-Non Aqueous Phase Liquids," in Proceedings of the Conference on Hazardous Waste Research, L.E. Erickson, ed., Kansas State University, Manhattan, Kansas, pp. 578-599 (1989).

Erickson, L.E., L.T. Fan, S. Dhawan, and P. Tuitemwong, "Modeling, Analysis, and Simulation of Bioremediation of Soil and Water," in Proceedings of the Conference on Hazardous Waste Research, L.E. Erickson, ed., Kansas State University, Manhattan, Kansas (1990).

George, W.O., and P.S. McIntyre, Infrared Spectroscopy, John Wiley, N.Y. (1987).

Griffin, D.M., "Water Potential as a Selective Factor on Microbial Ecology of Soils," in Water Potential Relations in Soil Microbiology, J.F. Parr, W.R. Gardner, and L.F. Elliott, eds., Soil Science Society of America, pp. 141-160 (1981).

Harris, R.F. "Effect of Water Potential on Microbial Growth and Activity, in Water Potential Relations in Soil Microbiology, J.F. Parr, W.R. Gardner, and L.F. Elliott, eds., Soil Science Society of America, pp. 23-26 (1981).

Hinchee, R.E., D.C. Downey, R.R. Dupont, and M. Arthur, "Enhanced Biodegradation through Soil Venting," Final report Prepared for Battelle for Scientific Services Program Task No. 88-427 (1989).

Huddleston, R.L., C.A. Bleckmann, and J.R. Wolfe, "Land Treatment Biological Degradation Process," in Land Treatment: A Hazardous Waste Management Alternative, R.C. Loehr, J.F. Malina, eds., University of Texas Press, Austin,TX (1986).

Linn, M.D. and J.W. Doran, "Effect of Water-Filled Pore Space on Carbon Dioxide and Nitrous Oxide Production in Tilled and Nontilled Soils," Soil Sci. Soc. Am. J., 38:1267-1272 (1984).

McGill, W.B., Factors Affecting Oil Degradation Rates in Soil," in Disposal of Industrial and Oily Sludges by Land Cultivation, D.M. Shilesky, ed., Resource Systems and Management Association, Northfield, N.J., pp. 103-122 (1980).

Overcash, M.R. and D. Pal, Design of Land Treatment Systems for Industrial Wastes-Theory and Practices, Ann Arbor Science Publ. Inc., Ann Arbor, MI (1979).

Papendick, R.I. and G.S. Campbell, "Theory and Measurement of Water Potential," in Water Potential Relations in Soil Microbiology, J.F. Parr, W.R. Gardner, L.F. Elliott, eds., Soil Science Society of America, pp. 1-22 (1981).

Routson, R.C. and R.E. Wildung, Ind. Water Eng., 7(10): 25-27 (1970).

Russo, M.F., D.S. Kosson, and R.C. Ahlert, "Biodegradation Process Analysis By Ultrafiltration," Chem. Engg. Commun., 42:53-59 (1986).

Sims, R.C., "Soil Remediation Techniques at Uncontrolled Hazardous Waste Sites," J. Air Waste Management Association, 40:704-732 (1990).

Sims, J.L., R.C. Sims, and J.E. Matthews, Bioremediation of Contaminated Soils, U.S. Environmental Protection Agency, Robert S. Kerr Environmental Research Laboratory, Ada, OK, EPA\600\9-89\073 (August, 1989).

Solmar Corporation, Treatment of Contaminated Soils, Solmar Corporation, 625 West Katella Ave., Suite 5, Orange, CA (1989).

Urban, J.E., Laboratory Manual for Microbiology, Avery Publishing Group, Wayne, New Jersey (1977).

U.S. EPA., Interim Protocol for Determining the Aerobic Degradation Potential of Hazardous Organic Constituents in Soil, Robert S. Kerr Environmental Research Laboratory, Ada, OK (1988).

Wilson, J.T., J.F. McNabb, D.L. Balkwill, and W.C. Ghiorse,"Enumeration and Characterization of Bacteria Indigenous to a Shallow Water-Table Aquifer," Groundwater, 21:134-141 (1983).

Table 1. Cell Numbers in Soil Samples at Several Different Water Contents at Days 1, 45, and 220; Units are Number/g.

Treatment	Day 1	Day 45	Day 220
No water added	1.2×10^6	8.6×10^6	4.4×10^5
25% WHC	1.2×10^6	1.6×10^7	6.2×10^5
60% WHC	1.2×10^6	1.2×10^7	9.9×10^5
75% WHC	1.0×10^6	9.6×10^6	3.1×10^6
100% WHC	1.0×10^6	8.3×10^6	1.0×10^6

Table 2. Cell Numbers in the Soil Samples from Different Treatments at Days 1, 45, and 220; Units are Number/g.

Treatment	Day 1	Day 45	Day 220
Control	1.0×10^6	6.1×10^6	9.7×10^5
Nutrient	1.0×10^6	7.2×10^6	1.1×10^6
Inoculum	1.2×10^7	2.2×10^7	9.0×10^5
Nutrient+Inoculum	1.2×10^7	4.4×10^7	1.1×10^6
No mixing	1.0×10^6	8.0×10^8	8.6×10^5

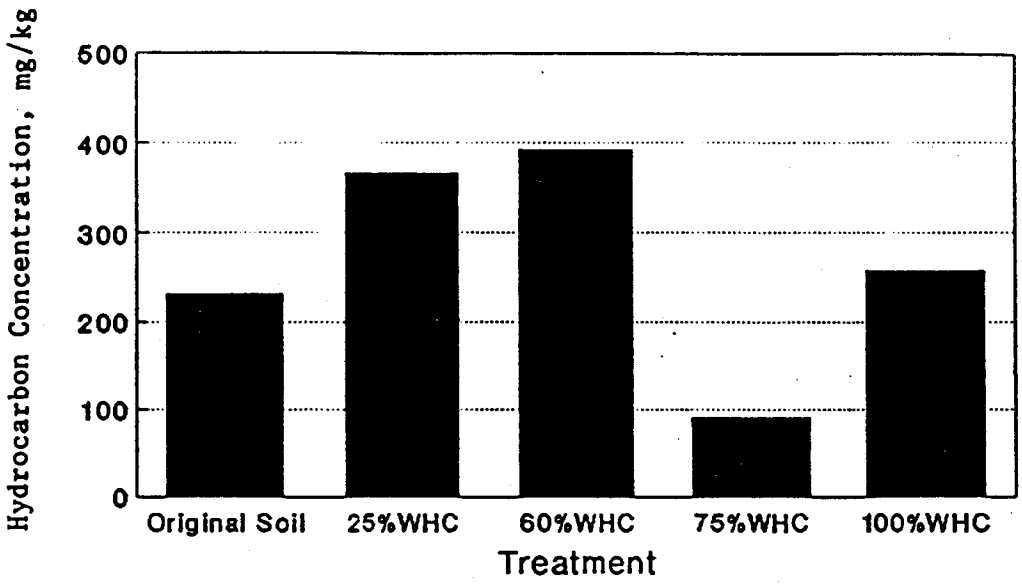

Figure 1. Final hydrocarbon concentrations (mg/kg at day 220) in the soil samples with different moisture contents.

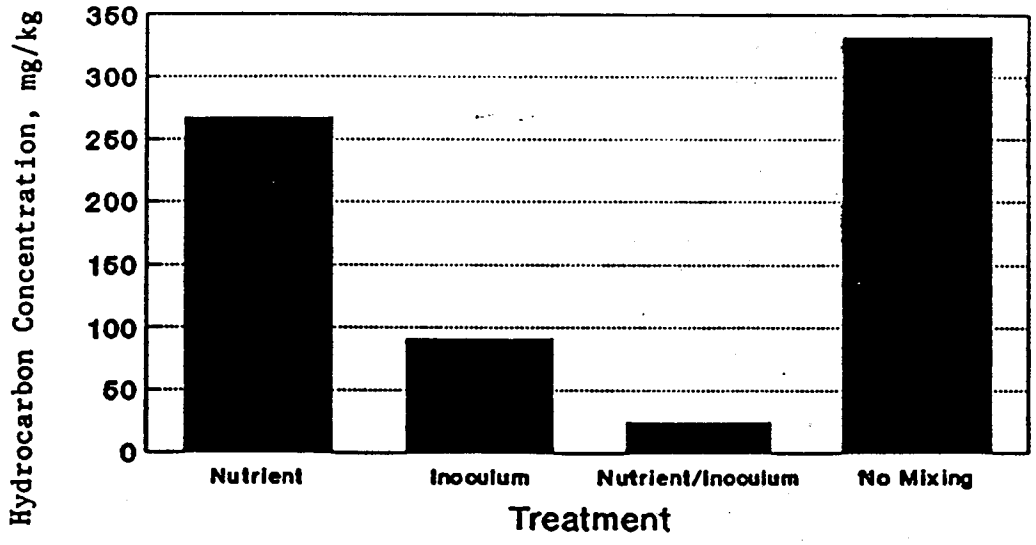

Figure 2. Final hydrocarbon concentrations (mg/kg at day 220) in soil samples supplemented with nutrient, inoculum, and nutrient and inoculum. The soil sample with no mixing was supplemented with deionized water. The moisture content was 60% WHC in all cases.

INSTITUTE FOR SYSTEMS DESIGN AND OPTIMIZATION*

76. Computer Simulation of Transient in Isothermal Fluid-Solid Reaction Systems - Effects of Mode and Magnitude of the Diffusivity Variation, by L.S. Fan, L.T. Fan and Kei Miyanami, June 1976.

77. A Mathematical Model for Pyrolysis of a Solid Particle - Effects of the Heat of Reaction, by Kei Miyanami, L.S. Fan, L.T. Fan and W.P. Walawender, June 1976.

78. Simulation of Cyclic Dynamics in Isothermal Gas-Solid Reaction Systems - Effects of the Frequency of Sinusoidal Perturbation on the Bulk Gas Concentration, by L.T. Fan, Liang-Shih Fan, and Kei Miyanami, August 1976.

79. Kinetics of Protective Coating Formation in Reactive Environments - Simulation by means of a Macroscopic, Distributed Parameter Model, by L.T. Fan, Kei Miyanami, and Liang-Shih Fan, October 1976.

80. Stochastic Diffusion Model of a Fluid-Solid Reaction, by L.T. Fan, L.S. Fan and S.H. Shin, September 1977.

81. Proceedings of the Ninth Annual Biochemical Engineering Symposium, L.T. Fan and L.E. Erickson Eds., April 1979.

82. Proceedings of the Twelfth Annual Biochemical Engineering Symposium, L.E. Erickson and L.T. Fan Eds., April 1982.

83. Shallow Fluidized Beds with Lateral Solids Flow: A Review and the Derivation of a General Model, by C.C. Chang and L.T. Fan, November 1982.

84. Shallow Fluidized Beds, by C.C. Chang and L.T. Fan, January 1985.

85. A Novel Fluidized-Bed Process for Toxic Waste Destruction, by S.K. Singh, D. Neogi, W.P. Walawender, L.T. Fan and C.C. Chang, April 1985.

86. Mathematical Models for Controlled Release Systems, by L.T. Fan and S.K. Singh, June 1986.

87. Proceedings of the Sixteenth Annual Biochemical Engineering Symposium, L.E. Erickson and L.T. Fan Eds., April 1986.

* Copies of these reports can be obtained by writing to:

Professor L.T. Fan
Director, Systems Institute
c/o Department of Chemical Engineering
105 Durland, Kansas State University
Manhattan, Kansas 66506-5102.